

# Dissertation

*submitted to the*

Combined Faculties of the Natural Sciences and Mathematics  
*of the* Ruperto-Carola University of Heidelberg, Germany

*for the degree of*

Doctor of Natural Sciences

*Put forward by*

Anton Konrad Cyrol

*born in:* Gießen, Germany

Oral examination: November 27th, 2017

# Non-perturbative QCD Correlation Functions

Referees: Prof. Dr. Jan M. Pawłowski  
Prof. Dr. Joerg Jaeckel

## Nichtperturbative QCD-Korrelationsfunktionen

Funktionale Methoden bieten Zugang zu dem stark gekoppelten Niedrigenergie-Sektor der Quantenchromodynamik. Diese ermöglichen folglich die Erforschung von Confinement und chiraler Symmetriebrechung. In dieser Dissertation werden Korrelationsfunktionen der Yang-Mills-Theorie und der Zwei-Quark-QCD mit der funktionalen Renormierungsgruppe hergeleitet. Mittels einer konsistenten Vertex-Entwicklung der effektiven Wirkung werden Yang-Mills-Korrelationsfunktionen sowohl in vier als auch in drei Raumzeit-Dimensionen berechnet. Dazu werden Bedingungen für Confinement und Slavnov-Taylor-Identitäten diskutiert. Die Resultate zeigen eine sehr gute Übereinstimmung mit Gitter-Ergebnissen. Anschließend wird QCD betrachtet, wobei festgestellt wird, dass der Gluon-Propagator weitgehend unabhängig von der Pionmasse ist. Außerdem wird die Notwendigkeit konsistenter Näherungen betont. Zuletzt werden die Korrelationsfunktionen der Yang-Mills-Theorie bei endlicher Temperatur berechnet. Dies geschieht in einer Näherung, die die durch das Wärmebad ausgezeichnete Richtung im Gluonfeld berücksichtigt. Insbesondere wird die ausgezeichnete Richtung auch in den Drei- und Vier-Gluon-Kopplungen unterschieden. Der errechnete Gluon-Propagator ermöglicht es eine Debye-Masse zu bestimmen. Diese stimmt bei hohen Temperaturen mit der störungstheoretischen thermischen Masse überein, ist im Gegensatz zu letzterer jedoch auch bei Temperaturen unterhalb der Phasenübergangstemperatur aussagekräftig.

## Non-perturbative QCD Correlation Functions

Functional methods provide access to the non-perturbative regime of quantum chromodynamics. Hence, they allow investigating confinement and chiral symmetry breaking. In this dissertation, correlation functions of Yang-Mills theory and unquenched two-flavor QCD are computed from the functional renormalization group. Employing a self-consistent vertex expansion of the effective action, Yang-Mills correlation functions are obtained in four as well as in three spacetime dimensions. To this end, confinement and Slavnov-Taylor identities are discussed. Our numerical results show very good agreement with corresponding lattice results. Next, unquenched two-flavor QCD is considered where it is shown that the unquenched two-flavor gluon propagator is insensitive to the pion mass. Furthermore, the necessity for consistent truncations is emphasized. Finally, correlation functions of finite-temperature Yang-Mills theory are computed in a truncation that includes the splitting of the gluon field into directions that are transverse and longitudinal to the heat bath. In particular, it includes the splitting of the three- and four-gluon vertices. The obtained gluon propagator allows to extract a Debye screening mass that coincides with the hard thermal loop screening mass at high temperatures, but is meaningful also at temperatures below the phase transition temperature.

# Contents

<b>1. Introduction</b>	<b>7</b>
1.1. Motivation	7
1.2. Publications	9
1.3. Outline	10
<b>2. Quantum Chromodynamics</b>	<b>11</b>
2.1. Action and BRST Symmetry	11
2.2. Asymptotic Freedom	16
2.3. Confinement	16
2.4. Chiral Symmetry Breaking	19
<b>3. Functional Methods</b>	<b>20</b>
3.1. Functional Renormalization Group	20
3.1.1. Wetterich Equation	20
3.1.2. Regulators	22
3.1.3. Vertex Expansion	25
3.2. Dyson-Schwinger Equations	26
<b>4. Tracing Large Expressions</b>	<b>28</b>
4.1. Features of FormTracer	28
4.2. Decomposition of Tensor Classes	29
4.3. Simple Compact Lie Groups	29
4.4. Dirac and Lorentz Tracing	30
4.4.1. Dirac Traces in General Dimensions	30
4.4.2. Finite Temperature and Density Tracing	31
4.5. Conclusion	32
<b>5. Yang-Mills Correlators</b>	<b>33</b>
5.1. Vertex Expansion and Transversality	34
5.1.1. Flow Equations	34
5.1.2. Tensor Structures	35
5.1.3. Modified STIs and Transversality	37
5.2. Confinement	40
5.2.1. Gluon Mass Gap and Irregularities	40
5.2.2. Necessity for Irregularities	41
5.2.3. Origin of Irregularities	44
5.2.4. Ghost Triangle	45
5.2.5. Purely Transverse System	45
5.3. Numerical Results	46
5.3.1. Correlation Functions and Running Couplings	47
5.3.2. Truncation Analysis	48

5.3.3.	Comparison to Other Results . . . . .	50
5.3.4.	Mass Gap, mSTIs and Types of Solutions . . . . .	50
5.3.5.	Discussion . . . . .	53
5.4.	More and Refined Results . . . . .	57
5.4.1.	Gauge Group Dependence . . . . .	57
5.4.2.	Beta Functions . . . . .	57
5.4.3.	Refined Mass Gap Analysis . . . . .	59
5.5.	Conclusion . . . . .	62
<b>6.</b>	<b>Yang-Mills Theory in Three Dimensions</b>	<b>63</b>
6.1.	Basics . . . . .	63
6.2.	Results . . . . .	64
6.2.1.	Propagators . . . . .	65
6.2.2.	Infrared Scaling Fixed Point . . . . .	66
6.2.3.	Vertices . . . . .	67
6.3.	Conclusion . . . . .	68
<b>7.</b>	<b>Unquenched Two-Flavor QCD</b>	<b>69</b>
7.1.	Setup . . . . .	69
7.1.1.	Flows and Dynamical Hadronization . . . . .	70
7.1.2.	Truncation . . . . .	72
7.1.3.	Tensor Bases . . . . .	75
7.1.4.	Quark-Gluon Vertex STI . . . . .	77
7.1.5.	Initial Cutoff Action . . . . .	79
7.2.	Numerical Results . . . . .	79
7.3.	Discussion . . . . .	84
7.4.	Conclusion . . . . .	85
<b>8.</b>	<b>Finite-Temperature Yang-Mills theory</b>	<b>87</b>
8.1.	Temperature . . . . .	87
8.1.1.	Finite-Temperature Vertex Expansion . . . . .	87
8.1.2.	Non-Trivial Vacuum and Backgrounds . . . . .	90
8.1.3.	Debye Screening Mass . . . . .	93
8.2.	Finite-Temperature Flows . . . . .	95
8.2.1.	Flow Equations . . . . .	95
8.2.2.	Renormalization and mSTIs . . . . .	96
8.2.3.	Gluon Mass Parameter . . . . .	97
8.3.	Results . . . . .	98
8.3.1.	Propagators . . . . .	98
8.3.2.	Gluonic Vertices . . . . .	100
8.3.3.	Comparison with Earlier Results . . . . .	100
8.4.	Discussion . . . . .	101
8.4.1.	Non-trivial Backgrounds and Propagators . . . . .	101
8.4.2.	Debye Mass and the Perturbative Regime . . . . .	103
8.4.3.	Three-Gluon Vertex and its Zero Crossing . . . . .	103
8.5.	Conclusion . . . . .	105
<b>9.</b>	<b>Summary and Outlook</b>	<b>106</b>

<b>A. Gluonic Vertices at Finite Temperature</b>	<b>108</b>
A.1. Tensor Splitting . . . . .	108
A.2. Zero Modes . . . . .	109
A.3. Projecting . . . . .	110
A.3.1. Three-Gluon Vertex . . . . .	111
A.3.2. Four-Gluon Vertex . . . . .	111
<b>B. Finite-Temperature Minutiae</b>	<b>115</b>
B.1. Vacuum Limit . . . . .	115
B.2. Initial Scale . . . . .	116
B.3. Mass Tuning and Decoupling . . . . .	117
<b>C. Technicalities</b>	<b>119</b>
C.1. fQCD Workflow . . . . .	119
C.2. Projecting Tensor Equations . . . . .	120
C.2.1. Incomplete Tensor Bases . . . . .	120
C.3. Regulator Parameterization . . . . .	121
C.4. Scale Setting and Renormalization . . . . .	122
C.5. Tensor Bases of Higher Vertices . . . . .	123
<b>D. FormTracer Details</b>	<b>126</b>
D.1. Installation and Usage . . . . .	126
D.1.1. Quick-Start Guide . . . . .	126
D.1.2. Basic Usage Examples . . . . .	127
D.2. Comparison with Other Programs . . . . .	128
D.3. Additional Algorithmic Details . . . . .	129
D.3.1. Partial Traces over Lorentz Tensors . . . . .	129
D.3.2. Other Algorithmic Improvements . . . . .	130
<b>Acknowledgments</b>	<b>131</b>
<b>Bibliography</b>	<b>132</b>

# 1. Introduction

In 1954, Yang and Mills [6] devised a non-Abelian gauge theory to explain isospin. Ever since, gauge theories have become a central pillar of physics. The standard model of particle physics is an  $SU(3) \otimes SU(2) \otimes U(1)$  gauge theory that describes fundamental interactions between all known elementary particles. It makes many precise predictions, the experimental discovery of the Higgs boson [7, 8] is a recent and also publicly well-known example. The  $SU(3)$  color group of the standard model describes the strong interaction between quarks and gluons. Leaving the subtleties of the Higgs mechanism [9–11] and potential hidden sectors [12] aside, the quarks have ordinary mass terms and the resulting theory is Quantum Chromodynamics (QCD). While the high-energy weak-coupling regime allows for a perturbative treatment and is relatively well under control, the low-energy strong-coupling regime still poses a major theoretical as well as experimental challenge [13]. This dissertation focuses on the strongly coupled non-perturbative regime of QCD.

## 1.1. Motivation

The elementary degrees of freedom of QCD are the color-charged quarks and gluons. Although their existence is experimentally well-established, they have not and cannot be observed in nature. Responsible for this is a peculiar property of QCD, confinement, which entails that only color-neutral objects can be observed. Gluons glue (hence their name) quarks together to form hadrons that are color-neutral composite particles, i.e., bound states. Thus, quarks and gluons are confined inside hadrons. Despite intense research, the confinement mechanism is still not understood. Hadrons show another characteristic of QCD: Most of their mass is binding energy that is dynamically generated by a process known as chiral symmetry breaking. Both confinement and spontaneous chiral symmetry breaking are strong-coupling phenomena and necessitate non-perturbative approaches.

While hadron properties are experimentally well-known [14], their theoretical description proves to be demanding. Two major non-perturbative ab initio approaches exist, lattice QCD and functional methods. Both have unique advantages and disadvantages that render them complementary. Lattice QCD relies on a discretization of Euclidean spacetime. The partition function is then given by a finite-dimensional path integral and can be solved with Monte Carlo methods. Although the infinite-dimensional physical limit can only be extracted with immense computing power, lattice QCD has achieved remarkable insights. For example, the light hadron masses have been computed and found to be in excellent agreement with the experimental values [15]. Another staggering success is the ab initio determination of the neutron-proton mass difference [16]. However, the calculation of nuclei and higher resonances still largely depends on effective descriptions. Within functional methods, bound states can be computed with Bethe-Salpeter equations [17] that require correlation functions between the elementary degrees of freedom, quarks and gluons, as input. Due to recent significant advances in solving these bound state equations, they now also contribute to our understanding of the baryon spectrum [18].

Functional methods comprise the Functional Renormalization Group (FRG) [19], Dyson-Schwinger Equations (DSEs) [20–22], and  $n$ PI approaches [23], see [24–37] for reviews. Correlation functions, i.e., the expectation values of operators, are the main constituents of these continuum path integral methods. The correlators carry the full information about all gauge-invariant observables. More precisely, functional methods yield sets of coupled equations for the correlation functions. Solving these coupled equations self-consistently generally requires truncations. Thus, while lattice methods have to overcome discretization artifacts, functional methods have to cope with finite truncations. The latter have a range of desirable properties. For example, they can be formulated on the Schwinger-Keldysh closed time path allowing for real-time and non-equilibrium applications [38–41]. Furthermore, functional methods can easily cope with problems that span over several orders of magnitude. Importantly, in contrast to lattice approaches, they are also applicable at high densities since they do not suffer from a sign problem as does lattice QCD [42]. This makes them ideally suited to study phase diagrams. Achieving progress towards a first-principle description of the QCD phase diagram is the overarching goal of this work.

The dependence of quark matter on temperature and baryon density (or, equivalently, chemical potential) has gained great attention over the past decades [43]. QCD at extreme conditions is highly relevant, e.g., for the evolution of the early universe or neutron stars. Heavy ion collisions allow for the creation of such extreme conditions on earth. Two colliders, namely RHIC at BNL [44] and LHC at CERN [45], are currently capable of creating quark-gluon plasmas. While these operate at relatively low baryon densities, two further facilities that are currently being built, CBM at FAIR [46] and NICA at JINR [47], are designed to test the regions of very high baryon densities. The QCD phase diagram has also been at the forefront of theoretical research [48–50]. Various methods such as effective models, perturbation theory, lattice simulations, and functional approaches have been employed to deduce aspects of the QCD phase structure. Nonetheless, only few properties are firmly established. For example, at very high densities and very low temperatures, quark-matter is color-superconducting and expected to be in a color-flavor-locked phase [48]. Various phases and inhomogeneous states are conjectured between this very high density phase and the zero-density vacuum [49]. At vanishing temperature and density lies the hadronic phase, i.e., quarks and gluons are confined inside hadrons, as described above. At finite temperature, QCD undergoes a transition to the deconfined quark-gluon plasma phase where quarks and gluons are the dominant degrees of freedom. Lattice simulations have established that the transition at vanishing density is a smooth crossover transition and lies at  $T_c \approx 155$  MeV [51, 52]. At high temperatures in the quark-gluon plasma phase, chiral symmetry is restored. Indeed, the chiral and deconfinement phase transitions are closely related [53]. At larger chemical potential, where lattice simulations suffer from the sign problem, the picture is less clear. It is conjectured that the crossover at zero chemical potential turns into a first order phase transition at finite density. This implies an experimentally detectable [54] critical endpoint in the phase diagram. Indeed, effective models and exploratory Dyson-Schwinger studies indicate the existence of such a critical endpoint, see, e.g., [55–58] and [59–62], respectively. Thus, QCD at large densities is dominated by fluctuations, which leads to large systematic errors if model parameters are phenomenologically fixed at vanishing density [63]. Hence, *ab initio* approaches are required for quantitatively reliable predictions on the phase structure. Functional methods are a unique tool to study the phase diagram since they can be applied to all regions, in particular also to the high densities regions not accessible with Monte-Carlo simulations.



In conclusion, the formal, algebraic, and numerical progress within functional methods sets the stage for a systematic exploration of the QCD phase diagram. In general, one distinguishes between bottom-up and top-down approaches. While the former model certain aspects of a theory with the help of external input or phenomenological parameters, the latter derive all properties from the microscopic action. The functional QCD (fQCD) collaboration [64] aims to explore the QCD phase diagram with the FRG, encompassing both top-down [1, 3, 4, 65] and bottom-up [66–73] approaches. While bottom-up approaches are extremely useful to understand the general properties of the QCD phase structure, only top-down approaches can provide quantitatively reliable predictions, rendering them imperative. Therefore, this work contributes to the top-down approach. To this end, we compute correlation functions in advanced truncations that require as only input the fundamental parameters of QCD, the strong running coupling at the renormalization scale and the bare quark masses. We motivate the individual projects in the specific chapters.

## 1.2. Publications

While the compilation of this dissertation was performed solely by the author, the results were obtained with my collaborators. These are largely published or available as preprint. Texts and figures taken from these articles are not marked explicitly, but incorporated as described below and in the introductions to the individual chapters. The publications are:

- [1] **Landau gauge Yang-Mills correlation functions**  
Anton K. Cyrol, Leonard Fister, Mario Mitter, Jan M. Pawłowski, Nils Strodthoff  
Published in Phys. Rev. D94 (2016) no.5, 054005  
E-Print: arXiv:1605.01856 [hep-ph]  
Comment: This article is contained in Chapter 5.
- [2] **FormTracer – A Mathematica Tracing Package Using FORM**  
Anton K. Cyrol, Mario Mitter, Nils Strodthoff  
Published in Comput. Phys. Commun. 219C (2017) 346-352  
E-Print: arXiv:1610.09331 [hep-ph]  
Comment: Chapter 4 and Appendix D are drawn from this publication.
- [3] **Non-perturbative quark, gluon and meson correlators of unquenched QCD**  
Anton K. Cyrol, Mario Mitter, Jan M. Pawłowski, Nils Strodthoff  
E-Print: arXiv:1706.06326 [hep-ph]  
Comment: Chapter 7 relies on this preprint.
- [4] **Non-perturbative finite-temperature Yang-Mills theory**  
Anton K. Cyrol, Mario Mitter, Jan M. Pawłowski, Nils Strodthoff  
E-Print: arXiv:1708.03482 [hep-ph]  
Comment: This preprint is the basis for Chapter 8 as well as Appendix A and B.

Another article was published during the time of my PhD:

- [5] **A Dyson-Schwinger study of the four-gluon vertex**  
Anton K. Cyrol, Markus Q. Huber, Lorenz von Smekal  
Published in Eur. Phys. J. C75 (2015) 102  
E-Print: arXiv:1408.5409 [hep-ph]

However, it stems from my Master thesis [74] and is not included in this dissertation.

### 1.3. Outline

Chapter 2 and 3 introduce basics of quantum chromodynamics and functional methods. As their content is well-known, they mainly serve to fix the notation and for future reference. In Chapter 4, we introduce a computational tool, called FormTracer. It is a high-performance general-purpose Mathematica tracing package. Albeit purely technical, it paves the way for following chapters. The reader familiar with the subjects and interested in the physics may start reading with Chapter 5.

In Chapter 5 we investigate Landau gauge Yang-Mills theory in a self-consistent vertex expansion scheme for the effective action. We compute ghost and gluon propagators as well as running couplings. Particular focus is put on the dynamical creation of a gluon mass gap at non-perturbative momenta since the latter reflects confinement.

Chapter 6 tackles Yang-Mills theory in three spacetime dimensions. It allows for detailed comparisons with Dyson-Schwinger results and is a preparation for the finite-temperature calculations in Chapter 8.

In Chapter 7 we consider unquenched two-flavor QCD in the vacuum. We present results for quark, gluon, ghost and meson correlation functions. We focus on the quantitatively correct running of different vertex couplings that is vital for describing the phenomena and scales of confinement and chiral symmetry breaking.

Chapter 8 is devoted to finite-temperature Yang-Mills theory as a first step towards the phase diagram of QCD. To this end, the systematic vertex expansion is generalized to account for the heat bath. We calculate the magnetic and electric components of the gluon propagator as well as the three- and four-gluon vertices for a wide range of temperatures. Additionally, we extract a Debye screening mass from the electric propagator.

Finally, we summarize our main findings and give an outlook in Chapter 9. Appendices A – D contain in-depth information on the finite-temperature computations as well as technical details.

## 2. Quantum Chromodynamics

Quantum Chromodynamics (QCD) has become subject to intense research over the past decades. In this introductory chapter<sup>1</sup>, we summarize aspects of QCD that are of pivotal importance to this thesis, but do not aim at a self-contained introduction. Throughout, we work in Euclidean spacetime ( $g_{\mu\nu} = \delta_{\mu\nu}$ ), employ natural units ( $c = \hbar = k_B = 1$ ), and use the sum convention over repeated indices.

### 2.1. Action and BRST Symmetry

Quarks are fermions with spin 1/2 and described by spinor fields  $q_f$ . They come in three generations with two members each, yielding  $N_f = 6$  quark flavors,  $f \in \{\text{u, d; c, s; t, b}\}$ , in total. Besides the electroweak charge, quarks are charged under the  $SU(N_c = 3)$  color gauge group. Hence, they interact via the algebra-valued gluon gauge field  $A_\mu = A_\mu^a T_c^a$ . Here,  $T_c^a$  are the Hermitian generators of the non-Abelian Lie color group. Although the strong interaction is described by the  $SU(3)$  gauge group, we consider a slightly generalized Lagrangian density with a simple compact Lie group. This is useful for the study of the pure glue sector for which we obtain universal results. We postpone the definition of Lie groups to Sec. 4.3. The generalized QCD Lagrangian density is given by

$$\mathcal{L} = \sum_f \bar{q}_f (\not{D} + m_f) q_f + \frac{1}{4} \text{Tr} (F_{\mu\nu} F_{\mu\nu}) , \quad (2.1)$$

where  $\not{D} = \gamma_\mu D_\mu$ . The covariant derivative,

$$D_\mu = \partial_\mu - ig A_\mu^a T_c^a , \quad (2.2)$$

couple quarks to gluons via the strong coupling  $g = \sqrt{4\pi\alpha}$ . We use Hermitian gamma matrices that obey the Euclidean Clifford algebra,

$$\{\gamma_\mu, \gamma_\nu\} = 2\delta_{\mu\nu} , \quad \{\gamma_\mu, \gamma_5\} = 0 , \quad \gamma_5 = \gamma_1\gamma_2\gamma_3\gamma_4 .$$

The field strength tensor  $F_{\mu\nu}$  is given by the commutator of the covariant derivative,

$$F_{\mu\nu} = \frac{i}{g} [D_\mu, D_\nu] = \partial_\mu A_\nu - \partial_\nu A_\mu - ig [A_\mu, A_\nu] ,$$

or, written in the  $N_A (= 8 \text{ for } SU(3))$  components of the adjoint representation, by

$$F_{\mu\nu}^a = \partial_\mu A_\nu^a - \partial_\nu A_\mu^a + g f^{abc} A_\mu^b A_\nu^c . \quad (2.3)$$

In (2.3) we use the structure constants  $f^{abc}$  of the Lie algebra to express the commutator of the gauge fields, see (4.2). In general, we suppress spinor as well as fundamental group indices. Furthermore, we omit unity operators, e.g.,  $\partial_\mu = \mathbb{1}_c \partial_\mu$  in (2.2).

<sup>1</sup> Most of the content is textbook knowledge and compiled from [75–78].

### Symmetries

QCD exhibits a global flavor symmetry for vanishing quark masses  $m_f = 0$ . In nature, this symmetry is explicitly and spontaneously broken. The latter generates the bulk of the hadron masses via chiral symmetry breaking. We discuss this point further in Sec. 2.4.

By construction, the QCD Lagrangian density (2.1) is invariant under local gauge transformations,

$$q_f \rightarrow U q_f, \quad \bar{q}_f \rightarrow \bar{q}_f U^\dagger; \quad A_\mu \rightarrow U A_\mu U^\dagger - \frac{i}{g} (\partial_\mu U) U^\dagger, \quad (2.4)$$

where  $U$  is an element of the Lie group,

$$U = \exp[-i T_c^a \theta^a(x)],$$

with  $N_A$  spacetime dependent functions  $\theta^a(x)$ .

### Gauge Fixing and Path Integral

Continuum path integral methods require gauge fixing to cope with the infinite number of physically equivalent field configurations that are connected by gauge transformations via (2.4). To factorize this infinite constant, we split the functional integration over the gluon fields  $\int \mathcal{D}A$  into an integration over physically inequivalent and physically equivalent configurations,  $\int \mathcal{D}A = \mathcal{D}A^\theta \int \mathcal{D}\theta$ . The general covariant gauge conditions,

$$G^a[A] = \partial_\mu A_\mu^a(x) - \omega^a(x) = 0, \quad (2.5)$$

with arbitrary functions  $\omega^a(x)$  are imposed with the Faddeev-Popov trick [79]. To this end, we exploit the identity

$$1 = \int \mathcal{D}G \delta(G) = \int \mathcal{D}\theta(x) \delta(G[A^\theta]) \det\left(\frac{\delta G[A^\theta]}{\delta \theta}\right), \quad (2.6)$$

where  $\delta$  is the functional Dirac delta distribution. The Faddeev-Popov determinant introduces the ghost and antighost fields,  $c = c^a T_c^a$  and  $\bar{c} = \bar{c}^a T_c^a$ :

$$\det\left(\frac{\delta G^a}{\delta \theta^b}\right) = \det\left(\frac{1}{g} \partial_\mu D_\mu^{ab}\right) = \int \mathcal{D}c \mathcal{D}\bar{c} \exp\left[\int_x \bar{c}^a \partial_\mu D_\mu^{ab} c^b\right]. \quad (2.7)$$

For the first equality we used  $\frac{\delta G^a}{\delta \theta^b} = \frac{\delta G^a}{\delta A_\mu^c} \frac{\delta A_\mu^c}{\delta \theta^b}$  as well as (2.4) and introduced the covariant derivative in the adjoint representation,

$$D_\mu^{ab} = \delta^{ab} \partial_\mu - g f^{abc} A_\mu^c.$$

For the second equality in (2.7), the determinant is represented by a functional integral over anti-commuting scalar (i.e. Grassmannian) fields in the adjoint representation, the Faddeev-Popov ghost fields. Furthermore, we abbreviated  $\int_x = \int d^d x$  in (2.7). The ghost fields violate the spin-statistics theorem and, hence, must be absent from the physical spectrum. Their sole purpose is to cancel unphysical degrees of freedom and thereby guarantee unitarity, cf. also Sec. 2.3. To eliminate the delta function in (2.6), we integrate over  $\omega^a$  with a Gaussian weighting function,  $\int \mathcal{D}\omega \exp(-\int_x (\omega^a)^2 / (2\xi))$ , whereby we introduce the gauge fixing parameter  $\xi$ .

We then arrive at the gauge-fixed generating functional of QCD:

$$Z[J] = \int \mathcal{D}\varphi e^{-S[\varphi] + \int_x J \cdot \varphi}, \quad \text{with} \quad \int \mathcal{D}\varphi = \int \mathcal{D}A \mathcal{D}c \mathcal{D}\bar{c} \mathcal{D}q \mathcal{D}\bar{q}, \quad (2.8)$$

where the gauge-fixed microscopic action is given by

$$S[\varphi] = \underbrace{\int_x \bar{q} (\not{D} + m) q}_{S_M} + \underbrace{\frac{1}{4} \int_x F_{\mu\nu}^a F_{\mu\nu}^a}_{S_G} + \underbrace{\frac{1}{2\xi} \int_x (\partial_\mu A_\mu^a)^2}_{S_{GF}} + \underbrace{\int_x \bar{c}^a \partial_\mu D_\mu^{ab} c^b}_{S_{GH}}. \quad (2.9)$$

For future reference, we label the individual terms matter  $S_M$ , glue  $S_G$ , gauge-fixing  $S_{GF}$ , and ghost  $S_{GH}$  terms, respectively. In addition, we use a flavor vector  $q = (q_u, q_d, \dots)$  to abbreviate the matter term, i.e., the mass  $m$  is matrix-valued in flavor space,  $m = \text{diag}(m_u, m_d, \dots)$ . The Yang-Mills (pure gauge) action is given by  $S_{YM} = S_G + S_{GF} + S_{GH}$ . Furthermore, in (2.8) we introduce the superfield  $\varphi = (A, c, \bar{c}, q, \bar{q})$  and source terms  $\int_x J \cdot \varphi$  with the currents  $J = (J_A, J_c, J_{\bar{c}}, J_q, J_{\bar{q}})$ .

The gauge fixing term  $S_{GF}$  can be rewritten by introducing the auxiliary Nakanishi-Lautrup field  $B^a$ ,

$$S_{GF}[A] = \frac{1}{2\xi} \int_x (\partial_\mu A_\mu^a)^2 \rightarrow S_{GF}[A, B] = \int_x \left( B^a \partial_\mu A_\mu^a - \frac{\xi}{2} (B^a)^2 \right), \quad (2.10)$$

To see that the latter term is equivalent, note that it can simply be integrated by completing the square since it has no derivative terms. The Nakanishi-Lautrup field facilitates the discussion of BRST symmetry and the Slavnov-Taylor identities below, but is ignored (i.e. integrated out) in all other chapters. The gauge fixing condition (2.5) is only locally unique, i.e., it prohibits infinitesimal gauge transformation, which is sufficient for perturbation theory. However, finite gauge transformations generate equivalent configurations that fulfill (2.5). These are called Gribov copies [80] and are related to the non-trivial structure of gauge theories [81]. We discuss non-perturbative gauge fixing further in Sec. 2.3.

### Generating Functional for 1PI correlators

The generating functional of the connected correlators  $W[J]$ , also called Schwinger functional, is given by

$$e^{W[J]} = Z[J] = \int \mathcal{D}\varphi e^{-S[\varphi] + \int_x J \cdot \varphi}.$$

For theoretical calculations, the one-particle irreducible (1PI) correlation functions are more convenient. The generating functional for them is obtained by a Legendre transformation of  $W[J]$ ,

$$\Gamma[\Phi] = \sup_J \left( \int_x \Phi \cdot J - W[J] \right). \quad (2.11)$$

This defines the effective action  $\Gamma[\Phi]$ , which is a functional of the expectation values of the fields. For the  $i$ -th component of the superfield, we have

$$\Phi_i = \frac{\delta W[J]}{\delta J_i} = \frac{1}{Z[J]} \frac{\delta Z[J]}{\delta J_i} = \langle \varphi_i \rangle_J.$$

Evaluating the derivative of (2.11) at  $J = J_{\text{sup}}$  yields the quantum equation of motions,

$$\frac{\delta\Gamma[\Phi]}{\delta\Phi_i} = J_i, \quad (2.12)$$

which are also called stationary conditions for  $J_i = 0$ . Here, we distinguish the fields  $\varphi$  from their expectation values  $\Phi$ .<sup>2</sup> However, notation-wise we do not distinguish their components to avoid cluttering the notation. In this work, we always compute the 1PI correlation functions.

### Landau Gauge

The propagators are given by the inverse two-point functions, i.e., we obtain the bare propagators from (2.9). Using the longitudinal and transverse projection operators,

$$\begin{aligned} \Pi_{\mu\nu}^{\parallel}(p) &= \frac{p_\mu p_\nu}{p^2}, \\ \Pi_{\mu\nu}^{\perp}(p) &= \delta_{\mu\nu} - \Pi_{\mu\nu}^{\parallel}(p), \end{aligned} \quad (2.13)$$

the bare gluon propagator is given by

$$\left[ S_{AA}^{(2)-1} \right]_{\mu\nu}^{ab}(p) = \frac{\delta^{ab}}{p^2} \left( \delta_{\mu\nu} - (1 - \xi) \frac{p_\mu p_\nu}{p^2} \right) = \frac{\delta^{ab}}{p^2} \left( \Pi_{\mu\nu}^{\perp}(p) + \xi \Pi_{\mu\nu}^{\parallel}(p) \right). \quad (2.14)$$

In Landau gauge, the gauge fixing parameter  $\xi$  is taken to zero,  $\xi \rightarrow 0$ . Throughout this work, we use Landau gauge as it has many convenient properties. For example, the gluon propagator (2.14) has only one tensor structure (in the absence of a thermal heat bath). Landau gauge is the standard choice within non-perturbative functional methods.

### BRST symmetry

Becchi, Rouet, Stora, and Tyutin (BRST) discovered that the gauge-fixed action exhibits a global residual symmetry [82, 83]. Expressing the gauge fixing term  $S_{\text{GF}}$  with the Nakanishi-Lautrup field, as done in (2.10), the infinitesimal BRST transformation reads [75]:

$$\begin{aligned} \delta_{\text{BRST}} A_\mu^a &= \epsilon D_\mu^{ab} c^b, & \delta_{\text{BRST}} c^a &= -\frac{1}{2} g \epsilon f^{abc} c^b c^c, \\ \delta_{\text{BRST}} q &= i g \epsilon c^a T_c^a q, & \delta_{\text{BRST}} \bar{c}^a &= \epsilon B, \\ \delta_{\text{BRST}} \bar{q} &= i g \epsilon \bar{q} c^a T_c^a, & \delta_{\text{BRST}} B^a &= 0, \end{aligned} \quad (2.15)$$

where  $\epsilon$  is an infinitesimal anti-commuting Grassmann number. The BRST operator  $\mathfrak{s}$  is defined by  $\delta_{\text{BRST}} \Phi = \epsilon \mathfrak{s} \Phi$ . The classical action (2.9) is invariant under BRST transformations,

$$\mathfrak{s} S[\Phi] = (\mathfrak{s} \Phi_i) \frac{\delta S[\Phi]}{\delta \Phi_i} = 0,$$

<sup>2</sup> We reserve  $\phi$  for the (expectation values of) auxiliary mesonic fields, see Chapter 7.

as can be shown straightforwardly by insertion. Also, the pure gauge action  $S_{\text{YM}}$  is invariant under BRST transformations. From (2.15) follows  $\mathfrak{s}(\mathfrak{s}\Phi) = 0$ , which reads in operator notation

$$\mathfrak{s}^2 = 0. \quad (2.16)$$

Thus, the BRST operator  $\mathfrak{s}$  is nilpotent.

### Slavnov-Taylor identities

The BRST symmetry allows deriving generalized Ward-Takahashi identities, commonly called Slavnov-Taylor identities (STIs) [84, 85]. However, deriving them requires some careful algebra and we therefore only sketch the derivation of the master Slavnov-Taylor identity. All STIs for the correlation functions follow from this master equation. For a more detailed and rigorous treatment we refer to [25, 32, 77]. To begin, we introduce source terms for the BRST transformation,

$$Z[J, Q] = \int \mathcal{D}\varphi e^{-S[\varphi] + \int_x J \cdot \varphi + \int_x Q \cdot \mathfrak{s}\varphi},$$

with BRST currents  $Q = (Q_A, Q_c, Q_{\bar{c}}, Q_q, Q_{\bar{q}}, Q_B = 0)$ . These source terms are invariant under BRST transformations due to (2.16). Furthermore, the path integral measure is also invariant, see, e.g., [77]. Hence, demanding invariance of the generating functional yields

$$\mathfrak{s}Z[J, Q] = \int \mathcal{D}\varphi \left( \int_x J \cdot \mathfrak{s}\varphi \right) e^{-S[\varphi] + \int_x J \cdot \varphi + \int_x Q \cdot \mathfrak{s}\varphi} = \int_x J_i(x) \frac{\delta Z[J, Q]}{\delta Q_i(x)} = 0.$$

Since  $Z[J, Q] = e^{W[J, Q]}$ , we are led to

$$\int_x J_i(x) \frac{W[J, Q]}{\delta Q_i(x)} = 0$$

The effective action in the presence of BRST sources  $\Gamma[\Phi, Q]$  is given by the Legendre transformation of  $W[J, Q] = \log Z[J, Q]$  with respect to  $J$ . Thus, it has the same  $Q$ -derivatives as  $W[J, Q]$ . Using this and (2.12) yields the master equation [25, 77]:

$$\int_x \frac{\delta \Gamma[\Phi, Q]}{\delta Q_i(x)} \frac{\delta \Gamma[\Phi, Q]}{\delta \Phi_i(x)} = 0, \quad (2.17)$$

where the BRST variations of the effective action are given by

$$-\frac{\delta \Gamma[\Phi, Q]}{\delta Q_i} = \frac{\delta W[J, Q]}{\delta Q_i} = \langle \mathfrak{s}\Phi_i \rangle.$$

The BRST variations can be interpreted as generalized vertices of the theory. The STIs for correlation functions are obtained by taking functional derivatives of (2.17). For example, the STI for the inverse gluon two-point function is given by (5.15), and the one for the three-gluon vertex by (5.22). Importantly, via (5.17) the STIs imply that the couplings of different vertices coincide in the perturbative regime, as becomes clear in Chapter 5.

## 2.2. Asymptotic Freedom

At small couplings the QCD beta function can be calculated using perturbation theory. The one- [86, 87] and two-loop [88–90] coefficients are given by

$$\begin{aligned} \beta(\alpha) := \frac{\mu^2}{4\pi} \frac{d\alpha}{d\mu^2} = & - \left( \frac{11}{3} C_A - \frac{4}{3} I_2 N_f \right) \left( \frac{\alpha}{4\pi} \right)^2 \\ & - \left( \frac{34}{3} C_A^2 - \frac{20}{3} C_A I_2 N_f - 4 C_F I_2 N_f \right) \left( \frac{\alpha}{4\pi} \right)^3 + \mathcal{O}(\alpha^4), \end{aligned} \quad (2.18)$$

where  $C_F$  and  $C_A$  are the quadratic Casimirs of the fermion and adjoint representation, respectively. Their values for all classical groups are given in (4.5), the normalization  $I_2$  ( $= \frac{1}{2}$  for  $SU(N)$ ) is defined in (4.4). Historically, the one-loop coefficient is of particular importance. For  $SU(3)$  it is given by  $-(11 - \frac{2}{3} N_f)$ . Thus, for not too many quark flavors,  $N_f < \frac{33}{2}$ , the one-loop coefficient is negative, which implies that QCD becomes asymptotically free at large energies. In RG terms, this means all couplings go to zero and approach the Gaussian fixed point. Asymptotic freedom explains Bjorken scaling [91] and led to the establishment of QCD as the theory of the strong interactions. Up to two loops, the beta function is independent of the renormalization scheme. By now, also the scheme-dependent three- [92, 93], four- [94, 95] and five-loop [96, 97] expressions are known. In Sec. 5.4.2 we crosscheck our non-perturbative results against the perturbative two-loop beta function given by (2.18).

### Pure Gauge Theory

If the running coupling of pure gauge theory ( $N_f = 0$ ) is rescaled with the quadratic Casimir of the adjoint representation,  $\alpha \rightarrow \tilde{\alpha} 4\pi/C_A$ , the beta function (2.18) becomes independent of the gauge group:

$$\tilde{\beta}(\tilde{\alpha}) = \mu^2 \frac{d\tilde{\alpha}}{d\mu^2} = -\frac{11}{3} \tilde{\alpha}^2 - \frac{34}{3} \tilde{\alpha}^3 + \mathcal{O}(\tilde{\alpha}^4).$$

Thus, the two-loop beta function of Yang-Mills theory has a trivial gauge group dependence, i.e., the group dependence can be absorbed by the definition of the scale. This property also holds at three-loop order but is spoiled at four- and five-loop order [96]. We come back to this point in Sec. 5.4.1 and 8.4.1.

## 2.3. Confinement

Understanding confinement still poses a major challenge. We limit this introduction to aspects that are important for the following chapters and refer to [32, 33, 35, 98, 99] for more comprehensive overviews. In particular, we focus on confinement scenarios that are based on correlation functions and do not discuss topological approaches such as vortices or magnetic monopoles; for those, see, e.g., [100, 101] and references therein.

Confinement in QCD is intimately related to the non-Abelian gauge group. Hence, it is worth considering Yang-Mills theory first. Proving that the lowest lying vacuum excitation of Yang-Mills theory has a non-zero mass gap is one of the seven millennium prize problems [102]. Such a mass gap is expected, inter alia, because Euclidean lattice simulations for specific gauge groups show that the lowest lying glue ball states have



non-zero mass, see, e.g., [103]. It is useful to consider QCD with static (i.e. infinitely heavy) quarks before looking at full dynamical QCD. In this case, a static quark and an antiquark (that may constitute a meson) serve as test color charges. The force between them is quantified by the Wilson loop [104]. Confinement necessitates that a quark-antiquark pair cannot be pulled apart and observed separately, which is the case if an infinite amount of energy is required to increase the distance between the quark and the antiquark to infinity. Indeed, the force between a quark-antiquark pair, known as string tension, is constant at large distances, leading to a linearly rising potential, see, e.g., [105]. Separating a quark-antiquark pair in dynamical QCD generates a new quark-antiquark pair once it is energetically favorable, i.e., the string breaks, which can also be observed on the lattice [106]. The Polyakov loop [107], which is the Wilson loop in temporal direction, serves as an order parameter for the finite-temperature confinement-deconfinement phase transition in Yang-Mills theory. Importantly, the Polyakov loop is accessible within functional methods [108, 109]. To be specific, the Polyakov loop is an order parameter for center symmetry. The latter is broken in the confined phase but restored in the deconfined phase at high temperatures, see Sec. 8.1.2 for more details.

In QCD, center symmetry is explicitly broken by the quarks and the finite-temperature confinement-deconfinement phase transition is replaced by a smooth crossover transition for physical quark masses. Confinement requires the absence of colored states from the physical asymptotic spectrum. Physical states must fulfill the Osterwalder-Schrader axioms [110, 111] to define a Wightman field theory. In particular, the propagators of physical particles must obey reflection positivity. Gluons violate this axiom and can therefore not be part of the physical spectrum, see, e.g., [112]. In contrast to an ordinary bosonic propagator, the gluon propagator exhibits a maximum at non-zero momenta, see, e.g., Fig. 5.6, which is a signal for violation of positivity [32]. In the following we discuss the so-called Kugo-Ojima and Gribov-Zwanziger confinement scenarios that predict the qualitative infrared behavior of Landau gauge Yang-Mills propagators.

### Kugo-Ojima Scenario

The Kugo-Ojima confinement scenario [113, 114] relies on BRST symmetry. It is based on the observation that the full state space  $\mathcal{W}$  is split into three disjoint parts by the nilpotent BRST operator  $\mathfrak{s}$ , cf. (2.16). The first subspace  $\mathcal{W}_1$  is defined by the states that are not annihilated by  $\mathfrak{s}$ . The second subspace  $\mathcal{W}_2 = \text{Im } \mathfrak{s} = \mathfrak{s} \mathcal{W}_1$  consists of the daughter states, i.e., those states that are obtained by acting with the BRST operator on non-vanishing states. The remaining states, i.e., those that are annihilated by  $\mathfrak{s}$  but are not contained in  $\mathcal{W}_2$ , form the subspace  $\mathcal{W}_0 = \text{Ker } \mathfrak{s} / \text{Im } \mathfrak{s}$ .

Perturbatively, the BRST transformations are given by (2.15). It can be shown that forward-polarized gluons and antighosts are contained in  $\mathcal{W}_1$ , while backward-polarized gluons and ghosts are elements of  $\mathcal{W}_2$ . Loosely speaking, gauge invariance requires that physical states are annihilated by the BRST operator. Thus, the states in  $\mathcal{W}_1$  cannot be part of the physical state space. Due to the nilpotency (2.16), the states in  $\mathcal{W}_2$  have zero norm. Hence, the physical state space is given by  $\mathcal{W}_{\text{phys}} = \overline{\text{Ker } \mathfrak{s} / \text{Im } \mathfrak{s}} = \overline{\mathcal{W}_0}$ , where the bar means closure. Again loosely speaking, the spaces  $\mathcal{W}_1$  and  $\mathcal{W}_2$  cancel each other out. This is known as quartet mechanism. It explains why longitudinally polarized gluons and (anti-)ghosts do not exist in the physical spectrum (see, e.g., [75] for a pedagogical introduction). Confinement, however, requires that also transversely polarized gluons are absent from the physical spectrum, which cannot be explained perturbatively.

To this end, Kugo and Ojima suggested extending the perturbative mechanism described above to all colored states. This requires a well-defined non-perturbative BRST symmetry. The crucial ingredient of the Kugo-Ojima confinement scenario is the assumption of an unbroken global color charge. This directly implies that  $\mathcal{W}_{\text{phys}}$  contains only color singlet states [113]. An unbroken global color charge has important implications for the Landau gauge gluon and ghost propagators: The gluon propagator has to be less singular than a massless propagator [115]. Furthermore, the ghost propagator must be enhanced [114], i.e., it has to be more singular than the tree-level propagator.

Indeed, the first solutions of Yang-Mills DSEs that took the ghosts appropriately into account [116–120] fulfilled these conditions. These solutions are called scaling solutions since the propagators are scale-invariant in the infrared, i.e., they approach an infrared fixed point [121], see (5.19). In Chapter 5, we find a scaling solution consistent with the Kugo-Ojima confinement scenario. We argue that scaling yields different contributions to the longitudinally and transversely polarized gluons also in zero momentum (infinite distance) limit. This enables an STI-consistent gapping of the transversely polarized gluons. However, lattice simulations [122–124] find propagators that do not fulfill the Kugo-Ojima conditions. We discuss this point further within the next subsection.

### Gribov-Zwanziger Scenario

The Gribov-Zwanziger scenario [80, 125] explicitly deals with Gribov copies, i.e., the fact that the gauge fixing condition (2.5) is not unique beyond perturbation theory [80, 81]. Physically equivalent field configurations that are connected by gauge transformations form a so-called gauge orbit. Moving along the gauge orbit, the Faddeev-Popov determinant (given by (2.7)) changes its sign. The hyper-surfaces at which the sign changes occur are called Gribov horizons. These separate the configuration space into so-called Gribov regions. The region that contains the origin is called first Gribov region. It has a few remarkable properties. For example, it is bounded and convex [126] and every gauge orbit passes through it at least once [127]. Consequently, it contains all information about all observables. Hence, the perturbative gauge fixing condition (2.5) can be supplemented with the condition that gauge field configurations lie inside the first Gribov region. However, the first Gribov region still contains multiple Gribov copies [128]. Therefore, any selection of Gribov copies within the first Gribov region corresponds to a further gauge-fixing condition. Gauge-fixed correlation functions depend on this choice, see, e.g., [35, 129].

Zwanziger suggested adding a non-local term to the classical action that restricts the integration domain of the path integral to the first Gribov region [125]. In its original version, the Gribov-Zwanziger scenario predicts an infrared vanishing gluon propagator and an infrared enhanced ghost propagator, similarly as the Kugo-Ojima scenario. However, triggered by new lattice results that unequivocally predict an infrared finite, non-vanishing gluon propagator and a non-enhanced, tree-level-like ghost propagator [122–124], the Gribov-Zwanziger scenario was refined. In [130, 131] it was shown that unexploited dynamical effects can account for a finite, non-vanishing gluon propagator that violates positivity at the perturbative level as well as a non-enhanced ghost propagator. More details can be found in the review on the Gribov-Zwanziger scenario [99]. Subsequently, similar solutions with a non-enhanced ghost propagator and an infrared finite but non-vanishing gluon propagator have also been found in the DSE framework [112, 132, 133]. These are called decoupling solutions since the gluons decouple (but do not scale) in the infrared, see (5.20). Noteworthy, decoupling solutions break global BRST symmetry [112].

### Summary

We discussed the Kugo-Ojima and Gribov-Zwanziger confinement scenarios. The former relies on BRST symmetry and assumes an unbroken global color charge. It implies an enhanced ghost propagator and is thus closely linked to the scaling solution. The latter scenario takes Gribov copies explicitly into account by including a non-local term in the classical action. It is consistent with decoupling solutions that show an infrared-finite gluon and a non-enhanced ghost propagator. Functional methods are able to produce both scaling and BRST-symmetry-breaking decoupling solutions, the former being consistent with the Kugo-Ojima scenario. Lattice simulations that are restricted to the first Gribov region only find decoupling solutions, consistent with the Gribov-Zwanziger scenario. In this thesis, we consider the standard functional setup, i.e., we do not add Gribov-Zwanziger terms to the action. We discuss necessary conditions for the generation of a gluon mass gap in Sec. 5.2.

## 2.4. Chiral Symmetry Breaking

The quarks are projected onto their left-handed and right-handed components with the chiral projection operators,

$$P_{L/R} = \frac{1 \mp \gamma_5}{2}. \quad (2.19)$$

In the chiral limit ( $m_f = 0$ ), the individual components can be separated with (2.19) and the action exhibits an  $U(N_f)_L \times U(N_f)_R$  flavor symmetry. Since the light bare quark masses are smaller than the intrinsic scale of QCD,  $m_u \approx m_d < m_s < \Lambda_{\text{QCD}}$ , the flavor symmetry is an approximate symmetry of the light quark sector, consisting of two (or, in an inferior approximation, three) flavors. To elucidate this, we rewrite the symmetry,

$$U(N_f)_L \times U(N_f)_R \rightarrow U(1)_V \times SU(N_f)_V \times U(1)_A \times SU(N_f)_A$$

with vector  $V = L + R$  and axial vector  $A = L - R$  transformations. The  $U(1)_V$  symmetry holds for arbitrary non-zero masses and implies baryon number conservation. Vector transformations  $SU(N_f)_V$  correspond to the isospin symmetry which is broken by the differing quark masses. The axial  $U(1)_A$  symmetry is broken by the chiral (or axial) anomaly [134–137] and explains the mass splitting of the  $\eta$  and the  $\eta'$  meson [138]. The remaining chiral symmetry,  $SU(N_f)_A$ , is spontaneously broken and leads for  $N_f = 2$  to three pseudo-Goldstone bosons, the pions. Chiral symmetry breaking is one of the main aspects of Chapter 7.

An order parameter for chiral symmetry breaking is given by the chiral condensate,

$$\langle \bar{q}q \rangle = \langle \bar{q}_L q_R + \bar{q}_R q_L \rangle,$$

where  $q_{L/R} = P_{L/R} q$ . Thus, chiral symmetry breaking generates the constituent quark masses. Indeed, hadron masses mainly originate from binding energy and only a tiny fraction stems from the bare quark masses. The latter are generated via the Higgs mechanism in the standard model.

## 3. Functional Methods

Functional methods encompass the Functional Renormalization Group (FRG) [19], Dyson-Schwinger Equations (DSEs) [20–22], and  $n$ PI techniques [23]. Since these approaches are well-known (see [24–30], [18, 31–37] and [39, 139] for QCD-related reviews), and even tools for the automated derivation of the equations exist [140, 141], we keep this introduction short. As is appropriate for this dissertation, the focus lies on the FRG.

Noteworthy, there is a fundamental difference between the FRG and the other functional methods. While quantum fluctuations are integrated out successively in the FRG, in the other approaches they are integrated all at once. We discuss advantages and disadvantages of this point further in Sec. 3.2. In the following we use a condensed notation, i.e., we use the superfield  $\varphi$  and its expectation value  $\Phi$ .

### 3.1. Functional Renormalization Group

The FRG in Wetterich’s formulation [19] is a non-perturbative functional method that allows fluctuations to be integrated in the Wilsonian spirit [142]. We first introduce the flow equation and then discuss regulators and the vertex expansion in Sec. 3.1.2 and 3.1.3.

#### 3.1.1. Wetterich Equation

The idea underlying the Wetterich equation is to regularize fluctuations below the renormalization group (RG) scale  $k$ . Technically, this is achieved by adding a momentum-dependent mass term to the bare action  $S \rightarrow S + \Delta S_k$ . This leads to an infrared regularization of the generating functional,

$$e^{W_k[J]} = Z_k[J] = e^{-\Delta S_k[\frac{\delta}{\delta J}]} Z[J] = \int \mathcal{D}\varphi e^{-S[\varphi] - \Delta S_k[\varphi] - \int_x J \cdot \varphi}. \quad (3.1)$$

In translationally invariant systems, the regulator term  $\Delta S_k$  is parameterized by

$$\Delta S_k[\varphi] = \frac{1}{2} \int \frac{d^d q}{(2\pi)^d} \varphi(-q) R_k(q) \varphi(q).$$

The matrix-valued regulator  $R_k(q)$  is chosen to satisfy the following conditions:

(A) To ensure the suppression of infrared modes, we require

$$\lim_{q^2/k^2 \rightarrow 0} R_k(q) > 0. \quad (3.2)$$

(B) Further, we demand

$$\lim_{k \rightarrow \infty} R_k(q) = \infty \quad (3.3)$$

such that the classical field configurations dominate the path integral for  $k \rightarrow \infty$ .

(C) To obtain the standard generating functional at  $k \rightarrow 0$ , the regulator has to fulfill

$$\lim_{k^2/q^2 \rightarrow 0} R_k(q) = 0. \quad (3.4)$$

The generalized Schwinger functional (3.1) allows defining the generalized effective action:

$$\Gamma_k[\Phi] = \sup_J \left( \int_x \Phi \cdot J - W_k[J] \right) - \Delta S_k[\Phi]. \quad (3.5)$$

It is identical to the classical action in the limit  $k \rightarrow \infty$  due to (3.2) and (3.3). Furthermore, the condition (3.4) implies that (3.5) converges to the 1PI effective action (2.11) in the limit of  $k \rightarrow 0$ . In summary,

$$\lim_{\Lambda \rightarrow \infty} \lim_{k \rightarrow \Lambda} \Gamma_k[\Phi] = S[\Phi], \quad \text{and} \quad \lim_{k \rightarrow 0} \Gamma_k[\Phi] = \Gamma[\Phi].$$

The Wetterich equation [19] describes the evolution of the generalized effective action between the two limits:

$$\partial_t \Gamma_k[\Phi] = \frac{1}{2} \text{Tr} G_k[\Phi] \partial_t R_k, \quad (3.6)$$

where  $t = \ln(k/\Lambda)$  is the RG-time and  $\Lambda$  a reference scale. The flow of the effective action depends on the full (field-, scale- and momentum-dependent) propagator,

$$G_k[\Phi] = \frac{1}{\Gamma^{(2)}[\Phi] + R_k}. \quad (3.7)$$

Here and in the following, we leave the scale-dependence of  $n$ -point functions implicit, i.e.,  $\Gamma^{(2)}[\Phi] \equiv \Gamma_k^{(2)}[\Phi]$ . The inverse two-point function  $\Gamma^{(2)}[\Phi]$  is matrix-valued in field space. It is composed of the scale-dependent two-point correlation functions  $\Gamma_{\Phi_i \Phi_j}^{(2)}[\Phi]$ . The scale-dependent 1PI  $n$ -point correlation functions are obtained by taking  $n$  functional derivatives of the generalized effective action,

$$\Gamma_{\Phi_{i_1} \dots \Phi_{i_n}}^{(n)}[\Phi] = \frac{\delta^n \Gamma_k[\Phi]}{\delta \Phi_{i_n} \dots \delta \Phi_{i_1}}. \quad (3.8)$$

We show a diagrammatic representation of the flow equation (3.6) in Fig. 3.1.

### Properties

The flow equation has a few remarkable properties that are discussed in the following. First of all, it is a non-perturbatively exact equation with a simple one-loop structure. The flows for the propagators and vertices are obtained from the flow of the generalized

$$\frac{\partial \Gamma_k}{\partial t} = \frac{1}{2} \text{Tr} \left( \text{circle with crossed circle} \right)$$

Figure 3.1.: Diagrammatic Wetterich equation (3.6). The crossed circle represents the regulator insertion  $\partial_t R_k(q)$  and the double line the super-propagator (3.7).

effective action by taking functional derivatives. Noteworthy, the flows for the  $n$ -point functions inherit the one-loop structure of the flow equation (3.6). Due to the presence of the full field-dependent propagator in the flow equation, this leads to an infinite number of coupled partial differential equations. Rendering this system finite requires an appropriate truncation. A systematic truncation scheme suitable for QCD is the vertex expansion, introduced below in Sec. 3.1.3.

By construction, the flow is infrared as well as ultraviolet finite and is peaked for momenta close to the RG scale. Thus, fluctuations are successively taken into account by integrating out momentum shells. This includes not only quantum but also thermal fluctuations. Furthermore, the flow depends solely on dressed vertices and propagators, which leads to a consistent RG and momentum scaling for each diagram stemming from derivatives of (3.6).

Last but not least, the flow equation can also be formulated on the Schwinger-Keldysh closed time path [40, 41, 143–145]. This allows to apply the flow equation to far-from-equilibrium systems and enables sophisticated regulator choices. In particular, the idea put forward in [40, 143] suggests integrating out fluctuations in time slices rather than in momentum shells. Such a time-dependent regulator merely implements causality and, thus, leaves all symmetries of causal theories intact. In particular, the time regulator does not violate gauge invariance. However, implementing this approach turns out to be challenging even for a simple  $\varphi^4$ -theory [146] and we do not pursue it any further here.

### 3.1.2. Regulators

To compute the effective action, we need to specify the regulator  $R_k$ , which is chosen to be block-diagonal in field space. The sub-matrices are diagonal for (gauge) bosons and antisymmetric for the anti-commuting quark and ghost fields,

$$\begin{pmatrix} 0 & -R_k^a \\ R_k^a & 0 \end{pmatrix}, \quad \text{with } a \in \{c, q\}.$$

Using  $\Gamma_{aa}^{(2)} = \Gamma_{\bar{a}\bar{a}}^{(2)} = 0$  and  $\Gamma_{\bar{a}a}^{(2)} = -\Gamma_{a\bar{a}}^{(2)}$  leads to the well-known  $-1$  factor for the fermion loops, see, e.g., Fig. 7.1. The regulators  $R_k^{\Phi_i}$  are parameterized by dimensionless shape functions  $r(x = q^2/k^2)$ :

$$R_k^q(q) = \tilde{Z}_q q r(x), \quad \text{and} \quad R_k^{\Phi_j}(q) = \tilde{Z}_{\Phi_j} q^2 r(x),$$

where  $\Phi_j \neq q$ . Here, we suppressed all tensor structures and introduced scaling factors  $\tilde{Z}_{\Phi_i}$  that are usually chosen to be the wave function renormalizations at vanishing momentum. The explicit regulators and the scaling factors used in this work are provided in Sec. C.3.

### Shape Functions

It remains to specify the shape functions. A common choice is the flat regulator [147]:

$$r_{\text{flat}}(x) = (x^{-1} - 1) \cdot \theta(x^{-1} - 1). \quad (3.9)$$

Its main advantage is that the theta function allows to integrate the loop momentum analytically in simple truncations. More advanced truncations with non-trivial momentum

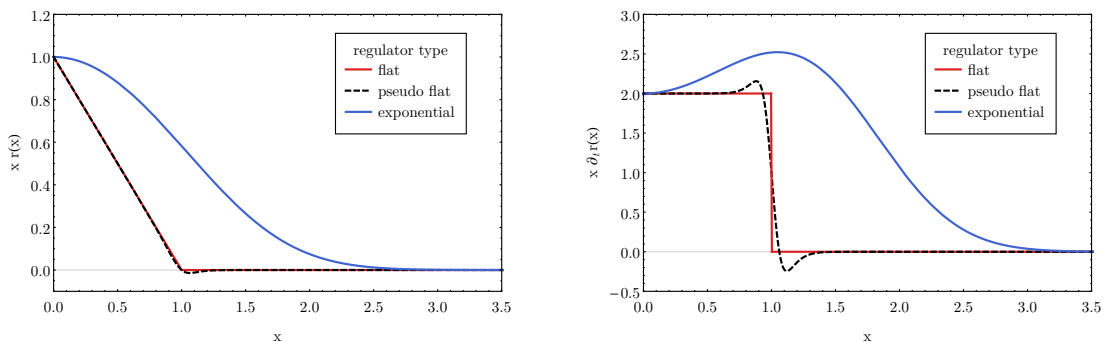


Figure 3.2.: Regulators (left) and their scale derivatives (right), normalized with  $Z_{\Phi_i} k^2$ , i.e.,  $R_k(q)/(Z_{\Phi_i} k^2) = x r(x)$  and  $\dot{R}_k(q)/(Z_{\Phi_i} k^2) = x \dot{r}(x)$ . For illustration purposes, the smoothed flat regulator (3.10) is shown for a rather large value of the smoothing parameter,  $a = 0.05$ . The exponential regulator (3.11) is plotted for  $m = 2$ .

dependencies require numerical integration. In Chapter 5, we use a smooth version of the flat regulator,

$$r_{\text{flat}}^{\text{smooth}}(x) = (x^{-1} - 1) \cdot \frac{1}{1 + e^{\frac{x-1}{a}}}. \quad (3.10)$$

For finite-temperature applications, the exponential regulator,

$$r_{\text{exp}}(x) = \frac{x^{m-1} e^{-x^m}}{1 - e^{-x^m}}, \quad (3.11)$$

is preferable since it carries the thermal exponential decay with the cutoff scale, see Sec. 8.2.1. We plot the shape functions (3.9) – (3.11) in Fig. 3.2. Although their shape is different, they lead to the same effective action if the truncation is sufficient. We illustrate this independence at the example of the gluon propagator dressing, given by  $p^2/\Gamma_{AA}^{(2)}(p)$ , in Fig. 3.3. The results shown are obtained with the smoothed flat regulator (3.10) with  $a = 0.02$  and with the exponential regulator (3.11) with  $m = 2$ . The calculation is explained in Chapter 5. Clearly, the dependence of the gluon propagator dressing on the shape function is negligible. In contrast, the momentum approximation for the vertices influences the gluon propagator. We find that a better approximation leads to better agreement with lattice results. This truncation dependence is further discussed in Sec. 5.3.2.

### Symmetry-breaking Regulators

Special attention must be paid if the regulator term  $\Delta S_k$  breaks a symmetry<sup>1</sup>. While symmetry-preserving regulators can be straightforwardly constructed for many scalar theories, this is not possible for non-Abelian gauge theories that exhibit BRST symmetry,

$$\mathfrak{s} \Delta S_k \neq 0. \quad (3.12)$$

Although many ideas on the construction of gauge invariant flows exist [40, 143, 149–153], none is yet mature enough to be applicable to non-perturbative QCD. Thus, we

<sup>1</sup> See, e.g., [26] for a pedagogical introduction and [25] for a more formal treatment.

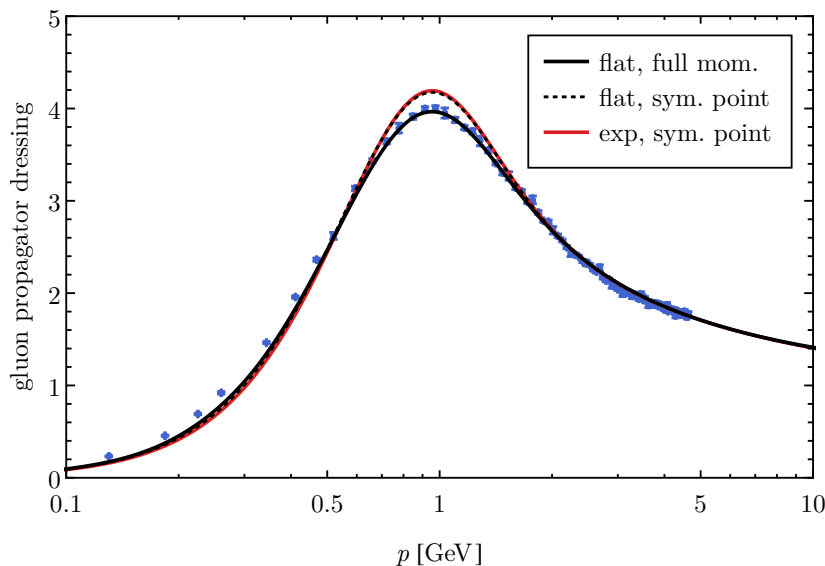


Figure 3.3.: Regulator and truncation dependence of the gluon propagator in pure gauge theory. The solid black line shows the gluon propagator dressing obtained in a truncation that includes the full momentum dependence of all three-point functions. The solid red and the dashed black lines are calculated with a symmetric momentum approximation for the vertices to test the dependence on the regulator shape function. Blue points are  $SU(3)$  lattice results from [148].

inevitably have to work with a BRST-symmetry-breaking regulator. However, this does not mean that the BRST symmetry (that encodes the gauge invariance of observables) is lost: as the regulator term is removed in limit of vanishing RG scale,  $\lim_{k \rightarrow 0} \Delta S_k = 0$ , also the explicit symmetry breaking is removed. Symmetry-breaking regulator terms lead to modified Slavnov-Taylor identities (mSTIs), i.e., the right-hand side of (2.17) is no longer vanishing for  $k > 0$  [25, 154–159]. The mSTIs imply that the action at the cutoff scale is modified,

$$\lim_{k \rightarrow \Lambda} \Gamma_k = S_\Lambda \neq S.$$

Hence, to compute the (physical) effective action from the flow (3.6), one must first determine the modified classical action  $S_\Lambda$ . In principle,  $S_\Lambda$  can be obtained by solving the mSTIs. However, besides being a technical challenge, such an approach is hampered by BRST-symmetry-breaking truncations as well as the high precision that is required for RG relevant operators. Therefore, we put forward a practical way to circumvent solving the mSTIs in the following: We choose the cutoff action  $S_\Lambda$  such that the original STIs are fulfilled at  $k = 0$ . While this procedure renders solving the mSTIs unnecessary, it turns computing the physical effective action into an additional initial value problem. This comes with the advantage that BRST-symmetry-breaking truncation artifacts are (partially) compensated by the choice for  $S_\Lambda$ . Fortunately, it turns out that relatively simple choices for  $S_\Lambda$  suffice to ensure the compliance of the effective action  $\Gamma_{k=0}$  with the STIs at momentum scales much smaller than the cutoff scale.



### 3.1.3. Vertex Expansion

The vertex expansion expresses the effective action in terms of the correlation functions defined by (3.8). It is a systematic expansion scheme that allows for error control in terms of apparent convergence. Loosely speaking, the vertex expansion is the functional version of a multidimensional Taylor series. To introduce it, we define the tuple<sup>2</sup>

$$n_\Phi = (n_{\Phi_A}, n_{\Phi_c}, n_{\Phi_{\bar{c}}}, n_{\Phi_g}, n_{\Phi_{\bar{g}}}) ,$$

where  $n_{\Phi_i}$  is the number of  $\Phi_i$ -legs of the correlator  $\Gamma_{\Phi_{i_1} \dots \Phi_{i_n}}^{(n)}$ . The generalized effective action is then expanded by

$$\Gamma_k[\Phi] = \sum_{n=0}^{\infty} \sum_{|n_\Phi|=n} \frac{1}{n_\Phi!} \int \Gamma_{\Phi_{i_1} \dots \Phi_{i_n}}^{(n)}(p_1, \dots, p_n) \bar{\Phi}_{i_1}(p_1) \cdots \bar{\Phi}_{i_n}(p_n) , \quad (3.13)$$

with

$$\bar{\Phi}_{i_j}(p_j) = \Phi_{i_j}(p_j) - \Phi_{i_j}^0(p_j) . \quad (3.14)$$

The first sum over  $n$  in (3.13) is simply the sum over all orders of the expansion. The second sum includes all contributions from the different  $n$ -point correlators that exist at the corresponding order. The sum integral  $\int$  includes momentum integration as well as summation over compactified dimensions, e.g., summation over Matsubara modes in finite temperature applications, see Chapter 8. Momentum conservation implies  $\sum_{i=1}^n p_i = 0$ . Hence, the correlation functions on the right-hand side of (3.13) contain a corresponding delta distribution. In (3.14), we introduce the expansion point  $\Phi_{i_j}^0$ . The best convergence is achieved if the effective action is expanded around the minimum of the effective action, i.e., the physical solution of the equation of motion (2.12).

For non-scalar fields, the 1PI  $n$ -point functions are tensor-valued. Thus, they have to be expanded in suitable tensor bases,

$$\Gamma_{\Phi_{i_1} \dots \Phi_{i_n}}^{(n)} = \sum_i \lambda_{\Phi_{i_1} \dots \Phi_{i_n}}^{(i)} \mathcal{T}_{\Phi_{i_1} \dots \Phi_{i_n}}^{(i)} ,$$

where  $\lambda_{\Phi_{i_1} \dots \Phi_{i_n}}^{(i)}$  are scalar dressing functions and  $\mathcal{T}_{\Phi_{i_1} \dots \Phi_{i_n}}^{(i)}$  are basis tensors comprising all indices. Hence, the effective action is determined by dressing functions that we compute in the following chapters.

### Truncating with the Vertex Expansion

In principle, one could simply specify the order of the vertex expansion (i.e. the upper bound for the sum over  $n$  in (3.13)) and compute the effective action self-consistently up to this order. In practice, this is seldom possible and it is often necessary to tailor the truncation to the specific problem at hand. Usually, one proceeds as follows:

1. Vertices:

Individual vertices  $\Gamma_{\Phi_{i_1} \dots \Phi_{i_m}}^{(m)}$  with  $m \leq n$  may be neglected if they are (expected to be) unimportant. For example, in Chapter 5 we include the four-gluon vertex in our truncation, but neglect the other four-point functions, the two-ghost-two-gluon and the four-ghost vertex. We know that this is a good approximation in the ultraviolet.

<sup>2</sup> The norm and factorial of a tuple are given by  $|n_\Phi| = \sum_i n_{\Phi_i}$  and  $n_\Phi! = \prod_i n_{\Phi_i}!$ , respectively.

## 2. Tensor bases:

Individual basis tensors  $\mathcal{T}_{\Phi_{i_1} \dots \Phi_{i_n}}^{(i)}$  that are expected to be sub-leading might be neglected. For example, below we include only the four-gluon vertex tensor that is present in the classical action. Note that such an approximation inevitably introduces an uncertainty in the projection operator, see Sec. A.3 and C.2 for details.

## 3. Momentum dependencies:

In general, the dressings  $\lambda_{\Phi_{i_1} \dots \Phi_{i_n}}^{(n)}(p_1, \dots, p_n)$  are momentum dependent functions. Especially for higher  $n$ -point functions, including the full momentum dependence rapidly increases the computational costs. The momentum dependence can often be reduced while still yielding semi-quantitative results, see, e.g., Fig. 3.3.

Apparent convergence requires that the observables are stable under extending the truncation in all ways listed above. This leaves us with many possibilities to truncate. To cope with these, symmetries may serve as a guide to construct approximations. In [65], BRST symmetry was used to deduce the dressings of higher quark-gluon vertices. There, it was found that such an approximation is important to guarantee the consistency of the truncation (to be precise, the degeneracy of the running couplings in the perturbative regime). This suggests that systematic expansions guided by BRST-invariant terms,

$$\bar{q} \not{D}^n q (\bar{q}q)^m, \quad F_{\mu\nu}^a F_{\mu\nu}^a, \quad \frac{(\partial_\mu A_\mu^a)^2}{2\xi} + \bar{c}^a \partial_\mu D_\mu^{ab} c^b, \quad F_{\mu\nu}^a D_\rho^{ab} D_\rho^{bc} F_{\mu\nu}^c \quad \dots \quad (3.15)$$

with  $m, n \geq 0$ , may yield consistent truncations. For the gauge sector, we include the tensor structures that stem from the second and the third term in (3.15), i.e., those that are also present in the classical action. In Chapter 7, we construct the tensor bases of the matter sector with  $\bar{q} \not{D}^n q$ , where  $n \in \{0, 1, 2, 3\}$ . We emphasize that the efficiency of this expansion is still under investigation at the present stage. It might well be that BRST-variant terms are needed to efficiently handle the BRST-variant flows.

## 3.2. Dyson-Schwinger Equations

We briefly introduce Dyson-Schwinger equations [20–22]. They can be derived by exploiting that the integral over a total derivative is zero if possible boundary terms vanish [32]:

$$0 = \int \mathcal{D}\varphi \frac{\delta}{\delta\varphi_i} e^{-S[\varphi] + \int_x J \cdot \varphi} = \left( -\frac{\delta S[\varphi]}{\delta\varphi_i} \Big|_{\varphi=\delta/\delta J} + J_i \right) Z[J] \quad (3.16)$$

This is the master equation for the disconnected correlation functions. The master DSE for the 1PI correlation functions is obtained by rewriting (3.16) with the relations given in Sec. 2.1. We obtain

$$\frac{\delta\Gamma[\Phi]}{\delta\Phi_i} = \frac{\delta S[\Phi]}{\delta\Phi_i} \Big|_{\Phi^{\text{eval}}}, \quad (3.17)$$

where the right-hand side is evaluated at

$$\Phi_j^{\text{eval}}(x) = \int_y G_{\Phi_j \Phi_k}[\Phi](x, y) \frac{\delta}{\delta\Phi_k(y)} + \Phi_j(x). \quad (3.18)$$

The full field-dependent propagator is denoted by  $G_{\Phi_j \Phi_k}$ . All DSEs for 1PI correlation functions can be derived by taking functional derivatives of (3.17).

### Properties and Comparison to the FRG

Dyson-Schwinger and FRG equations share many properties. For example, both are exact non-perturbative equations that can be used at non-zero chemical potential. Furthermore, DSEs as well as flow equations form an infinite tower of coupled equations. However, they also differ in some important aspects that are discussed in the following.

In contrast to the Wetterich equation (3.6), the master DSEs contain bare vertices due to the appearance of the classical action on the right-hand side of (3.17). Owing to the full field-dependent propagator in (3.18), the diagrams also depend on fully dressed propagators and vertices, given by (3.7) and (3.8) with  $R_k = 0$ , respectively. Therefore, DSEs constitute an infinite tower of coupled integral equations. As an illustrative example, we show the ghost propagator DSE in Fig. 3.4. Furthermore, DSEs can be viewed as integrated flow equations [25]. Vice versa, DSEs can also be formulated in the presence of a regulator. In contrast to flow equations, DSEs generally consist not only of one-loop but also of two-loop diagrams due to the integral in (3.18).

A further difference is that (3.17) is an equation for one-point functions whereas the Wetterich equation (3.6) describes the flow of the generalized effective action, a zero-point function. Since  $\Phi_i$  in (3.17) is arbitrary, there exists one master equation for every field. Consequently, DSEs for vertices with multiple different fields may be derived from different master equations. For example, the ghost-gluon vertex DSE can be derived from the ghost or the gluon DSE, yielding different but equivalent equations. These give rise to the so-called transverse Ward-Takahashi identities (tWTIs) [160–164] that essentially state that the differences of equivalent DSEs must vanish.

In general, solving DSEs self-consistently necessitates a numerical integration due to the fully dressed propagators and vertices appearing in the loop diagrams. For gauge theories, numerical integration inevitably involves a BRST-symmetry-breaking regulator or cutoff (such as, e.g., a sharp momentum cutoff). Hence, the Slavnov-Taylor identities are modified, similarly as in the FRG approach. This implies that the unmodified STIs cannot be used to infer, e.g., renormalization constants since the latter have to carry the information on the unphysical symmetry-breaking of the cutoff. These modifications of the vertex STIs are often ignored in the DSE literature [5, 165, 166], which has a significant impact if truncations free of phenomenological parameters are considered, as we can explicitly show. However, the absence of the artificial RG scale  $k$  makes it possible to directly enforce the unmodified vertex STIs at momentum scales well below the cutoff scale (also in every iteration step if an iterative solution method is used).

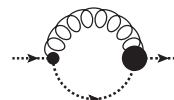
$$\Gamma_{\bar{c}c}^{(2)} = S_{\bar{c}c}^{(2)} + \text{diagram}$$


Figure 3.4.: Exact ghost propagator DSE, derived from (3.17). The thin blob represents the bare ghost-gluon vertex, the thick blob the fully dressed vertex.

## 4. Tracing Large Expressions

Computer-algebraic tools are the backbone of many recent advances in theoretical high energy physics. This is particularly true in perturbation theory where many tools for various tasks exist, see [167–169] for reviews. Recent progress in the application of non-perturbative continuum functional methods requires the ability to perform traces over increasingly complex algebraic expressions [18, 24–37]. These stem from the need to evaluate the one- and two-loop diagrams of these methods at off-shell momenta. In contrast to perturbation theory, the dressed propagators and vertices have to be expressed in terms of ever larger, ideally full, tensor bases. This dramatically increases the tracing effort. To summarize, typical workflows in perturbative as well as non-perturbative calculations involve the evaluation of traces in different sub-spaces, ranging from gauge group to Lorentz and Dirac traces.

Here, we present<sup>1</sup> *FormTracer – A Mathematica Tracing Package Using FORM* [2]. It is a high-performance general-purpose easy-to-use tracing tool that uses FORM [171–174] in combination with an efficient Mathematica decomposition algorithm. Crucial parts were developed along the lines of [1, 5, 65]. Meanwhile, it is published in [2] and this chapter as well as Appendix D are based on this article. FormTracer represents an integral part of the workflow of the fQCD collaboration (see Sec. C.1 for a description) and has been used within [1, 3, 4, 65, 68, 69, 73, 175] and outside [176–179] the fQCD collaboration [64].

We list the key functionalities in Sec. 4.1. Internally, the expressions to be traced are decomposed into their group product spaces as described in Sec. 4.2. In Sec. 4.3 and 4.4 we discuss Lie groups and peculiarities of Dirac and Lorentz tracing. A short conclusion is given in Sec. 4.5. Usage information, a comparison to other programs, and algorithmic details are provided in Appendix D.

### 4.1. Features of FormTracer

Here, we summarize the main features of FormTracer:

- High performance due to FORM back end combined with an efficient decomposition algorithm in Mathematica, see Sec. 4.2
- Evaluation of Euclidean Lorentz/Dirac traces in arbitrary dimensions, and traces over an arbitrary number of group product spaces, see Sec. 4.3
- Supports
  - the  $\gamma_5$  matrix in general dimensions within the Larin scheme, see Sec. 4.4.1
  - a special time-like direction for Euclidean finite temperature and density applications, see Sec. 4.4.2
  - partial traces involving open indices

---

<sup>1</sup> FormTracer is licensed under GNU General Public License Version 3 and available from [170].

- the creation of optimized output (including bracketing) using FORM’s optimization algorithm [173] for numerical processing in C/C++/Fortran
  - user-defined combined Lorentz tensors and identities, e.g., (transverse and longitudinal) projection operators and their orthogonality relations, for speedup
- Intuitive, easy-to-use and highly customizable Mathematica front end
  - Convenient installation and update procedure within Mathematica

## 4.2. Decomposition of Tensor Classes

This section explains details of the expansion algorithm, which is hidden from the user. Let  $x$  be an untraced expression, of which the trace over  $n$  Lie groups as well as Dirac and Lorentz space is to be taken. The straightforward way to perform the trace in  $x$  is to fully expand  $x$  into a sum of simple products of tensors and repeatedly apply the appropriate tensor identities to the summands. However, this strategy almost always entails multiple calculations of identical subtraces. Since FORM fully expands all expressions, we decompose  $x$  into its subspaces in Mathematica by bringing it into the form

$$x = c_0 \sum_{i_1} C_{i_1} \sum_{i_2} C_{i_1 i_2} \cdots \sum_{i_n} C_{i_1 i_2 \dots i_n} L_{i_1 i_2 \dots i_n}. \quad (4.1)$$

Here,  $c_0$  is a scalar prefactor,  $C_{i_1 \dots i_j}$  contains only tensors of the  $j$ -th group, and  $L_{i_1 i_2 \dots i_n}$  consists of Lorentz and Dirac tensors only. The summation boundary of  $i_j$  in (4.1) depends on  $i_1, \dots, i_{j-1}$ . In addition to the considerable performance gain due to the uniqueness of the  $C_{i_1 \dots i_j}$ , this decomposition allows to take the traces of the individual Lie groups separately. For tracing the combined Lorentz and Dirac tensors  $L_{i_1 i_2 \dots i_n}$  in (4.1), we provide two possibilities. By default, no further manipulation is performed and we let FORM handle the evaluation of the  $L_{i_1 i_2 \dots i_n}$ ’s. The second option seldom accelerates the tracing process and is detailed in Appendix D.

## 4.3. Simple Compact Lie Groups

FormTracer includes different group tracing algorithms that are implemented in FORM. The most general algorithm is provided by the FORM color package [180] and allows tracing of arbitrary simple compact Lie groups. Furthermore, we include explicit tracing algorithms for the fundamental representation in  $SU(N)$ ,  $SO(N)$  and  $Sp(N)$ , adapted from routines published with the color package [180] that use the Cvitanovic algorithm [181] with additional support for partial traces. Finally, we include dedicated tracing algorithms for the fundamental representations in  $SU(2)$  and  $SU(3)$  that support partial traces, explicit numerical indices as well as transposed group generators. The use of explicit numerical indices requires working in explicit representations. For  $SU(2)$  and  $SU(3)$  we choose generators proportional to Pauli and Gell-Mann matrices, respectively. The fundamental  $SU(N)$  tracing algorithm also supports partial traces but does not guarantee the same degree of simplification as the specific  $SU(2)$  and  $SU(3)$  routines. Due to the modular structure of the tracing procedure, the inclusion of further tracing algorithms at a later stage is easily possible.

The definitions of the group constants closely follow those of the color package [180], which we repeat here for the reader's convenience. We consider simple compact Lie algebras with Hermitian generators  $T$ , which obey

$$[T^a, T^b] = if^{abc} T^c, \quad (4.2)$$

where  $f^{abc}$  denote the structure constants. The dimensions of the (fermion) representation and the adjoint representation are denoted by  $N_F$  and  $N_A$ , respectively. The generators of the adjoint representation are given by  $(T_A^a)^{bc} = -if^{abc}$ . We define quadratic Casimir operators  $C_F$  and  $C_A$  via

$$\begin{aligned} (T^a T^a)_{ij} &= C_F \delta_{ij}, \\ f^{acd} f^{bcd} &= C_A \delta^{ab}. \end{aligned} \quad (4.3)$$

It remains to fix the normalization:

$$\text{Tr } T^a T^b = I_2 \delta^{ab}, \quad (4.4)$$

where  $I_2$  denotes the second-order index of the representation. All tracing algorithms except for the FORM color package produce tracing results just in terms of the dimension of the representation  $N_F$ , with all other group constants set to their default values. With  $N_F = N$  for the classical groups in the fundamental representations, these are given by

$$\begin{aligned} SU(N) : \quad C_F &= \frac{N^2 - 1}{2N}, \quad N_A = N^2 - 1, \quad C_A = N, \quad I_2 = \frac{1}{2}; \\ SO(N) : \quad C_F &= \frac{N - 1}{2}, \quad N_A = \frac{N(N - 1)}{2}, \quad C_A = N - 2, \quad I_2 = 1; \\ Sp(N) : \quad C_F &= \frac{N + 1}{4}, \quad N_A = \frac{N(N + 1)}{2}, \quad C_A = \frac{N + 2}{2}, \quad I_2 = \frac{1}{2}. \end{aligned} \quad (4.5)$$

## 4.4. Dirac and Lorentz Tracing

Dirac and Lorentz tracing is very well-known in the literature. Hence, we discuss only two peculiarities: dealing with the fifth gamma matrix in non-integer dimensions and tracing Lorentz vectors in the presence of a special direction.

### 4.4.1. Dirac Traces in General Dimensions

Although FORM has built-in support for Dirac traces in  $d$  dimensions it does not come with a solution for the handling of the fifth gamma matrix, which is defined as an inherently four-dimensional object. Nonetheless, the generalization of the  $\gamma_5$  matrix to  $d$  dimensions is very important, in particular for dimensional regularization. The implementation of the fifth gamma matrix in  $d \neq 4$  dimensions represents a subtle procedure and different prescriptions exist. Here, we closely follow [182, 183] and implement support for the fifth gamma matrix by means of the Larin scheme [182], translated to Euclidean spacetime, which exploits the relation

$$\gamma_\mu \gamma_5 = \frac{1}{3!} \epsilon_{\mu\nu\rho\sigma} \gamma_\nu \gamma_\rho \gamma_\sigma. \quad (4.6)$$

For expressions containing  $\gamma_5$  matrices, FormTracer applies the following algorithm to every spin line:

1. Replace any occurring  $\gamma_5\gamma_5$  with the unit matrix,  $\gamma_5\gamma_5 \rightarrow 1$ .
2. Read each Dirac sub-trace such that no  $\gamma_5$  is found on the leftmost position and replace all  $\gamma_5$  matrices using (4.6).
3. Contract all epsilon tensors that do not stem from step 2.
4. Contract all remaining epsilon tensors.
5. Perform Dirac trace in  $d$  dimensions with FORM.

The separate contraction of different sets of epsilon tensors in steps 3 and 4 is necessary, since there is no Schouten identity for general dimensions  $d \neq 4$ , which guarantees the equivalence of different contraction orders in four dimensions. When only a single  $\gamma_5$  matrix needs to be traced, a faster procedure based on an implicit application of (4.6) can be used [183]. By setting `FastGamma5Trace[True]`, FormTracer applies the above algorithm to all but the last  $\gamma_5$  matrix, which is then traced with the strategy from [183].

Due to the intricacies of the definition of  $\gamma_5$  in  $d \neq 4$  dimensions, we encourage users to ensure that the implemented prescription is suitable for their specific application. Particular caution is necessary in the case of multiple disconnected spin lines in the presence of connecting epsilon tensors.

#### 4.4.2. Finite Temperature and Density Tracing

FormTracer has a built-in functionality for a special time-like direction that is useful for Euclidean finite temperature and density applications. It supports the definition of space-like vectors

$$p_s = \begin{pmatrix} 0 \\ \vec{p} \end{pmatrix},$$

which hold the spatial components of the corresponding full vectors

$$p = \begin{pmatrix} p_0 \\ \vec{p} \end{pmatrix}.$$

By definition, these vectors obey the following relations:

$$p \cdot_s q \equiv \vec{p} \cdot \vec{q} = p_s \cdot q_s = p_s \cdot q, \quad (4.7)$$

where the space-like inner product  $\cdot_s$  has been introduced, which is supported by FormTracer. In the evaluation of traces, the spatial vectors,  $p_s$ , with full dimensions are kept until the trace is performed. The traced expressions are then represented in terms of standard and space-like inner products using (4.7). This implementation of finite temperature is limited to Euclidean signature, which is sufficient for finite temperature and density applications in equilibrium.

## 4.5. Conclusion

We presented the dedicated tracing package FormTracer for Mathematica, which has already proved its usefulness in a number of studies [1, 3, 4, 65, 68, 69, 73, 175–179]. Its most notable features are its usability, performance, and the capability to efficiently handle an arbitrary number of Lie groups as well as Dirac and Lorentz tensors in arbitrary dimensions. This includes an algorithm to deal with  $\gamma_5$  matrices in  $d \neq 4$  dimensions. FormTracer achieves its performance by using FORM as a powerful back end in combination with a decomposition algorithm in Mathematica. Furthermore, a simple but effective way to single out a special time-like direction for finite temperature and density applications in Euclidean field theory is provided. Although developed with specific applications in non-perturbative functional methods in mind, its flexible notation and usability facilitate the use in new and existing general purpose programs, in particular in perturbation theory. Albeit purely technical, tools for the automation of complex calculations such as FormTracer are necessary to obtain a quantitative grip on QCD.



## 5. Yang-Mills Correlators

The application of functional methods to QCD led to a number of breakthroughs, ranging from the first qualitatively correct calculation of Landau gauge propagators to investigations of the phase diagram, see [5, 112, 116–121, 132, 133, 155, 165, 166, 184–202] for studies of Yang-Mills theory and [24–37] for reviews. In general, many applications of functional methods use mixed approaches where the correlation functions are partly deduced from phenomenological constraints or external input. Despite their remarkable success, a first-principle description is required for some of the most pressing open questions of strongly-interacting matter [63]. The significant progress over the past two decades builds the basis for a systematic expansion in which reliability is obtained by apparent convergence. Qualitative and quantitative control over vacuum Yang-Mills theory is thereby a prerequisite for investigations of QCD.

In this chapter non-perturbative *Landau gauge Yang-Mills correlation functions* [1] are computed in a self-consistent truncation that needs the classical action as only input. This is the first study of four-dimensional Yang-Mills theory within functional methods that does not require any modeling of correlation functions. It is the central pillar of this thesis and embedded as follows. This work complements a previously performed study of chiral symmetry breaking in quenched QCD [65]. In Chapter 7, these studies are combined and unquenched correlators are obtained. The next step towards investigating the QCD phase structure is to extend this vacuum Yang-Mills study to finite temperature, which is done in Chapter 8.

This chapter is structured as follows: We detail the employed vertex expansion in Sec. 5.1. The most distinct feature of Yang-Mills theory is color confinement, which is reflected by the creation of a gluon mass gap in Landau gauge. Thus, we put particular focus on the dynamical generation of the gluon mass gap at non-perturbative momenta. We discuss the necessity of infrared irregularities as well as mechanisms for the generation of a mass gap in Sec. 5.2. This discussion is mostly not specific to the FRG, but holds for functional methods in general. Numerical results for the propagators and vertices are presented in Sec. 5.3. We demonstrate the importance of an accurate renormalization and present numerical evidence for the dynamic mass gap generation in our calculation. While Sec. 5.1 – 5.3 are based on [1], we report on newer results in Sec. 5.4. To be specific, we comment on the gauge group dependence, plot beta functions, and refine the mass gap analysis. Finally, we conclude in Sec. 5.5.

$$\frac{\partial \Gamma_k}{\partial t} = \frac{1}{2} \left( \text{Diagram 1} - \text{Diagram 2} \right)$$

Figure 5.1.: Wetterich equation for pure gauge theory. Wiggly (dotted) lines represent momentum-, scale- and field-dependent dressed gluon (ghost) propagators.

## 5.1. Vertex Expansion and Transversality

Quantum Chromodynamics and the functional renormalization group have been introduced in Chapter 2 and 3. Therefore, we discuss only the setup that is specific to Yang-Mills theory. In particular, we derive the flow equations in Sec. 5.1.1, specify the tensor bases in Sec. 5.1.2, and discuss transversality of Landau gauge in Sec. 5.1.3. For the derivation of the equations and the numerical implementation, we employ the tools of the fQCD collaboration, see Appendix C for details.

### 5.1.1. Flow Equations

The infrared regularization of the gluon and ghost fluctuations is achieved by adding an appropriate regulator term to the classical action,  $S_{\text{YM}} \rightarrow S_{\text{YM}} + \Delta S_{\text{YM}}$ , that is parameterized by

$$\Delta S_{\text{YM}} = \frac{1}{2} \int_x A_\mu^a R_{k,\mu\nu}^{A,ab} A_\nu^b + \int_x \bar{c}^a R_k^{c,ab} c^b. \quad (5.1)$$

The regulator functions  $R_k$  are given in Sec. C.3. Using the superfield  $\Phi = (A, c, \bar{c})$ , the Wetterich equation [19] for pure gauge theory in the vacuum reads

$$\partial_t \Gamma_k[\Phi] = \frac{1}{2} \int_p G_{k,\mu\nu}^{ab}[\Phi] \partial_t R_{k,\nu\mu}^{A,ba} - \int_p G_k^{ab}[\Phi] \partial_t R_k^{c,ba}, \quad (5.2)$$

where  $G_{k,\mu\nu}^{ab}[\Phi]$  and  $G_k^{ab}[\Phi]$  are the momentum-, scale- and field-dependent gluon and ghost propagators and  $\int_p = \int d^4 p / (2\pi)^4$ . Its diagrammatic representation is shown in Fig. 5.1. Taking functional derivatives of (5.2) yields exact flow equations for the  $n$ -point functions. The flow equations for the two-point functions, i.e., the inverse propagators, are shown in Fig. 5.2. To approximate the effective action, we employ the vertex expansion introduced in Sec. 3.1.3. We include all vertices that are present in the bare action, see Fig. 5.3 for a pictorial representation. Applying this truncation to the exact flow equations for the inverse propagators yields the truncated flow equations that are displayed alongside the truncated vertex equations in Fig. 5.4. We discuss the convergence of the vertex expansion in Sec. 5.3.2. In the next section, we specify the included basis tensors and the momentum approximations.

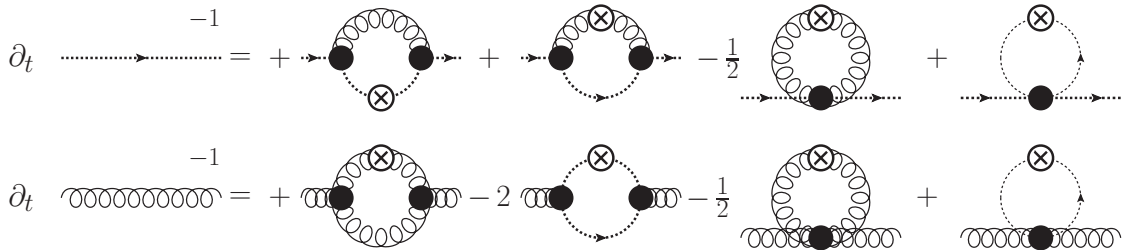


Figure 5.2.: Exact flow equations for Yang-Mills two-point functions. Filled circles denote fully dressed (1PI) vertices. The diagrammatic notation used here and in the following is sloppy but common: While the lines on the right-hand side represent regulated propagators  $G_k = (\Gamma_k^{(2)} + R_k)^{-1}$ , they represent inverse two-point functions  $(\Gamma_k^{(2)})^{-1}$  on the left-hand side.

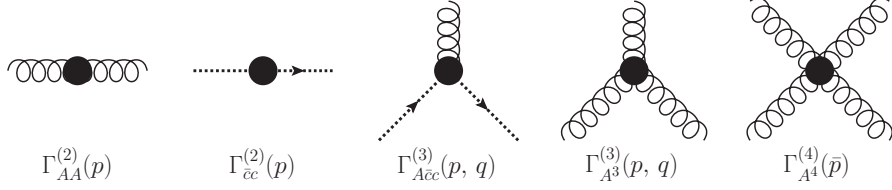


Figure 5.3.: Approximation for the effective action. We include only the classical tensor structures, see (5.3), (5.6) and (5.7). The corresponding diagrammatic equations are shown in Fig. 5.4.

### 5.1.2. Tensor Structures

The lowest order contributions in the vertex expansion are the inverse ghost and gluon propagators, parameterized by

$$\begin{aligned} [\Gamma_{cc}^{(2)}]^{ab}(p) &= Z_c(p) p^2 \delta^{ab}, \\ [\Gamma_{AA}^{(2)}]^{ab}(p) &= Z_A(p) p^2 \delta^{ab} \Pi_{\mu\nu}^\perp(p) + \frac{1}{\xi} p^2 \delta^{ab} \Pi_{\mu\nu}^\parallel(p), \end{aligned} \quad (5.3)$$

with dimensionless scalar dressing functions  $1/Z_c$  and  $1/Z_A$ , and  $\xi \rightarrow 0$  in Landau gauge. In (5.3),  $\Pi_{\mu\nu}^\perp(p)$  and  $\Pi_{\mu\nu}^\parallel(p)$  denote the transverse and longitudinal projection operators defined in (2.13). Similarly, we define dimensionless scalar dressings for the vertices. On the three-point level we include the (transversely projected) classical tensor structures of the ghost-gluon and three-gluon vertices,  $\mathcal{T}_{ccA}^{(1)}$  and  $\mathcal{T}_{A^3}^{(1)}$ :

$$\begin{aligned} [\Gamma_{ccA}^{(3)}]^{abc}(p, q) &= \lambda_{ccA}(|p|, |q|, t) [\mathcal{T}_{ccA}^{(1)}]^{abc}(p, q), \\ [\Gamma_{A^3}^{(3)}]^{abc}(p, q) &= \lambda_{A^3}(|p|, |q|, t) [\mathcal{T}_{A^3}^{(1)}]^{abc}(p, q). \end{aligned} \quad (5.4)$$

Here, the momentum  $p$  ( $q$ ) corresponds to the indices  $a$  ( $b$ ) and  $t$  denotes the cosine of the angle between the momenta  $p$  and  $q$ . In the case of the transversely projected ghost-gluon vertex,  $\mathcal{T}_{ccA}^{(1)}$  represents already a full basis whereas a full basis for the transversely projected three-gluon vertex consists of four elements. However, the effect of non-classical tensors has been found to be subleading [166] and we neglect them here.

The most important four-point function is given by the four-gluon vertex, which appears already in the classical action. As for the three-gluon vertex, we approximate it with its classical tensor structure

$$[\Gamma_{A^4}^{(4)}]^{abcd}(p, q, r) = \lambda_{A^4}(\bar{p}) [\mathcal{T}_{A^4}^{(1)}]^{abcd}(p, q, r). \quad (5.5)$$

The momentum dependence of the four-gluon vertex dressing function is approximated with its momentum dependence at the symmetric point via the average momentum  $\bar{p} \equiv \sqrt{p^2 + q^2 + r^2 + (p + q + r)^2}/2$ . This has been shown to be a good approximation of the full momentum dependence [5, 74] in the vertex equations. To improve this approximation, we additionally calculate the momentum dependence of the four-gluon vertex dressing function  $\lambda_{A^4}(|p|, |q|, t)$  on the special configuration  $(p, q, r) = (p, q, -p)$ . We use this special configuration exclusively in the tadpole diagram of the gluon propagator equation, cf. Sec. 5.3.2. We show the difference between the special configuration and the symmetric

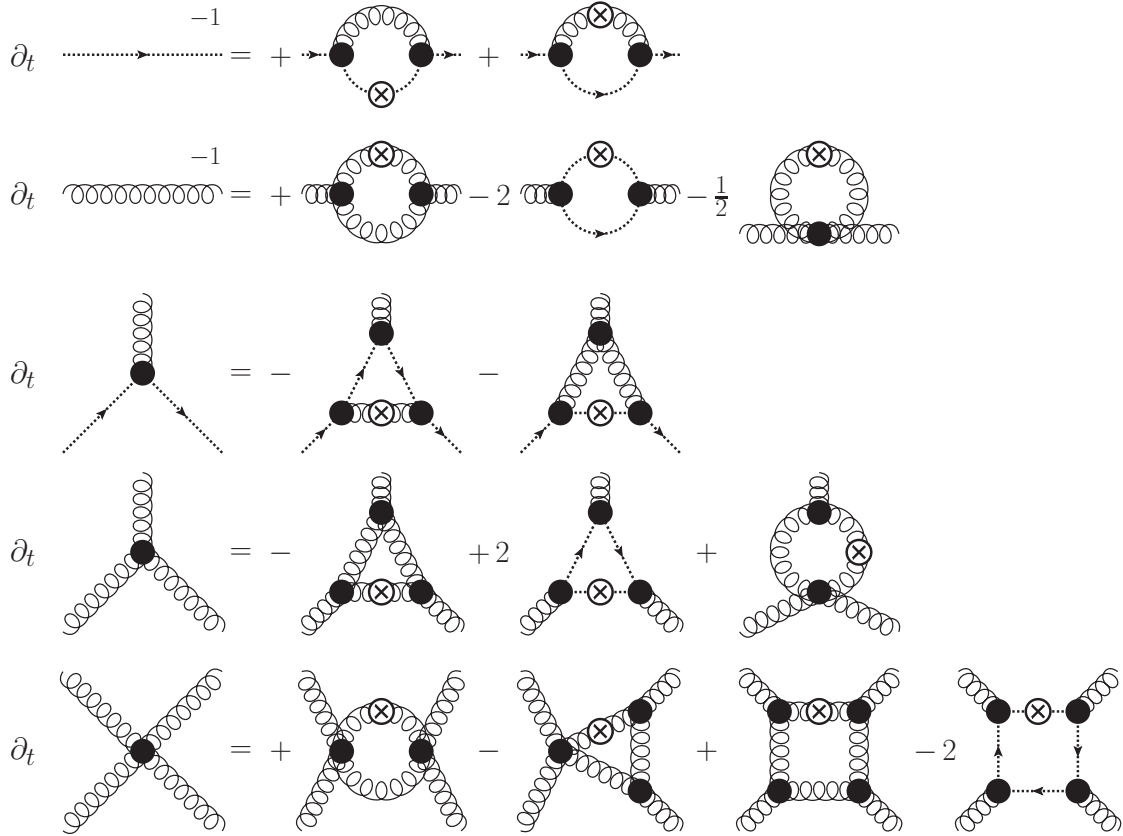


Figure 5.4.: Diagrams that contribute to the truncated flow of propagators and vertices. Distinct permutations include not only (anti-)symmetric permutations of external legs but also permutations of the regulator insertions.

momentum approximation in Fig. 5.14. Although the four-gluon vertex has been the subject of several studies [5, 74, 188, 196, 199], no fully conclusive statements about the importance of additional non-classical tensors structures are available.

In the present work we solve the coupled system of all momentum-dependent classical vertex structures and propagators self-consistently. For a comparison of the current approximation with that used in other functional works one has to keep in mind that FRG, Dyson-Schwinger or  $n$ PI equations implement different resummation schemes. Thus, even on an identical approximation level of a systematic vertex expansion, the included resummations differ. In former works (for references see above) with functional methods, only subsets of these correlation functions have been coupled back. A notable exception is [201], where a similar self-consistent approximation has been used for three-dimensional Yang-Mills theory. We come back to this point in the next chapter, where we compute correlation functions for three-dimensional Yang-Mills theory.

Although not marked explicitly, all dressing in (5.3), (5.4) and (5.5) are  $k$  dependent. Unless marked otherwise, we always plot the momentum dependence at vanishing RG scale. Furthermore, all vertex dressings are transverse dressings since they are projected transversely as detailed below.

### Projecting

In this section we define the classical tensors in which we expanded the vertices and the employed projection operators. The tensor structures for the classical three-point vertices are given by

$$\begin{aligned} \left[ \mathcal{T}_{\bar{c}cA}^{(1)} \right]_{\mu}^{abc} &= \left[ S_{\bar{c}cA}^{(3)} \right]_{\mu}^{abc} = i f^{abc} q_{\mu}, \\ \left[ \mathcal{T}_{A^3}^{(1)} \right]_{\mu\nu\rho}^{abc} &= \left[ S_{A^3}^{(3)} \right]_{\mu\nu\rho}^{abc} = i f^{abc} \left\{ (p - q)_{\rho} \delta_{\mu\nu} + \text{perm.} \right\}, \end{aligned} \quad (5.6)$$

and by

$$\left[ \mathcal{T}_{A^4}^{(1)} \right]_{\mu\nu\rho\sigma}^{abcd} = \left[ S_{A^4}^{(4)} \right]_{\mu\nu\rho\sigma}^{abcd} = f^{abn} f^{cdn} \delta_{\mu\rho} \delta_{\nu\sigma} + \text{perm.} \quad (5.7)$$

for the four-point function. For the transversely projected ghost-gluon vertex this single tensor constitutes a full basis and the projection is unique. However, additional tensors exist in the case of the three-gluon and four-gluon vertices. To obtain scalar dressing functions we contract the flow equations with

$$\left[ \mathcal{T}_{A^3}^{(1)} \right]_{\mu'\nu'\rho'}^{abc} \Pi_{\mu'\mu}^{\perp}(p) \Pi_{\nu'\nu}^{\perp}(q) \Pi_{\rho'\rho}^{\perp}(p+q) \quad (5.8)$$

and

$$\left[ \mathcal{T}_{A^4}^{(1)} \right]_{\mu'\nu'\rho'\sigma'}^{abcd} \Pi_{\mu'\mu}^{\perp}(p) \Pi_{\nu'\nu}^{\perp}(q) \Pi_{\rho'\rho}^{\perp}(r) \Pi_{\sigma'\sigma}^{\perp}(p+q+r), \quad (5.9)$$

respectively, which is an approximation if non-classical tensors are generated. We discuss this point further in Sec. [A.3](#) and [C.2](#).

#### 5.1.3. Modified STIs and Transversality

In Landau gauge, the dynamical system of correlation functions consists of the transversely projected correlators [[112](#)]. Those with at least one longitudinal gluon leg do not feed back into the dynamics. To make these statements precise, it is useful to split correlation functions into purely transverse ones and their complement with at least one longitudinal gluon leg. The purely transverse vertices  $\Gamma_{\perp}^{(n)}$ , are defined by attaching transverse projection operators to all gluon legs,

$$\left[ \Gamma_{\perp}^{(n)} \right]_{\mu_1 \dots \mu_{n_A}} \equiv \Pi_{\mu_1 \nu_1}^{\perp} \dots \Pi_{\mu_{n_A} \nu_{n_A}}^{\perp} \left[ \Gamma^{(n)} \right]_{\nu_1 \dots \nu_{n_A}}, \quad (5.10)$$

where  $n_A$  is the number of gluon legs and group indices as well as momentum arguments have been suppressed for the sake of brevity. This defines a unique decomposition of  $n$ -point functions into

$$\Gamma^{(n)} = \Gamma_{\perp}^{(n)} + \Gamma_{\parallel}^{(n)},$$

where the longitudinal  $n$ -point functions,  $\Gamma_{\parallel}^{(n)}$ , have at least one longitudinal gluon leg. Hence, they are always projected to zero by the transverse projection operators of ([5.10](#)).

Functional equations for the transverse correlation functions close in Landau gauge, leading to the structure [112],

$$\Gamma_{\perp}^{(n)} = \text{Func} \left[ \left\{ \Gamma_{\perp}^{(n)} \right\} \right]. \quad (5.11)$$

Here,  $\text{Func} [\#]$  stands for functional diagrammatic expressions of either integrated FRG, Dyson-Schwinger or  $n$ PI equations. Equation (5.11) follows from the fact that all internal legs are transversely projected by the Landau gauge gluon propagator. Hence, by using transverse projections for the external legs one obtains (5.11). In contrast, the functional equations for the  $n$ -point functions with at least one longitudinal gluon leg,  $\Gamma_{\parallel}^{(n)}$ , are of the form

$$\Gamma_{\parallel}^{(n)} = \text{Func} \left[ \left\{ \Gamma_{\parallel}^{(n)} \right\}, \left\{ \Gamma_{\perp}^{(n)} \right\} \right]. \quad (5.12)$$

In other words, solving the functional equations for  $\Gamma_{\parallel}^{(n)}$  requires the solution of the closed transverse set of equations (5.11).

In the FRG, gauge invariance is encoded in modified Slavnov-Taylor identities (mSTIs) and modified Ward-Takahashi identities (mWTIs). They are derived similarly as the Slavnov-Taylor identities, see Sec. 2.1, by including the gauge or BRST variations of the regulator terms (cf. (3.12)), see [25, 154–156, 158, 159] for details. The mSTIs are of the schematic form

$$\Gamma_{\parallel}^{(n)} = \text{mSTI} \left[ \left\{ \Gamma_{\parallel}^{(n)} \right\}, \left\{ \Gamma_{\perp}^{(n)} \right\}, R_k \right], \quad (5.13)$$

and reduce to the standard STIs in the limit of vanishing regulator,  $R_k \rightarrow 0$ . The STIs and mSTIs have a similar structure as (5.12) and can be used to obtain information on the longitudinal part of the correlators. Alternatively, they provide a non-trivial consistency check for approximate solutions of (5.12).

### Consequences of the modified Slavnov-Taylor Identities

For the purposes of this work, the most important effect of the modification of the STIs is the appearance of a non-vanishing gluon mass parameter [154],

$$\Delta_{\text{mSTI}} \left[ \Gamma_{AA}^{(2)} \right]_{\mu\nu}^{ab} \propto \delta^{ab} \delta_{\mu\nu} \alpha(k) k^2. \quad (5.14)$$

At  $k = 0$ , where the regulators vanish, this modification disappears, as the mSTIs reduce to the standard STIs. In particular, this entails that, at  $k = 0$ , the inverse longitudinal gluon propagator,  $\Gamma_{AA,\parallel}^{(2)}$ , reduces to the classical one, solely determined by the gauge fixing term,

$$p_{\mu} \left( \left[ \Gamma_{AA}^{(2)} \right]_{\mu\nu}^{ab}(p) - \left[ S_{AA}^{(2)} \right]_{\mu\nu}^{ab}(p) \right) = 0. \quad (5.15)$$

This provides a unique condition for determining the gluon mass parameter, cf. (5.14), at the ultraviolet initial scale  $\Lambda$ . However, it can only be used if the longitudinal system is solved.

One further conclusion from (5.13) is that the mSTIs do not constrain the transverse correlation functions without further input. This is not in tension with one of the main

applications of STIs in perturbation theory, i.e., with relating the running of the relevant vertices of Yang-Mills theory that require renormalization. As Yang-Mills theory is renormalizable, only the classical vertex structures are renormalized and hence the renormalization functions of their transverse and longitudinal parts have to be identical.

As an instructive example, we consider the ghost-gluon vertex. For this example and the following discussions we evaluate the STIs within the approximation used in the present work: we only consider contributions from the primitively divergent vertices on the right-hand side of the STIs. In particular, this excludes contributions from the two-ghost–two-gluon vertex. The full ghost-gluon vertex is parameterized by two tensors,

$$[\Gamma_{\bar{c}cA}^{(3)}]_{\mu}^{abc}(p, q) = i f^{abc} [q_{\mu} \lambda_{\bar{c}cA, \text{cl}}(p, q) + p_{\mu} \lambda_{\bar{c}cA, \text{ncl}}(p, q)]. \quad (5.16)$$

In (5.16) we have introduced two dressing functions,  $\lambda_{\bar{c}cA, \text{cl}}$  and  $\lambda_{\bar{c}cA, \text{ncl}}$ , which are functions of the gluon momentum  $p$  and the anti-ghost momentum  $q$ . In a general covariant gauge only  $\lambda_{\bar{c}cA, \text{cl}}$  requires renormalization. Similar splittings into a classical tensor and the rest can be used in the other vertices. Trivially, this property relates the perturbative RG running of the transverse and longitudinal projections of the classical tensors. Then, the STIs can be used to determine the perturbative RG running of the classical tensor structures, leading to the well-known perturbative relations,

$$\frac{\lambda_{\bar{c}cA, \text{cl}}^2}{Z_c^2 Z_A} = \frac{\lambda_{A^3, \text{cl}}^2}{Z_A^3} = \frac{\lambda_{A^4, \text{cl}}^2}{Z_A^2}, \quad (5.17)$$

at the renormalization scale  $\mu$ . Consequently, (5.17) allows for the definition of a unique renormalized two-loop coupling  $\alpha(\mu)$  from the vertices.

The momentum dependent STIs can also be used to make the relation (5.17) momentum-dependent. Keeping only the classical tensor structures, we are led to the momentum dependent transverse running couplings

$$\begin{aligned} \alpha_{\bar{c}cA}(p) &= \frac{1}{4\pi} \frac{\lambda_{\bar{c}cA}^2(p)}{Z_A(p) Z_c^2(p)}, \\ \alpha_{A^3}(p) &= \frac{1}{4\pi} \frac{\lambda_{A^3}^2(p)}{Z_A^3(p)}, \\ \alpha_{A^4}(p) &= \frac{1}{4\pi} \frac{\lambda_{A^4}(p)}{Z_A^2(p)}. \end{aligned} \quad (5.18)$$

The vertex dressings in (5.18) are evaluated at the symmetric momentum configurations, defined in Sec. 5.3.2. The Slavnov-Taylor identities and two-loop universality demand that these running couplings are degenerate at large, perturbative momentum scales, where the longitudinal and transverse parts of the vertices agree.

In Landau gauge, the ghost-gluon vertex is not renormalized [84] on specific momentum configurations. This allows for an alternative definition of a running coupling from the wave function renormalization of the ghost and the gluon [116, 117, 203],

$$\alpha_s(p) = \frac{1}{4\pi} \frac{g^2}{Z_A(p) Z_c^2(p)}.$$

This running coupling is called propagator coupling in the following. The decisive distinction between the propagator and the vertex couplings, given by (5.18), is the differing momentum dependence. This is best seen from considering the ratio of the ghost-gluon vertex and the propagator coupling,  $\alpha_{\bar{c}cA}(p)/\alpha_s(p) = \lambda_{\bar{c}cA}^2(p)/g^2$ .

## 5.2. Confinement

It has been shown in [53, 108, 109, 204–206] that a mass gap in the gluon propagator signals confinement in QCD in covariant gauges. Furthermore, in Yang-Mills theory formulated in covariant gauges, the gapping of the gluon relative to the ghost is necessary and sufficient for producing a confining potential for the corresponding order parameter, the Polyakov loop, see [53, 108, 109, 204–212] for studies thereof. Hence, understanding the details of the dynamical generation of a gluon mass gap gives insight into the confinement mechanism.

This relation holds for all potential infrared closures of the perturbative Landau gauge. The standard infrared closure corresponds to a full average over all Gribov regions. This leads to the standard Zinn-Justin equation as used in the literature, e.g., [32]. In turn, the restriction to the first Gribov regime can be implemented within the refined Gribov-Zwanziger formalism, see, e.g., [130, 131, 213–215], that leads to infrared modifications of the STIs. In the following we discuss the consequences of the standard STIs, a discussion of the refined Gribov-Zwanziger formalism is deferred to future work.

### 5.2.1. Gluon Mass Gap and Irregularities

In order to study the dynamical generation of the mass gap, we first discuss the consequences of the STI for the gluon two point function (5.15). It states that no quantum fluctuations contribute to the inverse longitudinal gluon propagator, i.e., the longitudinal gluon propagator is defined by the gauge fixing term. Therefore, the dynamical creation of a gluon mass gap requires different contributions to the longitudinal and transverse gluon mass parameter. The discussion of the prerequisites for meeting this condition is qualitatively different for the scaling and the decoupling solutions. Hence, these two cases are discussed separately.

The scaling solution is characterized by the infrared behavior [116, 118–121, 216–219]

$$\begin{aligned}\lim_{p \rightarrow 0} Z_c(p) &\propto (p^2)^\kappa, \\ \lim_{p \rightarrow 0} Z_A(p) &\propto (p^2)^{-2\kappa},\end{aligned}\tag{5.19}$$

with the scaling coefficient  $1/2 < \kappa < 1$  in four dimensions. A simple calculation presented below in Sec. 5.2.2 shows that the ghost loop with an infrared constant ghost-gluon vertex and a scaling ghost propagator is already capable of inducing a splitting in the longitudinal and transverse gluon mass parameter.

Next, we investigate the decoupling solution [112, 132, 133], which is characterized by

$$\begin{aligned}\lim_{p \rightarrow 0} Z_c(p) &\propto 1, \\ \lim_{p \rightarrow 0} Z_A(p) &\propto (p^2)^{-1}.\end{aligned}\tag{5.20}$$

Assuming regular vertices in the limit of one gluon momentum vanishing, one finds that all diagrammatic contributions to the longitudinal and transverse gluon mass parameter are identical. For example, if the ghost loop were to yield a non-vanishing contribution to the gluon mass gap, the ghost-gluon vertex would have to be a function of the angle  $\theta = \arccos(t)$  between the gluon and anti-ghost momenta  $p$  and  $q$ ,

$$\lim_{|p| \rightarrow 0} [\Gamma_{\bar{c}cA}_\mu^{(3)abc}(|p|, |q|, t) = [\Gamma_{\bar{c}cA}_\mu^{(3)abc}(0, |q|, t),\tag{5.21}$$



even in the limit of vanishing gluon momentum  $|p| \rightarrow 0$ . If the limit in (5.21) depends on the angular variable  $t$ , the vertex is irregular. This example is discussed in great detail in the next section. The same conclusions can be drawn for all vertices appearing in the exact equation for the inverse gluon propagator, see Fig. 5.2. Consequently, if all vertices were regular, no gluon mass gap would be created. Thus, regular vertices entail the absence of confinement. The necessity of irregularities for the creation of a gluon mass gap was already realized by Cornwall [220].

In the light of these findings, it is interesting to investigate the consistency of irregularities with vertex Slavnov-Taylor identities. Therefore, we consider the Slavnov-Taylor identity of the three-gluon vertex, see, e.g., [32],

$$i r_\rho [\Gamma_{A^3}^{(3)}]_{\mu\nu\rho}^{abc}(p, q, r) \propto \frac{f^{abc}}{Z_c(r)} \left( \tilde{G}_{\mu\sigma}(p, q) q^2 Z_A(q) \Pi_{\sigma\nu}^\perp(q) - \tilde{G}_{\nu\sigma}(q, p) p^2 Z_A(p) \Pi_{\sigma\mu}^\perp(p) \right), \quad (5.22)$$

where  $\tilde{G}_{\mu\nu}$  relates to the ghost-gluon vertex via

$$[\Gamma_{\bar{c}cA}^{(3)}]_{\mu}^{abc}(p, q) = i g f^{abc} q_\nu \tilde{G}_{\mu\nu}(p, q).$$

For a regular  $\tilde{G}_{\mu\nu}$  in the limit  $p \rightarrow 0$  in (5.22), the scaling solution leads to a singular contribution of the type

$$\lim_{p \rightarrow 0} (p^2)^{1-2\kappa} \tilde{G}_{\nu\sigma}(q, 0) \Pi_{\sigma\mu}^\perp(p) + \text{regular},$$

where  $\kappa$  is the scaling coefficient from (5.19). This is consistent with the expected scaling exponent of the three-gluon vertex in this limit [218]. In the same limit, the decoupling solution leads to a singular contribution of the form

$$\lim_{p \rightarrow 0} \tilde{G}_{\nu\sigma}(q, 0) \Pi_{\sigma\mu}^\perp(p) + \text{regular}.$$

Since the transverse projection operator  $\Pi_{\sigma\mu}^\perp(p)$  introduces an angular dependence in the limit  $p \rightarrow 0$ , the STI again demands an irregularity in limit of one vanishing momentum. Note that this is just a statement about the three-gluon vertex projected with one non-zero longitudinal leg  $r_\rho$ . Although this momentum configuration does not enter the gluon mass gap directly, crossing symmetry suggests the necessary irregularity. In summary, these arguments illustrate that also the three-gluon vertex STI is consistent with the necessity of irregularities for both types of solutions. Although the above STI arguments were made independently, very similar observations have been made in [221–223].

We close the discussion of vertex irregularities with the remark that the infrared modification of the propagator STI in the refined Gribov-Zwanziger formalism may remove the necessity for irregularities in the vertices.

### 5.2.2. Necessity for Irregularities

In this section we substantiate the arguments from above with an explicit calculation of the ghost loop contribution to the gluon mass gap. We first show that the infrared behavior of the scaling propagators generically induces a mass gap. Subsequently, we demonstrate that the decoupling solution necessitates irregular vertices for a mass gap generation due

to the infrared finiteness of the decoupling propagators. One might skip this section at first reading since the main findings have already been stated above.

A rather general comment is in place here: When one is dealing with the gluon mass gap, it is crucial to take the vanishing momentum limit carefully. In the FRG approach this includes that one must first take the limit  $k \rightarrow 0$  and then  $p \rightarrow 0$ , otherwise no mass gap can be generated. A similar dependence on the order of limits has been found with one-point sources in [224].

### Scaling Solution

The relevant part of the self-energy contribution of the ghost loop to the inverse gluon propagator is given by

$$\left[ \Gamma_{AA}^{(2),\text{gh-loop}} \right]_{\mu\nu}(p) \propto \int_{\epsilon}^{\Lambda} dq \int_{-1}^1 dt q^3 \sqrt{1-t^2} \frac{q_{\mu}}{(q^2)^{1+\kappa}} \frac{(q+p)_{\nu}}{((q+p)^2)^{1+\kappa}}, \quad (5.23)$$

where we inserted the infrared ghost propagator from (5.19) and a classical ghost-gluon vertex, i.e.,  $[\Gamma_{\bar{c}cA}^{(3)}]_{\mu}^{abc}(p, q) = if^{abc} q_{\mu}$ . Ignoring the angular integration in (5.23) for the moment and setting  $p = 0$ , we find

$$\left[ \Gamma_{AA}^{(2),\text{gh-loop}} \right]_{\mu\nu}(p) \propto \int_{\epsilon}^{\Lambda} dq q_{\mu} q_{\nu} q^{-1-4\kappa},$$

which is infrared-divergent with  $\epsilon^{2-4\kappa}$  if  $\kappa > 0.5$ . This has to be the case in order to obtain a divergent gluon mass gap consistent with (5.19). In order to investigate the mass gap, given by the difference of the transverse and the vanishing longitudinal mass, we project (5.23) with  $\frac{1}{3}\Pi_{\mu\nu}^{\perp}(p) - \Pi_{\mu\nu}^{\parallel}(p)$ , where the factor  $\frac{1}{3}$  accounts for the three modes of the transverse projection operator. We obtain

$$\left[ \Gamma_{AA,\perp}^{(2),\text{gh-loop}} - \Gamma_{AA,\parallel}^{(2),\text{gh-loop}} \right](p) \propto \int_0^{\Lambda} dq \int_{-1}^1 dt \frac{q^5}{3} \sqrt{1-t^2} \frac{1 - 4t^2 - \frac{|p|}{|q|}t}{(q^2)^{1+\kappa} \cdot ((q+p)^2)^{1+\kappa}}. \quad (5.24)$$

One can easily show, e.g., numerically, that the integral in (5.24), and thus the mass gap, does not vanish in the limit  $p \rightarrow 0$ , but diverges with  $(p^2)^{1-2\kappa}$ , in line with (5.19).

### Decoupling Solution

Using again the ghost-loop as an example, we show that a decoupling gluon mass gap requires irregular vertices. We choose this diagram since the ghost-gluon vertex has the smallest tensor space of all vertices, which makes the example simple. We carried out the same analysis for all diagrams and came to the same conclusion for all vertices contributing to the inverse gluon propagator. This is most easily done by assuming regular vertices (which allows setting  $p = 0$ ) and then showing that the mass gap is zero.

To make this point absolutely clear, we demonstrate this argument for two different tensor bases, for the basis from Sec. 5.2 and for one with an explicit splitting into transverse and longitudinal tensors. The former basis, given in (5.16), reads

$$[\Gamma_{\bar{c}cA}^{(3)}]_{\mu}^{abc}(p, q) = if^{abc} [q_{\mu} \lambda_{\bar{c}cA,\text{cl}}(p, q) + p_{\mu} \lambda_{\bar{c}cA,\text{ncl}}(p, q)],$$

where  $p$  is the gluon and  $q$  the anti-ghost momentum. We assume that the ghost-gluon vertex is regular. Therefore, the second tensor structure has to be less divergent than  $1/|p|$  in the limit of vanishing gluon momentum, i.e.,

$$\lim_{|p| \rightarrow 0} |p| \lambda_{\bar{c}cA, \text{ncl}}(q, p) = 0. \quad (5.25)$$

Note that logarithmic infrared divergences, which, for example, occur in the dressings of the classical tensor of the three-gluon vertex and the non-classical tensors of the four-gluon vertex, do not suffice to violate their respective equivalents of (5.25). Utilizing the finiteness of the ghost dressing function and (5.25), we can take the limit  $|p| \rightarrow 0$  to obtain the mass gap contribution of the ghost loop diagram:

$$\partial_t (m_{\text{gh-loop}, \perp}^2 - m_{\text{gh-loop}, \parallel}^2) \propto \int_{-1}^1 dt \sqrt{1-t^2} (1-4t^2) \lambda_{\bar{c}cA, \text{cl}}(0, |q|, t) \lambda_{\bar{c}cA, \text{cl}}(0, |q|, -t), \quad (5.26)$$

where  $\theta = \arccos(t)$  is the angular variable between the loop momentum and the gluon momentum that is taken to zero. The dressing  $\lambda_{\bar{c}cA, \text{cl}}(0, |q|, t)$  is independent of the angular variable  $t$  if the ghost-gluon vertex is regular. Thus, the mass gap contribution evaluates to zero since

$$\int_{-1}^1 dt \sqrt{1-t^2} (1-4t^2) = 0.$$

Hence, a gluon mass gap requires irregular vertices in the case of the decoupling solution.

Since we consider differences between the vanishing longitudinal and the transverse mass, it might seem more appropriate to split the tensor basis of the ghost-gluon vertex into a purely longitudinal and a purely transverse part. We show below that this leads to the same conclusion. Transverse and longitudinal projection of the classical ghost-gluon vertex tensor yields a complete orthogonal basis,

$$[\Gamma_{\bar{c}cA\mu}^{(3)}]^{abc}(p, q) = i f^{abc} \left[ \Pi_{\mu\nu}^{\perp}(p) q_{\nu} \lambda_{\bar{c}cA}(p, q) + \Pi_{\mu\nu}^{\parallel}(p) q_{\nu} \lambda_{\bar{c}cA, \parallel}(p, q) \right], \quad (5.27)$$

where  $p$  is the gluon and  $q$  the anti-ghost momentum. The basis defined in (5.27) contains a discontinuity at  $p = 0$  due to the projection operators. The mass gap contribution of the ghost diagram with this ghost-gluon vertex basis is given by

$$\begin{aligned} \partial_t (m_{\text{gh-loop}, \perp}^2 - m_{\text{gh-loop}, \parallel}^2) &\propto \int_{-1}^1 dt \sqrt{1-t^2} \cdot \\ &\left( \frac{1-t^2}{3} \lambda_{\bar{c}cA}(0, |q|, t) \lambda_{\bar{c}cA}(0, |q|, -t) - t^2 \lambda_{\bar{c}cA, \parallel}(0, |q|, t) \lambda_{\bar{c}cA, \parallel}(0, |q|, -t) \right). \end{aligned} \quad (5.28)$$

Regularity implies a degenerate tensor space in the limit of vanishing gluon momentum. The ghost-gluon vertex can then be fully described by  $\lambda_{\bar{c}cA, \text{cl}}(0, |q|)$ . Using the identity  $\delta_{\mu\nu} = \Pi_{\mu\nu}^{\perp}(p) + \Pi_{\mu\nu}^{\parallel}(p)$ , we find

$$\lambda_{\bar{c}cA, \text{cl}}(0, |q|) = \lambda_{\bar{c}cA}(0, |q|) = \lambda_{\bar{c}cA, \parallel}(0, |q|). \quad (5.29)$$

Using (5.29) we can perform the angular integration in (5.28) and find that the mass gap contribution vanishes.

We want to stress that these findings are general and hold for any functional method. For example, the same conclusion can be drawn for the ghost-loop diagram of the gluon propagator Dyson-Schwinger equation that is also proportional to (5.26) or (5.28). Consequently, for the decoupling solution there can be no mass gap with regular vertices.

### 5.2.3. Origin of Irregularities

As discussed in the previous section, self-consistency in terms of the Slavnov-Taylor identities entails a correspondence between the dynamical generation of a gluon mass gap and the presence of irregularities. But the STIs do not provide a mechanism for the creation of irregularities, the gluon mass gap, and in turn confinement.

In the scaling solution, (5.19), the irregularities arise naturally from the non-trivial scaling. Hence, they are tightly linked to the original Kugo-Ojima confinement scenario [113] that requires non-trivial scaling. Note, however, that this simply links different signatures of confinement but does not reveal the mechanism at work.

For the decoupling solution, (5.20), we want to discuss two possible scenarios. In the first scenario, the irregularities are generated in the far infrared. A second possibility is that they are triggered via a condensate and/or a resonance, providing a direct connection of confinement and spontaneous symmetry breaking.

In the first scenario it is sufficient to focus on ghost loops as possible sources of such irregularities, since the gluonic diagrams decouple from the infrared dynamics due to the gluon mass gap. This is a seemingly appealing scenario as it is the dynamical ghost that distinguishes confining Yang-Mills theory from quantum electrodynamics. However, in the decoupling solution both the ghost-gluon vertex and the ghost propagator have infrared finite quantum corrections: no pure ghost-loops contribute to their equation and (infrared) constant dressing functions can be assumed for both. Therefore, the ghost loop contributions to correlation functions have the same infrared structure as perturbative ghost-loop contributions. However, none of these perturbative ghost loops yields the required irregularities, see Sec. 5.2.4 for an explicit example calculation.

In the second scenario, the generation of irregularities can be based on the dynamical generation of a non-vanishing transverse background,  $F_{\mu\nu}^a F_{\mu\nu}^a \neq 0$ , in the infrared. This gluon condensate is the Savvidi vacuum [225], and its generation in the present approach has been discussed in [226] with  $F_{\mu\nu}^a F_{\mu\nu}^a \approx 1 \text{ GeV}^4$ . Then, a vertex expansion about this non-trivial infrared solution of the equation of motion introduces an infrared splitting of transverse and longitudinal vertices due to the transversality of the background field. This IR splitting automatically implies irregularities as discussed in Sec. 5.2.1, and is sufficient for creating a physical mass gap in the gluon. This scenario provides a direct relation of confinement and spontaneous symmetry breaking. Therefore, it is possibly connected to the presence of resonances that are triggered in the longitudinal sector of the theory, where they do not spoil the gapping of the completely transverse sector. A purely longitudinal massless mode, as a source for irregularities in the gluonic vertices, has been worked out in [227, 228], for a concise summary see [229]. As a consequence, an irregularity appears in the purely longitudinal three-gluon vertex in a way that preserves the corresponding STI. The creation of a purely transverse background and the presence of longitudinal massless mode would then be two sides of the same coin. Furthermore, the longitudinal resonance has to occur at about the same scale as the gluon condensate, in order to trigger the correct gluon mass gap. A more detailed discussion and computation of this scenario cannot be assessed in the purely transverse system and is deferred to future work.

### 5.2.4. Ghost Triangle

In Sec. 5.2.1 and 5.2.2 it is shown that the decoupling solution requires irregular vertices. In the three gluon vertex, this irregularity has to occur if one momentum is sent to zero while the others are non-vanishing. Those vertex irregularities can be generated either dynamically, by back-coupling of momentum dependence, or by diagrammatic infrared singularities. We cannot observe the former in our computation of the purely transverse system. To investigate the latter case we exploit that the gluonic diagrams decouple from the infrared dynamics due to the gluon mass gap. Therefore, we can focus on the ghost loops as possible sources of diagrammatic infrared irregularities without loss of generality. The ghost-gluon vertex as well as the ghost propagator are constant and finite in the infrared. Below we demonstrate that the three-gluon vertex does not obtain an irregular contribution from the ghost triangle diagram, shown in Fig. 5.4. For this purpose it is sufficient to consider the perturbative diagram since it differs only quantitatively from the non-perturbative infrared contribution as argued above in Sec. 5.2.3. It is given by

$$[\Gamma_{A^3}^{(3),\text{gh-loop}}]_{\mu\nu\rho}^{abc}(p, q, r) \propto f^{abc} \int \frac{d^d l}{(2\pi)^d} \frac{(l+p)_\mu l_\nu (l-q)_\rho}{(l+p)^2 l^2 (l-q)^2}. \quad (5.30)$$

To confirm that (5.30) does not generate an irregularity in the limit  $\frac{|p|}{|q|} \rightarrow 0$ , we consider the high and low momentum integration regions separately. If the loop momentum  $|l|$  is of the order of  $|q|$ , then  $|p| \ll |l|$  and the  $p$  dependence in (5.30) is suppressed. Thus, no irregular structure can be generated from this integration region. For small loop momenta,  $|l| \approx |p|$ , we have  $|l| \ll |q|$  and the contribution to the integral in the limit  $\frac{|p|}{|l|} \rightarrow 0$  is given by

$$\frac{q_\rho}{q^2} \int \frac{d^d l}{(2\pi)^d} \frac{(l+p)_\mu l_\nu}{(l+p)^2 l^2}. \quad (5.31)$$

This integral can easily be solved analytically for  $d = 4 - 2\epsilon$  to show that it has no irregularities, which one also expects from a dimensional analysis of (5.31). Hence, we conclude that the decoupling ghost triangle cannot generate the irregularity necessary for the dynamical generation of a gluon mass gap. Note that the ghost triangle develops a non-trivial pole structure in the case of the scaling solution [230]. We have verified these findings numerically, and since they are in accordance with perturbation theory, we expect similar arguments to hold for the ghost loops contributing to higher  $n$ -point functions.

### 5.2.5. Purely Transverse System

In this work we restrict ourselves to a numerical solution of the purely transverse sub-system, (5.11), which is closed. The only relevant ultraviolet parameters in this system are the strong coupling and the transverse gluon mass parameter. In the ultraviolet the transverse mass parameter agrees with the longitudinal one. The latter is fixed by the mSTI for the longitudinal gluon propagator. Hence, the only information needed from the longitudinal system is the initial value for the transverse gluon mass parameter, see (5.14). Note that there is at least one value for the initial gluon mass parameter that yields a valid, confining solution. In what follows we vary the gluon mass parameter and discuss the properties of the ensuing solutions. We find a confining branch with both scaling and decoupling solutions. In addition, we observe a transition to a deconfined

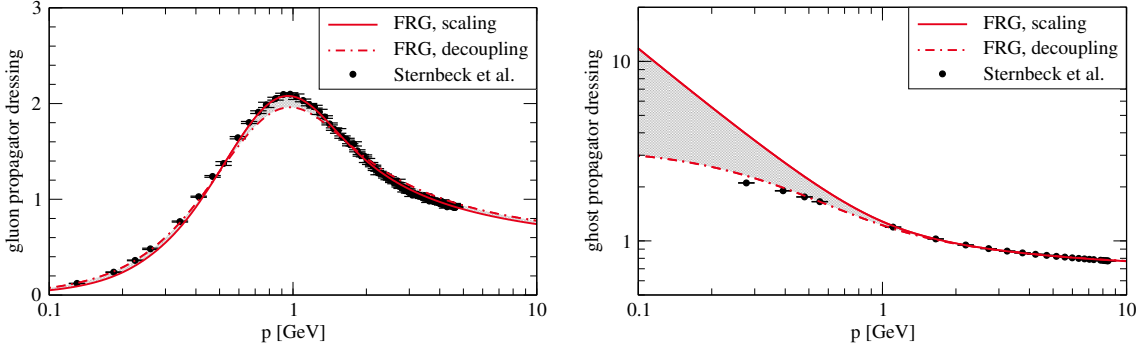


Figure 5.5.: Gluon dressing  $1/Z_A(p)$  (left) and ghost dressing  $1/Z_c(p)$  (right), defined in (5.3), in comparison to lattice results from [148]. Newer lattice results [231] agree with [148] if the largest physical volumes are compared.

Higgs-like branch. No Coulomb branch is found. The unique scaling solution satisfies the original Kugo-Ojima confinement criterion [113, 114] with  $Z_c(p=0) = 0$ . We emphasize that the scaling solution is dynamically generated and its existence is highly non-trivial. A thorough discussion is provided in Sec. 5.3.4.

### 5.3. Numerical Results

We calculate Yang-Mills correlation functions by integrating the self-consistent system of flow equations obtained from functional derivatives of (5.2), see Fig. 5.4 for diagrammatic representations. Technical details on the numerical procedure are given in Appendix C. We use constant dressing functions as initial values for the 1PI correlators at the ultraviolet initial scale  $\Lambda$ . Consequently, the initial action  $\Gamma_\Lambda$  is determined by the classical action of QCD. The (modified) Slavnov-Taylor identities enforce relations between these initial correlation functions. As is well-known, and also discussed in Sec. 5.1.3, the Landau gauge STIs leave only three of the renormalization constants independent, the value of the strong running coupling and two trivial field renormalizations that drop out of all observables. To eliminate cutoff effects, we choose constant initial values for the vertex dressings such that the momentum-dependent running couplings, as defined by (5.18), are degenerate at perturbative momentum scales  $\mu$  with  $\Lambda_{\text{QCD}} \ll \mu \ll \Lambda$ , i.e., the STIs (5.17) are only fulfilled on scales below the ultraviolet cutoff scale. The modification of the STI (5.15), caused by the regulator term, requires a non-physical gluonic mass term  $m_\Lambda^2$  at the cutoff scale  $\Lambda$ . The initial value for the inverse gluon propagator is therefore taken as

$$[\Gamma_{AA,\Lambda}^{(2)}]_{\mu\nu}^{ab}(p) = (Z_A p^2 + m_\Lambda^2) \delta^{ab} \Pi_{\mu\nu}^\perp(p),$$

where  $Z_A$  is the gluon wave function renormalization, which is momentum-independent at the cutoff scale. The non-physical contribution  $m_k^2$  to the gluon propagator vanishes only as the renormalization group scale,  $k$ , is lowered to zero, where the mSTIs reduce to the standard Slavnov-Taylor identities. The initial value  $m_\Lambda^2$  can be uniquely fixed by demanding that the resulting propagators and vertices are of the scaling type. Consequently, the only parameter in this calculation is the value of the strong running coupling at the renormalization scale,  $\alpha(\mu)$ . We also produce decoupling solutions by varying the gluon mass parameter towards slightly larger values. Our reasoning for their validity as confining solutions is presented in Sec. 5.3.4.

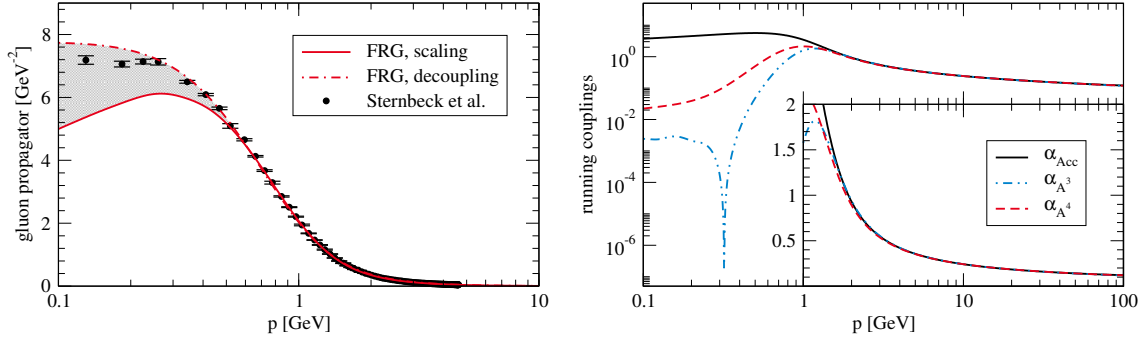


Figure 5.6.: Gluon propagator (left) in comparison to lattice results from [148], and running couplings (right) as defined from different vertices in (5.18).

### 5.3.1. Correlation Functions and Running Couplings

We present our results for the Yang-Mills correlation functions as well as the momentum-dependent transverse running couplings in Fig. 5.5 – 5.8. We show more momentum configurations of the vertex dressings and compare them to recent lattice and DSE results in Fig. 5.13 – 5.15. A discussion of truncation effects is deferred to Sec. 5.3.2. In order to be able to compare to results from lattice simulations, we set the scale and normalize the dressings as described in Sec. C.4. At all momenta, where the difference between the scaling (solid line) and decoupling (band bounded by dashed-dot line) solutions is negligible, our results for the correlations functions agree very well with the corresponding lattice results. In the case of the scaling solution we find the consistent scaling exponents

$$\kappa_{\text{ghost}} = 0.579 \pm 0.005,$$

$$\kappa_{\text{gluon}} = 0.573 \pm 0.002,$$

where the uncertainties stem from a least square fit with the ansatz (cf. (5.19))

$$Z_c(p) \propto (p^2)^{\kappa_{\text{ghost}}},$$

$$Z_A(p) \propto (p^2)^{-2\kappa_{\text{gluon}}}.$$

As discussed in Sec. 5.2.5, the scaling solution is a self-consistent solution of the purely transverse system in the present setup, and has no systematic error related to the lack of the solution of the longitudinal system. In turn, the presented decoupling solutions suffer from the missing solution of the longitudinal system, leading to a small systematic error indicated by the gray band. This argument already suggests that it is the presented scaling solution that should agree best with the lattice results in the regime  $p \gtrsim 1 \text{ GeV}$ , where the solutions show no sensitivity to the Gribov problem. This is confirmed by the results, see in particular Fig. 5.5.

At small momenta,  $p \lesssim 1 \text{ GeV}$ , the different solutions approach their infrared asymptotics. In Fig. 5.5 and 5.6 we compare the FRG solutions with the lattice data from [148]. In agreement with other lattice results [123, 232–234] in four dimensions, these propagators show a decoupling behavior, for a review see [35]. Taking the infrared behavior of all correlators into account, cf. also Fig. 5.15, the lattice solution [148] is very close to the decoupling solution (dot-dashed line) that is furthest from the scaling solution (solid

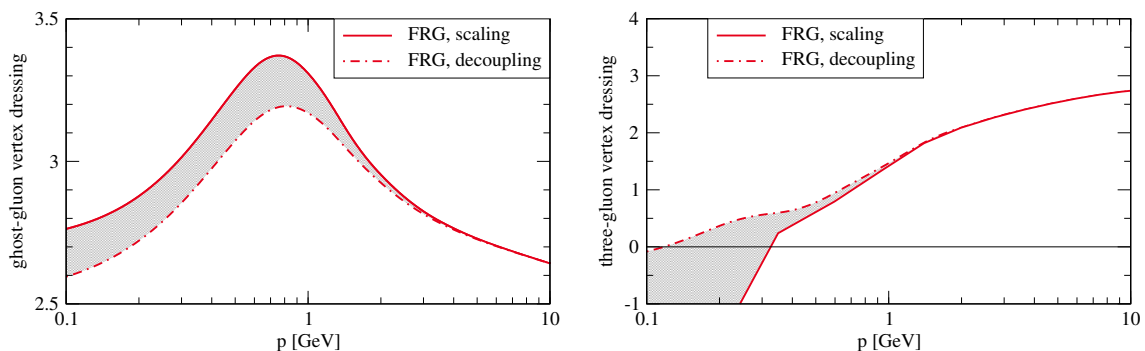


Figure 5.7.: Ghost-gluon (left) and three-gluon (right) vertex dressings,  $\lambda_{\bar{c}cA}(p, p, -1/2)$  and  $\lambda_{A^3}(p, p, -1/2)$ , at the symmetric point. More momentum configurations and comparisons to Dyson-Schwinger and lattice results are provided in Fig. 5.13 – 5.15. In contrast to Fig. 5.5, the decoupling dressings are normalized to the scaling solution in the UV.

line). Note however, that the systematic errors of both approaches, FRG computations and lattice simulations increase towards the infrared. While the FRG computations lack apparent convergence in this regime, the lattice data are affected by the non-perturbative gauge fixing procedure, i.e., the choice of Gribov copies [235–237] and discretization artifacts [231]. Consequently, comparing the FRG infrared band to the lattice propagators has to be taken with a grain of salt. In the case of the vertices, we compare also to results obtained within the DSE approach [5, 165, 191], see Fig. 5.9 and 5.15, the corresponding discussion is given in Sec. 5.3.3.

We find that it is crucial to ensure the degeneracy of the different running vertex couplings at perturbative momentum scales in order to achieve quantitative accuracy. The transverse running couplings, as defined in (5.18), are shown in the right panel of Fig. 5.6. To be able to cover a larger range of momenta with manageable numerical effort, the shown running couplings have been obtained within an approximation that takes only one momentum variable into account in the vertices, see Sec. 5.3.2. At large perturbative momentum scales, we find them to be perfectly degenerate, as is demanded by the Slavnov-Taylor identities. The degeneracy of the running couplings is lifted at a scale of roughly 1 to 2 GeV, which coincides with the gapping scale of the gluon. Furthermore, the three-gluon vertex shows a zero crossing at scales of 0.1 to 0.33 GeV, which is the reason for the spike in the corresponding running coupling. This zero crossing, which is caused by the infrared-dominant ghost-loop, is well-known in the literature [1, 165, 166, 193, 238–244]. Even though we are looking at the scaling solution, we find that the running couplings defined from the purely gluonic vertices are still strongly suppressed in the infrared. In particular the three-gluon vertex running coupling becomes more strongly suppressed than the four-gluon vertex running coupling. However, as demanded by scaling, they seem to settle at tiny but finite fixed point values, which has also been seen in Dyson-Schwinger studies [5, 166, 188].

### 5.3.2. Truncation Analysis

In Fig. 5.8 (right panel), we show the scaling solution for the propagators in different truncations. In all cases, the full momentum dependence of the propagators is taken into



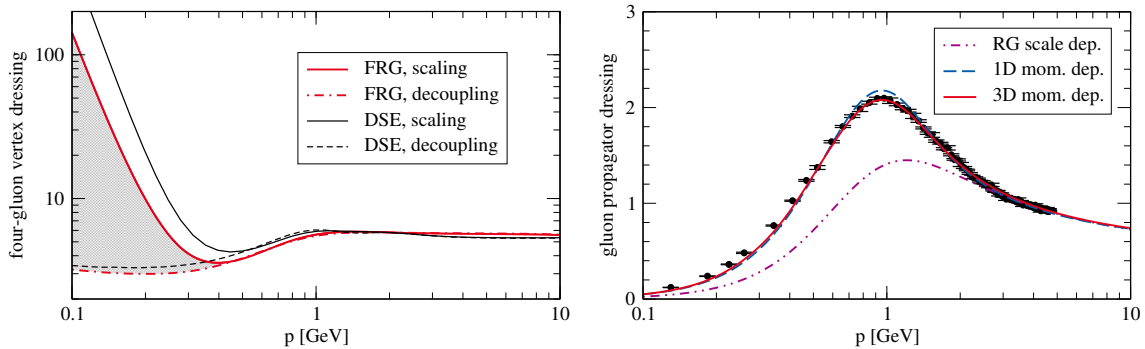


Figure 5.8.: Left: Four-gluon vertex dressing function as defined in (5.5) at the symmetric point in comparison to Dyson-Schwinger results [5]. We normalized all curves to match the scaling result at  $p = 2$  GeV.

Right: Gluon propagator dressings obtained with different momentum approximations for the vertices, see Sec. 5.3.2.

account whereas different approximations are used for the vertices. Including only RG-scale-dependent constant vertex dressing functions is the minimal approximation that can produce a scaling solution with a physical gluon mass gap. The dot-dashed magenta line corresponds to an approximation with such constant vertex dressing functions evaluated at the symmetric configuration with momentum  $p \approx 250$  MeV. In stark contrast to the other approximations discussed below, this particularly cheap approximation requires the specification of an evaluation scale, which is an additional parameter that has a sizable influence on the results. It is only shown for illustration purposes here. For the dashed blue result in Fig. 5.8, the dressing functions for the transversely projected classical tensors have been approximated with a single momentum variable  $\bar{p}^2 \equiv \frac{1}{n} \sum_{i=1}^n p_i^2$ . Reducing the momentum dependence to a single variable requires the definition of an angular configuration to evaluate the flow. Here, we use the symmetric point configuration, defined by  $p_i \cdot p_i = \bar{p}^2$  and  $p_i \cdot p_j = -\bar{p}^2/(n-1)$  for  $i \neq j$ , where  $n = 3(4)$  for the three(four)-gluon vertex. Finally, the solid red line corresponds to our best truncation. As described in Sec. 5.1.2, it takes into account the full momentum dependence of the classical tensor structures of the three-point functions as well as the four-gluon vertex in a symmetric point approximation. Additionally, all (three-dimensional) momentum configurations of the four-gluon vertex that are needed in the tadpole diagram of the gluon propagator equation have been calculated and coupled back into this diagram.

The reliability of our approximation can be assessed by comparing the results of the two simpler truncations to the result obtained with our best truncation, see Fig. 5.8. We observe that our results apparently converge towards the lattice result as we improve the momentum dependence of the vertices. Although computationally significantly less demanding, the so-called symmetric momentum approximation (labeled 1D in the legend) yields results that are accurate on the 10% level. Thus, it may serve as a testing ground and we exploit this in the following chapters. The effects of non-classical tensors and vertices are beyond the scope of the current work and have to be checked in future investigations. Within the present work, the already very good agreement with lattice results suggests that their combined influence on the propagators is small.

The final gluon propagator is sensitive to the correct renormalization of the vertices. For example, a one percent change of the three-gluon vertex dressing at an ultraviolet scale of

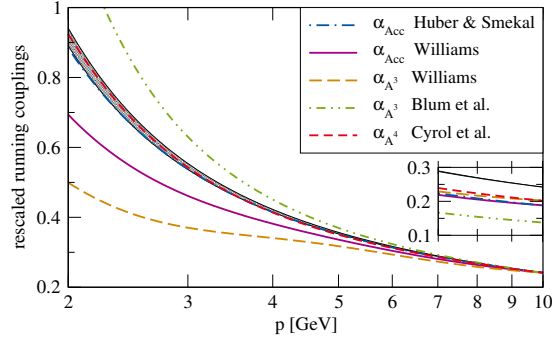


Figure 5.9.: Running couplings (5.18) in comparison with DSE couplings. The gray band gives the spread of vertex couplings from the FRG in the present work. DSE results are shown rescaled to fit our ghost-gluon vertex running coupling at 10 GeV to facilitate the comparison. The inlay shows the unscaled couplings. Note that the FRG running couplings naturally lie on top of each other and are not rescaled.

20 GeV magnifies by up to a factor of ten in the final gluon propagator. Therefore, small errors in the perturbative running of the vertices propagate, via renormalization, into the two-point functions. We expect a five percent uncertainty in our results due to this.

Despite these uncertainties, we interpret the behavior in Fig. 5.8 (right panel) as an indication for apparent convergence.

### 5.3.3. Comparison to Other Results

In Fig. 5.15, numerical results for the ghost-gluon and three-gluon vertices are shown in comparison to other functional method calculations as well as lattice results. In summary, the results from various functional approaches and the lattice agree to a good degree. However, these correlation functions are not renormalization group invariant, and a fully meaningful comparison can only be made with RG invariant quantities. Therefore, we compare our results for the RG invariant running couplings with the respective results from DSE computations. To be more precise, the beta functions of the different vertices are tied together by two-loop universality in the sense that they should agree in the regime where three-loop effects are negligible. Since constant factors drop out of the beta functions, we have normalized the DSE running couplings to the FRG result at large momentum scales in Fig. 5.9. For the sake of visibility, we only have provided a band for the spread of the FRG couplings as obtained from different vertices. The shown DSE running couplings are based on a series of works [5, 165, 191, 198, 245], where the explicitly shown results are taken from [5, 165, 246, 247]. Additionally, we provide the raw DSE running couplings that have not been rescaled by a constant factor in the inlay. The running couplings from the FRG are accurate enough to allow for the extraction of meaningful beta functions, which are discussed below in Sec. 5.4.2.

### 5.3.4. Mass Gap, mSTIs and Types of Solutions

As discussed in Sec. 3.1.2 and 5.1.3, the introduction of the regulator in the FRG leads to a modification of the Slavnov-Taylor identities. In turn the inverse gluon propagator

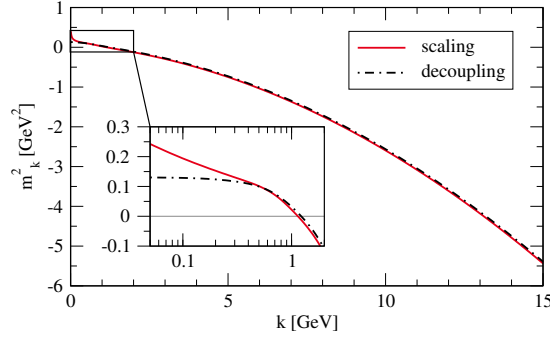


Figure 5.10.: Gluon mass parameter  $m_k^2 = \Gamma_{AA,k}^{(2)}(p=0)$  as a function of  $k$ .

obtains a contribution proportional to  $\Delta\Gamma_{AA}^{(2)} \propto \alpha(k)k^2$  for all  $k > 0$ , see (5.14). Disentangling the physical mass gap contribution from this mSTI contribution to the gluon mass parameter is intricate, both conceptually and numerically. The resulting numerical challenge is illustrated in Fig. 5.10, where we show the  $k$ -running of the gluon mass parameter. This is the analogue of the problem of quadratic divergences in Dyson-Schwinger equations with a hard momentum cutoff, see, e.g., [194]. However, there has to exist at least one choice for the gluon mass parameter  $m_\Lambda^2$  that yields a valid confining solution, see Sec. 5.1.3. To resolve the issue of finding this value, we first recall that a fully regular solution has no confinement and necessarily shows a Higgs- or Coulomb-type behavior. Although we do not expect these branches to be consistent solutions, we can trigger them by an appropriate choice of the gluon mass parameter in the UV. The confinement branch then lies between the Coulomb and the Higgs branch. We need, however, a criterion for distinguishing between the confinement and the Higgs-like branch.

To investigate the possible solutions in a controlled way, we start deep in the Higgs-like branch. An asymptotically large initial gluon mass parameter  $m_\Lambda^2$  triggers an explicit mass term of the gluon also at vanishing cutoff. If we could trigger this consistently, it would constitute a Higgs-like solution. In the current approximation, it cannot be distinguished from massive Yang-Mills theory, which has been investigated in, e.g., [189, 202, 248, 249]. Starting from this Higgs-like deconfined branch, we can explore the limit of smaller initial mass parameters. This finally leads us to the scaling solution, which forms the boundary towards an unphysical region characterized by Landau-pole-like singularities. It is left to distinguish between the confining and Higgs-like solutions, shown in Fig. 5.11, without any information from the longitudinal set of equations. For that purpose we use two criteria:

In the left panel of Fig. 5.12, we show the gluon mass gap  $m^2 = \Gamma_{AA,k=0}^{(2)}(p=0)$  as a function of the initial value for the gluon mass parameter  $m_\Lambda^2$  subtracted by the unique value corresponding to the scaling solution  $m_{\Lambda,\text{scaling}}^2$ . The latter solution corresponds to zero on the x-axis in Fig. 5.12. As mentioned before, going beyond the scaling solution,  $m_\Lambda^2 < m_{\Lambda,\text{scaling}}^2$ , leads to Landau-pole-like singularities, which prevent the complete removal of the regulator term. We interpret their presence as a signal for the invalidity of the Coulomb branch as a possible realization of Yang-Mills theory. The decisive feature of the left panel of Fig. 5.12 is the presence of a minimum at  $m_{\min}^2$ . If there were no dynamical mass gap generation,  $m^2$  would have to go to zero as we lower  $m_\Lambda^2$ . In contrast, we find that the resulting gluon mass gap is always larger than the value it takes at  $m_\Lambda^2 = m_{\min}^2$ . This entails that all solutions to the left of the minimal value,  $m_\Lambda^2 < m_{\min}^2$ , are characterized by a large dynamical contribution to the gluon mass gap, which we interpret as

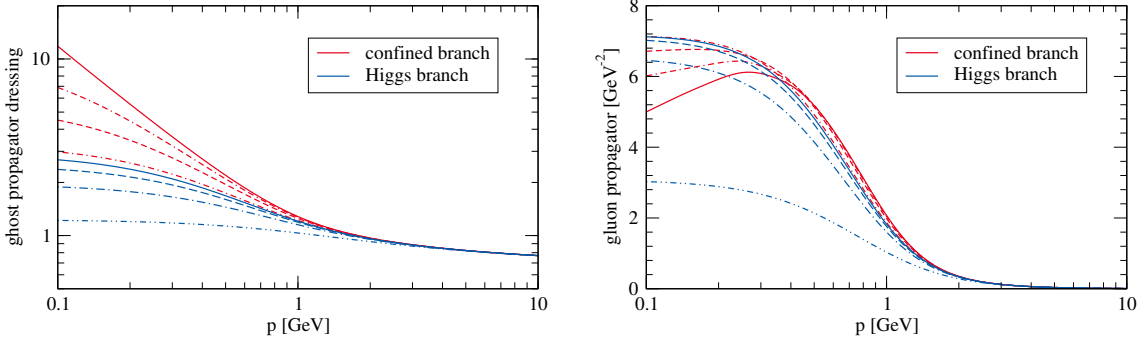


Figure 5.11.: Ghost dressing functions  $1/Z_c(p)$  (left) and gluon propagators  $1/(p^2 Z_A(p))$  (right) for different values of the ultraviolet gluon mass parameter. Blue results correspond to the Higgs-like branch, red results to the confined branch, and the solid red line to the scaling solution.

confinement. The decoupling solution in Fig. 5.5 – 5.8 corresponds to the solution obtained with  $m_\Lambda^2 = m_{\min}^2$ . Smaller values of the gluon mass parameter,  $m_{\Lambda, \text{scaling}}^2 < m_\Lambda^2 < m_{\min}^2$ , also yield decoupling solutions. This is indicated by the gray bands. Without resolving the longitudinal sector, it is not possible to discriminate between the different decoupling solutions. The lattice simulations, however, seem to favor a gluon propagator that is at least close to this minimal mass gap, as is best seen from the left panel of Fig. 5.6.

As a second criterion for distinguishing between confined and deconfined Higgs-like solutions, we use the presence of a maximum at non-vanishing momenta in the gluon propagator, which signals positivity violation [32]. In the right panel of Fig. 5.12, we show the location of the maximum in the gluon propagator, again as a function of the gluon mass parameter,  $m_\Lambda^2 - m_{\Lambda, \text{scaling}}^2$ . We clearly see a region of confining solutions that show a back-bending of the gluon propagator at small momenta, see Fig. 5.11. The dashed line, separating the shaded from the white region in the right panel of Fig. 5.12, indicates the smallest momentum value at which the gluon propagator has been calculated (in [1]). With this restriction in mind, the fit in the inset demonstrates that the location of the maximum of the propagator scales to zero as one approaches the critical value  $m_c^2$ . We fit with

$$p_{\max}(m_\Lambda^2) \propto \left( \frac{m_\Lambda^2 - m_c^2}{m_c^2} \right)^\alpha, \quad (5.32)$$

which yields the critical exponent

$$\alpha = 1.95 \pm 0.6,$$

in the symmetric momentum approximation. This power law behavior has been disputed in [202]. There, it is proposed that the scale of positivity violation  $p_{\max}$  does not disappear for large gluon mass parameters but, instead, is pushed to much lower scales not resolved numerically here. The authors of [202] argue that it is not a transition between qualitatively different phases but a smooth crossover between quantitatively different regimes. Therefore, we refine the numerical analysis and discuss analytic arguments in Sec. 5.4.3. Albeit an important detail, this does not alter the conclusions of this chapter (and, equivalently, [1]). In particular, to plot the results we defined the decoupling solution to be

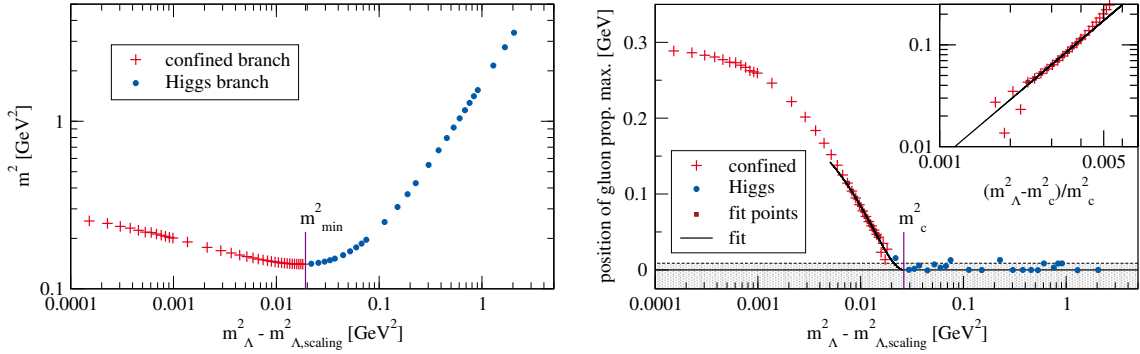


Figure 5.12.: Left: Gluon mass gap over the gluon mass parameter  $m_\Lambda^2 - m_{\Lambda,\text{scaling}}^2$ , where  $m_{\Lambda,\text{scaling}}^2$  denotes the parameter that yields the scaling solution.

Right: Momentum value at which the gluon propagator assumes its maximum as a function of the gluon mass parameter  $m_\Lambda^2 - m_{\Lambda,\text{scaling}}^2$ , cf. also Fig. 5.11. The inlay exposes the power law behavior of the gluon propagator maximum in the vicinity of the transition region, see (5.32).

Both plots were obtained from our numerically less-demanding symmetric momentum approximation. We have repeated this analysis in the transition regime from Higgs-like to confinement branch also with the best approximation and find the same behavior. The shaded area marks momentum scales that are not numerically resolved in the present work. The points in this region rely on a generic extrapolation. See Sec. 5.4.3 and in particular Fig. 5.18 for a refined version of this plot.

the one that has the minimal mass gap, which is unaffected by the (non-)existence of a maximum at non-vanishing momenta.

As discussed in detail in Sec. 5.2, a gluon mass gap necessitates irregularities. The scaling solution contains these irregularities in the propagators, cf. (5.19), by definition. For the decoupling-type solutions, we excluded infrared irregularities of diagrammatic origin in Sec. 5.2.4. Thus, for the decoupling-type solutions our arguments for the validity of the solutions are weaker and remain to be investigated in computations that include at least parts of the longitudinal system, cf. the discussions in Sec. 5.1.3 and 5.2.1. Additionally, it might be necessary to expand about the solution of the equation of motion, see [226].

We end this section with a summary of the findings on the gluon mass gap. In the right panel of Fig. 5.12 we can distinguish a confining branch with positivity violation and a Higgs-like deconfined branch with a massive gluon propagator. A Coulomb-type solution, on the other hand, can never be produced with the functional renormalization group since any attempt to do so leads to Landau-pole-like singularities. The non-existence of the Coulomb branch is tightly linked to the non-monotonous dependence of the mass gap on the initial gluon mass parameter, see the left panel of Fig. 5.12. This behavior is of dynamical origin and is also responsible for the existence of the scaling solution for the smallest possible ultraviolet gluon mass parameter.

### 5.3.5. Discussion

As discussed in Sec. 5.3.1, one non-trivial feature of the different vertex couplings is their quantitative equivalence for momenta down to  $p \approx 2 \text{ GeV}$ , see Fig. 5.6. This property

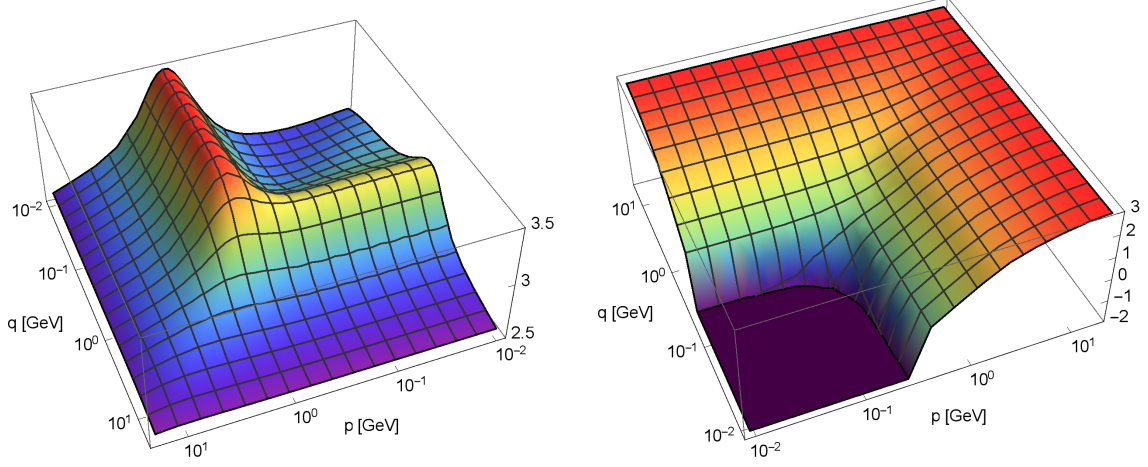


Figure 5.13.: Ghost-gluon (left) and three-gluon (right) vertex dressings,  $\lambda_{\bar{c}cA}(p, q, 0)$  and  $\lambda_{A^3}(p, q, 0)$ , at orthogonal momentum configurations.

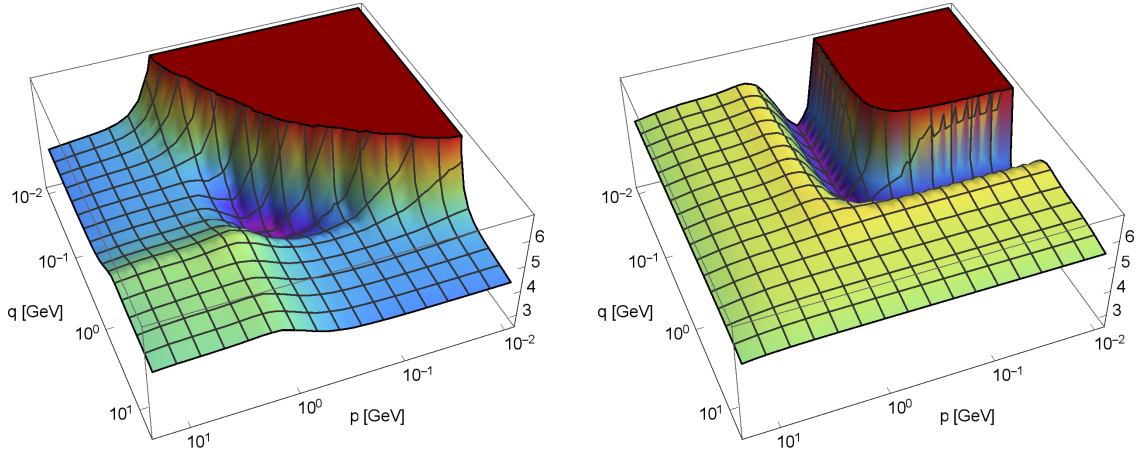


Figure 5.14.: Left: Four-gluon vertex dressing function  $\lambda_{A^4}(p, q, t = 0)$  in the tadpole configuration. The angular dependence is small compared to the momentum dependence.

Right: Four-gluon tadpole configuration evaluated in the symmetric momentum approximation  $\lambda_{A^4}(\bar{p} = \sqrt{(p^2 + q^2)}/2)$ , showing a quantitative and qualitative deviation from the full calculation.

extends the universal running of the vertex couplings into the semi-perturbative regime. On the other hand, the couplings violate universality in the non-perturbative regime for  $p \lesssim 2 \text{ GeV}$ . The universality down to the semi-perturbative regime is a very welcome feature of Landau gauge QCD, as it reduces the size of the non-perturbative regime and hence potential systematic errors. In particular, one running coupling is sufficient to describe Landau gauge Yang-Mills theory down to momentum scales of the order of the gluon mass gap. This suggests using the propagators together with the ghost-gluon vertex coupling for simple semi-quantitative calculations. The above structure explains and supports the semi-quantitative nature of the results in less advanced approximations.

This implies that self-consistent calculations of vertices have to reproduce this universality of the vertex running couplings, in particular for semi-perturbative momenta  $2 \text{ GeV} \lesssim p \lesssim 10 \text{ GeV}$ . We find that a violation of the degeneracy even leads to the loss of qualitative properties of the non-perturbative results. This sensitivity extends to QCD, where it is found that deviations on the percent level have a qualitative impact on chiral symmetry breaking [3, 65]. This is one of the main subjects of Chapter 7.

We close this discussion with the remark that universality in the semi-perturbative regime is tightly linked with the consistent renormalization of all primitively divergent correlation functions. We find it crucial to demand the validity of the Slavnov-Taylor identities, given by (5.17), only at momentum scales considerably below the ultraviolet cutoff scale  $\Lambda$ . Close to the ultraviolet cutoff scale, (5.17) is violated. This constitutes no restriction to any practical applications since the cutoff can always be chosen large enough, such that no cutoff effects can be found at momenta  $p \leq \mu \ll \Lambda$ .

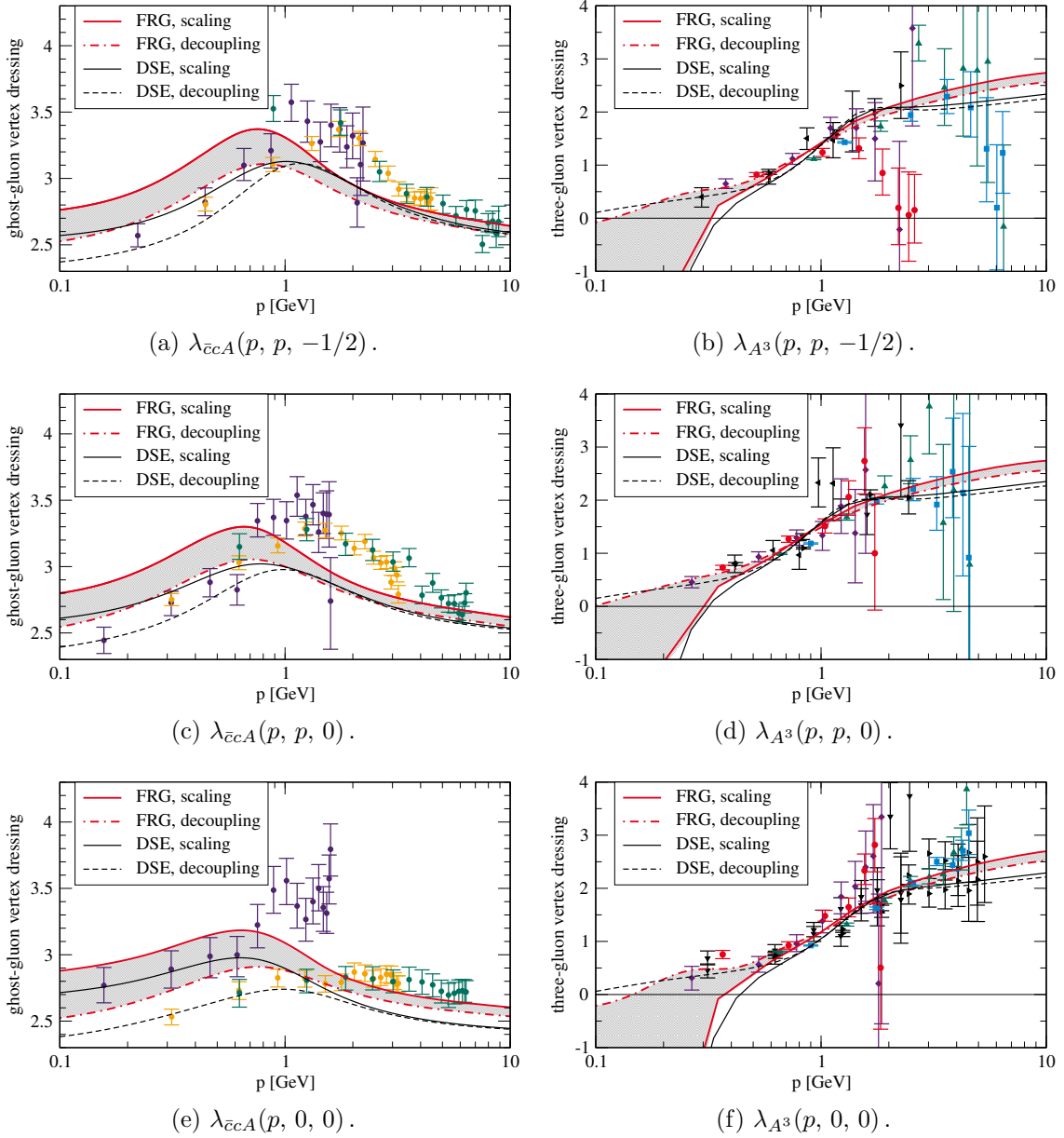


Figure 5.15.: Left: Ghost-gluon vertex dressing function  $\lambda_{\bar{c}cA}(p, q, \cos \angle(p, q))$  in comparison to  $SU(2)$  lattice [238, 239, 250] and DSE results [191, 246].

Right: Three-gluon vertex dressing function  $\lambda_{A^3}(p, q, \cos \angle(p, q))$  compared to  $SU(2)$  lattice [238, 239, 250] and Dyson-Schwinger [165] results. While the colored lattice points are taken from [238, 239], the black ones are based on [238, 239], but stem from [251]. These were obtained from  $N \in \{24^4, 32^4\}$  lattices with  $\beta \in \{2.13, 2.39, 2.60\}$  and lattice spacing  $a^{-1} \in \{0.8 \text{ GeV}, 1.6 \text{ GeV}, 3.2 \text{ GeV}\}$ .

We rescaled all DSE results to match our scaling solution at the symmetric momentum configuration at  $p = 2 \text{ GeV}$ . Note that the scaling and decoupling solutions differ in the ultraviolet due to the different field renormalizations, cf. Fig. 5.5. The running couplings, given by (5.18), agree. We elaborate on the gauge group dependence of our results in Sec. 5.4.1.



## 5.4. More and Refined Results

This section contains additional and refined results<sup>1</sup> that are not already published in [1]. In particular, we discuss a central aspect of Yang-Mills theory, the gauge group. We then consider beta functions defined from different vertices. Last but not least, we refine the mass gap analysis and revisit the infrared behavior.

### 5.4.1. Gauge Group Dependence

We only assumed that the gauge group is non-Abelian, but did not specify the Lie group any further. We did not need to do so because in the truncation used all color traces can be taken without specifying the gauge group: The Jacobi identity for the structure constants,

$$f^{abe} f^{cde} + f^{cbe} f^{dae} + f^{dbe} f^{ace} = 0, \quad (5.33)$$

and the definition of the quadratic Casimir operator, see (4.3), directly lead to

$$f^{amn} f^{bno} f^{com} = \frac{C_A}{2} f^{abc}. \quad (5.34)$$

All color traces can be taken by repeatedly applying (4.3), (5.33) and (5.34). This also holds for the box(-like) four-gluon vertex diagrams with color structures of the form  $f^{amn} f^{bno} f^{col} f^{dlm}$  since we project the four-gluon vertex with the classical tensor.

The only group constant appearing in the equations is the quadratic Casimir operator of the adjoint representation  $C_A$  since the dimension of the adjoint representation  $N_A$  cancels. Furthermore, the quadratic Casimir  $C_A$  occurs only in combination with the coupling at the renormalization point,  $\alpha(\mu) \cdot C_A \equiv \tilde{\alpha}(\mu)$ . Thus, it can be absorbed into a redefinition of the running coupling, or, equivalently, the scale of the theory. Therefore, the propagators are identical for all groups, and the different couplings can be obtained by a trivial rescaling with  $C_A$ . All couplings shown correspond to  $C_A = 3$  (which is also the value for  $SU(3)$ , see (4.5)). We emphasize that this does not indicate a poor truncation. Also perturbatively, the beta function of Yang-Mills theory has a trivial group dependence up to three loops, cf. Sec. 2.2. Furthermore, lattice simulations at vanishing temperature show that the propagators of  $SU(2)$  and  $SU(3)$  Yang-Mills theory agree well in the mid-momentum regime [253, 254]. Finally, the infrared scaling fixed point has at most a small gauge group dependence since the running couplings of the classical tensor structures are of the form  $\alpha_i/C_A = \tilde{\alpha}_i$  at the fixed point, see, e.g., [216].

### 5.4.2. Beta Functions

We discussed asymptotic freedom and the perturbative QCD beta function in Sec. 2.2. Our truncation includes all primitively divergent  $n$ -point functions and, thus, all ultraviolet relevant couplings. Therefore, our solution does not only exhibit asymptotic freedom, but

<sup>1</sup> The results presented here are obtained in the semi-quantitative symmetric momentum approximation discussed in Sec. 5.3.2. It was already shown in Sec. 3.1.2 that the choice of the regulator shape function has no influence on the vacuum results. Nonetheless, here we employ the exponential regulator given with  $m = 2$  instead of the smooth flat regulator since we consider finite temperature in Chapter 8 and the exponential regulator is better suited for the calculation of thermodynamic quantities [252].

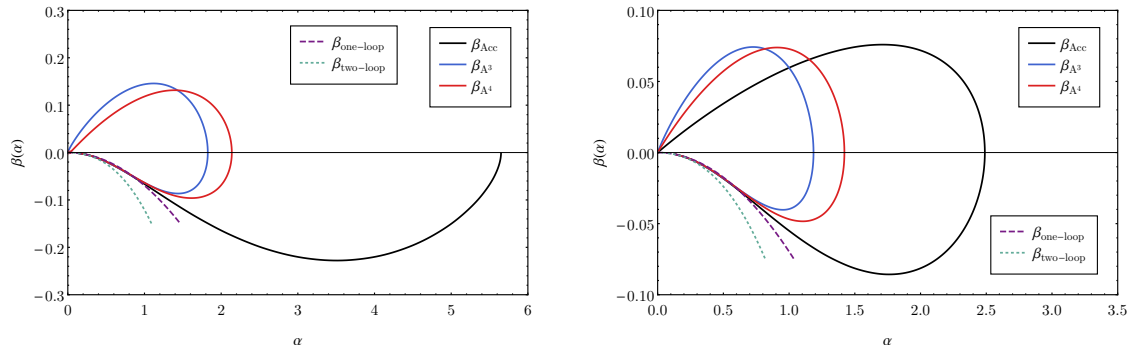


Figure 5.16.: Beta functions extracted from different running couplings for the scaling (left) and the decoupling solution (right). Dotted and dashed lines depict the one- and two-loop beta functions, respectively.

also allows for the calculation of beta functions beyond the perturbative Landau pole. We compute beta functions from the different running couplings, defined in (5.18), by

$$\beta_i(\alpha_i) := \frac{p^2}{4\pi} \frac{d\alpha_i}{dp^2}. \quad (5.35)$$

Here,  $i \in \{\bar{c}cA, A^3, A^4\}$  stands for any of the classical vertices, cf. Fig. 5.6 and 5.9 for plots of the running couplings. On the two-loop level, the beta functions are renormalization scheme independent, which makes them suited for comparisons in the region where three-loop effects are negligible. Perturbatively, the different beta functions coincide. However, the occurrence of the gluon mass gap causes the transverse non-perturbative running couplings to differ at low momentum scales. Assuming that (5.35) is sensible in the infrared, we present the beta functions of the scaling and decoupling solution for the full theory space in Fig. 5.16. At small couplings, we recover the perturbative behavior, given by (2.18), and thus asymptotic freedom. Once the couplings reach a certain strength, they leave the perturbative regime and deviate from each other.

In the strong-coupling regime, the beta functions of the scaling and decoupling solutions differ qualitatively. This is best seen from the ghost-gluon vertex beta function. In the case of the scaling solution, it stays negative for all values of the coupling. While it shows the expected perturbative behavior at small couplings, it assumes its infrared fixed point with vanishing beta function at large couplings. This reflects that the ghost-gluon vertex coupling monotonously increases from the ultraviolet to the infrared.<sup>2</sup> In contrast, the infrared behavior of the decoupling solution given by (5.20) entails positive beta functions in the infrared where the couplings vanish again. Note that the running couplings of the gluonic vertices, similar to the ghost-gluon vertex running coupling, assume fixed point values with  $\beta_i(\alpha_i > 0) = 0$  in the infrared, but at such tiny coupling values that they are not visible in Fig. 5.16. To conclude, the beta functions make the infrared difference of the scaling and decoupling solutions apparent: While the decoupling running couplings flow

<sup>2</sup> Indeed, our numerical data shows (see Fig. 5.6) a decrease of the ghost-gluon vertex running coupling in the deep infrared, which corresponds to a positive beta function. However, the behavior of all  $n$ -point correlation functions at the scaling fixed point is analytically known, see Sec. 6.2.2 and in particular (6.1), and yields that the beta functions defined by (5.35) become zero in the infrared. Thus, we attribute this to numerical artifacts and cut the line of the ghost-gluon vertex beta function at  $\beta_{\bar{c}cA}(\alpha_{\bar{c}cA}) = 0$  in Fig. 5.16.

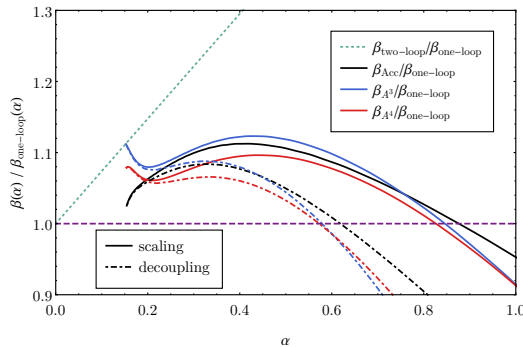


Figure 5.17.: Scaling (solid) and decoupling (dot-dashed) beta functions in the perturbative regime normalized with the one-loop beta function.

into a fixed point at the origin at which both the beta functions and the couplings vanish, the scaling solution remains strongly interacting down to arbitrarily low scales since the couplings flow into a fixed point for which  $\beta_i(\alpha_i) = 0$  with  $\alpha_i > 0$ .

We close this section with a precision test of our truncation at high momenta. To this end, Fig. 5.17 shows the scaling as well as the decoupling beta functions normalized with the perturbative one-loop result along with the normalized two-loop beta function. This plot reveals small deviations of the different beta functions also in the ultraviolet for  $0.2 \lesssim \alpha \lesssim 0.4$ . These exist because we aim to enforce the STI, (5.17), which entails the exact degeneracy of the beta functions at the renormalization scale, at vanishing cutoff  $k \rightarrow 0$ . However, since the vertex dressings can only be chosen at the cutoff scale  $k = \Lambda$ , this is an initial value problem and the deviations at small couplings correspond to our numerical uncertainty of this initial value problem. At the smallest couplings shown in Fig. 5.17, the beta functions show a seemingly odd behavior. This behavior stems from cutoff effects discussed in Sec. 5.3.5. Hence, Fig. 5.17 underlines the arguments from Sec. 5.3.5 that an appropriate treatment of the cutoff effects is important.

All our beta functions lie between the one- and two-loop result. This can be understood from the employed truncation: We self-consistently back-couple the momentum dependence of the dressing functions. Thus, our truncation is better than one-loop. However, we have not included any non-classical tensors. These are generated at the one-loop level and contribute at the two-loop level. Thus, two-loop precision requires the inclusion of non-classical tensors in the truncation, as can be seen from Fig. 5.17.

### 5.4.3. Refined Mass Gap Analysis

We first present refined numerical results and then discuss analytical arguments. Here we improve the results for the mass gap and the back-bending scale shown in Fig. 5.12 by increasing the numerical precision and computing the gluon propagator down to lower momenta  $p = 3 \text{ MeV}$ . These results are shown in Fig. 5.18. Clearly, the gluon mass parameter that yields the minimal mass gap,  $m_{\min}^2$ , and the parameter that moves the scale of positivity violation below our resolved momentum range,  $m_c^2$ , do not coincide any longer, leaving us with an intermediate phase. The propagators corresponding to the boundary values of the different phases are displayed in Fig. 5.19 and 5.20. In contrast to the previous section where the propagator dressings are normalized to the lattice data, here the dressings are normalized in the ultraviolet.

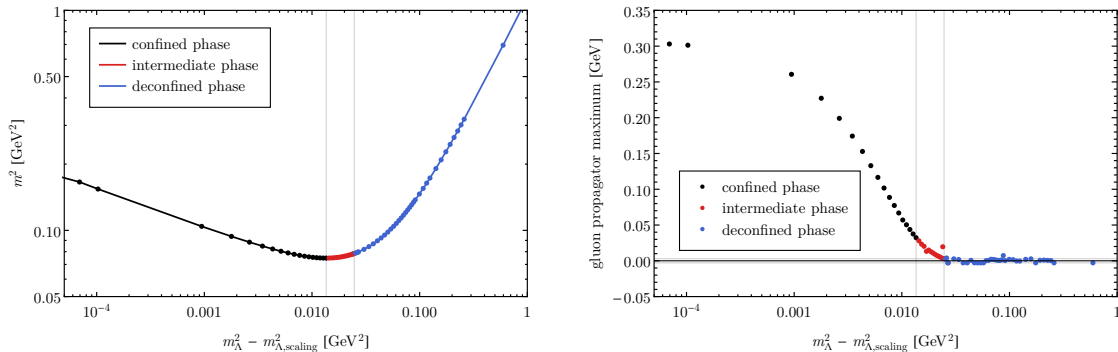


Figure 5.18.: Gluon mass gap and scale of positivity violation as a function of the gluon mass parameter  $m_\Lambda^2 - m_{\Lambda,scaling}^2$ . In contrast to Fig. 5.12, this more precise calculation shows the existence of an intermediate phase between the deconfined and the confined phase.

The decisive question is the physical meaning of the intermediate phase. To understand the different solutions, we first note that the back-bending of the gluon propagator is driven by the ghost-loop. The latter causes dimensionally suppressed logarithmic divergences in the case of a decoupling solution. Thus, the infrared momentum dependence of the decoupling gluon propagator is schematically given by  $\Gamma_{AA}^{(2)}(p) \approx m^2 + c_{gh-loop} p^2 \log(p^2/\Lambda_{QCD}^2)$ , which leads for  $c_{gh-loop} > 0$  to backbending at small momenta,

$$\lim_{p \rightarrow 0} \frac{\partial \Gamma_{AA}^{(2)}(p)}{\partial p^2} = \lim_{p \rightarrow 0} \log \left( \frac{p^2}{\Lambda_{QCD}^2} \right) + \text{const.} < 0. \quad (5.36)$$

For all solutions apart from the scaling solution, the massless ghost loops have the same infrared structure as the perturbative ghost-loops. In essence, the dressed ghost propagator and ghost-gluon vertex are bounded from below by their classical counterparts. Thus, a contribution of the type (5.36) is present for all gluon mass parameters  $m_\Lambda^2 > m_{\Lambda,scaling}^2$ . Therefore, the authors of [202] argue that the back-bending cannot disappear. However, the ghosts do not only cause a (suppressed) logarithmic divergence in the gluon propagator but also induce a logarithmic divergence in, e.g., the three-gluon vertex. Feeding back these logarithmic divergences in the gluonic vertices into the propagator equations may lead to (suppressed) logarithmic divergences with the opposite sign compared to the ghost-loop contribution (5.36). This could lead to a dynamic non-trivial vanishing of the backbending of the gluon propagator. Our numerical results shown in Fig. 5.18 are compatible with both scenarios, the vanishing and the non-vanishing of the backbending at large gluon mass parameters. Clarifying this situation requires the full analytical infrared momentum structure of the ghost-loop contributions to the gluonic vertices. This is beyond the scope of the present investigation. In the light of these findings, the intermediate phase can be understood easily. At very large unphysical values for the gluon mass parameter, the backbending either vanishes or occurs at very small momenta. Lowering the gluon mass parameters strengthens the ghost propagator, which induces the backbending in our numerical results. Further decreasing the gluon mass parameter also lowers the gluon mass gap until at some value  $m_{min}^2$  the mass gap starts to increase again and the so-called confined phase, which is distinguished by a large dynamical contribution to the physical mass gap, begins. The crucial question is for which gluon mass parameter the unphysical

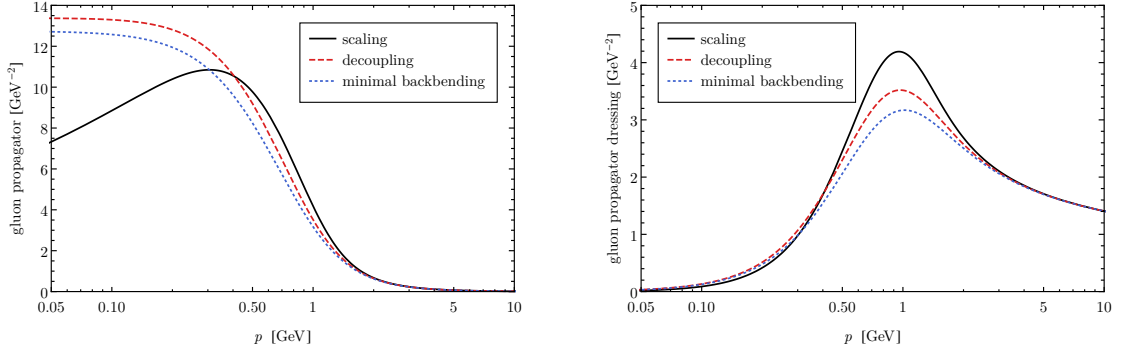


Figure 5.19.: Gluon propagator (left) and gluon propagator dressing (right) as obtained with different values for the gluon mass parameter. The decoupling solution corresponds the maximal gluon mass parameter that yields a solution in the confined phase, the minimal backbending solution to the maximal parameter that gives a solution in the intermediate phase, cf. Fig. 5.18.

contribution becomes zero at vanishing RG scale. If this is not the scaling solution, for which we presented arguments in Sec. 5.2, it cannot be resolved without solving the longitudinal sector or the mSTIs.

We close this section with a comment on the formal possibility to obtain a family of solutions in the standard functional setup without Gribov-Zwanziger terms in the action. First of all, we can ignore the existence of the gluon mass parameter in BRST-symmetry-breaking regularization schemes. Although it is used to trigger different solutions above, it is uniquely fixed by a corresponding mSTI. Thus, we are left with five renormalization constants for the primitively divergent Greens functions. However, only two of the five renormalization constants, say, e.g., the ones of the propagators, can be chosen freely since the others are then fixed by the STI, see (5.17). The freedom to choose these corresponds to simple field renormalizations that result in a momentum-independent rescaling of the dressings. Consequently, there is no parameter left to dial the infrared behavior. Hence, it is impossible to choose between the scaling and the (family of) decoupling solution(s) if multiplicative renormalizability holds non-perturbatively. This also implies that the value of the ghost propagator dressing in the infrared cannot be changed without rescaling the dressing in the ultraviolet accordingly, which is, however, often seen in the literature [112].

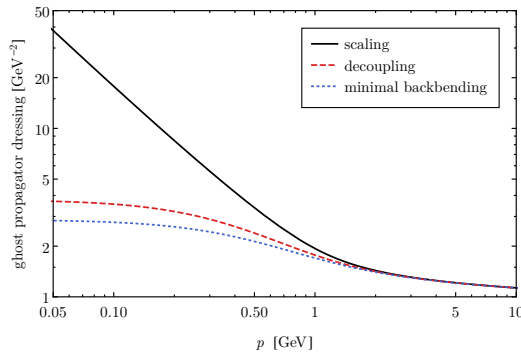


Figure 5.20.: Ghost propagator dressing for different values of the gluon mass parameter.

## 5.5. Conclusion

We investigated Landau gauge Yang-Mills theory with a systematic vertex expansion of the effective action. Our truncation includes not only ghost and gluon propagators but also momentum-dependent dressings of the transverse ghost-gluon, three-gluon and four-gluon vertices. The approximation is self-consistent and self-contained such that no modeling of correlation functions is required. We circumvented solving the modified STIs of the vertices by demanding that the STIs are fulfilled at vanishing RG scale. This leads to a consistent running of all vertices in the perturbative regime and requires as only input the running coupling at the renormalization scale, i.e., the physical parameter of Yang-Mills theory. The presented beta functions of different vertices highlight the infrared differences between the scaling and decoupling solutions. The numerical results, and in particular the gluon propagator, are in very good agreement with  $SU(3)$  lattice results. Moreover, the comparison of different momentum approximations for the vertices indicates apparent convergence of the expansion scheme. However, the importance of non-classical tensors as well as non-classical vertices has to be checked in future investigations.

Special emphasis was put on the analysis of the dynamical generation of the gluon mass gap at non-perturbative momenta. We presented clear numerical evidence for a dynamical mass gap contribution in our calculation. Self-consistency in terms of the STIs necessitates infrared irregularities in the correlation functions. The source of these irregularities is traced back to the infrared-divergent ghost propagator for the scaling solution. In decoupling-type solutions, the source of these irregularities is harder to identify, where the creation of diagrammatic infrared irregularities is ruled out by general arguments as well as explicit calculations. Within our truncation, we can exclude irregularities of non-diagrammatic origin in the purely transverse subsystem. Hence, it is necessary to solve the longitudinal system to answer whether the required irregularities are generated for decoupling-type solutions, which is deferred to future work. Furthermore, we pointed out that we cannot formally obtain an infrared family of solutions in the present approach.

## 6. Yang-Mills Theory in Three Dimensions

Yang-Mills theory in four dimensions shares many of its qualitative features such as confinement with the three-dimensional theory, see, e.g., [255]. In this chapter correlation functions of three-dimensional Yang-Mills theory are computed. The motivation is twofold:

(A) Testing ground:

Since lattice simulations are significantly less demanding in three than in four dimensions, the three-dimensional theory may serve as a test bed. Propagators have been studied intensively on the lattice [35, 123, 232–234, 238, 239, 256–265], with DSEs [230, 241, 266–270], and in semi-perturbative settings [189, 193, 240]. Vertices have also been investigated on the lattice [238, 239] as well as with functional methods [193, 201, 241]. Particularly noteworthy is [201], where for the first time a closed set, in the sense that no modeling of correlation functions is required, of Yang-Mills DSEs has been solved. Hence, the three-dimensional theory is ideally suited to compare DSE, FRG, and lattice results.

(B) High temperature limit:

In the limit of asymptotically high temperatures, four-dimensional Yang-Mills theory becomes dimensionally reduced, i.e., it is equal to the three-dimensional theory coupled to an effective adjoint Higgs field, see, e.g., [266] for a DSE study and [271] for generic high-temperature reduction rules. We come back to this point in Chapter 8.

The outline of this chapter is as follows: In Sec. 6.1 we discuss the basic differences of the theory in three and four spacetime dimensions. In Sec. 6.2 we report our results and compare them to DSE and lattice results. We briefly conclude in Sec. 6.3.

The calculations in this chapter were performed by the author of this thesis alone. However, with the foundations provided here, Lukas Corell [272] investigated the influence of additional momentum dependencies and tensor structures. These results are deferred to a forthcoming publication [273].

### 6.1. Basics

To begin, we perform a standard dimensional analysis. Demanding that the action (2.9) is dimensionless implies that the Lagrangian density is of mass dimension  $[\mathcal{L}] = d$ . From the kinetic terms we obtain the field dimensions,

$$[A] = [c] = [\bar{c}] = \frac{d}{2} - 1 \quad \text{and} \quad [q] = [\bar{q}] = \frac{d-1}{2}.$$

Reading off the dimension of the coupling from any of the vertex terms yields

$$[g] = 2 - \frac{d}{2} \implies [\alpha] = 4 - d.$$

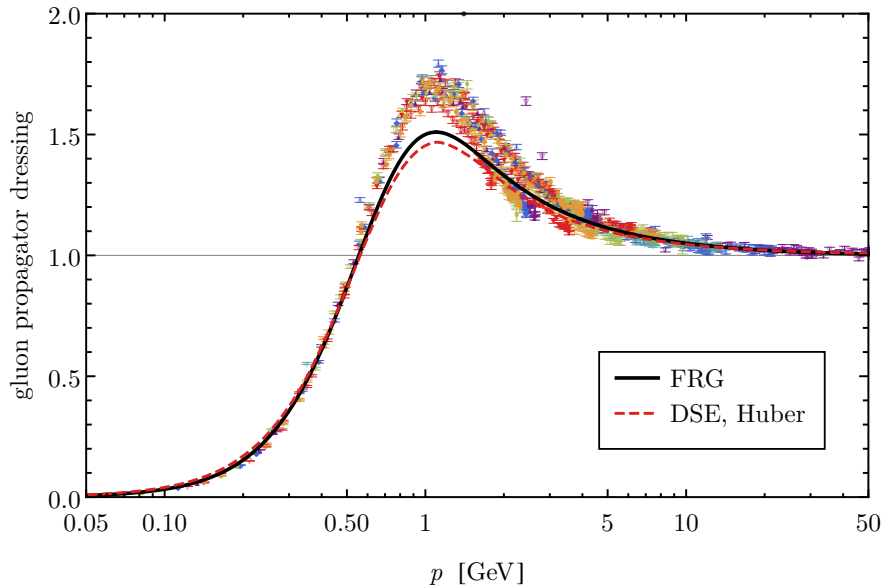


Figure 6.1.: Gluon propagator compared to DSE [201] and lattice [238, 239, 251] results.

Thus, for  $d = 3$ , the running coupling  $\alpha$  is of mass dimension one and, therefore, QCD is super-renormalizable in three dimensions. Hence, no ultraviolet divergences appear and all propagator and vertex dressings become unity in the limit of large momenta.

Here, we strive to compute Yang-Mills correlators in three dimensions. Based on Chapter 5, this is a straightforward task. Therefore, we only point out the differences to four dimensions:

1. The momentum integration in the Wetterich equation has to be carried out in three dimensions, i.e.,  $\int \frac{d^4 q}{(2\pi)^4} \rightarrow \int \frac{d^3 q}{(2\pi)^3}$ .
2. To derive the equations, the trace has to be taken in three dimensions, which is supported by FormTracer, see Chapter 4. For the case of pure gauge theory with Euclidean metric, this simply amounts to setting  $\delta_{\mu\mu} = d \rightarrow 3$ .
3. Since the running coupling is now dimensionful and defines the initial cutoff scale, it must be chosen appropriately.

In the next section we present results obtained from solving the coupled system of FRG equations shown in Fig. 5.4. We restrict the discussion to the unique scaling solution since the decoupling solution brings little additional insights here. Furthermore, we employ the symmetric momentum approximation for the vertices, which has proven to be reliable in four dimensions (see Sec. 5.3.2 and in particular Fig. 5.8) and is even better in three dimensions [272, 273]. We use the exponential regulator shape function (3.11), see Sec. C.3 for more details. However, the dressings are independent of regulator choice in four dimensions (as demonstrated in Sec. 3.1.2) as well as in three dimensions [272, 273].

## 6.2. Results

Below we discuss the propagators, the scaling fixed point, and the vertex dressings.



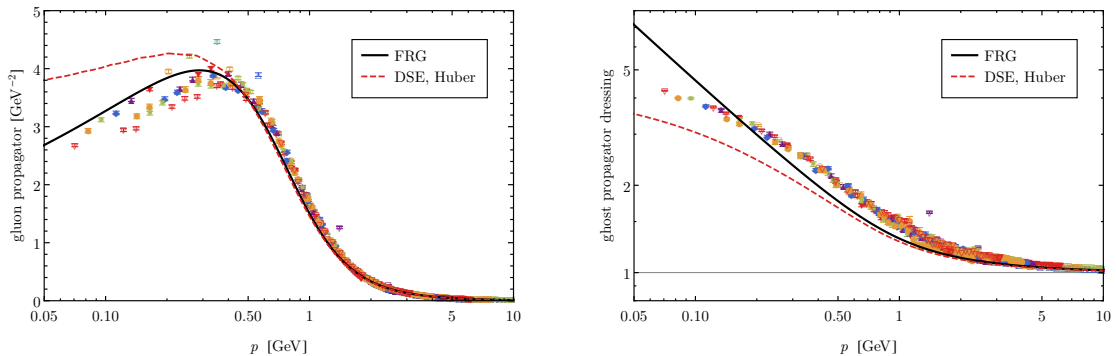


Figure 6.2.: Gluon propagator (left) and ghost propagator dressing (right) in comparison with DSE [201] and lattice [238, 239, 251] results.

### 6.2.1. Propagators

Figure 6.1 depicts our gluon propagator dressing in comparison with DSE [201] and lattice [238, 239, 251] results. In the limit of large momenta, all gluon propagator dressings converge to unity as expected. In the mid-momentum, the lattice gluon propagator dressings show a much stronger bump than the functional results, which lie relatively close to each other. The DSE and FRG results were obtained in a similar truncation. Both calculations included all classical tensor structures but no non-classical vertices or tensor structures. While our results are computed with the symmetric momentum approximation for the vertices, the DSE results were calculated with the full momentum dependence. However, the effect of additional momentum dependencies is negligible compared to the effect of additional tensor structures [272]. However, the DSE result is a decoupling solution whereas our solution is the unique scaling solution. In general, a stronger ghost propagator entails a higher bump in the gluon propagator dressing. This may be one of the reasons why the FRG gluon propagator dressing shows a somewhat stronger bump than the DSE dressing. To summarize, the functional results agree within truncation and resummation uncertainties but show a less pronounced bump than the lattice gluon propagator dressing. We attribute the missing strength to the non-converged truncation with respect to tensor structures and vertices.

Figure 6.2 displays the gluon propagator and the ghost propagator dressing. The left panel reveals the back-bending of the gluon propagator, which is a necessary condition for confinement. Although not clearly visible from the plot, our gluon propagator vanishes with a power law in the infrared, cf. also the next Sec. 6.2.2, whereas the DSE and lattice gluon propagators converge to a constant at vanishing momentum. This difference between the scaling and the decoupling solution is apparent in the ghost propagator dressing shown in the right panel of Fig. 6.2. The agreement between our, the DSE and lattice ghost dressing function is not good. The scales of the functional results are set such that the gluon propagator dressings assume their maximal values at the corresponding lattice scale,  $p \approx 1.1 \text{ GeV}$ . The agreement between the ghost propagator dressing functions could be improved by dramatically changing the scale-setting procedure. In turn, however, the agreement with the gluon propagator shown in the left panel of Fig. 6.2 would be worse. Furthermore, the bump height of the gluon propagator dressing in Fig. 6.1 is not affected by the scale setting prescription. We conclude that the functional results and the lattice do not agree well, no matter how the scale is set.

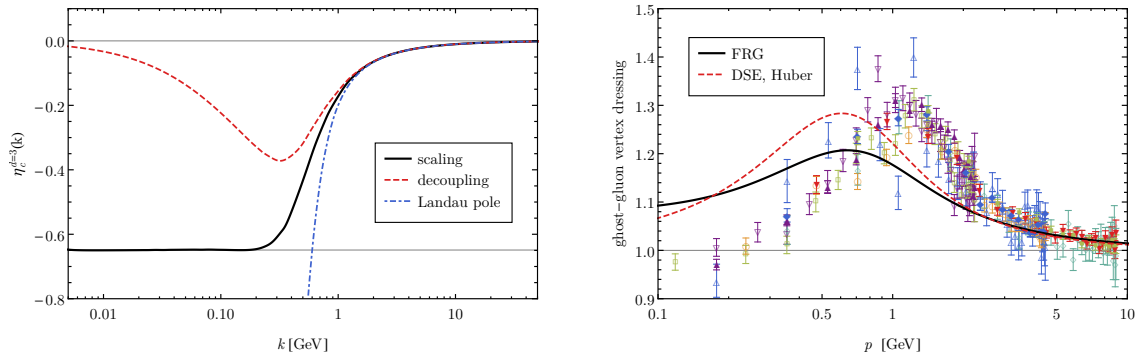


Figure 6.3.: Ghost anomalous dimension (left) and ghost-gluon vertex dressing (right) at the symmetric point compared to DSE [201] and lattice [238, 239, 251] results.

### 6.2.2. Infrared Scaling Fixed Point

The scaling behavior of any  $(2n + m)$ -point function with  $2n$  ghost and  $m$  gluon legs in  $d$  dimensions is given by [217–219]:

$$\lim_{p \rightarrow 0} \lambda^{(2n,m)}(p) \propto (p^2)^{(n-m)\kappa + (1-n)(\frac{d}{2}-2)}. \quad (6.1)$$

For the two-point functions, the scaling power laws are given by [118, 119]

$$\begin{aligned} \Gamma^{\bar{c}c}(p) &\propto p^2 \cdot (p^2)^\kappa \\ \Gamma^{AA}(p) &\propto p^2 \cdot (p^2)^{-2\kappa + \frac{d}{2} - 2}, \end{aligned} \quad (6.2)$$

where we took their canonical dimensions into account. The double-logarithmic ghost propagator dressing plot in Fig. 6.2 clearly reveals the scaling behavior. Fitting the propagators with (6.2), we obtain the scaling exponent in three dimensions,

$$\kappa^{d=3} = 0.321 \pm 0.001,$$

where the uncertainty stems from the difference of the ghost and gluon propagator fits.

In the FRG framework, the propagators depend not only on the momentum  $p$ , but also on the RG scale  $k$ . Above we considered only the behavior at vanishing cutoff scale  $k = 0$  and implicitly used the notation  $Z(p) \equiv Z(k = 0, p)$ . However, it is worthwhile studying the ghost propagator dressing at non-vanishing cutoff to understand how the theory flows into the repulsive scaling infrared fixed point. To this end, we define a scale-dependent ghost anomalous dimension,

$$\eta_c(k) = -\frac{k \partial_k Z_c(k, p = k)}{Z_c(k, p = k)}.$$

It is shown in the left panel of Fig. 6.3. At high scales, it converges to zero as required by perturbation theory. To obtain the scaling solution, we fine-tune the gluon mass parameter at the cutoff scale such that the theory flows into its repulsive infrared fixed point. At the fixed point, the ghost anomalous dimension becomes

$$\eta_c^{d=3} = \lim_{k \rightarrow 0} \eta_c^{d=3}(k) = -0.649 \pm 0.001.$$

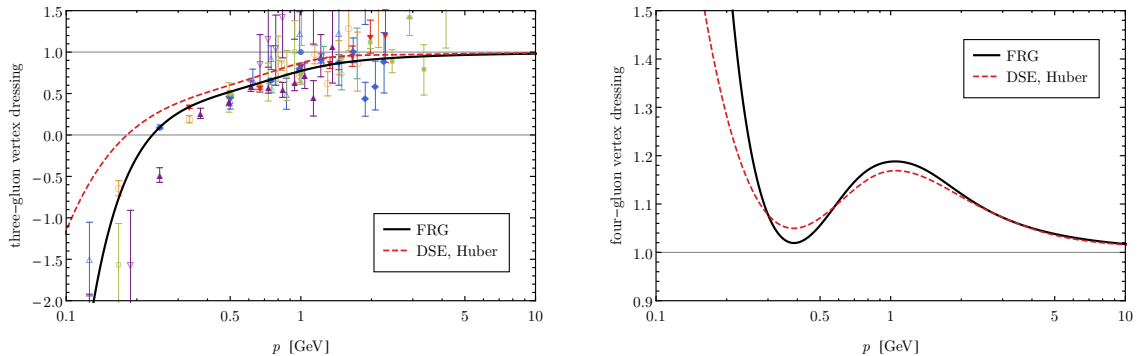


Figure 6.4.: Three-gluon (left) and four-gluon (right) vertex dressings in comparison with DSE [201] and lattice [238, 239, 251] results at the symmetric momentum configuration.

It is a non-trivial result that one can reach the scaling fixed point by simply fine-tuning the gluon mass parameter. If one chooses a lower gluon mass parameter at the ultraviolet cutoff scale, the theory flows into a Landau pole and the ghost anomalous dimension diverges at a finite cutoff scale, see Fig. 6.3. This entails that the regulator terms cannot be fully removed. In contrast, a higher gluon mass parameter at the cutoff scale leads to a constant ghost dressing function in the infrared, i.e., a decoupling solution. In this case we have  $\lim_{k \rightarrow 0} \eta_c^{d=3}(k) = 0$ , which is also shown in Fig. 6.3.

### 6.2.3. Vertices

The ghost-gluon and gluonic vertex dressings are shown in comparison with DSE [201] and lattice [238, 239, 251] results in Fig. 6.3 and 6.4. As for the propagators, all dressings converge to unity in the ultraviolet. The lattice ghost-gluon vertex dressing has its peak at a higher scale than the dressings computed with functional methods. This is expected since the ghost propagator dressing shows a similar scale mismatch. The DSE ghost-gluon vertex is stronger than the FRG vertex in the mid-momentum regime. The former matches the lattice ghost-gluon vertex strength within the uncertainties. As discussed in Sec. 3.2, there exist two DSEs for the ghost-gluon vertex that are equivalent unless truncations are applied. In the truncation used in [201], the quantum contributions to the ghost-gluon vertex differ by almost a factor of two depending on which DSE is used. The dressing shown in Fig. 6.3 corresponds to the one that shows better agreement with the lattice results. The other DSE dressing from [201] lies beneath the FRG result.

The FRG three-gluon vertex dressing shows very good agreement with the lattice results over all momenta. The agreement in the infrared is surprising since the lattice features a decoupling solution, which has a linearly divergent three-gluon vertex dressing function [193, 201, 241], whereas our solution is the scaling solution, which has a stronger divergence in the infrared,  $\lambda_{A^3}(p) \propto (p^2)^{-3\kappa-1/2}$ , as given by (6.1). However, the mid-momentum and ultraviolet regimes, that are less affected by non-perturbative gauge fixing issues and more important for hadronic observables, also agree very well.

The FRG and DSE four-gluon vertices agree within the resummation and truncation uncertainties discussed above. As of now, lattice measurements of the four-gluon vertex are not available. The four-gluon vertex dressing function is qualitatively similar to the dressing function in four dimensions, cf. Fig. 5.8.

### 6.3. Conclusion

We compared correlators of three-dimensional Yang-Mills theory from functional methods to lattice results and found a sizable mismatch. This is most obvious from the height of the gluon propagator dressing bump in Fig. 6.1 but can also be seen from the scale mismatch of the correlation functions with ghost legs, see, e.g., Fig. 6.3. This discrepancy can be attributed to the truncations in functional studies that are being extended [273]. Although we used the same truncation, the agreement of FRG and lattice results is better in four than in three dimensions. While the precise reason for this should be clarified in the future, it is reassuring that the truncation seems to converge faster in the physical case of four dimensions.

## 7. Unquenched Two-Flavor QCD

Within functional continuum methods, the focus is gradually shifting from qualitative bottom-up towards ab-initio top-down approaches [65–73, 198, 274–287]. Here, we calculate *Non-perturbative quark, gluon and meson correlators of unquenched QCD* [3] in the vacuum with the aim of quantitative precision. This technically sophisticated analysis constitutes a prerequisite and a major step towards quantitative first-principle studies of the QCD phase structure within the FRG approach. In addition, such top-down approaches allow the formulation of QCD-enhanced effective models for different aspects of the strong interaction, see, e.g., [66–73].

Our large truncation is necessitated by the delicate mechanism of spontaneous chiral symmetry breaking. Even small deviations of the running couplings in the semi-perturbative regime can lead to the absence of dynamical chiral symmetry breaking [65]. In addition, a quantitative resolution of the quark-gluon interaction turns out to be of qualitative importance [65, 198, 288, 289]. To guarantee the crucial self-consistent running of the vertices, we exploit the quark-gluon vertex STI to constrain the transverse quark-gluon vertex in the perturbative and semi-perturbative regimes. In particular, we take loop corrections to the STI into account [164, 289–292]. In the non-perturbative regime, the STI cannot be used to constrain the transverse vertex. Therefore, we solve its full flow equation below a certain scale that we estimate by means of the gluonic couplings.

This chapter is based on [3], which, in turn, is based on a study of chiral symmetry breaking in quenched QCD [65] as well as Chapter 5 (i.e., [1]). While the author of this thesis was involved in all stages of accomplishing [3], the final numerical simulations and many of the plots were made by my collaborators. In Sec. 7.1 we setup the calculation. The numerical results are presented in Sec. 7.2 and subsequently discussed in Sec. 7.3. We conclude in Sec. 7.4.

### 7.1. Setup

Most of the setup has already been introduced in Chapters 2 – 5. Thus, we focus on the changes specific to the inclusion of quarks. In Sec. 7.1.1 we elaborate on the flow equations and the dynamical hadronization of resonant four-quark channels. We elaborate on the truncation and the tensor bases in Sec. 7.1.2 and 7.1.3, respectively. On that basis, we discuss the application of the STI in Sec. 7.1.4. We specify the cutoff action in Sec. 7.1.5

$$\frac{d\Gamma_k}{dt} = \frac{1}{2} \left( \text{Diagram 1} \right) - \left( \text{Diagram 2} \right) - \left( \text{Diagram 3} \right) + \frac{1}{2} \left( \text{Diagram 4} \right)$$

The diagram shows the Wetterich equation for QCD. It consists of four terms: a gluon loop with a quark loop (Diagram 1), a ghost loop (Diagram 2), a quark loop (Diagram 3), and a ghost loop with a quark loop (Diagram 4). The first term is multiplied by 1/2, the second and third by -1, and the fourth by 1/2.

Figure 7.1.: Wetterich equation for QCD, see Fig. 7.2 for the line coding.

### 7.1.1. Flows and Dynamical Hadronization

To obtain the flow equation shown in Fig. 7.1, an appropriate regulator term that suppress ghost, gluon and quark fluctuation is added to the classical action,  $S \rightarrow S + \Delta S$ . The regulator term  $\Delta S = \Delta S_{\text{YM}} + \Delta S_{\text{M}}$  consists of the Yang-Mills part, given by (5.1), and a part that suppresses quark fluctuations,

$$\Delta S_{\text{M}} = \int_x \bar{q} R_k^q q + \frac{1}{2} \int_x \phi R_k^\phi \phi. \quad (7.1)$$

The regulator functions  $R_k$  are given in Sec. C.3. In order to capture resonant four-quark channels, we introduced auxiliary hadronic degrees of freedom in (7.1) that represent the sigma meson and the pions,

$$\phi = (\sigma, \vec{\pi}).$$

The super-field now includes the auxiliary mesonic fields,

$$\Phi = (A_\mu, c, \bar{c}, q, \bar{q}, \phi).$$

The evolution of the effective action  $\Gamma_k$ , is then given by a generalized version of the Wetterich equation [19, 25, 293] (see also [294] for a pedagogical derivation),

$$\partial_t \Gamma_k[\Phi] = \frac{1}{2} \text{Tr} G_k[\Phi] \partial_t R_k - \frac{\delta \Gamma_k[\Phi]}{\delta \phi_k^a} \partial_t \phi_k^a. \quad (7.2)$$

Analogously to [25, 65, 68], the last term in (7.2) introduces the scale-dependent auxiliary fields via their flows. In order to hadronize the scalar-pseudoscalar channel of the four-quark interaction, we define the scale derivative to be

$$\partial_t \phi_k^a(p) = \int_q \partial_t A_{\bar{q} T_f^a q, k}(p-q, q) [\bar{q} T_f^a q](p-q, q), \quad (7.3)$$

where  $A_{\bar{q} T_f^a q, k}$  is still at our disposal. Further, in (7.3) we introduced generators for the flavor symmetry  $T_f^a$ . For  $a \in \{1, 2, 3\}$  the generators correspond to  $SU(2)$  generators, i.e., the Pauli matrices divided by 2, and  $T_f^0$  is the unit matrix divided by 2. Thus,  $\phi_k^a$  represents a bosonic field with the quantum numbers of the pions ( $f_0(500)$ ) for  $a = 1, 2, 3$  ( $a = 0$ ). Due to (7.2) and (7.3), any  $(2+n)$ -point function that includes at least one quark-antiquark pair  $\bar{q} T_f^a q$  gets an additional contribution to the flow,

$$\Delta \partial_t \Gamma_{\bar{q} T_f^a q \Phi_{i_1} \dots \Phi_{i_n}}^{(2+n)}(p_{\bar{q}}, p_q, p_1, \dots, p_n) = - \frac{\delta^n \delta \left( \frac{\delta \Gamma_k}{\delta \phi^a} \partial_t A_{\bar{q} T_f^a q, k} [\bar{q} T_f^a q] \right)}{\delta \Phi_{i_n}(p_n) \dots \delta \Phi_{i_1}(p_1) \delta [\bar{q} T_f^a q](p_{\bar{q}}, p_q)},$$

where we imply momentum integration in the numerator. In particular, the flow of the four-quark interaction channel  $\Delta \partial_t \Gamma_{(\bar{q} T_f^a q)^2}^{(4)}$ , corresponding to pion or sigma-meson exchange, and the quark-meson Yukawa interaction  $\Delta \partial_t \Gamma_{(\bar{q} T_f^a q) \phi^a}^{(3)}(p, q)$  are modified. We choose  $\partial_t A_{\bar{q} T_f^a q, k}(p, q)$  such that

$$\partial_t \Gamma_{(\bar{q} T_f^a q)^2}^{(4)}(p, -p, p, -p) \equiv 0,$$

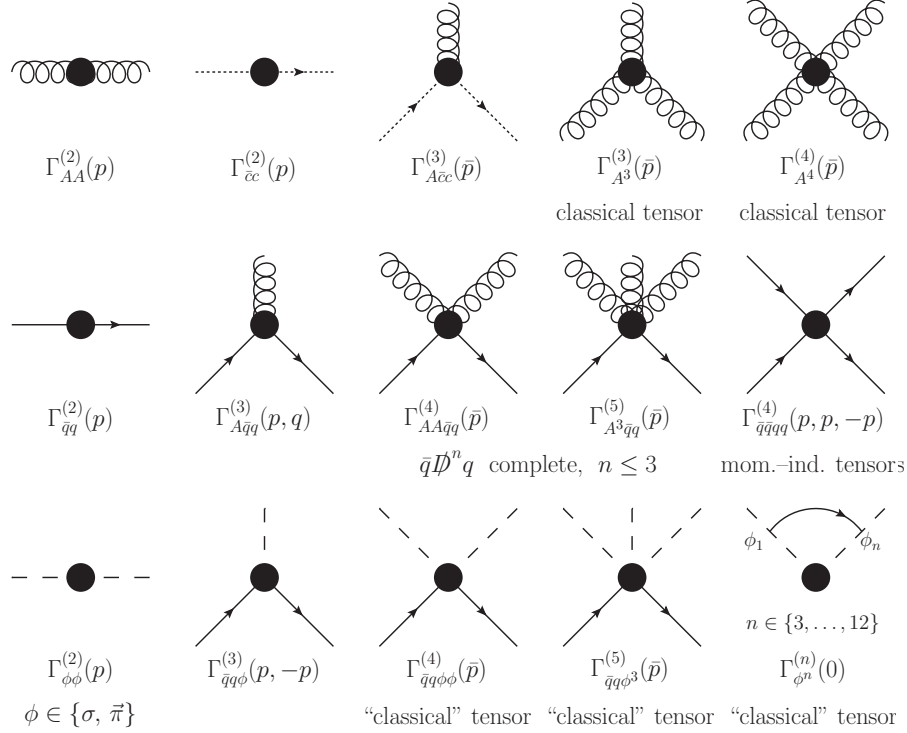


Figure 7.2.: Vertex expansion of the effective action. Wiggly lines represent gluons, dotted lines ghosts, solid lines quarks and dashed lines represent mesons introduced via dynamical hadronization to capture resonant structures in four-quark interactions. The effective action is expanded about the expectation value of the scalar meson field, which acquires a non-vanishing value in the chirally broken phase. The symmetric momentum configuration is denoted by  $\bar{p}$ .

i.e., the quantum corrections to the four-quark interaction are re-written as an exchange of the auxiliary degrees of freedom  $\phi_k^a$  in each RG step. With this re-parameterization of the effective action, the remaining channels of the four-quark vertex remain finite, see Fig. 7.7b. This dynamical hadronization procedure results in a redefinition of one-particle irreducibility. In the present case, a 1PI four-quark interaction is transformed into the one-particle reducible exchange of mesons. This allows to efficiently include the effects of the multi-scatterings of the resonant channels via the inclusion of the corresponding higher interactions, see the bottom line of Fig. 7.2. Since dynamical hadronization is merely a technical means to tame resonant interaction channels, no information loss occurs and the auxiliary fields can be removed again with their equations of motion,

$$\left. \frac{\delta\Gamma[\Phi]}{\delta\phi} \right|_{\phi=\phi_{\text{EoM}}} = 0,$$

yielding the standard effective action in terms of the fundamental QCD degrees of freedom,

$$\Gamma_{\text{QCD}}[A, c, \bar{c}, q, \bar{q}] = \Gamma[\Phi]_{\phi=\phi_{\text{EoM}}}.$$

We discuss the four-quark interactions further in Sec. 7.1.4, but refer to [25, 65, 68, 69, 293–295] for more and in particular technical details on dynamical hadronization.

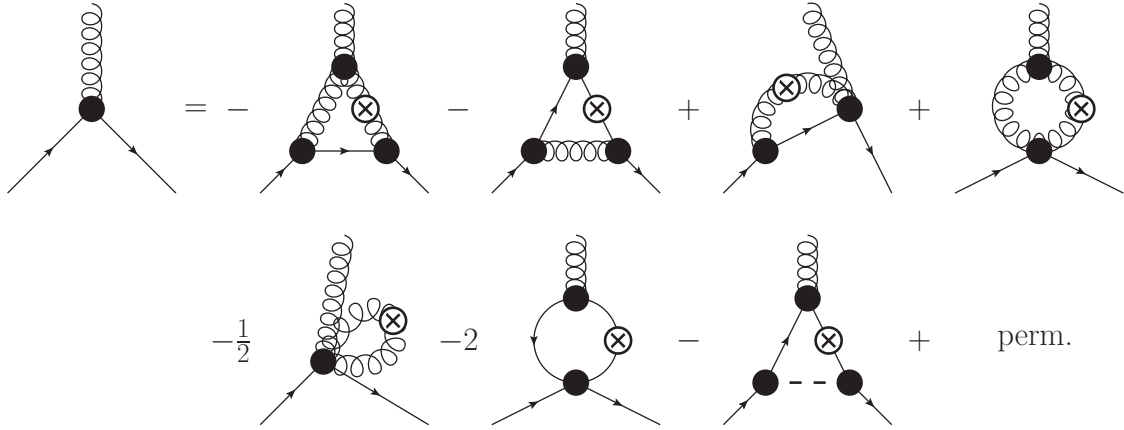


Figure 7.3.: Truncated flow equation for the quark-gluon vertex. Permutations of regulator insertions as well as (anti-)symmetric permutations of external legs are omitted.

### 7.1.2. Truncation

We approximate the effective action within a vertex expansion scheme, cf. Sec. 3.1.3. We summarize the truncation in Fig. 7.2. Due to its extraordinary size, we refrain from giving explicit diagrammatic representations for all flow equations. However, as a representative example, we show the truncated flow equation for the quark-gluon vertex in Fig. 7.3. We want to point out that the flow equations and their diagrammatic representation can easily be derived with the computer algebraic tool DoFun [141]. To handle the vast system of coupled integro-differential equations, we employ the workflow of the fQCD collaboration, see Sec. C.1.

In the remainder of this section, we mainly discuss those points that are not already contained in the previous works [1, 65]. Using the vertex expansion, the effective action is described in terms of 1PI correlation functions, which are parameterized by<sup>1</sup>

$$\Gamma_{\Phi_{i_1} \dots \Phi_{i_n}}^{(n)} = \sum_i \lambda_{\Phi_{i_1} \dots \Phi_{i_n}}^{(i)} \mathcal{T}_{\Phi_{i_1} \dots \Phi_{i_n}}^{(i)}. \quad (7.4)$$

For vertices that appear in the classical action, the classical tensor structure corresponds to the index  $i = 1$ . The discussion of the non-classical tensors is postponed to Sec. 7.1.3. While the quark-gluon vertex tensor basis is explicitly given in Sec. 7.1.3, the tensor bases of higher vertices are deferred to the appendix, see Sec. C.5. In contrast to the previous studies, the improved truncation considered here includes the two-quark-two-gluon, the two-quark-three-gluon, the two-quark-two-meson and the two-quark-three-meson vertices. We discuss the impact of the extended truncation in Sec. 7.3.

<sup>1</sup> The parameterization of the proper vertices given in (7.4) differs from the RG-invariant parameterization used in [65] by factors of the scalar wave function renormalizations. In advanced truncations that include momentum dependencies the simple parameterization chosen here is preferable for both numerical and conceptual reasons. Conceptually, the parameterization given in (7.4) is advantageous because only the momentum-dependent wave function renormalizations at vanishing cutoff are relevant for observables.



back-coupled into	classical	leading	sub-leading
classical	✓	✓	✓
leading	✓	✓	×
sub-leading	✓	×	×

Table 7.1.: Back-coupling of tensor classes. For the classification of tensors see Table 7.2. As described in Sec. 7.1.2, we deviate from this scheme in some cases.

### Truncation Scheme

On the level of the propagators, we use complete tensor bases and compute the full momentum dependence. However, in order to make the computation technically feasible, we neither include all vertex dressings nor do we calculate their full momentum dependence, as indicated in Fig. 7.2. To make the vertex expansion systematic, we sort the constituents of our truncation into three groups:

- (A) classical tensors,
- (B) leading non-classical tensors, and
- (C) sub-leading non-classical tensors.

In addition to the tensors present in the bare QCD action, we interpret the Yukawa interactions between quarks and mesons as well as the meson propagators as classical. The latter are present because of a momentum-dependent version of the dynamical hadronization technique as described above. The explicit assignment of the remaining tensors is given in Table 7.2.

In the present implementation of this scheme we assume that leading non-classical tensors which are plugged into the equations of sub-leading non-classical tensors have only a sub-sub-leading overall effect. Analogously, we assume that sub-leading non-classical tensors have only a sub-sub-leading overall effect in the equations of the leading non-classical tensors. The above assumptions have been verified in many cases. In particular, the sub-leading non-classical tensors have been found to yield only sub-sub-leading corrections to the leading non-classical tensors of the quark-gluon vertex [65]. Apart from a few exceptions discussed below, we take into account all contributions up to the sub-leading level, which is illustrated in Table 7.1. Within functional methods, the resulting truncation consists of the largest set of correlation functions that has been solved so far. Nevertheless, an assessment of truncation artifacts is essential. We discuss these and the leading truncation error further in Sec. 7.2 and 7.3.

### Exceptions to the Truncation Scheme

The classification of basis tensors introduced above equips us with a systematic expansion scheme. However, the remaining equations are still very large and we deviate in a controlled manner from this expansion scheme in some equations:

1. We neglect sub-leading non-classical quark-gluon vertex tensors, which we checked explicitly to be a very good approximation, see also [65, 198, 245, 279].
2. We ignore sub-leading non-classical contributions to the four-gluon vertex. Since this vertex is the least important of the classical vertices, we expect this to be a good approximation, although explicit checks are amiss due to the size of these equations.

	classical	leading	sub-leading
$\Gamma_{\bar{c}cA}^{(3)}$	$\mathcal{T}_{\bar{c}cA}^{(1)}$		
$\Gamma_{A^3}^{(3)}$	$\mathcal{T}_{A^3}^{(1)}$		
$\Gamma_{A^4}^{(4)}$	$\mathcal{T}_{A^4}^{(1)}$		
$\Gamma_{\bar{q}qA}^{(3)}$	$\mathcal{T}_{\bar{q}qA}^{(1)}$	$\mathcal{T}_{\bar{q}qA}^{(4)}, \mathcal{T}_{\bar{q}qA}^{(7)}$	remaining $\mathcal{T}_{\bar{q}qA}^{(i)}$
$\Gamma_{\bar{q}qA^2}^{(4)}$		$\mathcal{T}_{\bar{q}qA^2}^{(1)} \dots \mathcal{T}_{\bar{q}qA^2}^{(18)}$	
$\Gamma_{\bar{q}qA^3}^{(5)}$			$\mathcal{T}_{\bar{q}qA^3}^{(1)} \dots \mathcal{T}_{\bar{q}qA^3}^{(5)}$
$\Gamma_{\bar{q}qqq}^{(4)}$		$\mathcal{T}_{\bar{q}qqq}^{(\pi)}, \mathcal{T}_{\bar{q}qqq}^{(\eta')}$	remaining $\mathcal{T}_{\bar{q}qqq}^{(i)}$
$\Gamma_{qcQq}^{(3)}$		$\mathcal{T}_{qcQq}^{(1)}, \mathcal{T}_{qcQq}^{(4)}$	
$\Gamma_{\bar{q}q\phi}^{(3)}$	$\mathcal{T}_{\bar{q}q\phi}^{(1)}$		$\mathcal{T}_{\bar{q}q\phi}^{(2)} \dots \mathcal{T}_{\bar{q}q\phi}^{(4)}$
$\Gamma_{\bar{q}q\phi^2}^{(4)}$			$\mathcal{T}_{\bar{q}q\phi^2}$
$\Gamma_{\bar{q}q\phi^3}^{(5)}$			$\mathcal{T}_{\bar{q}q\phi^3}$
$\Gamma_{\phi^n}^{(n)}$	$\mathcal{T}_{\phi^3}, \mathcal{T}_{\phi^4}$		$\mathcal{T}_{\phi^5} \dots \mathcal{T}_{\phi^{12}}$

Table 7.2.: Assignment of vertex tensor basis elements to the three classes, cf. Table 7.1.

- Contributions from the tensor  $\mathcal{T}_{\bar{q}qA}^{(4)}$  are ignored in the equation for the dressing of  $\mathcal{T}_{\bar{q}qA}^{(7)}$  and vice versa, which we tested to be a very good approximation.
- We include the effect of the two-quark-three-gluon vertex in the leading non-classical tensors of the quark-gluon as well as the two-quark-two-gluon vertex.
- We neglected  $\mathcal{T}_{\bar{q}qA}^{(4)}$  and  $\mathcal{T}_{\bar{q}qA}^{(7)}$  as well as some two-quark-two-gluon vertex tensors in some equations for the two-quark-two-gluon vertex dressings. In all cases we explicitly checked that the approximations have no effect on the results.
- We always feed back all purely mesonic interactions.

### Momentum Dependence

We do not calculate the full momentum dependence of all vertices. The resolved momentum dependency of each constituent of our truncation is shown in Fig. 7.2. Here,  $\bar{p}$  represents the symmetric momentum configuration defined by  $\bar{p}^2 = p_i \cdot p_i = -(n-1)p_i \cdot p_j$  with  $i \neq j \in \{1, \dots, n\}$  for any  $n$ -point function, cf. also Sec. 5.3.2. The momentum dependence on this symmetric configuration is then used to approximate the full momentum dependence by

$$\Gamma_{\Phi_{i_1} \dots \Phi_{i_n}}^{(n)}(p_1, \dots, p_n) \approx \Gamma_{\Phi_{i_1} \dots \Phi_{i_n}}^{(n)}(\bar{p}),$$

where  $\bar{p} = \sqrt{(p_1^2 + \dots + p_n^2)/n}$ . A similar momentum approximation is used for the quark-meson interactions, see Sec. C.5 for details. An exemption are the purely mesonic interactions. As indicated in Fig. 7.2, these are calculated at vanishing momentum and approximated as momentum-independent.

In comparison to the approximation used in Chapter 5, we ignore additional momentum dependencies in the pure gauge sector due to the computational costs of taking these into account. The effect of this approximation is an overestimation of the bump in the gluon propagator of 5 to 10 %, see Fig. 5.8. Exploratory tests that include more momentum dependencies in the two-quark-two-gluon vertex indicate an underestimation of the gluon propagator bump of 10 % in our current truncation. Consequently, we expect the net effect of these approximations to be small.

### 7.1.3. Tensor Bases

The tensor bases of the Yang-Mills  $n$ -point functions used in this chapter are identical to the ones used in Chapter 5. The parameterization of the quark propagator is given below in (7.15). It remains to provide the tensor bases of the two-quark- $n$ -gluon and the mesonic vertices. In this section the employed general construction principle is described and explicitly worked out for the quark-gluon vertex. The tensor bases of the other vertices are provided in Sec. C.5.

In general, one can simply write down any full tensor basis for a given  $n$ -point function, cf. (7.4). However, in the presence of symmetries and in particular in the case of additional approximations a suitable tensor basis should be used. See Sec. C.2 for the construction of projection operators and the hazards of using incomplete bases. We classify the full tensor decompositions of the two-quark- $n$ -gluon vertices in tensors that can be related to operators of the type

$$\bar{q} \not{D}^n q, \quad (7.5)$$

where  $D_\mu = \partial_\mu - ig A_\mu^a T_c^a$  is the covariant derivative, cf. (2.2). This yields bases that are ordered according to the number of explicit momentum variables. Importantly, this expansion leads to a natural separation of chirally symmetric and symmetry-breaking tensors. All tensors stemming from odd  $n$  are chirally symmetric, whereas even  $n$  lead to operators that violate chiral symmetry. It is noteworthy that this expansion contains the bare action:  $n = 0$  corresponds to the quark mass term and  $n = 1$  contains the other classical tensors.

#### Quark-gluon vertex

Using the projection operators from (2.13), we split the basis of quark-gluon vertex into a transverse and a longitudinal part. Suppressing all fundamental as well as spinor indices, it is given by<sup>2</sup>

$$\begin{aligned} \left[ \Gamma_{\bar{q}qA}^{(3)} \right]_\mu^a(p, q) &= \mathbb{1}_f T_c^a \times \\ &\left( \Pi_{\mu\nu}^\perp(p+q) \sum_{i=1}^8 \lambda_{\bar{q}qA}^{(i)}(p, q) \left[ \mathcal{T}_{\bar{q}qA}^{(i)} \right]_\nu(p, q) + \Pi_{\mu\nu}^\parallel(p+q) \sum_{i=9}^{12} \lambda_{\bar{q}qA}^{(i)}(p, q) \left[ \mathcal{T}_{\bar{q}qA}^{(i)} \right]_\nu(p, q) \right), \end{aligned} \quad (7.6)$$

where the summation boundaries become clear below. Here, the  $T_c^a$  are the generators of the fundamental representation of the  $SU(3)$  color group and  $\mathbb{1}_f$  is the unit matrix that

<sup>2</sup> In (7.6) we factorized the projection operators as well as the group tensors for the sake of brevity. However, in the sense of basis elements, cf. (7.4), these are considered to be contained in the  $\mathcal{T}_{\bar{q}qA}^{(i)}$ .

makes the quark-gluon vertex diagonal in flavor space. The quark and antiquark momenta are denoted by  $q$  and  $p$ , and thus  $-p - q$  is the gluon momentum. It remains to specify the tensors  $\mathcal{T}_{\bar{q}qA}^{(i)}$ , which are, using (7.5), given by

$$\begin{aligned}
\bar{q} \not{D} q : \quad & \left[ \mathcal{T}_{\bar{q}qA}^{(1)} \right]_{\mu} (p, q) = -i \gamma_{\mu}, \\
\bar{q} \not{D}^2 q : \quad & \left[ \mathcal{T}_{\bar{q}qA}^{(2)} \right]_{\mu} (p, q) = (p - q)_{\mu} \mathbb{1}_s, \\
& \left[ \mathcal{T}_{\bar{q}qA}^{(3)} \right]_{\mu} (p, q) = (\not{p} - \not{q}) \gamma_{\mu}, \\
& \left[ \mathcal{T}_{\bar{q}qA}^{(4)} \right]_{\mu} (p, q) = (\not{p} + \not{q}) \gamma_{\mu}, \\
\bar{q} \not{D}^3 q : \quad & \left[ \mathcal{T}_{\bar{q}qA}^{(5)} \right]_{\mu} (p, q) = i (\not{p} + \not{q})(p - q)_{\mu}, \\
& \left[ \mathcal{T}_{\bar{q}qA}^{(6)} \right]_{\mu} (p, q) = i (\not{p} - \not{q})(p - q)_{\mu}, \\
& \left[ \mathcal{T}_{\bar{q}qA}^{(7)} \right]_{\mu} (p, q) = \frac{i}{2} [\not{p}, \not{q}] \gamma_{\mu}, \\
\bar{q} \not{D}^4 q : \quad & \left[ \mathcal{T}_{\bar{q}qA}^{(8)} \right]_{\mu} (p, q) = -\frac{1}{2} [\not{p}, \not{q}] (p - q)_{\mu}. \tag{7.7}
\end{aligned}$$

Equation (7.6) together with (7.7) yields a complete basis for the transverse quark-gluon vertex. In Landau gauge, the transverse correlation functions close among themselves and contain all information on the observables. However, we strive to exploit the (longitudinal) Slavnov-Taylor identities to constrain the transverse correlations functions at high momentum scales, cf. Sec. 5.1.3 and 7.1.4. Therefore, we also introduce basis tensors for the longitudinal part in (7.6). Simply attaching the longitudinal projector to all tensors generated by (7.5) (i.e. those given in (7.7)), yields a degenerate basis. It can easily be shown that four basis tensors are sufficient to describe the longitudinal quark-gluon vertex. Omitting momentum arguments, we choose

$$\begin{aligned}
\mathcal{T}_{\bar{q}qA}^{(9)} &= \mathcal{T}_{\bar{q}qA}^{(1)}, \\
\mathcal{T}_{\bar{q}qA}^{(10)} &= \mathcal{T}_{\bar{q}qA}^{(2)}, \\
\mathcal{T}_{\bar{q}qA}^{(11)} &= \mathcal{T}_{\bar{q}qA}^{(6)}, \\
\mathcal{T}_{\bar{q}qA}^{(12)} &= \mathcal{T}_{\bar{q}qA}^{(8)}
\end{aligned}$$

to complete the basis construction of the full quark-gluon vertex given by (7.6).

As a preparation for the application of the quark-gluon vertex STI, we discuss the consequences of a generalized regularity assumption. In this case the full quark-gluon vertex is spanned by the unprojected tensors given in (7.7), i.e.,

$$\left[ \Gamma_{\bar{q}qA}^{(3)} \right]_{\nu}^a (p, q) \stackrel{!}{=} \mathbb{1}_f T_c^a \times \sum_{i=1}^8 \lambda_{\bar{q}qA}^{(i)}(p, q) \left[ \mathcal{T}_{\bar{q}qA}^{(i)} \right]_{\nu} (p, q). \tag{7.8}$$

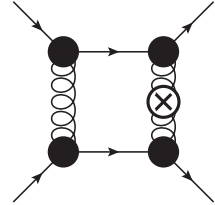
In the limit of vanishing gluon momentum, a regular quark-gluon vertex can be expressed by (7.8) since otherwise singularities are introduced by the projection operators (7.6). Assuming that (7.8) holds also for finite gluon momenta, i.e., assuming generalized regularity, implies that the transverse and longitudinal dressing functions are not independent. By construction, the transverse dressings in (7.6) are identical to the dressings of (7.8). Due to the degeneracy, the longitudinal dressings are given by linear combinations of the transverse dressings,

$$\begin{aligned}\lambda_{\bar{q}qA}^{(9)} &= \lambda_{\bar{q}qA}^{(1)} + \left[ \frac{1}{2} \lambda_{\bar{q}qA}^{(7)} - \lambda_{\bar{q}qA}^{(5)} \right] (p^2 - q^2), \\ \lambda_{\bar{q}qA}^{(10)} &= \lambda_{\bar{q}qA}^{(2)} + \lambda_{\bar{q}qA}^{(3)} + \lambda_{\bar{q}qA}^{(4)} \frac{(p+q)^2}{p^2 - q^2}, \\ \lambda_{\bar{q}qA}^{(11)} &= \lambda_{\bar{q}qA}^{(6)} + \frac{1}{2} \lambda_{\bar{q}qA}^{(7)} \frac{(p+q)^2}{q^2 - p^2}, \\ \lambda_{\bar{q}qA}^{(12)} &= \lambda_{\bar{q}qA}^{(8)} + 2 \lambda_{\bar{q}qA}^{(3)} \frac{1}{q^2 - p^2},\end{aligned}\tag{7.9}$$

where we omit momentum arguments. The STI constrains these four longitudinal dressings. Therefore, even under the generalized regularity assumption (7.8), the STI only constrains the combinations of transverse dressings given by the right-hand side of (7.9).

#### 7.1.4. Quark-Gluon Vertex STI

In the resummation scheme defined by the FRG, spontaneous chiral symmetry breaking is triggered by the dynamical creation of a four-quark interaction from box-diagrams with two exchanged gluons proportional to  $\alpha_{\bar{q}qA}^2$ , see [29] for a review. The presence or absence of spontaneous chiral symmetry breaking is therefore very sensitive to the strength of the quark-gluon vertex. Even small quantitative errors may lead to the absence or unphysical enhancement of dynamical chiral symmetry breaking [65]. In order to minimize this sensitivity, we use the Slavnov-Taylor identity to constrain the quark-gluon vertex. At the symmetric momentum configuration, the STI leads to the identity [164, 289–292]



$$\lambda_{\bar{q}qA}^{(9)}(\bar{p}) = \frac{Z_q(\bar{p})}{Z_c(\bar{p})} \left[ \lambda_{cqQ_q}^{(1)}(\bar{p}) - \frac{3}{2} \bar{p}^2 \lambda_{cqQ_q}^{(4)}(\bar{p}) \right],\tag{7.10}$$

where  $\lambda_{\bar{q}qA}^{(9)}(\bar{p})$  is the dressing function of the longitudinally projected classical tensor introduced in Sec. 7.1.3. The generalized BRST-vertex dressings  $\lambda_{cqQ_q}^{(1)}(\bar{p})$  and  $\lambda_{cqQ_q}^{(4)}(\bar{p})$  are field derivatives of the quantum BRST variation of the quark, see Sec. 2.1. These are fully dressed and are computed with the flow equation. A derivation of (7.10) in the presence of a regulator can be found in [3].

In the literature, (7.10) is often used to constrain the leading dressing function  $\lambda_{\bar{q}qA}^{(1)}$  of the transversely projected quark-gluon vertex via the approximate identification

$$\lambda_{\bar{q}qA}^{(1)}(p, q) \equiv \lambda_{\bar{q}qA}^{(9)}(p, q),\tag{7.11}$$

which holds exactly at the classical level. As discussed above (cf. (7.9)), the assumption of generalized regularity results in a more general relation than (7.11),

$$\lambda_{\bar{q}qA}^{(9)}(p, q) = \lambda_{\bar{q}qA}^{(1)}(p, q) + \left[ \frac{1}{2} \lambda_{\bar{q}qA}^{(7)}(p, q) - \lambda_{\bar{q}qA}^{(5)}(p, q) \right] (p^2 - q^2) .$$

However, the transverse quark-gluon vertex dressings fulfill [65]

$$\frac{1}{2} \lambda_{\bar{q}qA}^{(7)}(p, q) = \lambda_{\bar{q}qA}^{(5)}(p, q) \quad (7.12)$$

to a very high precision at momenta larger than 1 GeV. Thus, the application of the STI to the transversely projected classical tensor via the identification (7.11) is based on the assumption of generalized regularity (7.8) as well as the validity of (7.12). While (7.12) holds at large momenta, it is clearly violated at non-perturbative momenta [65]. Therefore, the STI cannot be straightforwardly used to constrain the non-perturbative behavior of the dressing  $\lambda_{\bar{q}qA}^{(1)}$  via (7.11).

In the remainder of this section we estimate the scale down to which the quark-gluon vertex can be constrained by its STI, (7.10), via (7.11). To understand the implications of the assumption of generalized regularity, we look at the quark-gluon vertex in the limit of vanishing gluon momentum. Due to the structure of the longitudinal and transverse projection operators, see (2.13), a violation of (7.11) at vanishing gluon momentum,

$$\lim_{q \rightarrow -p} \lambda_{\bar{q}qA}^{(1)}(p, q) \neq \lim_{q \rightarrow -p} \lambda_{\bar{q}qA}^{(9)}(p, q) ,$$

implies an irregularity of the quark-gluon vertex at vanishing gluon momentum. Note that the dynamical creation of the gluon mass gap, and hence confinement [108, 109], requires irregularities in at least one vertex as discussed in detail in Sec. 5.2. Even though this does not imply an irregularity of the quark-gluon vertex, the gapping scale of the gluon propagator provides an estimate for the scale below which (7.11) is invalid.

From these regularity arguments and the findings in [65] on the validity of (7.12), we conclude that a scale,

$$\Lambda_{\text{STI}} = \mathcal{O}(1 \text{ GeV}) ,$$

exists below which (7.11) cannot be safely applied anymore. To obtain a better estimate of the STI scale  $\Lambda_{\text{STI}}$ , we consider the transverse running couplings extracted from the different gluonic vertices, defined in (5.18). As is the case for the quark-gluon vertex, the STIs of the gluonic vertices constrain only their longitudinal projection, see, e.g., (5.22). The transverse gluonic running couplings are degenerate if all non-classical tensors are negligible or if all non-classical dressings fulfill conditions analogous to (7.12). Therefore, the scale at which the transverse gluonic couplings are no longer degenerate yields an approximation for  $\Lambda_{\text{STI}}$ . Based on our results for the transverse gluonic running couplings shown in Fig. 7.8a, we identify the scale where the degeneracy is lost as

$$\Lambda_{\text{STI}} \lesssim 3 \text{ to } 5 \text{ GeV} . \quad (7.13)$$

The degeneracy of the gluonic couplings is violated by more than 5% below 3 GeV. Thus, the STIs cannot be used to constrain the transverse running couplings below this scale. Above 5 GeV, we observe near-degeneracy of the gluonic couplings.

With this non-trivial estimate of the scale  $\Lambda_{\text{STI}}$  we can apply the STI to constrain the quark-gluon vertex, for which the transverse running coupling is defined by

$$\alpha_{\bar{q}qA}(\bar{p}) = \frac{1}{4\pi} \frac{\left(\lambda_{\bar{q}qA}^{(1)}(\bar{p})\right)^2}{Z_A(\bar{p}) Z_q^2(\bar{p})}. \quad (7.14)$$

We use (7.10) together with (7.11) to calculate the symmetric momentum configurations of the dressing function  $\lambda_{\bar{q}qA}^{(1)}$  of the transversely projected classical tensor  $\mathcal{T}_{\bar{q}qA}^{(1)}$ . Due to the presence of the RG scale,  $\Lambda_{\text{STI}}$  plays a two-fold role. For RG scales  $k > \Lambda_{\text{STI}}$ , we use the STI to constrain the full range of symmetric momenta  $\bar{p} \in [0, \infty)$ . All other momentum configurations of  $\lambda_{\bar{q}qA}^{(1)}(p, q)$  are calculated as relative offset to the symmetric configurations. For RG scales  $k \lesssim \Lambda_{\text{STI}}$ , we use the STI to constrain only the restricted range of symmetric momenta  $\bar{p} \in [\Lambda_{\text{STI}}, \infty)$  of  $\lambda_{\bar{q}qA}^{(1)}$ . The non-classical dressings  $\lambda_{\bar{q}qA}^{(i)}(p, q)$ ,  $i > 1$  are for all momenta and all RG scales calculated from the quark-gluon vertex flow equation. We vary the transition scale  $\Lambda_{\text{STI}}$  from 3 to 7 GeV, i.e., beyond the estimate given (7.13), to obtain an estimate of our truncation error. This error estimate is indicated by the bands in our results. The solid lines correspond to the upper value of 5 GeV for the transition scale in (7.13).

### 7.1.5. Initial Cutoff Action

The fundamental parameters of QCD, viz. the strong running coupling at the renormalization scale and the bare quark masses, completely determine the action at the cutoff scale,  $k = \Lambda \approx 100$  GeV, via the modified Slavnov-Taylor identities. As in Chapter 5, we choose constant vertex dressings such that the resulting running couplings fulfill the STIs at the renormalization scale, i.e., we demand,

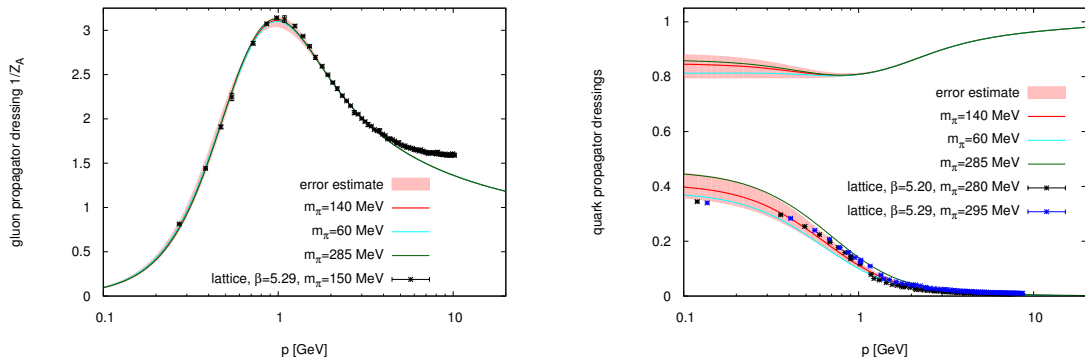
$$\alpha_{\bar{q}qA}(\mu) = \alpha_{\bar{c}cA}(\mu) = \alpha_{A^3}(\mu) = \alpha_{A^4}(\mu) \quad \text{with} \quad \mu = 10 \text{ GeV} \quad \text{at} \quad k = 0,$$

Furthermore, we choose the bare quark mass at the cutoff  $k = \Lambda$  such that the desired pion mass is obtained, cf. [65] for more details. The gluon mass parameter acquires a non-zero value because of the BRST-symmetry-violating regulator. Here, we determine it uniquely by requiring IR scaling in the glue sector, see Chapter 5 and 6.

In first-principle calculations one chooses a value for the strong running coupling at the renormalization scale and translates the internal units into physical units by the use of an observable. In order to compare to lattice simulations, we use the location of the gluon propagator dressing bump (see Fig. 7.4a) to convert our units to lattice units which are given in GeV.

## 7.2. Numerical Results

As the main result we present the unquenched gluon, quark and ghost propagators in Fig. 7.4 and 7.5. The parameterization of the Yang-Mills propagators is identical to the one in Chapter 5, given by (5.3). Suppressing fundamental color, flavor and spinor indices,



(a) Gluon propagator dressing  $1/Z_A(p)$  in comparison to lattice results [296]. The discrepancy at large momenta stems from finite lattice spacing artifacts. (b) Quark propagator dressing functions,  $M_q(p)$  (lower lines, GeV) and  $1/Z_q(p)$  (upper lines), in comparison to lattice results [297, 298]. We do not show lattice results for the quark wave function  $Z_q(p)$  since the currently available two-flavor results are still plagued by considerable systematic errors.

Figure 7.4.: Unquenched two-flavor QCD propagators for different pion masses.

the inverse quark propagator is decomposed by<sup>3</sup>

$$\Gamma_{\bar{q}q}^{(2)}(p) = Z_q(p) (i\not{p} + M_q(p)) . \quad (7.15)$$

The results in this chapter are obtained with two quark flavors at different pion masses. We indicate our best estimate of the systematic error via bands, as discussed in Sec. 7.1.4 and 7.3.

The gluon propagator dressing function  $1/Z_A(p)$ , displayed in Fig. 7.4a, shows unprecedented agreement with unquenched two-flavor lattice results [296]. While the lattice propagator dressing flattens out at large momenta due to finite spacing artifacts, our gluon propagator connects smoothly to perturbation theory. At very small momenta, we find small deviations to the lattice result because our gluon propagator is of the scaling type, whereas the lattice propagator is of the decoupling type. The non-perturbative gauge-fixing procedure is still an open issue, see Sec. 2.3 and 5.2, which potentially affects any infrared comparison of gauge-fixed correlation functions. It is noteworthy that the gluon propagator is insensitive to the pion mass. This insensitivity to the details of the matter sector is a very welcome property for investigations of the phase structure of QCD at finite temperature and density. There significant changes in the dynamics of the matter sector are expected, whose impact on the glue sector are limited by the above mechanism. Consequently, this stabilizes the current vertex expansion scheme at finite temperature and density. In particular, these findings strengthen the predictive power of approaches that use lattice input for the gauge sector [59–62].

The quark propagator dressings are shown in Fig. 7.4b. At intermediate and large momenta we find good agreement of the quark mass function  $M_q(p)$  with the corresponding lattice results [297, 298]. However, we find a larger IR value for the quark mass function

<sup>3</sup> The gluon and ghost wave function renormalizations  $Z_A(p)$  and  $Z_c(p)$  introduced in (5.3) are the inverse of the dressing functions  $Z(p)$  and  $G(p)$  often used in the DSE literature, whereas  $Z_q(p)$  corresponds to the  $A(p)$  function, used to parametrize the quark propagators, see, e.g., [18, 32].



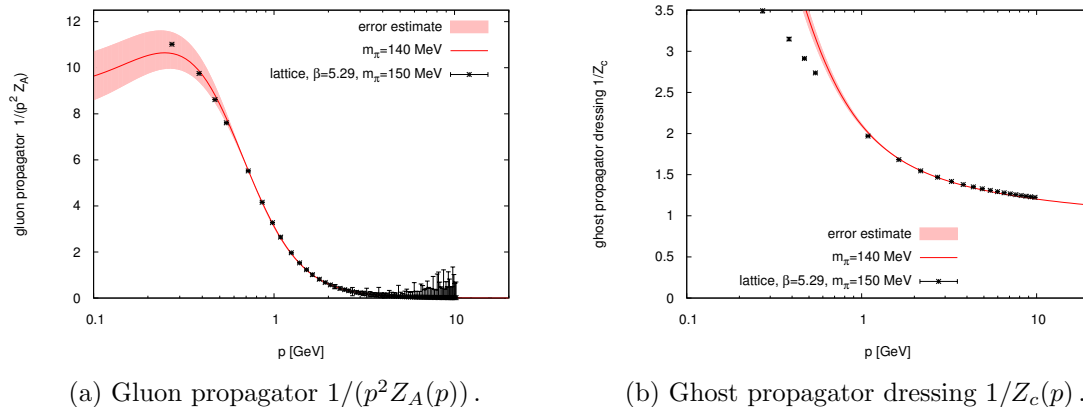
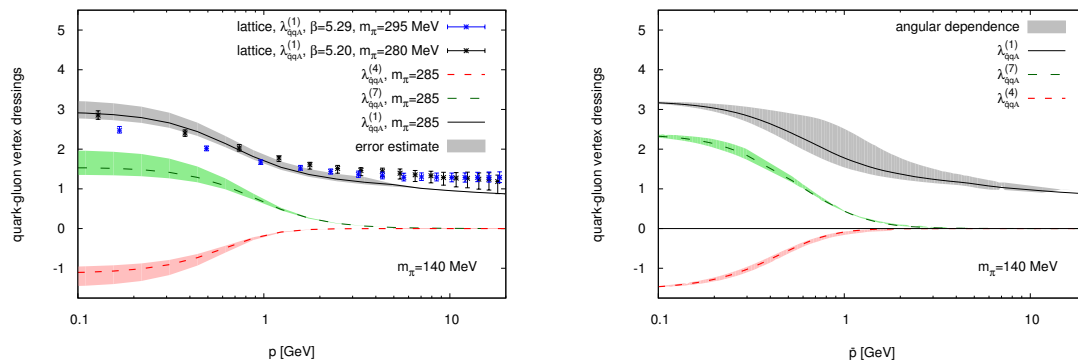


Figure 7.5.: Two-flavor gluon and ghost propagators in comparison to lattice data [296].

than the lattice. As discussed in more detail in Sec. 7.3, this is most likely due to the presence of a slight scale mismatch between the matter and glue sector in our calculation. We refrain from a lattice comparison of the quark wave function renormalization since presently no two-flavor continuum-extrapolated results with reliable systematic errors are available. It is interesting to compare the qualitative behavior of  $1/Z_q(p)$  with other functional method calculations. We find a slight backbending of the quark wave function renormalization at small momentum scales. A similar but more pronounced effect has also been observed in Dyson-Schwinger studies of the quark propagator, see, e.g., [245, 289, 291, 299, 300]. We find that the backbending increases with increasing pion mass, see Fig. 7.4b. This is the opposite effect to the one found in [245, 289, 291, 299, 300]. The quark mass function  $M_q(p)$  also increases with increasing pion mass, which is the expected behavior. To summarize, the qualitative behavior of quark wave function renormalization at low momenta is an intricate result of our large unquenched system of equations.

We compare the ghost propagator dressing  $1/Z_c(p)$  to the lattice results from [296] in Fig. 7.5b. As for the scaling solution of pure gauge theory, see Fig. 5.5, the ghost propagator agrees with the lattice decoupling solution down to momenta of roughly 1 GeV. In contrast, the gluon propagator agrees remarkably well with the decoupling lattice propagator down to very low momenta, see Fig. 7.5a. This can be understood by the fact that scaling is driven by the massless ghosts.

The solution of our large truncation provides us with a wealth of non-trivial 1PI vertex functions. This includes the momentum dependencies of classical and non-classical tensors, many of which are calculated here for the first time. However, we focus on the quark-gluon vertex as the most crucial ingredient for quantitative accuracy in the unquenched system. The transversely projected quark-gluon vertex can be represented with eight basis elements [301]. They include four chirally symmetric tensors, one of them being the classical tensor, and four tensors that break chiral symmetry, see Sec. 7.1.3. In line with earlier investigations [65, 198, 245, 279], we find that only two non-classical tensors are quantitatively important. The first and most important one is the chirally symmetric tensor  $\mathcal{T}_{\bar{q}qA}^{(7)}$ , the second is given by the chiral-symmetry-breaking tensor  $\mathcal{T}_{\bar{q}qA}^{(4)}$ , see (7.7) for the definition of the basis. The leading dressing functions of the quark-gluon vertex are shown in Fig. 7.6a where the dressing of the classical tensor is also compared to lattice results [297, 298]. Within the uncertainties, we find good agreement with the



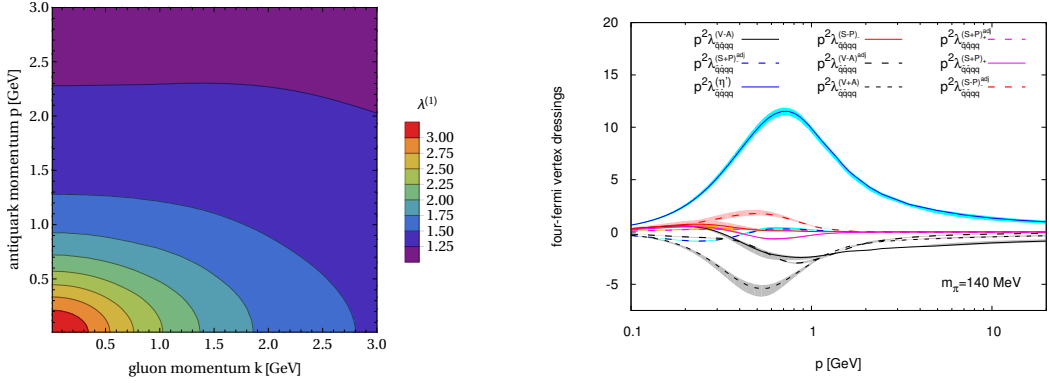
(a) Dressings in the soft gluon limit,  $\lambda_{\bar{q}qA}^{(i)}(p, -p)$ . The dressing of the classical tensor is compared to lattice results [297, 298] and normalized to match our results at  $p = 1$  GeV. (b) Dependence on relative and angular momentum variables for fixed momentum scales  $\bar{p} = \sqrt{(p_1^2 + p_2^2 + p_3^2)}/3$ . Lines correspond to the symmetric point momentum configuration.

Figure 7.6.: Two-flavor quark-gluon vertex dressing functions  $\lambda_{\bar{q}qA}^{(i)}$ .

lattice results in the limit of vanishing gluon momentum. In line with [65], we find that the dressing of the classical tensor structure of the quark-gluon vertex shows a sizable angular dependence, as illustrated in Fig. 7.6b and 7.7a. We checked that this angular dependence is genuine and cannot be removed by a re-parameterization with wave function renormalizations. Therefore, the resolution of the full, three-dimensional momentum dependence is necessary for quantitative accuracy. This lies in contrast to the gluonic vertices, which yield quantitatively reasonable results if their full momentum dependence is approximated with a one-dimensional momentum approximations, see Sec. 5.3.2. While the chirally symmetric tensor  $\mathcal{T}_{\bar{q}qA}^{(7)}$  takes sizable values already in the semi-perturbative regime,  $\mathcal{T}_{\bar{q}qA}^{(4)}$  is of quantitative importance only in the chirally broken phase, as can be seen from Fig. 7.6.

The channels of the four-quark interaction that are not dynamically hadronized are shown in Fig. 7.7b at the u-channel momentum configuration. Clearly, all of these channels remain finite on these Euclidean momentum configurations since the poles that correspond to the respective bound-state masses are too far away from the investigated Euclidean momentum configurations. No conclusions about the spectrum can be drawn at this stage, see [69] for dynamically hadronized vector channels.

The quark-gluon vertex running coupling is given by (7.14). It is shown along with the gluonic running couplings, defined by (5.18), in Fig. 7.8a. The Slavnov-Taylor identity for the quark-gluon vertex with a trivial quark-ghost scattering kernel implies a deviation of the quark-gluon vertex running coupling from the pure glue running couplings in the (semi-)perturbative regime. Only by including quantum corrections to the quark-ghost scattering, cf. [164, 289–292] and Sec. 7.1.4, the corresponding quantum corrections to the ghost-gluon vertex are compensated and degeneracy of all vertex running couplings is restored. The quark-gluon coupling is the most important ingredient for a quantitatively and even qualitatively correct description of spontaneous chiral symmetry breaking. In particular, the range of momenta, where it exceeds the critical value of the coupling  $\alpha_{\text{cr}} \approx 0.86$  determines, if, and to which extent, chiral symmetry breaking occurs [29, 65].

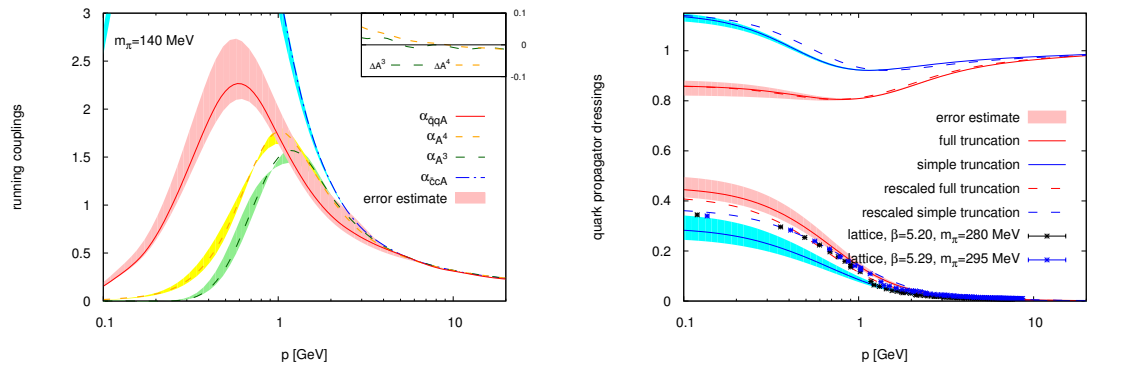


(a) Classical tensor structure  $\lambda_{\bar{q}qA}^{(1)}$  of the quark-gluon vertex as a function of orthogonal gluon and antiquark momenta. (b) Dressing functions of four-quark channels that are not dynamically hadronized. Here the same conventions as in [65] have been used for labeling the dressing functions.

Figure 7.7.: Quark-gluon and four-quark vertices.

Consequently, a precise determination of the quark-gluon running coupling is of utmost importance since the corresponding error directly translates into the quark mass function, as can be seen by comparing the bands in Fig. 7.4b and 7.8a. Although the resummation scheme, and as a consequence also the mechanism for chiral symmetry breaking, is different, an analogous sensitivity on the quark-gluon interaction strength is also found in Dyson-Schwinger studies [279].

Further results on higher-order vertex functions are presented in Fig. 7.9 and are only briefly discussed. Turning to higher quark-gluon interaction vertices, we want to highlight that this work incorporates the first direct computation of these interactions. Already earlier investigations found clear evidence for their quantitative importance [65], but inferred their value only indirectly from the quark-gluon vertex, exploiting the idea of an expansion in terms of BRST-invariant operators  $\bar{q} \not{D}^n q$ . Here we still use this idea as an organizing principle for the basis construction, see Sec. 7.1.3. The crucial improvement in comparison to [65] is the direct calculation of the corresponding dressing functions and their back-coupling into the system of equations at the symmetric momentum configuration. In comparison to the approximation used in [65], the directly calculated two-quark-two-gluon vertex leads to a moderately enhanced quark-gluon vertex. Exemplary results for the dressing functions of the two-quark-two-gluon vertex are shown in Fig. 7.9a, 7.9b and 7.9c. Furthermore, we present also exemplary results for the leading tensors in the two-quark-three-gluon vertex, see Fig. 7.9d. However, they turn out to be of sub-subleading importance for the overall system of correlation functions. These results are complemented by results on quark-meson interaction vertices in the soft-pion channel, see Fig. 7.9e. For the classical tensor  $\mathcal{T}_{\bar{q}q\pi}^{(1)}$ , see (C.8) for its definition, this is the momentum-channel that is relevant to the momentum-dependent dynamical hadronization procedure discussed in Sec. 7.1.1. Although of sub-subleading importance for the system of equations, the other momentum-dependent tensor structures of the quark-meson Yukawa interaction shown in Fig. 7.9e are important ingredients in bound-state studies, see, e.g., [18, 31, 32]. The same applies to higher-order quark-pion scattering operators, also resolved momentum-dependently and depicted in Fig. 7.9f.



(a) Running couplings as defined in (5.18) and (7.14). The inset shows the relative deviations  $\Delta\alpha_i = (\alpha_{\bar{c}cA} - \alpha_i)/\alpha_{\bar{c}cA}$  to the ghost-gluon vertex running coupling in the semi-perturbative regime. The abscissas are identical.

(b) Quark propagator dressing functions,  $M_q(p)$  (lower lines, GeV) and  $1/Z_q(p)$  (upper lines) for different truncations in comparison to lattice results [297, 298]. Here, our results have a pion mass of  $m_\pi \approx 285$  MeV.

Figure 7.8.: Running couplings and truncation dependence of the quark propagator.

### 7.3. Discussion

The main conclusion we draw from the results is that a reliable description of spontaneous chiral symmetry breaking requires very precise results on the quark-gluon interactions, see [279] for similar observations in the DSE framework. We find that the transverse running couplings defined from the different vertices deviate considerably from each other at momenta around and below the scale of QCD. We interpret this as evidence for the non-applicability of the STIs to constrain the transversely projected vertices in this regime. Unfortunately, it is difficult to find truncations that lead to a consistent (semi-)perturbative running of the matter and gauge couplings. The reason behind this is that a classification of vertices and diagrams in, e.g., loop orders is difficult to achieve within non-perturbative functional approaches. As a result, the different vertices may run with different loop orders in the (semi-)perturbative regime.

These findings emphasize the necessity for truncations that lead to a consistent running of all couplings. We find this to be a considerably harder task in unquenched QCD than in the gauge sector where consistent running is found, cf. also Chapter 5. The STIs allow to check the running of the different correlators. However, this requires the computation of their longitudinal and transverse dressings. To this end, also other functional relations such as DSEs and  $n$ PI approaches or transverse Ward-Takahashi identities (see Sec. 3.2 and [160–164]) can be employed. However, this is beyond the scope of this work.

Instead, we use the STI for the quark-gluon vertex, cf. Sec. 7.1.4, to constrain the perturbative behavior of its transversely projected classical tensor structure. In particular, we find that using the STI enforces the degeneracy of the running couplings of the matter and glue sector in the perturbative regime. In addition, we extend the truncation to include higher quark-gluon interactions, namely the two-quark-two-gluon and the two-quark-three-gluon correlators. This enables us to compute the non-perturbative features of the quark-gluon interactions in an unprecedentedly large truncation while keeping the degeneracy of the vertices in the perturbative regime intact.

This procedure yields two means to estimate the systematic error. First, we vary the transition scale down to which the STI is used to constrain the quark-gluon vertex. In line with the reasoning to determine  $\Lambda_{\text{STI}}$ , we observe sizable differences between the gluonic couplings below 3 GeV, see Fig. 7.8a. Therefore, at least two of the three gluonic couplings deviate from the STI. Thus, we vary the transition scale from STI-constrained to fully-calculated quark-gluon vertex,  $\Lambda_{\text{STI}}$ , between 3 and 7 GeV to obtain the bands. Our main results (solid lines) are obtained with  $\Lambda_{\text{STI}} = 5$  GeV.

Second, we compare our best quark propagator to one obtained with a simpler truncation, see Fig. 7.8b. The blue results are obtained in a truncation that takes only the classical tensor of the quark-gluon vertex into account. Additionally, the momentum dependence of the quark-gluon vertex is restricted to the symmetric momentum configuration. Thus, the approximation of the quark-gluon vertex is comparable to the approximation of the gluonic vertices. The difference between the blue and red result gives an estimate for the upper bound of the truncation error.

We want to point out that the difference between the bands in Fig. 7.8b makes the error estimate look worse than it is. In applications to the phase structure and the bound state spectrum, the scale is set in terms of observables. Simulating this procedure by using the lattice value of the constituent quark mass  $M_q(p)$  at  $p = 0.5$  GeV to set the scale, we obtain the dashed curves in Fig. 7.8b. The difference between the resulting quark mass functions gives a better estimate of the truncation uncertainty on observables since only relative effects are important in this case.

## 7.4. Conclusion

We investigated unquenched two-flavor QCD for various pion masses, including very small ones that are notoriously difficult to study on the lattice. The coupled system of equations for the correlation function is the largest hitherto solved. Our gluon propagator shows very good agreement with two-flavor lattice results. Furthermore, we find that the gluon propagator depends only very mildly on the pion mass which is a very welcome feature for investigations of the QCD phase structure. Our quark propagator agrees with the lattice results but suffers from large systematic errors due to the uncertainty in the quark-gluon vertex. We had to constrain the latter with its STI to ensure its correct running in the perturbative regime. At low momentum scales, the STI cannot be used to infer the strength of the transverse vertex. Therefore, we calculated the quark-gluon vertex via the flow equation in this non-perturbative regime. To conclude, the STI-consistent running of the vertices is of utmost importance for the qualitative and quantitative description of chiral symmetry breaking. Any non-perturbative truncation has to ensure a consistent running of different vertices. Finding an expansion scheme that preserves the degeneracy of the couplings in the perturbative regime without exploiting the STIs is a key issue in unquenched QCD studies within functional methods.

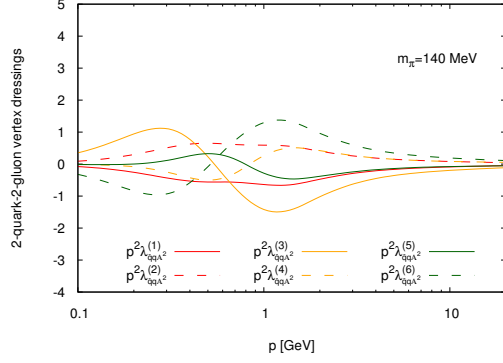
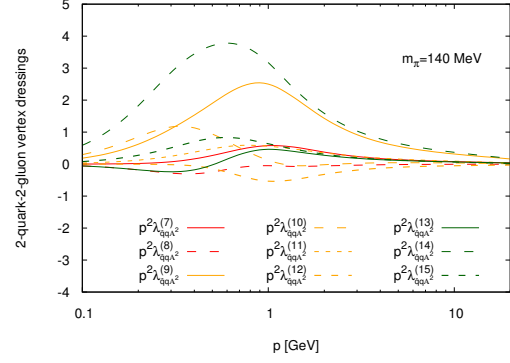
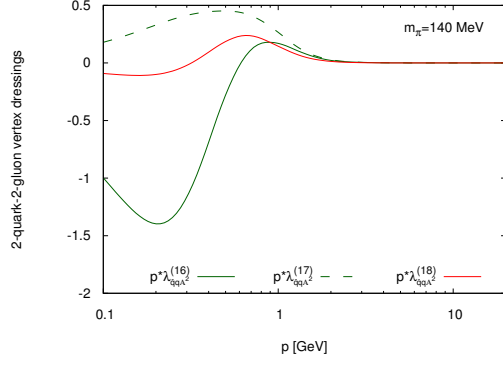
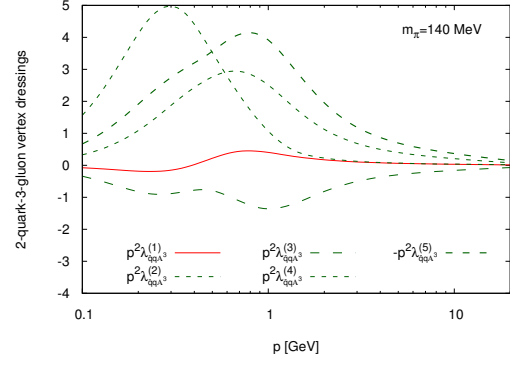
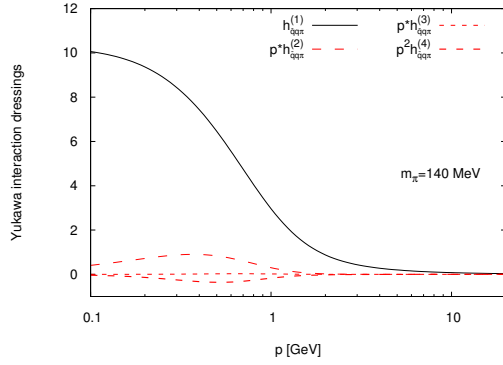
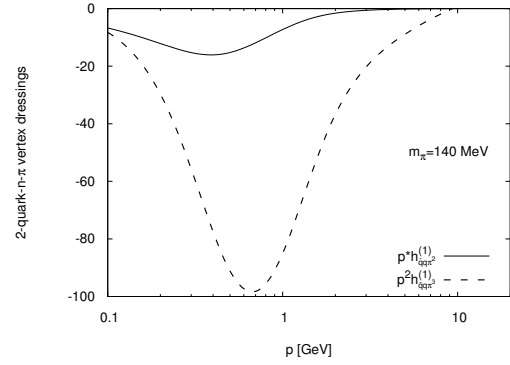
(a) Two-quark-two-gluon vertex  $\Gamma_{\bar{q}qA^2}^{(4)}(\vec{p})$ , symmetric tensors.(b) Two-quark-two-gluon vertex  $\Gamma_{\bar{q}qA^2}^{(4)}(\vec{p})$ , symmetric tensors.(c) Two-quark-two-gluon vertex  $\Gamma_{\bar{q}qA^2}^{(4)}(\vec{p})$ , symmetry-breaking tensors.(d) Two-quark-three-gluon vertex  $\Gamma_{\bar{q}qA^3}^{(5)}(\vec{p})$ .(e) Yukawa interactions  $\Gamma_{\bar{q}q\phi}^{(3)}(p, -p)$ .(f) Two-quark- $n$ -meson vertex  $\Gamma_{\bar{q}q\phi^n}^{(2+n)}(p, -p, \vec{0})$ .

Figure 7.9.: Dressing functions of the two-quark- $n$ -gluon and two-quark- $n$ -meson interactions defined in Sec. C.5. All shown dressing have been made dimensionless by multiplication with according powers of the average momentum.

## 8. Finite-Temperature Yang-Mills theory

Predictive investigations of the QCD phase structure necessitate quantitative control over the pure gauge sector. While vacuum Yang-Mills correlation functions have been studied intensively in the past, see Chapter 5 and references therein, finite-temperature propagators are scarce [302–311]. For the vertices, the situation is even less satisfactory and only exploratory studies exist [312, 313].

In this chapter we study *Non-perturbative finite-temperature Yang-Mills theory* [4] with the aim of obtaining quantitative correlation functions. These can be used to investigate, e.g., the center-symmetry phase transition via the Polyakov loop [53, 108, 109, 204–212]. Furthermore, the correlation functions allow for the computation of spectral functions and the shear viscosity [314, 315]. Also the Debye mass, which has been studied intensively on the lattice [316–319] as well as with hard thermal loop perturbation theory [320–324], can be extracted from the gluon propagator, see Sec. 8.1.3.

The zero-temperature baseline for this calculation is provided by Chapter 5. We generalize the vacuum truncation by taking into account the special direction of the thermal heat bath. In particular, we provide results for the electric and magnetic gluon propagators as well as the electric and magnetic components of the three- and four-gluon vertices. The propagators are compared to results obtained from lattice simulations. In addition, we use the Debye screening mass to determine a lower bound for the temperature range in which hard thermal loop perturbation theory can be applied straightforwardly. Furthermore, the finite-temperature behavior of the ghost-induced zero crossing of the three-gluon vertex is investigated.

This chapter is organized as follows: In Sec. 8.1 we discuss the finite-temperature vertex expansion, order parameters, and the screening mass. The peculiarities of finite-temperature flows of gauge theories are considered Sec. 8.2. Next, we present our numerical results in Sec. 8.3 and discuss them in Sec. 8.4. Finally, we summarize our findings and give an outlook in Sec. 8.5. Appendix A and B complement this chapter with technical details and numerical checks. Most of this chapter is taken from [4].

### 8.1. Temperature

We discuss the employed vertex expansion and intricacies of the expansion point in Sec. 8.1.1 and 8.1.2, respectively. The Debye mass is shown in Sec. 8.1.3.

#### 8.1.1. Finite-Temperature Vertex Expansion

We use a vertex expansion (cf. Sec. 3.1.3) about the vanishing expectation values of the gluon and ghosts fields,  $A_\mu = 0$  and  $c = \bar{c} = 0$ . These field values are solutions to the equations of motion and constitute the vacuum at vanishing temperature. At finite temperature, the vacuum  $O(4)$ -symmetry is replaced by  $\mathbb{Z}_2 \otimes O(3)$ . This reduced symmetry implies a difference between the magnetic and electric components, which correspond to

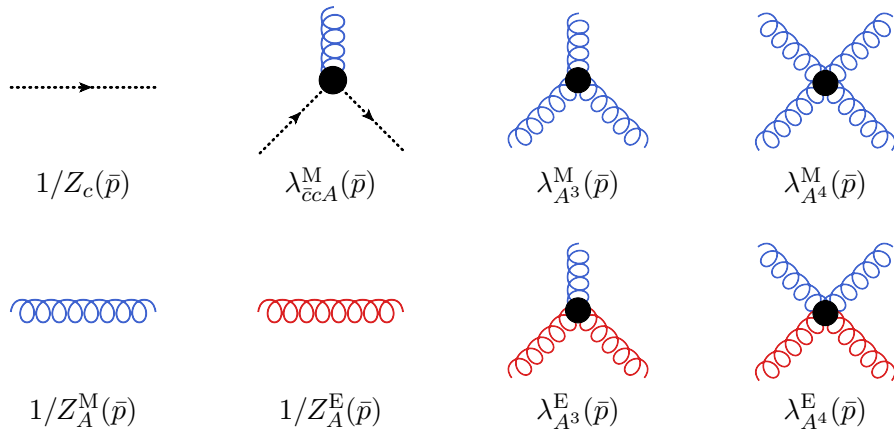


Figure 8.1.: Constituents of our vertex expansion. We use the classical tensors that are present in the bare action and attach magnetic (blue) and electric (red) projection operators to the gluon legs. Missing combinations, e.g., vertices with one electric leg, vanish if the Matsubara modes are set to zero and are not computed in our truncation.

the directions that are transverse and longitudinal with respect to the thermal heat bath. We decompose four-vectors by

$$p = \begin{pmatrix} \omega_n \\ \vec{p} \end{pmatrix} = \begin{pmatrix} 2\pi T n \\ \vec{p} \end{pmatrix},$$

where  $n \in \mathbb{Z}$  are the discrete Matsubara modes and  $\omega_n = 2\pi T n$  the corresponding frequencies. This leads to the magnetic and electric projection operators at finite temperature,

$$\Pi_{\mu\nu}^M(p) = (1 - \delta_{0\mu})(1 - \delta_{0\nu}) \left( \delta_{\mu\nu} - \frac{p_\mu p_\nu}{p^2} \right),$$

$$\Pi_{\mu\nu}^E(p) = \Pi_{\mu\nu}^\perp(p) - \Pi_{\mu\nu}^M(p), \quad (8.1)$$

where  $\Pi_{\mu\nu}^\perp(p) = \delta_{\mu\nu} - \frac{p_\mu p_\nu}{p^2}$  is the transverse projection operator, see (2.13). A crucial consequence of the breaking of the vacuum  $O(4)$ -symmetry by (8.1) is the splitting of Lorentz tensors into electric and magnetic components. In particular, the propagators are given by

$$\begin{aligned} [\Gamma_{AA}^{(2)}]_{\mu\nu}^{ab}(p) &= \delta^{ab} p^2 [Z_A^M(p) \Pi_{\mu\nu}^M(p) + Z_A^E(p) \Pi_{\mu\nu}^E(p)], \\ [\Gamma_{\bar{c}c}^{(2)}]^{ab}(p) &= \delta^{ab} p^2 Z_c(p), \end{aligned} \quad (8.2)$$

with dimensionless scalar dressing functions  $1/Z_A^M$  and  $1/Z_A^E$  for the magnetic and electric components of the gluon propagator. As in Chapter 5, we take all tensors present in the classical action into account. As for the gluon propagator, we split their dressings into electric and magnetic components. See Fig. 8.1 for an illustration of the constituents of our truncation and Appendix A for further details. As a consequence of the restriction to classical tensors, the tensor bases of the gluonic vertices are incomplete. Thus, the projection of the tensor equations onto the scalar dressing functions is not unique, cf. Sec. C.2. We use vacuum calculations to identify uncertainties that stem from the projections in order to disentangle them from finite-temperature effects, which is detailed in Sec. A.3.



### Momentum Dependence

Due to the breaking of  $O(4)$ -invariance, the dressings depend in general on the Matsubara modes and spatial momenta separately, e.g.,  $Z(p) = Z(\omega_n^2, \vec{p}^2)$  for a generic wave function renormalization  $Z$ . However, the thermal contributions to the correlation functions decay rapidly for spatial momenta and frequencies that fulfill  $p^2 \gtrsim (2\pi T)^2$ . Hence, the thermal correlation functions converge quickly towards their  $O(4)$ -symmetric vacuum counterparts for these momenta, see, e.g., Fig. 8.5 and 8.7. Consequently, the correlation functions exhibit an approximate  $O(4)$ -symmetry for all higher Matsubara modes, and most of the finite temperature effects are encoded in the zero mode at small spacial momenta  $\vec{p}^2 \lesssim (2\pi T)^2$ . Therefore, the spatial momentum dependence of the Matsubara zero modes can be used to obtain a very good approximation of the full frequency and momentum dependence via

$$Z(\omega_n^2, \vec{p}^2) \approx Z(0, \omega_n^2 + \vec{p}^2), \quad (8.3)$$

or in short  $Z(p) = Z(0, p^2)$ . In this work we compute the zero modes of the propagators and employ (8.3) to close the equations. This  $O(4)$ -symmetric approximation has been found to be quantitatively reliable for gluon [252, 302] as well as quark propagators [307].

This pattern carries over to the scalar dressings of higher order correlation functions  $\lambda^{(n)}(p_1, \dots, p_n)$ . Analogously to the propagator dressings, we base our computation on the zero modes

$$\lambda^{(n)}(\vec{p}_1, \dots, \vec{p}_n) = \lambda^{(n)}(\omega_{n_1} = 0, \vec{p}_1, \dots, \omega_{n_n} = 0, \vec{p}_n).$$

In contradistinction to the propagator dressings, the zero modes of the vertex dressings  $\lambda^{(n)}$  depend on all  $\vec{p}_i \cdot \vec{p}_j$  and not only  $\vec{p}^2$ . However, the spatial momentum dependence of the vertices is well described by a one-dimensional symmetric-point approximation in four as well as three dimensions [272, 273], see Sec. 5.3.2. This leads to

$$\lambda^{(n)}(\vec{p}_1, \dots, \vec{p}_n) \approx \lambda^{(n)}(\bar{p}), \quad \bar{p}^2 \equiv \frac{1}{n} \sum_{i=1}^n \vec{p}_i^2, \quad (8.4)$$

which allows to compute the flows of the zero modes of the vertex dressings in a quantitatively reliable approximation, cf. the right panel of Fig. 5.8. However, the flows of the zero modes depend on the full frequency and spatial momentum dependence. Analogously to the propagator dressings, we approximate the full momentum dependence with an  $O(4)$ -symmetric generalisation of (8.4),

$$\lambda^{(n)}(\omega_{n_1}, \vec{p}_1, \dots, \omega_{n_n}, \vec{p}_n) \approx \lambda^{(n)}(\bar{p}), \quad (8.5)$$

where the symmetric momentum  $\bar{p}$  is then given by

$$\bar{p}^2 \equiv \frac{1}{n} \sum_{i=1}^n (\omega_{n_i}^2 + \vec{p}_i^2).$$

In summary, we use two quantitatively reliable approximations for the dressing functions: the approximate  $O(4)$ -invariance of all non-vanishing Matsubara modes which allows using only information from the lowest Matsubara mode, and the well-tested symmetric momentum approximation. This truncation generalizes the symmetric momentum vacuum truncation used in Chapter 5, see Appendix B for an explicit numerical check.

### 8.1.2. Non-Trivial Vacuum and Backgrounds

As discussed in the last section, we use a vertex expansion about vanishing field expectation values  $A_\mu = 0$  and  $c = \bar{c} = 0$ . This necessitates a thorough discussion of the implications of this choice, in particular for comparisons to lattice results. We argue that such an expansion about vanishing background fields leads to correlation functions that agree with the lattice correlators for temperatures outside a small region around the phase transition. Furthermore, even near the phase transition, sizable effects are mainly expected for correlation functions that have electric gluon legs such as the electric gluon propagator. This becomes most evident by investigating the relation of the physical solution of the equation of motion in non-vanishing gluon background fields and the Polyakov loop, the canonical order parameter of the confinement-deconfinement phase transition. For convenience of the reader, the first two parts briefly review corresponding relevant advances in functional approaches [53, 108, 109, 204–212, 305].

#### Correlation Functions

To facilitate the discussion, we use the background extension of Landau gauge,

$$(\partial_\mu - ig\bar{A}_\mu) a_\mu = 0 \quad \text{with} \quad A_\mu = \bar{A}_\mu + a_\mu,$$

called Landau-deWitt gauge. Here,  $\bar{A}_\mu$  is a general background and  $a_\mu$  is the quantum fluctuation field. In this formulation, the effective action is gauge invariant under background gauge transformations, which allows for a simpler interpretation of physical backgrounds and simpler technical implementations. Besides being a functional of the superfield  $\Phi = (a, \bar{c}, c)$ , the effective action in Landau-deWitt gauge depends also on the background  $\bar{A}$ . Accordingly, the vertices  $\Gamma^{(n)}[\bar{A}, \Phi]$  are correlation functions in the background,

$$\Phi = \langle \varphi \rangle_{J(\bar{A}, \Phi)}.$$

The background current  $J(\bar{A}, \Phi)$  satisfies  $J(\bar{A}, \Phi) = \delta\Gamma/\delta\Phi$ . The correlation functions in the absence of external sources,  $J(\bar{A}, \Phi) = 0$ , are then given by  $\Gamma^{(n)}[\bar{A}, \Phi_{\text{EoM}}]$ , where  $\Phi_{\text{EoM}}$  is a solution of the equation of motion in the chosen background  $\bar{A}$ ,

$$\left. \frac{\delta\Gamma[\bar{A}; \Phi]}{\delta\Phi} \right|_{\Phi_{\text{EoM}}} = 0. \quad (8.6)$$

In general, this conditions yields stationary points of the effective action. In particular, the expansion point  $(\bar{A}, \Phi) = 0$  satisfies (8.6), but does not necessarily single out the physical minimum. Contrarily, the physical correlators that correspond to scattering amplitudes are obtained at the physical solution of the equation of motion (8.6), i.e., at the minimum of the effective action  $(\bar{A}, \Phi_{\text{min}}[\bar{A}])$ . This is also the field value about which the vertex expansion is expected to be most stable and converge most rapidly. Furthermore, only an expansion around the physical solution of the equation of motion allows for a direct comparison with correlation functions from lattice simulations since the latter are measured on the physical ground state. In general, any other expansion point requires information about higher correlation functions in order to evaluate  $\Gamma^{(n)}[\bar{A}, \Phi_{\text{min}}]$ . In particular, in a vertex

expansion with expansion point  $(\bar{A}, \Phi) = 0$ , the inverse propagator is given by

$$\Gamma_{\Phi_k \Phi_l}^{(2)}[\bar{A}, \Phi_{\min}] = \sum_{n=0}^{\infty} \sum_{|n_{\Phi}|=n} \frac{1}{n_{\Phi}!} \not\sum_{p_1, \dots, p_n} \Gamma_{\Phi_k \Phi_l \Phi_{i_1} \dots \Phi_{i_n}}^{(2+n)}[\bar{A}, 0] \times \Phi_{i_1, \min} \dots \Phi_{i_n, \min}. \quad (8.7)$$

Therefore, we expect deviations between the correlation functions  $\Gamma^{(n)}[0, 0]$ , computed in this work, and those from lattice simulations. However, these differences are sizable only if the momentum scales of the solution  $(\bar{A}, \Phi_{\min}) \neq 0$  are of the same order as  $T_c$ , the characteristic scale of the finite-temperature Yang-Mills system. Only in this case, the higher correlation functions would lead to noticeable contributions in (8.7).

We can utilize the background field to achieve a technical simplification. Since it is arbitrary, we can choose  $\bar{A} = \bar{A}_{\min} \equiv \langle \bar{A} \rangle$  such that

$$\Phi_{\min}[\bar{A}_{\min}] = 0.$$

For this particular choice, the background carries all the non-trivial information about the ground state whereas the (classical) fluctuation field vanishes on the equation of motion. The physical correlators are then given by  $\Gamma^{(n)}[\langle \bar{A} \rangle, 0]$ . In particular, the inverse propagator (8.7) for the gluon is then given by

$$\Gamma_{AA}^{(2)}[\bar{A}, \Phi_{\min}] = \Gamma_{AA}^{(2)}[\langle \bar{A} \rangle, 0].$$

Semi-perturbative studies in the Curci-Ferrari model for Yang-Mills theory confirm that the background has large effects on the electric propagator at temperatures close to the phase transition [305]. Furthermore, the calculation of quantitatively correct values for the chiral phase transition temperature as well as its observed coincidence with the confinement-deconfinement crossover temperature requires taking into account such a non-trivial minimum [53]. Finally, such a consistent treatment was also required for the description of the Roberge-Weiss transition [53] as well as the study of criticality in  $SU(2)$  Yang-Mills theory [204].

### Order Parameters

A further advantage of the background  $\langle \bar{A} \rangle$  is its relation to the Polyakov loop [53, 108, 109, 206], the standard order parameter of the confinement-deconfinement phase transition. The traced Polyakov loop is expressed as a correlator of the temporal gauge field by

$$L[A_0] = \frac{1}{N_c} \text{Tr} P[A_0],$$

$$P[A_0] = \mathcal{P} e^{ig \int_0^\beta dt A_0(t, \vec{x})} \equiv e^{2\pi i \varphi[A_0]},$$

where  $\mathcal{P}$  stands for path ordering. The functional  $\varphi[A_0]$  is the gauge-covariant algebra element of the Polyakov loop. It transforms as  $\varphi \rightarrow U \varphi[A_0] U^\dagger$  under time-periodic gauge transformation  $U \in SU(N)$ . This entails that the eigenvalues of  $\varphi[A_0]$  are gauge invariant, and consequently the eigenvalues of its expectation value  $\bar{\varphi} \equiv \langle \varphi[A_0] \rangle$  are observables. This expectation value, as well as  $L[\langle \varphi \rangle]$ , are order parameters for the confinement-deconfinement phase transition. In Polyakov gauge, the expectation value of the algebra element takes the particularly simple form

$$\bar{\varphi} = \beta g \bar{A}_0,$$

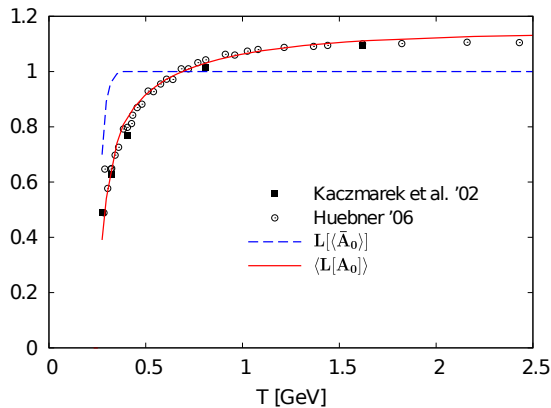


Figure 8.2.: Expectation value of  $\langle L[A_0] \rangle$  versus  $L[\langle \bar{A}_0 \rangle]$ , taken from [206]. Both observables are order parameters for the confinement-deconfinement phase transition. Moreover,  $L[\langle \bar{A}_0 \rangle] = 1$  entails  $\langle \bar{A}_0 \rangle = 0$ .

for a given background  $\bar{A}_0$ . Due to background gauge invariance, the eigenvalues of  $\bar{\varphi}$  can be calculated from the eigenvalues of  $\bar{A}_0$  in any background gauge. In particular, the effective potential  $V[\bar{A}_0]$  of Landau-deWitt gauge carries the full information about the eigenvalues of the expectation value of  $\varphi$ .

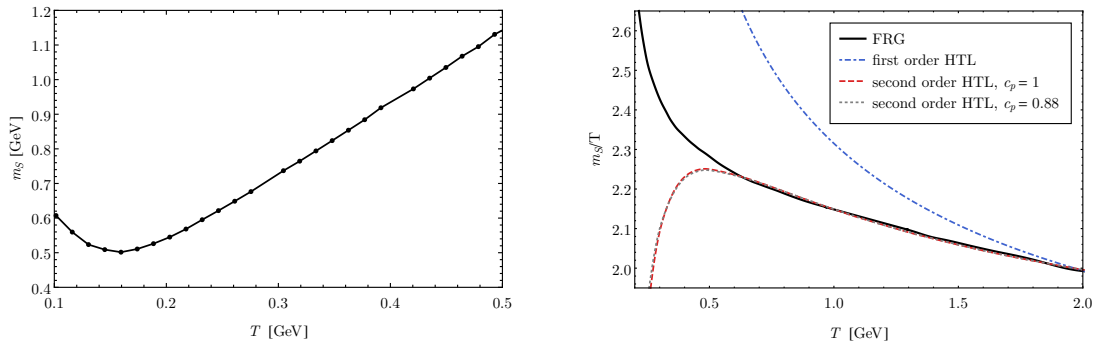
In conclusion, the effective potential  $V[\bar{A}_0]$  is an order parameter potential for center symmetry. The gauge invariant observables,  $\langle L[A_0] \rangle$  and  $L[\langle \bar{A}_0 \rangle]$ , or equivalently also  $\langle \bar{A}_0 \rangle$ , serve as order parameters for the confinement-deconfinement phase transition, see Fig. 8.2. Therefore, the vanishing of  $\langle L[A_0] \rangle$  in the confined phase relates to a non-vanishing value for  $\langle \bar{A}_0 \rangle$ . This has recently been demonstrated explicitly by the first computation of  $\langle L[A_0] \rangle$  within functional methods [206]. Finally, the electric propagator  $\langle A_0(p)A_0(-p) \rangle$  is closely related to the propagator of an order parameter field, and as such should show critical properties, see [109]. Hence, we expect the electric correlators to be affected most by the background field.

### Comparison to Lattice Simulations

The previous discussion of the non-trivial  $\bar{A}_0$  background and its relation to the order parameters of the confinement-deconfinement phase transition allows to derive a theoretical estimate of the temperature range, in which our present results potentially deviate from the respective lattice results due to the different background configurations. The first important piece of information is given by the fact that the order parameter  $L[\langle \bar{A}_0 \rangle]$  approaches unity rapidly for temperatures above the phase transition temperature, as shown in Fig. 8.2. Contrarily, the Polyakov loop  $\langle L[A_0] \rangle$ , which is usually calculated in lattice simulations, reaches its asymptotic value only for  $T \gg T_c$ , which can be understood from fluctuation effects [206]. The fact that  $L[\langle \bar{A}_0 \rangle]$  quickly approaches unity above the transition temperature can be formulated as the more precise statement,

$$\langle \bar{A}_0 \rangle \approx 0 \quad \text{if} \quad T \gtrsim 1.3 T_c.$$

As a consequence, we can expect quantitative effects due to the non-trivial background only at temperatures  $T \lesssim 1.3 T_c$ . The most immediate effect of this non-trivial background is a shift in the Matsubara frequencies  $\omega_n \rightarrow \omega_n \pm 2\pi T \nu_i$ , where  $\nu_i$  are the eigenvalues of  $\bar{\varphi}$ ,



(a) Screening mass  $m_s$  in units of GeV at low temperatures. (b) Dimensionless Debye screening mass  $m_s/T$  at high temperatures in comparison with first (8.12) and second (8.13) order perturbation theory [320].

Figure 8.3.: Debye screening mass  $m_s$ , see Fig. 8.4 for the fits of (8.11) to  $G_T(x)$ .

or equivalently of  $\beta g \langle \bar{A}_0 \rangle / (2\pi)$ . Rotating the constant field into the Cartan sub-algebra, these are given by

$$\begin{aligned} \nu_{SU(2)} &= \{0, \pm\varphi_3\}, \\ \nu_{SU(3)} &= \left\{0, 0, \pm\varphi_3, \pm\frac{\varphi_3 \pm \sqrt{3}\varphi_8}{2}\right\}, \end{aligned} \quad (8.8)$$

for  $SU(2)$  and  $SU(3)$ , see, e.g., [206]. However, for  $T \lesssim 0.5 T_c$  the effect of the shifts of the Matsubara frequencies is suppressed by the zero temperature gapping  $m_{\text{gap}}$  of the gluon propagator  $2\pi\nu_i T / m_{\text{gap}} \ll 1$ . Therefore, we expect sizable effects due to the non-trivial background only in the regime

$$T \in (0.5 T_c, 1.3 T_c), \quad (8.9)$$

and in particular in the electric gluon propagator.

### 8.1.3. Debye Screening Mass

Gluons are screened at zero as well as at finite temperature. Our non-perturbative results allow extracting a screening mass. We compute it from the zero mode of the electric gluon propagator  $G_T^E(p) = 1/(p^2 Z_A^E(p))$  whose computation is detailed below in Sec. 8.2. To this end, we Fourier transform the propagator,

$$G_T^E(x) = \int_{-\infty}^{\infty} \frac{dp}{2\pi} G_T^E(p) e^{ipx}. \quad (8.10)$$

At high temperatures, the propagator shows an exponential decay at large distances,

$$\lim_{x \rightarrow \infty} G_T^E(x) = c_e \exp(-m_s x). \quad (8.11)$$

The screening mass  $m_s$  obtained by fitting (8.11) to  $G_T^E(x)$  is shown in Fig. 8.3. The left panel shows that the screening mass is finite across the phase transition and possesses a minimum at some finite temperature. Perturbatively, the Debye mass is given by

$$m_D^0 = \sqrt{\frac{N}{3}} g_T T + \mathcal{O}(g_T^2 T), \quad (8.12)$$

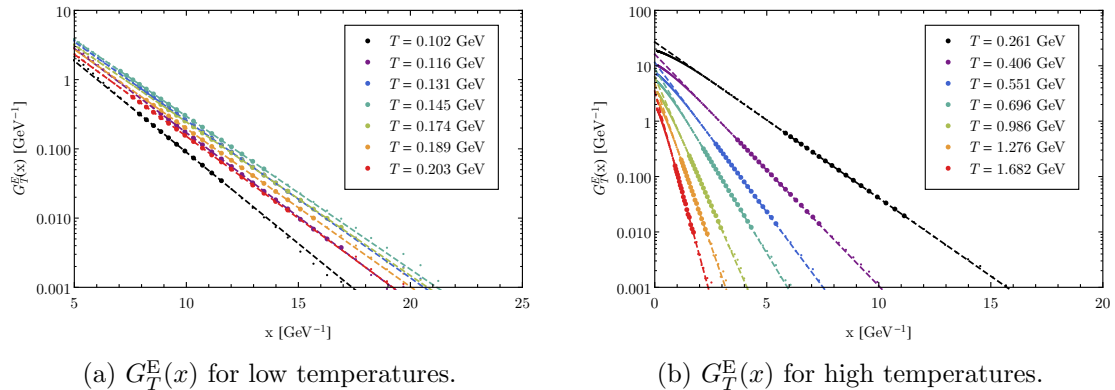


Figure 8.4.: Exponential tail of the Fourier transformed electric propagator,  $G_T^E(x)$ , given by (8.10). See Fig. 8.5b for the original propagator in momentum space. The dashed lines are fits of (8.15) with  $c_a = 0$ , i.e., (8.11), to the large points. Small points show  $G_T^E(x)$  beyond the fit regions.

and to second order by [320]

$$m_D = m_D^0 + \left( c_D + \frac{N}{4\pi} \ln \left( \frac{m_D^0}{g_T^2 T} \right) \right) g_T^2 T + \mathcal{O}(g_T^3 T). \quad (8.13)$$

In order to compare our screening mass to the perturbative expressions (8.12) and (8.13), we have to determine  $g_T$  and  $c_D$ . We use

$$g_T = \sqrt{4\pi \alpha_{A^3}^E(T, p = c_p 2\pi T)}, \quad (8.14)$$

where  $\alpha_{A^3}^E$  is the (electric) coupling of the three-gluon vertex. We fit  $c_D$  at large temperatures to our result because it is not computable within perturbation theory.

As shown in Fig. 8.3b, the second-order electric Debye mass agrees almost perfectly with our non-perturbative result down to  $T \approx 0.6$  GeV. In contrast, the first-order perturbative Debye mass deviates instantly from our result. By default, we set  $c_p = 1$  in (8.14) because this is the scale that is expected to contribute most. This yields for the non-perturbative constant  $c_D = 0.100(3)$ . To substantiate the choice  $c_p = 1$ , we also leave it as a free fit parameter and find  $c_p = 0.88(64)$ , where the non-perturbative constant  $c_D = 0.105(30)$  changes only within the fit uncertainties. The effect on the perturbative Debye mass is negligible, see Fig. 8.3b. The excellent agreement at very high temperatures provides a non-trivial check of our calculation. Further physical consequences are discussed in Sec. 8.4.2.

We close this section with a short discussion on the screening mass at very low temperatures not shown in Fig. 8.3. In general, the thermal propagators at large distances show a combination of an exponential and an algebraic decay,

$$\lim_{x \rightarrow \infty} G_T^E(x) = c_a x^{1-4\kappa} + c_e \exp(-m_s x). \quad (8.15)$$

The algebraic decay originates from the infrared scaling at vanishing temperature with  $1 - 4\kappa$  being the scaling exponent in position space, cf. (6.1). At low enough temperatures  $T \ll T_c$ , we see remnants of this zero-temperature algebraic part. At higher temperatures we have  $c_a = 0$ , i.e., (8.11).

In Fig. 8.4, we show  $G_T^E(x)$  for low (left panel) and high (right panel) temperatures. For all shown temperatures, the exponential decay is apparent as linear regime. For even lower temperatures, the linear regime shrinks considerably due to the algebraic decay, and we need a higher numerical precision for extracting the then sub-leading exponential decay. This is clearly seen in the lowest temperature shown,  $T = 0.102$  GeV.

## 8.2. Finite-Temperature Flows

In this section we first introduce the flow equation at finite temperature. We then discuss the implications of the regulator term and the gluon mass parameter at finite temperature.

### 8.2.1. Flow Equations

For the pure gauge theory at finite temperature, the Wetterich equation reads

$$\partial_t \Gamma_k[\Phi] = \sum_q \frac{1}{2} G_{k,\mu\nu}^{ab}[\Phi] \partial_t R_{k,\nu\mu}^{A,ba} - \sum_q G_k^{ab}[\Phi] \partial_t R_k^{c,ba}. \quad (8.16)$$

Using the Matsubara formalism, the momentum integrals in (8.16) are given by

$$\sum_q = \int \frac{d^3 q}{(2\pi)^3} T \sum_n,$$

where  $q_0 = 2\pi T n \equiv \omega_n$  since both gluon and ghost fields have symmetric boundary conditions, see, e.g., [78]. The regulators  $R_k$  in (8.16) can be chosen very similarly to the regulators at zero temperature, see Sec. C.3 for details. The flow equations for the correlation functions are obtained by taking functional derivatives of (8.16). Diagrammatically, they are identical to the vacuum equations shown in Fig. 5.4. The only difference is that gluon lines now represent sums over electric and magnetic propagators, cf. (8.2), which are connected to the corresponding magnetic and electric components of the vertices.

Instead of the flat regulator used in the beginning of Chapter 5, we use an exponential regulator. As demonstrated in Sec. 3.1.2, the results for the correlation functions do not depend on this choice within our error bars. However, analytic regulators such as the exponential regulator are better suited for numerical calculations of thermodynamic quantities since they carry the thermal exponential decay with the cutoff scale  $\sim e^{-ck/T}$  in the flow [252, 302], see [325] for a detailed study.

For the numerical implementation we employ the workflow described in Sec. C.1. In the remaining part of this section we comment on details specific to this application. To reduce the numerical effort of the finite-temperature calculation, we exploit the degeneracy of the dressings for  $k \gg 2\pi T$ . We integrate the finite-temperature flows starting from the non-trivial vacuum effective action at

$$\Lambda_T = \max(\lambda 2\pi T, \Lambda_T^{\min}),$$

with  $\lambda = 4$  and  $\Lambda_T^{\min} = 1$  GeV. We check the independence of the effective action from the initial cutoff scale and provide further details in Sec. B.2.

In the derivation of the equations, tracing the four-gluon vertex equation, and in particular the gluon box diagrams, is the most challenging part. To this end, we generate

FORM [171–174] files with FormTracer [2] for each of the twelve permutations of the box diagrams. Executing one of these with FORM can take up to eight core days and intermediate expressions reach more than 1 TB in size. Since the resulting expressions are still very large, we sum all permutations, factorize all dressing functions and then use the simultaneous optimization feature of FORM’s optimization routine [173] in combination with a parallelized version of FORM [326] to optimize the result. Concerning the numerical computation, integrating the flow once takes roughly one day on an ordinary quad-core desktop computer. This has to be done multiple times for each temperature due to the gluon mass parameter.

### 8.2.2. Renormalization and mSTIs

As discussed in great detail in the previous chapters, the regulator leads to modified Slavnov-Taylor identities (mSTIs) for non-vanishing RG scales,  $k > 0$ , that reduce to the standard STIs in the limit  $k \rightarrow 0$  [1, 25, 154–159]. Thus, the underlying BRST symmetry is restored. We emphasize that any regularization scheme in momentum space leads to such a modification of BRST symmetry in terms of modified STIs. This is also well-known from perturbation theory, where a cutoff regularization, among other modifications, requires a gluon mass counter term in order to guarantee gauge invariance. Modified STIs are also present within other functional methods such as non-perturbative DSE and  $n$ PI approaches that rely on numerical momentum integration.

As in Chapter 5, we choose constant vertex dressings  $\lambda_{\bar{c}cA}$ ,  $\lambda_{A^3}$  and  $\lambda_{A^4}$  at the cutoff scale,  $k = \Lambda$ , such that the STIs for the running couplings,

$$\alpha_{\bar{c}cA}(\mu) = \alpha_{A^3}(\mu) = \alpha_{A^4}(\mu) \equiv \alpha(\mu),$$

are fulfilled at  $\mu = 20 \text{ GeV}$ ,  $k = 0$ . This takes the modification of the vertex STIs (5.17) into account. The running couplings are defined as in the vacuum, see (5.18). We always choose  $\mu \gg 2\pi T$  such that the magnetic and electric wave functions renormalizations are identical and the running coupling definitions are unique.

As explained in Chapter 5, the mSTI of the gluon propagator implies a non-vanishing longitudinal gluon mass term at the cutoff scale [154] (where longitudinal refers to Landau gauge, not the thermal heat bath). In the perturbative regime, it can be shown that the transverse mass agrees with the longitudinal one. However, while the longitudinal mass parameter vanishes at  $k = 0$ , the transverse mass term encodes the gapping of the transverse gluon propagator at  $k = 0$ . At the initial ultraviolet cutoff scale  $k = \Lambda$  the gluon mass parameter is uniquely determined by the mSTI and cannot be chosen freely. Its precise determination is at the root of confinement, which is encoded in the transverse mass gap at vanishing cutoff scale. Since the mass parameter is proportional to the cutoff,  $m_\Lambda^2 \propto \alpha(\Lambda) \Lambda^2$ , quadratic precision is required in its determination from the mSTI. The solution of this quadratic fine-tuning problem requires both a BRST-consistent quantitative level of the approximation and sufficient numerical precision. Consequently, in truncated systems of flow equations, its computation from the mSTI at the required precision level is extremely challenging.

In this chapter we use that it is possible to uniquely determine the gluon mass parameter by demanding a scaling solution. We exploit that this also holds at finite temperature. Requiring scaling in the magnetic sector provides us with a unique value for the gluon mass parameter at each temperature. This procedure resolves the necessity of a BRST-



consistent level of the approximation, but still requires quadratic precision in the fine-tuning. The details are discussed in the following Sec. 8.2.3 that can be safely skipped by non-expert readers.

### 8.2.3. Gluon Mass Parameter

The gluon mass parameter is fixed at the cutoff scale  $k = \Lambda$  which is far bigger than the temperature scale,  $\Lambda \gg 2\pi T$ . Temperature effects are exponentially suppressed for the used regulators [325]. Hence, the initial conditions for the flow at  $k = \Lambda$  converge exponentially to that at vanishing temperature. However, in the present scaling solution the initial conditions compensate for the violation of the modified BRST symmetry during the flow, and in particular at low cutoff scales. Therefore, we expect a temperature-dependent change of the initial conditions for compensating temperature-dependent truncation artifacts at low scales. Keeping this in mind, we extend the BRST-consistent fine-tuning of the initial conditions to finite temperature,

$$\Gamma_{AA,k=\Lambda_T}^{(2),M,\text{raw}}(p) = \Gamma_{AA,k=\Lambda_T}^{(2),E,\text{raw}}(p) = \Gamma_{AA,k=\Lambda_T}^{(2),T=0}(p) + \Delta m_T^2. \quad (8.17)$$

The temperature-dependent part of the gluon mass parameter  $\Delta m_T^2$  is fixed such that we obtain infrared scaling in the purely magnetic sector. Its sole purpose is to adjust the modified BRST symmetry as in the  $T = 0$  case. Requiring scaling fixes  $\Delta m_T^2$  uniquely. While adjusting the correct infrared behavior, this introduces truncation artifacts in the ultraviolet. The RG-relevant part of the temperature dependence at large momentum has to vanish identically. It is uniquely removed with

$$\Gamma_{AA,k=0}^{(2),M/E} = \Gamma_{AA,k=0}^{(2),M/E,\text{raw}} - \left( \Gamma_{AA,k=k_T}^{(2),M/E,\text{raw}} - \Gamma_{AA,k=k_T}^{(2),T=0} \right), \quad (8.18)$$

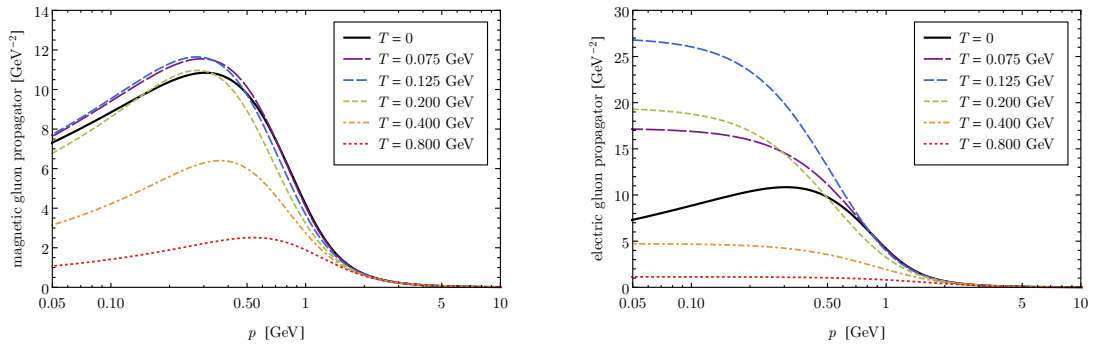
where  $k_T \approx 4\pi T \leq \Lambda_T$  is the scale above which temperature effects are absent, i.e.,

$$\Gamma_{AA,k \geq k_T}^{(2),M,\text{raw}} = \Gamma_{AA,k \geq k_T}^{(2),E,\text{raw}}.$$

Note that (8.18) keeps the physical temperature-dependent polynomially suppressed large momentum corrections. Equation (8.18) removes in particular  $\Delta m_T^2$  from the final result. The mass correction (8.17) leads to modifications of the flows due to the back coupling of the changed gluon mass parameter. Consequently, the subtraction (8.18) removes back-coupling artifacts that are accumulated during the integration of the flow from  $\Lambda_T$  to  $k_T$ . In the case  $\Lambda_T = k_T$ , no back-coupling artifacts are created at scales larger than  $k_T$  and the correction becomes trivial,

$$\Gamma_{AA,k=k_T}^{(2),M/E,\text{raw}} - \Gamma_{AA,k=k_T}^{(2),T=0} = \Delta m_T^2.$$

We demonstrate in Sec. B.2, Fig. B.1b, that neither the raw nor the final gluon propagators, obtained with (8.18), depend on the initial cutoff scale  $\Lambda_T$ . Thus,  $\Lambda_T = k_T$  is the numerically least demanding and most stable choice that includes all thermal fluctuations. Note that (8.17) modifies the magnetic and electric propagators identically. Thus, the electric mass is an observable at vanishing cutoff. We investigate the effects of (8.18) in Appendix B.



(a) Magnetic gluon propagator,  $1/(p^2 Z_A^M(p))$ . (b) Electric gluon propagator,  $1/(p^2 Z_A^E(p))$ .

Figure 8.5.: Gluon propagator, (8.2).

### 8.3. Results

The main results are displayed in Fig. 8.5 – 8.11. We show results for the magnetic and electric dressing functions of propagators and vertices for various temperatures. The magnetic and electric dressings coincide for momenta  $p \gg 2\pi T$ , and become degenerate with the vacuum dressings. This is required by the recovery of  $O(4)$ -invariance. The convergence towards the vacuum dressings for small temperatures is explicitly checked in Sec. B.1. This apparently obvious property is non-trivial within frequency and momentum-dependent non-perturbative truncations.

At low momenta  $p \ll 2\pi T$  the dimension of the theory is effectively reduced and the magnetic dressings behave as they do in three dimensions. In the case of the scaling solution, all magnetic dressing functions scale with a power-law that is known for general dimensions [217–219], see Sec. 6.2.2. The different scaling in four and three dimensions is best seen from Fig. 8.6a. Due to dimensional reduction, the temperature-independent scaling coefficient  $\kappa$  is determined by three-dimensional Yang-Mills theory. Fitting the magnetic gluon propagators to (6.1) with  $d = 3$  at  $p \ll 2\pi T$ , we find  $\kappa = 0.323(3)$ . This agrees with the scaling exponent  $\kappa = 0.321(1)$  of the three-dimensional vacuum theory found in Chapter 6. We summarize the scaling exponents in Table 8.1.

#### 8.3.1. Propagators

As is clearly seen from Fig. 8.5, the electric and magnetic gluon propagators show a qualitatively different behavior at low momenta. While the magnetic gluon propagator decreases

	simple vertices	symmetric momentum approximation	full momentum dependence
$d = 4$	0.5953 [118, 119, 121]	0.567(3)	0.576(5)
$d = 3$	0.3976 [118]	0.321(1)	×
$d = 4, T > 0$	×	0.323(3)	×

Table 8.1.: Scaling exponents. The symmetric momentum approximation is defined in Sec. 8.1.1, see Fig. 5.8 for its effect in the vacuum.

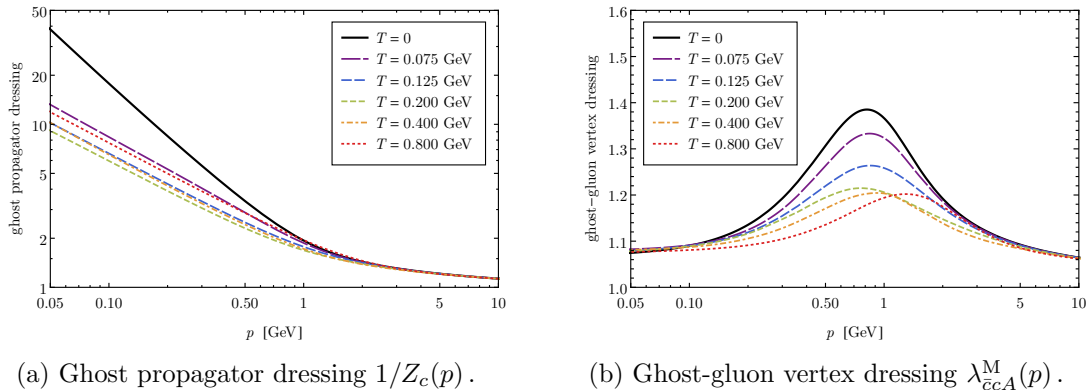


Figure 8.6.: Ghost propagator, (8.2), and magnetic ghost-gluon vertex, (A.1).

almost monotonously with increasing temperature, the electric gluon propagator increases at small temperatures. At high temperatures, where the growth of thermal contributions to the mass becomes dominant, see Fig. 8.3, also the electric gluon propagator decreases.

We compare our gluon propagators to  $SU(2)$  [250, 309] and  $SU(3)$  [311] lattice results in Fig. 8.9 and 8.10. This comparison requires the setting of a relative scale as well as renormalization of the lattice results, detailed in Sec. C.4. As a consequence, a potential relative offset of functional and lattice results has to be considered in addition to the systematic errors of the truncation when juxtaposing the results from the different calculations. The comparison with  $SU(2)$  as well as  $SU(3)$  lattice data is legitimate because the employed truncation – although being state-of-the-art – yields only a trivial dependence on the gauge group as explained in Sec. 5.4.1. This changes immediately once a background field is introduced since the group structure then enters via the Cartan sub-algebra, cf. (8.8). We emphasize that the effects of the background field are significant only at temperatures close to the phase transition temperature, see (8.9).

For the magnetic gluon propagator we find agreement with the lattice results on the 10% accuracy level we expect from the truncation of the vertices. Furthermore, we see that the deviation assumes its maximum for temperatures about the phase transition temperature where we expect large-scale dynamical fluctuations to be most relevant. On the one hand, our truncation is tested maximally in this regime. On the other hand, discretization and finite volume effects in the lattice calculation are strongest there. In contradistinction to the very satisfactory situation for the magnetic propagator, we observe a significant deviation of the electric gluon propagator for temperatures about the phase transition temperature  $T_c$ . However, the agreement is very good for small and large temperatures. As discussed in great detail in Sec. 8.1.2 and 8.4, the deviation about  $T_c$  can be explained by the missing non-trivial  $\langle A_0 \rangle$ -background in the present calculation.

The ghost propagator agrees qualitatively, but deviates quantitatively, from the lattice results, as shown in Fig. 8.11b. We discuss this point further in Sec. 8.4.1. The ghost-gluon vertex is plotted in Fig. 8.6b. It is weaker around the phase transition temperature than in the vacuum. At high temperatures it shows a broader and less pronounced bump than at zero temperature.

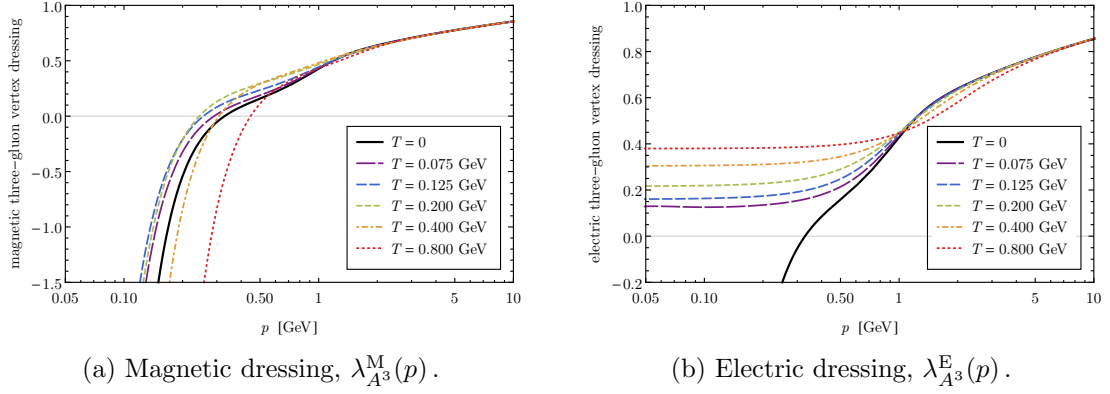


Figure 8.7.: Temperature dependence of the three-gluon vertex, (A.1).

### 8.3.2. Gluonic Vertices

The gluonic vertex dressing functions are shown in Fig. 8.7 and 8.8. The magnetic dressings of both vertices show scaling in the infrared. Contrarily, the corresponding electric components decouple at  $p \approx 2\pi T$  and become constant in the infrared. We show the position of the zero crossing of the magnetic three-gluon vertex dressing function as a function of temperature in Fig. 8.11a. At small temperatures the zero crossing moves towards lower momenta as the temperature is increased. At high temperatures, the magnetic zero crossing rises linearly with the temperature. In contrast, the zero crossing of the electric three-gluon vertex dressing function disappears at  $T \approx 40$  MeV. Similarly, the electric dressing of the four-gluon vertex undergoes a drastic change from zero to small temperatures, and goes on to increase with growing temperature.

### 8.3.3. Comparison with Earlier Results

In this section we compare our results to previous FRG results [252, 302]. An important difference is that in [302] only thermal fluctuations encoded in the differences of zero- and finite-temperature flows were computed. This requires the full quantum effective action  $\Gamma_{k=0}(T=0)$  as input. The temperature-independent cutoff action is then obtained by integrating the flow from  $k=0$  to  $k=\Lambda$ , i.e.,  $\Gamma_{k=\Lambda} = \Gamma_{k=0} + \int_0^\Lambda dk \partial_k \Gamma$ . We found it necessary to adjust the gluon mass parameter at  $k=\Lambda$  via (8.17) due to truncation artifacts. If we do not re-tune the gluon mass parameter and start from a scaling vacuum action, the theory flows into a Landau-pole-like singularity, even for infinitesimal temperatures. If we start from a decoupling cutoff action (which has a small positive mass offset compared to the scaling cutoff action), we can raise the temperature to  $T \lesssim 75$  MeV before the theory flows into a singularity. This clearly asks for a temperature-dependent gluon mass parameter. In [302] the gluon mass parameter was not tuned, which is a further major difference to our calculation. Consequently, in the truncations used no scaling solution can be obtained with the procedure from [302]. Furthermore, the temperature range in which decoupling solutions can be computed is limited. Given our findings, it is surprising that the authors of [302] were able to raise the temperature to  $T \approx 1$  GeV, which can only be attributed to the vertex approximation used there. While the procedure applied in [302] leads to similar results for the electric gluon propagator, the effects on the ghost propagator and the magnetic gluon propagator are more pronounced. Increasing the tem-

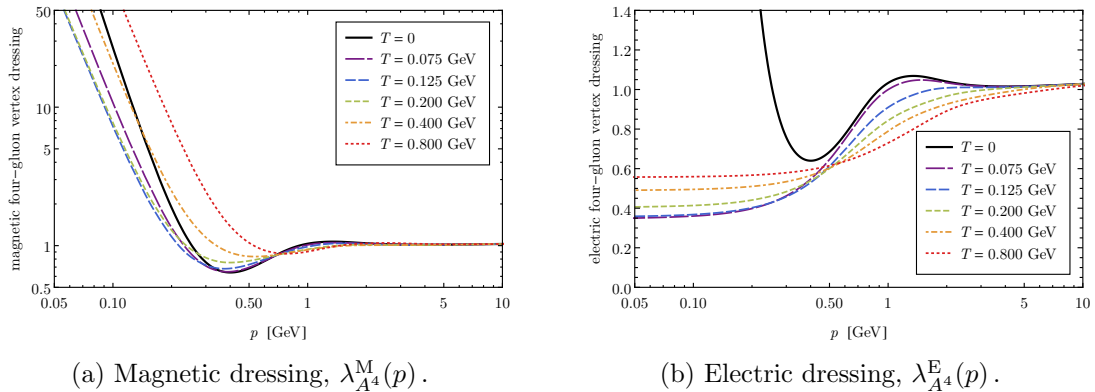


Figure 8.8.: Temperature dependence of the four-gluon vertex, (A.1).

perature from zero, our ghost propagator dressing first decreases and then slowly increases at high temperatures, as can be seen from Fig. 8.6a. This is in line with the lattice result, see Fig. 8.11b. In contrast, the ghost propagator dressing in [302] does (virtually) not decrease but is enhanced already at small temperatures. For small temperatures  $T < T_c$ , our magnetic gluon propagator varies only very mildly, see Fig. 8.5a. This is different in [302]. There, the magnetic gluon propagator decreases significantly already at small temperatures. Since the ghost loop contribution to the gluon propagator is negative, this is a direct consequence of the unphysical ghost propagator enhancement in [302].

## 8.4. Discussion

The presented non-perturbative results are obtained with the most comprehensive truncation within functional methods to date. The overall agreement with lattice results is very good. An exception is the electric propagator at temperatures close to the critical temperature. The explanation has already been indicated in Sec. 8.3 and is discussed below. The agreement of the magnetic propagator and the electric propagator for high temperatures is of the order of 10%. These small deviations can be attributed to lattice artifacts and the systematic error within our truncation. The latter stems from incomplete momentum dependencies of the vertices and missing non-classical tensors, see Sec. 5.3.2 and A.3 for estimates of their respective importance.

### 8.4.1. Non-trivial Backgrounds and Propagators

A potential source of the discrepancy of the electric gluon propagator near the phase transition temperature is an insufficient order in our approximation scheme. However, such deviations of the electric gluon propagator from lattice results were already observed in much simpler truncations [302]. Furthermore, if truncation artifacts were the main source, we would expect larger discrepancies also in the magnetic gluon propagator.

In contrast to this, the electric propagator that is closely related to the order parameter  $L[\langle \bar{A}_0 \rangle]$  is particularly sensitive to a non-vanishing background field [305]. As argued in Sec. 8.1.2, the non-trivial solution of the equation of motion,  $\bar{A}_0 \neq 0$ , is important in the temperature regime (8.9), i.e.,

$$T \in (0.5 T_c, 1.3 T_c).$$

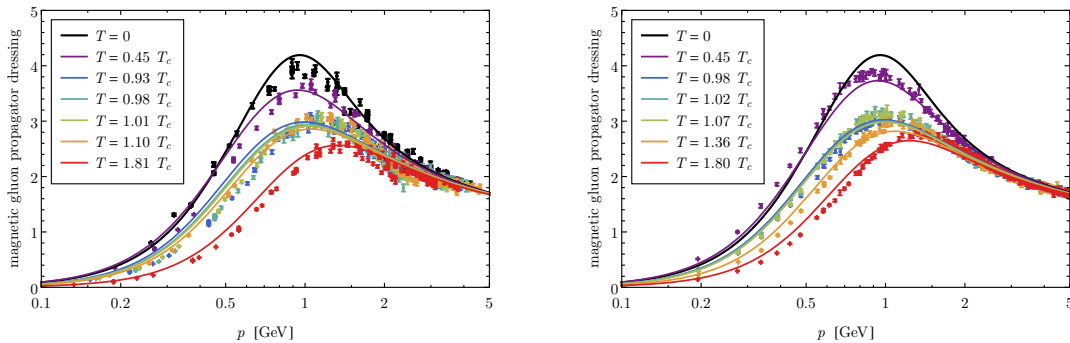
(a) Comparison with  $SU(2)$  results [250, 309].(b) Comparison with  $SU(3)$  results [311].

Figure 8.9.: Magnetic gluon propagator dressing, (8.2).

This is exactly the temperature range where the deviations from the lattice results, that are evaluated on the equation of motion, are most pronounced. We expect a considerable improvement in the electric propagator if our correlation functions are evaluated on the non-trivial background. At this point, we want to emphasize that the observed deviations do not invalidate our results for the electric two-point correlator. It simply represents the correlation functions at a non-minimal configuration, cf. (8.7). Furthermore, these findings underline that Polyakov-enhanced low-energy effective models should be constructed in  $\bar{A}_0$ -backgrounds and the effective potential  $V[\bar{A}_0]$  rather than Polyakov loop backgrounds and the Polyakov loop potential  $V[L]$ : since the electric propagators agree on the 10% level above  $T \gtrsim 1.3 T_c$ . This entails that the relevant background for the shifts in the Matsubara frequencies is  $\langle \bar{A}_0 \rangle$ .

The above analysis is also important for the comparison of the present results with  $SU(2)$  and  $SU(3)$  lattice simulations. As discussed in detail in Sec. 5.4.1, the gauge group enters only at very high orders of the approximation in an expansion of the effective action around vanishing background fields. Thus, our results depend only trivially on the gauge group. However, the gauge group, and in particular the universality class, enters via the Polyakov loop background, or, more precisely  $\langle \bar{A}_0 \rangle$ . The different orders of the phase transition for  $SU(2)$  and  $SU(N > 2)$  are encoded in the Polyakov loop potential  $V[\bar{A}_0]$  and the respective expectation values  $\nu$  in (8.8), rather than in the propagator equations [108, 205]. The Ising critical exponents for  $SU(2)$  can also be extracted from critical fluctuations encoded in the effective potential [204]. Furthermore, the critical fluctuations are the cause of the higher phase transition temperature in comparison to  $SU(N > 2)$  [204]. Thus, the gauge group dependence of the order of the phase transition and the value of transition temperature are to leading order caused by the effective potential, and hence by the related expansion about the physical ground state, i.e.,  $\langle \bar{A}_0 \rangle$  in the current setting.

We close the discussion of the propagators with the remark that the comparison of our results with the lattice results at small momenta  $p^2 \ll \Lambda_{\text{QCD}}^2$  has to be taken with a grain of salt. The lattice results are of the decoupling type whereas our results are of the scaling type. Consequently, the non-perturbative gauge fixing is not unique, see, e.g., [129, 233, 235–237]. This concerns in particular the ghost propagator, shown in Fig. 8.6a and 8.11b, which is more sensitive to the treatment of the Gribov copies than the gluon propagator [129, 233].

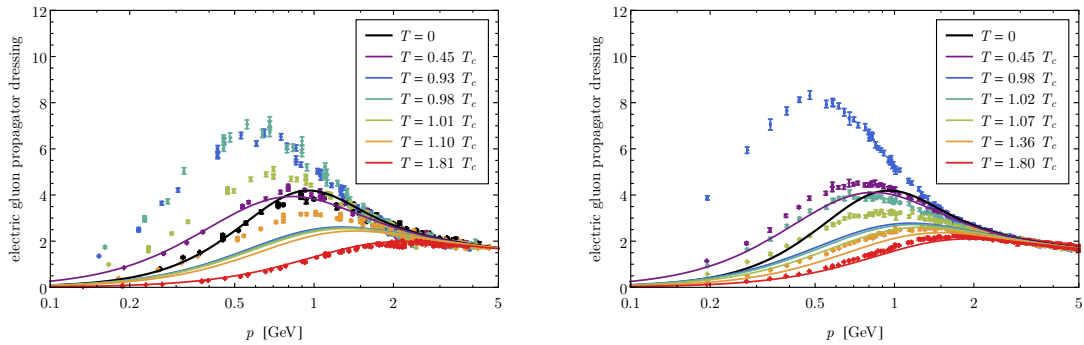
(a) Comparison with  $SU(2)$  results [250, 309].(b) Comparison with  $SU(3)$  results [311].

Figure 8.10.: Electric gluon propagator dressing, (8.2).

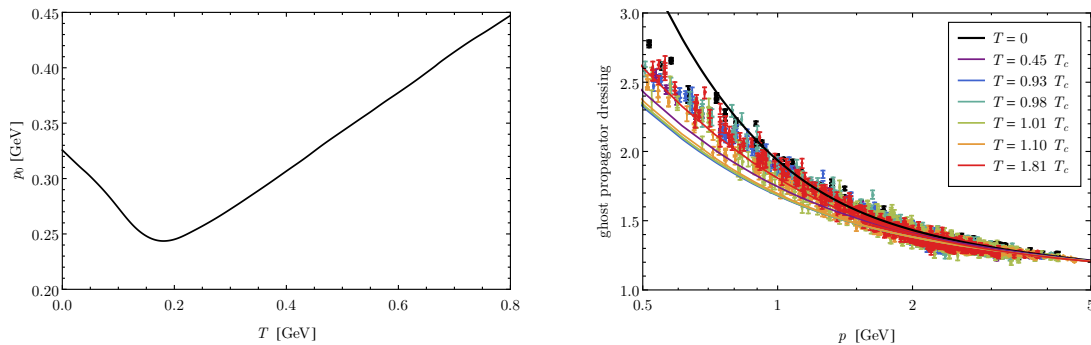
### 8.4.2. Debye Mass and the Perturbative Regime

We find very good agreement of our non-perturbative Debye screening mass with two-loop hard thermal loop perturbation theory down to  $T \approx 0.6 \text{ GeV}$ , see Fig. 8.3. This remarkable agreement down to comparably low temperatures is in line with earlier findings, see, e.g., [316–324]. In general, perturbative resummation schemes have been found to be applicable at surprisingly large couplings. An explanation of this unexpectedly large range of validity can be given by the structural similarity of higher order perturbative resummation schemes and the non-perturbative resummations performed within functional methods. This opens the door for applications of functionally assisted analytic perturbative computations beyond the validity bounds of perturbation theory, in particular to the transport and kinetic realm of heavy ion collisions.

### 8.4.3. Three-Gluon Vertex and its Zero Crossing

The magnetic three-gluon vertex dressing function has been studied on the lattice [312] and with a semi-perturbative approximation of its DSE [313]. Both studies show a significant enhancement of the magnetic dressing at low momenta  $p \approx 0.2 \text{ GeV}$  for temperatures just below the critical temperature. While we also observe this effect qualitatively, see Fig. 8.7, we find a much weaker enhancement. This is consistent with the finding that our electric gluon propagator is weaker than the electric lattice propagator, cf. Fig. 8.10. This electric propagator enters the triangle diagram in the three-gluon vertex equation which yields a positive contribution to the dressing function [74, 166]. Thus, a stronger electric propagator increases the strength of the magnetic three-gluon vertex.

At zero temperature, the three-gluon vertex shows a zero crossing in four as well as in three dimensions [1, 165, 166, 193, 201, 238–244], see also Chapter 5 and 6. Analytical studies show that it is caused by the divergent ghost triangle diagram. We find that the zero crossing persists in the magnetic dressing function for all temperatures. This stands in line with [313] but in contrast to [312], where the lowest investigated momenta show a positive sign at temperatures somewhat below the critical temperature. Here, we present an analytical argument for the persistence of the magnetic zero crossing at all temperatures. The argument is first presented for vanishing gluonic background fields and is based on the infrared dominance of ghost loops. Finally, we discuss the case of non-vanishing gluonic backgrounds relevant for temperatures about  $T_c$ .



(a) Magnetic three-gluon vertex zero crossing  $\lambda_{A3}^M(p_0) = 0$  as a function of temperature. (b) Ghost propagator dressing  $1/Z_c(p)$  compared to  $SU(2)$  lattice results [250, 309].

Figure 8.11.: Zero crossing and ghost propagator dressing.

All gluonic diagrams are gapped below a certain scale. In contrast, the ghost triangle effectively contributes like the corresponding three-dimensional diagram for  $p^2 \ll (2\pi T)^2$ . Therefore, it causes a divergence in the magnetic three-gluon vertex dressing function at low momenta for all temperatures and, thus, the magnetic zero crossing cannot vanish. At high temperatures, this zero crossing moves then to higher scales, which is in line with the high temperature limit and [312]. This qualitative argument is independent of the type of the solution, since the three-dimensional ghost triangle diagram diverges with a power-law in the case of the scaling solution and linearly [193, 201, 241] in the case of the decoupling solution. We find that the zero crossing of the electric component vanishes at a temperature of  $T \approx 40$  MeV. This can be understood by observing that the zero mode of the ghost triangle diagram, evaluated at zero external Matsubara frequencies, contributes to the magnetic three-gluon vertex dressing, but vanishes analytically if projected with the electric three-gluon vertex projection operator. Our numerical results show precisely the expected behavior, see Fig. 8.11a and 8.7.

We extend the argument to the case of non-vanishing backgrounds. They introduce a color structure in the ghost propagator and the ghost-gluon vertex. After diagonalization, we are left with gapped and ungapped modes in the ghost propagator, as well as background-dependent and background-independent (color) tensor structures in the ghost-gluon vertex. The remaining ungapped ghost modes couple to the latter tensor structure, which is the original tensor structure at vanishing background. Therefore, the background simply leads to a weakening of the infrared dominance by gapping some but not all ghost modes. Accordingly, the zero crossing moves towards smaller momenta, but does not disappear, in the presence of non-trivial backgrounds. Furthermore, for small temperatures  $T/\Lambda_{\text{QCD}} \rightarrow 0$ , the gapping of the ghost modes occurs only at very small momenta  $\vec{p}^2 \lesssim (2\pi T)^2$ , and we are left with the temperature regime (8.9), in which a weakening of the infrared ghost dominance is to be expected. This structure is compatible with the results in [312], where no zero crossing was observed at temperatures about  $T_c$  in the accessible momentum regime.



## 8.5. Conclusion

We presented non-perturbative first-principles results for finite-temperature Yang-Mills correlation functions, obtained from the functional renormalization group. Our comprehensive truncation for the effective action includes the computationally especially expensive magnetic and electric components of the purely gluonic vertices, see Fig. 8.1. We gauged our truncation by comparing our propagators to lattice results and found very good agreement for the magnetic gluon propagator. Our result for the Debye screening mass shows excellent agreement with two-loop hard thermal loop perturbation theory at high temperatures and the electric gluon propagator compares very well to lattice results for all temperatures except  $T \in (0.5 T_c, 1.3 T_c)$ . We argued that these deviations originate from the different backgrounds used. Particular focus was put on the fate of the zero crossing of the three-gluon vertex. In the electric component the zero crossing disappears at  $T \approx 40$  MeV. The zero crossing of the magnetic component moves to lower momenta at small temperatures but it never vanishes. At high temperatures, its position increases linearly with the temperature. We gave an analytic argument for the observed qualitative behavior of the zero crossing.

The obtained results form the foundation for a number of subsequent studies. The capability to perform first-principles studies of gauge theories at finite temperatures with functional methods provides a crucial prerequisite for investigations of the QCD phase structure. In particular, the QCD calculation from the last chapter can now be straightforwardly extended to finite temperature. Furthermore, the presented correlators may be used to compute thermodynamic quantities such as the pressure, the shear viscosity, the Polyakov loop, and spectral functions. Finally, we expect that improving the current investigation by expanding the effective action about the non-trivial solution of the equation of motion will lead to the disappearance of the discrepancy in the electric gluon propagator near the phase transition temperature.

## 9. Summary and Outlook

We computed QCD correlation functions by means of a systematic vertex expansion within the FRG approach. They contain the full information on confinement and chiral symmetry breaking. Regularization schemes in momentum space, that are typically used in such non-perturbative applications of functional methods to gauge theories, lead to modifications of the STIs. Taking these modifications into account is of pivotal importance since the STIs encode the gauge-invariance of observables in gauge-fixed settings. In the FRG approach all the information about the microscopic theory is stored in the action at the cutoff scale, which is determined by the modified STIs. We found that it is possible to determine the cutoff action by demanding that the STIs are fulfilled at vanishing RG scale. This insight, together with sophisticated technical tools such as FormTracer, enabled us to compute consistent correlation functions in unprecedentedly large self-consistent truncations.

We first studied Yang-Mills theory where we put particular focus on the gluon mass gap generation. We established necessary conditions for confining solutions. Functional equations as well as STIs show that irregularities are required for the dynamical creation of a gluon mass gap. For the scaling solution, these arise trivially due to the divergent ghost propagator. For the decoupling solution, we excluded irregularities of simple diagrammatic origin. Thus, they have to originate from resonances in the longitudinal sector or the dynamical generation of a transverse background. We presented clear evidence for a dynamical mass gap contribution in our numerical calculation. Furthermore, our gluon propagator shows backbending, a signal for positivity violation. Our parameter-free solution is in excellent agreement with corresponding lattice results. Noteworthy, our coupled system of equations is fully self-consistent and does not require any modeling or external input. The computed running couplings of different vertices are degenerate in the ultraviolet but deviate in the infrared, exactly as expected.

We also investigated Yang-Mills theory in three spacetime dimensions and found good agreement with Dyson-Schwinger results. In contrast to the physical four-dimensional case, both functional results deviate from lattice results. We attributed this discrepancy to truncation artifacts. Resolving it will yield a better understanding of the differences between Yang-Mills theory in three and four dimensions.

Next, we considered unquenched two-flavor QCD. In line with earlier studies, we found that chiral symmetry breaking is very sensitive to the strength of the quark-gluon vertex. To minimize truncation errors, we constrained it with its STI in the perturbative regime. We observed that the STI constrained quark-gluon vertex coupling and the gluonic couplings are degenerate in the ultraviolet. Varying the scale down to which the STI is enforced left us with an estimate for the truncation error. In all cases, the unquenched gluon propagator shows very good agreement with two-flavor lattice results and proves to be insensitive to the pion mass. In contrast, the truncation uncertainty in the quark propagator is significant and the agreement only reasonable. It is therefore necessary to find a systematic expansion scheme that leaves the degeneracy of the running couplings in the perturbative regime intact such that the quark-gluon vertex STI is automatically fulfilled. Finding such a scheme is a challenging but vital task for future investigations.

In the last chapter we considered Yang-Mills theory at finite temperature. We split all tensors present in the classical action into components longitudinal and transverse with respect to the thermal heat bath. The electric three-gluon as well as the four-gluon vertex finite-temperature dressings were computed here for the first time. Furthermore, we extracted a screening mass from the electric propagator that shows excellent agreement with two-loop hard thermal loop perturbation theory down to temperatures of two times the critical temperature where the validity range of the perturbation theory ends. The computed correlators agree on the ten percent level with lattice results at very high and very low temperatures. Near the phase transition temperature, we found a significant deviation of the electric gluon propagator from lattice simulations. We attributed this discrepancy to the missing non-trivial background field in our truncation whose effects are most prominent at temperatures around the critical temperature. However, given that the Polyakov loop and the related background field have been studied intensively, it can be incorporated straightforwardly into our calculation. This study will be the foundation for many future applications such as the computation of the pressure, the equation of state, and spectral functions.

All in all, parameter-free first-principle FRG predictions on the QCD phase structure are still amiss and require collective efforts. This is partially due to QCD's enormous complexity that has to be under control in any non-perturbative approach, but also due to conceptual challenges already present in the vacuum. Nonetheless, we made significant progress towards ab initio calculations of QCD observables within the FRG framework. As of now, functional methods are the only first-principle approach known to be applicable in the strong-coupling regime and at large chemical potential. Thus, in the pursuit of the QCD phase structure, and in particular the critical endpoint, they are an indispensable approach although several mostly technical obstacles still have to be overcome until they can provide accurate predictions.

# A. Gluonic Vertices at Finite Temperature

Gluonic vertices (and in particular the four-gluon vertex) prove to be subtle at finite temperature. These intricacies are discussed in this appendix which is largely borrowed from [4]. In Sec. A.1 we split the classical Yang-Mills tensors into electric and magnetic components. Section A.2 deals with the vanishing of some components in the limit of vanishing Matsubara frequencies. Finally, we discuss the projection onto the components in Sec. A.3, where we also comment on elaborate effects of the gluon mass parameter tuning that are not contained in [4].

## A.1. Tensor Splitting

We generalize the vertex expansion used in Chapter 5 to finite temperature by attaching all combinations of magnetic and electric projection operators to the classical tensor structures of the vertices. Leaving momentum arguments implicit, we obtain

$$[\Gamma_{\bar{c}cA}^{(3)}]_{\mu}^{abc} = [S_{\bar{c}cA}^{(3)}]_{\mu'}^{abc} \cdot \left( \lambda_{\bar{c}cA}^M \Pi_{\mu'\mu}^M + \lambda_{\bar{c}cA}^E \Pi_{\mu'\mu}^E \right)$$

for the ghost-gluon vertex,

$$\begin{aligned} [\Gamma_{A^3}^{(3)}]_{\mu\nu\rho}^{abc} = [S_{A^3}^{(3)}]_{\mu'\nu'\rho'}^{abc} \cdot \left( \lambda_{A^3}^{MMM} \Pi_{\mu'\mu}^M \Pi_{\nu'\nu}^M \Pi_{\rho'\rho}^M + \right. \\ \lambda_{A^3}^{EMM} \Pi_{\mu'\mu}^E \Pi_{\nu'\nu}^M \Pi_{\rho'\rho}^M + \text{perm.} + \\ \lambda_{A^3}^{EEM} \Pi_{\mu'\mu}^E \Pi_{\nu'\nu}^E \Pi_{\rho'\rho}^M + \text{perm.} + \\ \left. \lambda_{A^3}^{EEE} \Pi_{\mu'\mu}^E \Pi_{\nu'\nu}^E \Pi_{\rho'\rho}^E \right) \end{aligned}$$

for the three-gluon vertex, and

$$\begin{aligned} [\Gamma_{A^4}^{(4)}]_{\mu\nu\rho\sigma}^{abcd} = [S_{A^4}^{(4)}]_{\mu'\nu'\rho'\sigma'}^{abcd} \cdot \left( \lambda_{A^4}^{MMMM} \Pi_{\mu'\mu}^M \Pi_{\nu'\nu}^M \Pi_{\rho'\rho}^M \Pi_{\sigma'\sigma}^M + \right. \\ \lambda_{A^4}^{EMMM} \Pi_{\mu'\mu}^E \Pi_{\nu'\nu}^M \Pi_{\rho'\rho}^M \Pi_{\sigma'\sigma}^M + \text{perm.} + \\ \lambda_{A^4}^{EEMM} \Pi_{\mu'\mu}^E \Pi_{\nu'\nu}^E \Pi_{\rho'\rho}^M \Pi_{\sigma'\sigma}^M + \text{perm.} + \\ \lambda_{A^4}^{EEEM} \Pi_{\mu'\mu}^E \Pi_{\nu'\nu}^E \Pi_{\rho'\rho}^E \Pi_{\sigma'\sigma}^M + \text{perm.} + \\ \left. \lambda_{A^4}^{EEEE} \Pi_{\mu'\mu}^E \Pi_{\nu'\nu}^E \Pi_{\rho'\rho}^E \Pi_{\sigma'\sigma}^E \right) \end{aligned} \quad (\text{A.1})$$

for the four-gluon vertex. The orthogonality of the electric and magnetic projection operators implies that the dressings of the components are degenerate at zero temperature. As discussed in length in Sec. 8.1.1, the finite temperature information is predominantly

stored in the spatial momentum dependence of the zero modes. We exploit this and compute only zero modes. However, only the purely magnetic tensors and those with exactly two electric legs do not vanish if the Matsubara modes are set to zero, see the next Sec. A.2. To obtain the correct ultraviolet behavior, and to recover the vacuum results in the zero-temperature limit, the vanishing tensors must not be neglected since the non-zero loop modes contribute to the zero mode correlation functions if  $k \gtrsim 2\pi T$ . Thus, we approximate the dressings of the tensors vanishing in the limit of vanishing Matsubara frequencies by

$$\begin{aligned}\lambda_{\bar{c}cA}^E &\approx \lambda_{\bar{c}cA}^M, \\ \lambda_{A^3}^{\text{EMM}} &= \lambda_{A^3}^{\text{EEE}} \approx \lambda_{A^3}^{\text{MMM}}, \\ \lambda_{A^4}^{\text{EMMM}} &= \lambda_{A^4}^{\text{EEEM}} = \lambda_{A^4}^{\text{EEEE}} \approx \lambda_{A^4}^{\text{MMMM}}.\end{aligned}\tag{A.2}$$

Due to the  $O(4)$ -symmetry of the vacuum, this approximation becomes exact for large momenta  $p^2 \gg (2\pi T)^2$ , where finite-temperature effects are suppressed. We want to emphasize that it is also very good for small momenta  $p^2 \lesssim (2\pi T)^2$  since the dimension of the tensor spaces is reduced for vanishing Matsubara frequencies, see Sec. A.2. Hence, the approximation of some electric dressings by (A.2) affects only intermediate Matsubara modes, which are only slightly influenced by finite temperature effects, see Sec. 8.1.1. Since the three-gluon and the four-gluon vertices have only two dressings in our approximation, we employ the following shorthand notation in Chapter 8:

$$\begin{aligned}\lambda_{A^3}^M &\equiv \lambda_{A^3}^{\text{MMM}}, \\ \lambda_{A^3}^E &\equiv \lambda_{A^3}^{\text{EEM}}, \\ \lambda_{A^4}^M &\equiv \lambda_{A^4}^{\text{MMMM}}, \\ \lambda_{A^4}^E &\equiv \lambda_{A^4}^{\text{EEMM}},\end{aligned}$$

as illustrated in Fig. 8.1.

## A.2. Zero Modes

We generalized the classical tensors by attaching all combinations of magnetic and electric projection operators, see (A.1). However, contracting the electric ghost-gluon vertex with itself and evaluating it at vanishing Matsubara modes yields

$$[S_{\bar{c}cA}^{(3)}]_{\mu}^{abc} \Pi_{\mu\mu'}^E [S_{\bar{c}cA}^{(3)}]_{\mu'}^{abc} \Big|_{\{n_i=0\}} = 0.$$

Hence, the electric component of the ghost-gluon vertex disappears in the limit of vanishing Matsubara frequencies. Similarly, we find for the three-gluon vertex,

$$\begin{aligned}[S_{A^3}^{(3)}]_{\mu\nu\rho}^{abc} \Pi_{\mu\mu'}^E \Pi_{\nu\nu'}^M \Pi_{\rho\rho'}^M [S_{A^3}^{(3)}]_{\mu'\nu'\rho'}^{abc} \Big|_{\{n_i=0\}} &= 0, \\ [S_{A^3}^{(3)}]_{\mu\nu\rho}^{abc} \Pi_{\mu\mu'}^E \Pi_{\nu\nu'}^E \Pi_{\rho\rho'}^E [S_{A^3}^{(3)}]_{\mu'\nu'\rho'}^{abc} \Big|_{\{n_i=0\}} &= 0,\end{aligned}$$

and for the four-gluon vertex,

$$\begin{aligned} [S_{A^4}^{(4)}]_{\mu\nu\rho\sigma} \Pi_{\mu\mu'}^E \Pi_{\nu\nu'}^M \Pi_{\rho\rho'}^M \Pi_{\sigma\sigma'}^M [S_{A^4}^{(4)}]_{\mu'\nu'\rho'\sigma'} \Big|_{\{n_i=0\}} &= 0, \\ [S_{A^4}^{(4)}]_{\mu\nu\rho\sigma} \Pi_{\mu\mu'}^E \Pi_{\nu\nu'}^E \Pi_{\rho\rho'}^E \Pi_{\sigma\sigma'}^M [S_{A^4}^{(4)}]_{\mu'\nu'\rho'\sigma'} \Big|_{\{n_i=0\}} &= 0, \\ [S_{A^4}^{(4)}]_{\mu\nu\rho\sigma} \Pi_{\mu\mu'}^E \Pi_{\nu\nu'}^E \Pi_{\rho\rho'}^E \Pi_{\sigma\sigma'}^E [S_{A^4}^{(4)}]_{\mu'\nu'\rho'\sigma'} \Big|_{\{n_i=0\}} &= 0. \end{aligned}$$

Thus, for  $p^2 \ll (2\pi T)^2$  the classical tensors are fully described by the remaining basis tensors, to wit, those with only magnetic legs and those with exactly two electric legs.

### A.3. Projecting

The tensor bases for the propagators as well as for the ghost-gluon vertex are complete, and therefore the projection onto the dressings is unique. For the gluonic vertices we do not take the full transverse tensor bases into account. Consequently, already in the vacuum, any projection is an approximation that relies on the assumption that non-included basis elements are small. If the flows are projected onto their electric and magnetic components, the incompleteness of the bases can lead to intricate complications. The reason is that the magnetic and electric projection operators can yield differing contributions from non-classical tensor structures that are created by quantum fluctuations. As a consequence, the magnetic and electric dressings differ by momentum-dependent terms. This effect occurs already at vanishing temperature, and is therefore in contradiction with the  $O(4)$ -symmetry of the vacuum. If one uses a complete basis, projecting with magnetic and electric projection operators does not spoil the  $O(4)$ -symmetry although the projection operators themselves are not  $O(4)$ -symmetric.

In the following two subsections we discuss in detail the quantitative relevance of these effect caused by the incomplete bases for the gluonic vertices. In order to disentangle genuine finite-temperature contributions from these projection artifacts, we consider only vacuum flows. By splitting the projection into electric and magnetic components and comparing them to the  $O(4)$ -symmetric projection, we are able to quantify these basis artifacts. Unfortunately, we find that the emergence of certain non-classical tensors yields sizable artifacts on the dressing of the classical tensor structure of the four-gluon vertex. As discussed in detail in this and the following Appendix B, implementing a proper treatment of these artifacts of the incomplete bases turns out to be vital to obtain the correct ultraviolet behavior and cutoff independence of the finite-temperature results. This section assumes that the reader is familiar with the basics of projecting of tensors onto scalar dressings, which are provided in Sec. C.2 for the sake of self-containment.

### A.3.1. Three-Gluon Vertex

We project onto the magnetic and electric components of the three-gluon vertex by

$$\begin{aligned}\lambda_{A^3}^M &= \frac{[S_{A^3}^{(3)}]_{\mu\nu\rho}^{abc} \Pi_{\mu\mu'}^M \Pi_{\nu\nu'}^M \Pi_{\rho\rho'}^M [\Gamma_{A^3}^{(3)}]_{\mu'\nu'\rho'}^{abc}}{[S_{A^3}^{(3)}]_{\mu\nu\rho}^{abc} \Pi_{\mu\mu'}^M \Pi_{\nu\nu'}^M \Pi_{\rho\rho'}^M [S_{A^3}^{(3)}]_{\mu'\nu'\rho'}^{abc}}, \\ \lambda_{A^3}^E &= \frac{[S_{A^3}^{(3)}]_{\mu\nu\rho}^{abc} \Pi_{\mu\mu'}^E \Pi_{\nu\nu'}^E \Pi_{\rho\rho'}^M [\Gamma_{A^3}^{(3)}]_{\mu'\nu'\rho'}^{abc}}{[S_{A^3}^{(3)}]_{\mu\nu\rho}^{abc} \Pi_{\mu\mu'}^E \Pi_{\nu\nu'}^E \Pi_{\rho\rho'}^M [S_{A^3}^{(3)}]_{\mu'\nu'\rho'}^{abc}},\end{aligned}\quad (\text{A.3})$$

as generalization of the vacuum projection (cf. (5.8))

$$\lambda_{A^3} = \frac{[S_{A^3}^{(3)}]_{\mu\nu\rho}^{abc} \Pi_{\mu\mu'}^\perp \Pi_{\nu\nu'}^\perp \Pi_{\rho\rho'}^\perp [\Gamma_{A^3}^{(3)}]_{\mu'\nu'\rho'}^{abc}}{[S_{A^3}^{(3)}]_{\mu\nu\rho}^{abc} \Pi_{\mu\mu'}^\perp \Pi_{\nu\nu'}^\perp \Pi_{\rho\rho'}^\perp [S_{A^3}^{(3)}]_{\mu'\nu'\rho'}^{abc}}.\quad (\text{A.4})$$

In explicit numerical checks we find that the projections (A.3) and (A.4) agree at the per mille level at  $T = 0$  and therefore also for  $k \gg 2\pi T$ . We conclude that our projection is not sensitive to the possible emergence of non-classical tensors structures in the three-gluon vertex. This is also consistent with the sub-leading importance of non-classical tensor structures found in earlier three-gluon vertex studies [166].

### A.3.2. Four-Gluon Vertex

We project onto the vacuum dressing function with (cf. (5.9))

$$\lambda_{A^4} = \frac{[S_{A^4}^{(4)}]_{\mu\nu\rho\sigma}^{abcd} \Pi_{\mu\mu'}^\perp \Pi_{\nu\nu'}^\perp \Pi_{\rho\rho'}^\perp \Pi_{\sigma\sigma'}^\perp [\Gamma_{A^4}^{(4)}]_{\mu'\nu'\rho'\sigma'}^{abcd}}{[S_{A^4}^{(4)}]_{\mu\nu\rho\sigma}^{abcd} \Pi_{\mu\mu'}^\perp \Pi_{\nu\nu'}^\perp \Pi_{\rho\rho'}^\perp \Pi_{\sigma\sigma'}^\perp [S_{A^4}^{(4)}]_{\mu'\nu'\rho'\sigma'}^{abcd}}.\quad (\text{A.5})$$

Assuming vanishing non-classical tensor structures, this generalizes to

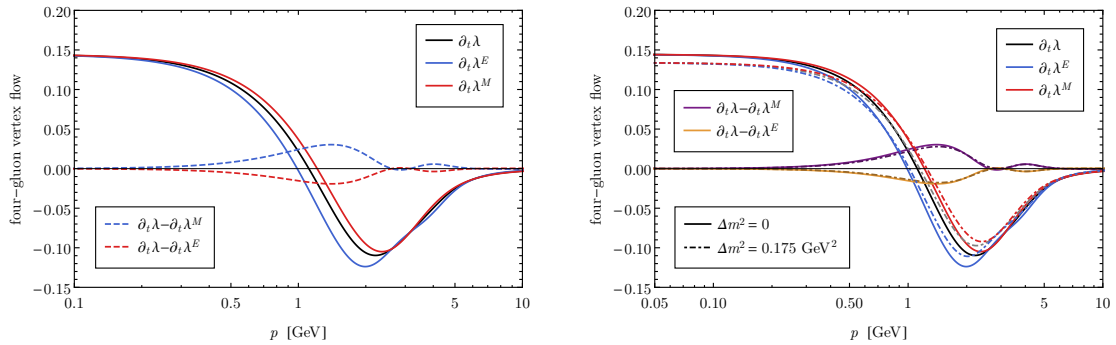
$$\begin{aligned}\lambda_{A^4}^M &= \frac{[S_{A^4}^{(4)}]_{\mu\nu\rho\sigma}^{abcd} \Pi_{\mu\mu'}^M \Pi_{\nu\nu'}^M \Pi_{\rho\rho'}^M \Pi_{\sigma\sigma'}^M [\Gamma_{A^4}^{(4)}]_{\mu'\nu'\rho'\sigma'}^{abcd}}{[S_{A^4}^{(4)}]_{\mu\nu\rho\sigma}^{abcd} \Pi_{\mu\mu'}^M \Pi_{\nu\nu'}^M \Pi_{\rho\rho'}^M \Pi_{\sigma\sigma'}^M [S_{A^4}^{(4)}]_{\mu'\nu'\rho'\sigma'}^{abcd}}, \\ \lambda_{A^4}^E &= \frac{[S_{A^4}^{(4)}]_{\mu\nu\rho\sigma}^{abcd} \Pi_{\mu\mu'}^E \Pi_{\nu\nu'}^E \Pi_{\rho\rho'}^M \Pi_{\sigma\sigma'}^M [\Gamma_{A^4}^{(4)}]_{\mu'\nu'\rho'\sigma'}^{abcd}}{[S_{A^4}^{(4)}]_{\mu\nu\rho\sigma}^{abcd} \Pi_{\mu\mu'}^E \Pi_{\nu\nu'}^E \Pi_{\rho\rho'}^M \Pi_{\sigma\sigma'}^M [S_{A^4}^{(4)}]_{\mu'\nu'\rho'\sigma'}^{abcd}},\end{aligned}\quad (\text{A.6})$$

for the magnetic and the electric components. If the only tensor generated by the flow were the classical one,

$$[\Gamma_{A^4}^{(4)}]_{\mu\nu\rho\sigma}^{abcd} \propto [S_{A^4}^{(4)}]_{\mu\nu\rho\sigma}^{abcd} = f^{abn} f^{cdn} \delta_{\mu\rho} \delta_{\nu\sigma} + \text{perm.},$$

the projections (A.5) and (A.6) would yield  $\lambda_{A^4} = \lambda_{A^4}^M = \lambda_{A^4}^E$ . However, this equality can be spoiled by the presence of non-classical tensors that are generated by the flow equation. Consider, for example, the following  $O(4)$ - and Bose-symmetric non-classical tensor:

$$[\Gamma_{A^4, \text{ncl}}^{(4)}]_{\mu\nu\rho\sigma}^{abcd}(p, q, r, s) = f^{abn} f^{cdn} (q+s)_\mu (q+s)_\rho (p+r)_\nu (p+r)_\sigma + \text{perm.}\quad (\text{A.7})$$



- (a) To evaluate the flows, we use the vacuum correlation functions at  $k = 2 \text{ GeV}$  in the right-hand side of the flow equations. The flows in this panel are also shown in the right panel as solid lines ( $\Delta m^2 = 0$ ).
- (b) Dashed lines with  $\Delta m^2 = 0.175 \text{ GeV}^2$  show the flows if the gluon propagator is modified with an additional mass offset. Notably, the differences of the flows are hardly affected by the modification of the gluon propagator.

Figure A.1.: Four-gluon vertex vacuum flows from different projection operators, (A.5) and (A.6), and their differences at the RG scale  $k = 2 \text{ GeV}$ .

Inserting (A.7) into (A.5) and (A.6) yields differing contributions to the dressing functions  $\lambda_{A^4}$ ,  $\lambda_{A^4}^M$ , and  $\lambda_{A^4}^E$ . Therefore,  $O(4)$ -invariance is lost due to the incompleteness of the basis that was used to construct the projection operators, (A.5) and (A.6).

In Fig. A.1 we show the vacuum flows of the four-gluon vertex obtained with different projection operators and identical vacuum vertices on the right-hand side of the flow equation. In contrast to the three-gluon vertex, we find a considerable difference in the resulting momentum dependence of the projections (A.5) and (A.6). We conclude, that sizable non-classical tensors, which affect the difference between the magnetic and electric projection operators, are generated. This evidence for the importance of non-classical four-gluon vertex tensor structures is consistent with earlier findings [5]. To summarize, the zero-temperature limit is spoiled by the presence of non-classical tensors such as (A.7) since they imply  $\lambda_{A^4}^M(T=0) \neq \lambda_{A^4}^E(T=0)$  and, hence,  $O(4)$ -invariance is not recovered.

A simple estimate of the unphysical projection artifacts is given by the vacuum differences of the projections (A.5) and (A.6),

$$\begin{aligned} \partial_t \lambda_{A^4} - \partial_t \lambda_{A^4}^M(T=0), \\ \partial_t \lambda_{A^4} - \partial_t \lambda_{A^4}^E(T=0), \end{aligned} \quad (\text{A.8})$$

which are also shown in Fig. A.1a. In Fig. A.1b we additionally show the four-gluon vertex flows that are obtained if the gluon propagator is modified with an additional mass offset to simulate the temperature-dependent mass re-adjustment, see Sec. 8.2.3. Fortunately, this re-tuning of the gluon mass parameter has only a sub-leading effect on the differences of the flows, which enables us to determine the flow differences (A.8) using the (scale-dependent) vacuum dressings on the right-hand side of the flow equations. Assuming that these unphysical projection artifacts depend only mildly on the temperature yields a natural strategy to account for them: subtract (A.8) from the finite-temperature flows. However, there is an additional complication in the case of the scaling solution. The vertex dressings obey a power law behavior at small momenta, see (6.1), and the corresponding exponent changes as one goes from the vacuum to finite temperature, see Fig. 8.6a. This



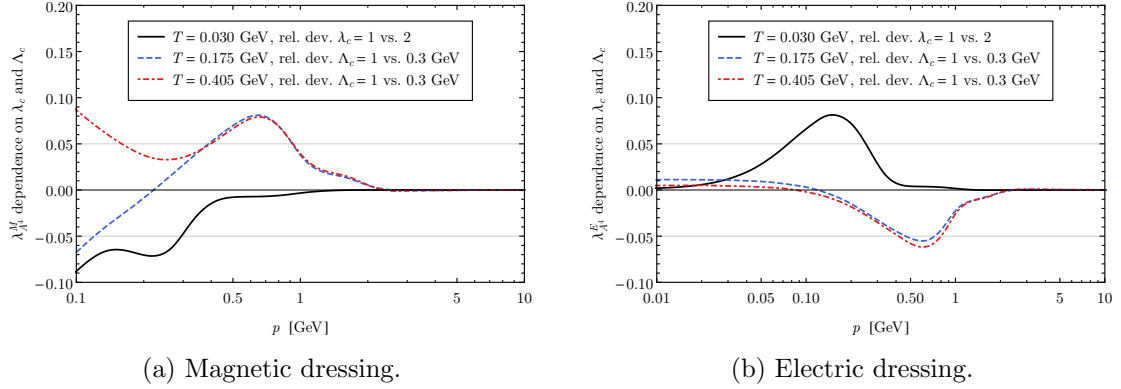


Figure A.2.: Relative deviations, e.g.,  $(\lambda_{A^4}^M(\lambda_c = 1) - \lambda_{A^4}^M(\lambda_c = 2)) / \lambda_{A^4}^M(\lambda_c = 1)$ , of the four-gluon vertex dressings, (A.9), calculated with different parameters in the smoothed theta function (A.10). Depending on the temperature, the dressings depend either on  $\lambda_c$  or  $\Lambda_c$ , see (A.11).

has to be taken into account when subtracting (A.8) from the finite-temperature flows. Consequently, we modify the flows of the magnetic and electric components by

$$\begin{aligned} \partial_t \lambda_{A^4}^M(T) &\equiv \partial_t \lambda_{A^4}^M(T) + \theta_\epsilon(k, k_c) [\partial_t \lambda_{A^4} - \partial_t \lambda_{A^4}^M(T=0)] , \\ \partial_t \lambda_{A^4}^E(T) &\equiv \partial_t \lambda_{A^4}^E(T) + \theta_\epsilon(k, k_c) [\partial_t \lambda_{A^4} - \partial_t \lambda_{A^4}^E(T=0)] . \end{aligned} \quad (\text{A.9})$$

The purpose of the smoothed step function,

$$\theta_\epsilon(k, k_c) = \frac{1}{1 + \exp\left[\frac{1}{\epsilon} \left(1 - \frac{k}{k_c}\right)\right]} , \quad (\text{A.10})$$

is to provide a transition from the corrected flows to the pure finite-temperature flows with the correct scaling behavior at very low momenta. We set the transition scale  $k_c$  to

$$k_c = \min(\lambda_c 2\pi T, \Lambda_c) , \quad (\text{A.11})$$

which is defined in terms of the parameters  $\Lambda_c$  and  $\lambda_c$ . By construction, the modified dressings fulfill

$$\lim_{T \rightarrow 0} \lambda_{A^4}^M(T) = \lim_{T \rightarrow 0} \lambda_{A^4}^E(T) = \lambda_{A^4} .$$

This guarantees that we recover the vacuum results in the limit of vanishing temperature while our best estimates for the basis artifacts are subtracted above the transition scale.

In order to investigate the influence of the transition scale  $k_c$ , we vary  $\Lambda_c$  and  $\lambda_c$  in reasonable ranges. Since temperature effects are expected to be small at momentum scales  $k \geq 2\pi T$ ,  $\lambda_c$  should be of order unity and we vary it from 1 to 2. Furthermore, the gapping scale of the gluon propagator gives us an estimate on the scale below which scaling is expected. Consequently, we vary  $\Lambda_c$  between the location of the maxima of the gluon propagator and the gluon propagator dressing, i.e.,  $\Lambda_c \in [0.3, 1]$  GeV. We find only a very mild dependence of the four-gluon vertex dressings on these parameters as shown in Fig. A.2. Since the four-gluon vertex is the least important of all classical tensors in

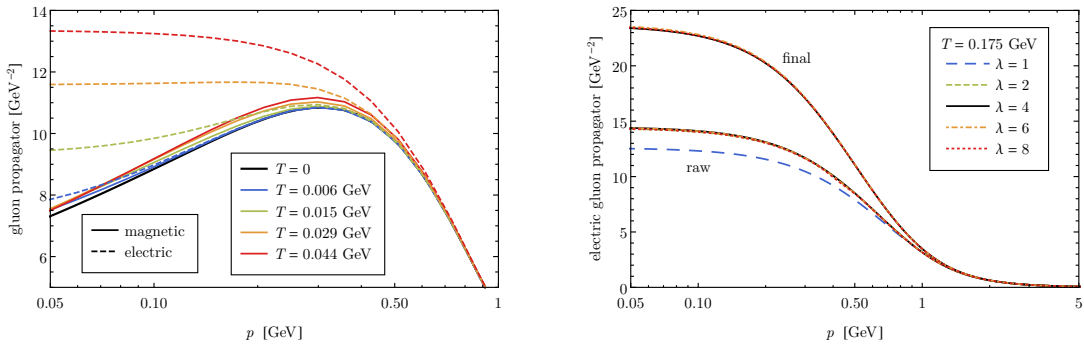
the self-consistently coupled system, we find that the dependence of all other dressings on these parameters is even smaller. For example, the induced uncertainty on the electric gluon propagator is at most 3%, but for a wide range of temperatures and momenta it is even smaller than 0.5%. In all cases the dependence on the smoothing parameter,  $\epsilon = 0.05$ , is negligible.

## B. Finite-Temperature Minutiae

The first two sections contain consistency checks and are taken from [4]. In particular, in Sec. B.1 we scrutinize the limit of vanishing temperature. In Sec. B.2, we confirm that the finite-temperature dressings at vanishing RG scale are independent from the initial cutoff scale. Finally, we investigate the mass gap generation and present decoupling solutions at non-zero temperature in Sec. B.3.

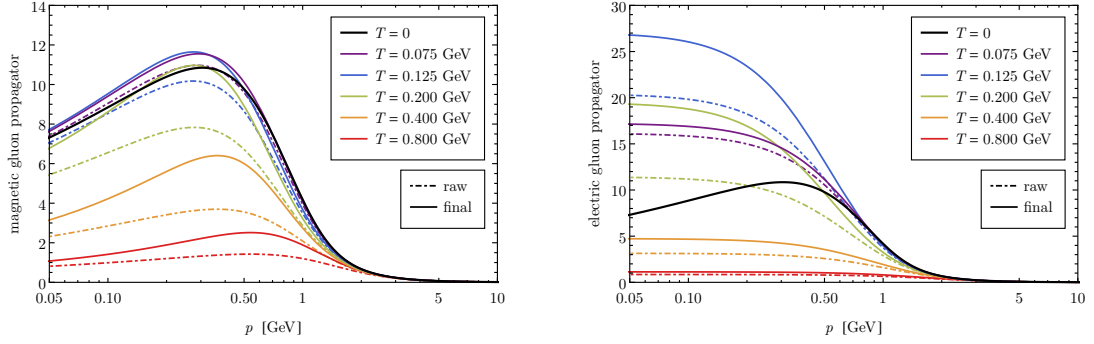
### B.1. Vacuum Limit

In Chapter 8 and Appendix A we constructed the finite-temperature truncation such that it converges to the vacuum truncation in the limit  $T \rightarrow 0$ . In Fig. B.1a, we show the gluon propagator for small temperatures. We clearly see that the magnetic as well as the electric propagators approach the vacuum propagator in the zero temperature limit. In particular, for each temperature there exists a threshold momentum above which the magnetic and electric dressings agree. This is not only a strong check of the code but also confirms the validity of the vertex truncation, detailed in Appendix A, as well as the consistency of our  $O(4)$ -symmetric momentum approximations, i.e., (8.3) and (8.5). Similarly, the magnetic and electric dressings of the vertices become degenerate in the vacuum limit. As discussed in the next section, this allows to significantly reduce the computational effort by starting from a non-trivial  $O(4)$ -symmetric cutoff action.



- (a) Convergence towards the vacuum results. The magnetic and electric gluon propagators are degenerate for  $p \gtrsim 2\pi T$ . (b) Gluon propagator obtained with different initial scales  $\Lambda_T = \lambda 2\pi T$ . See Sec. 8.2.3 for the definition of raw and final. We do not show the final propagator for  $\lambda = 1$  since in this case the start scale  $\Lambda_T = 2\pi T$  lies below the correction scale  $k_T = 4\pi T$ , cf. (8.18).

Figure B.1.: Vacuum limit and initial scale independence of gluon propagator.



(a) Magnetic gluon propagator  $1/(p^2 Z_A^M(p))$ . (b) Electric gluon propagator  $1/(p^2 Z_A^E(p))$ .

Figure B.2.: Gluon propagators with and without mass subtraction procedure, (8.18).

## B.2. Initial Scale

The regulator suppresses quantum as well as thermal fluctuations below the RG scale  $k$ . Therefore, the temperature-dependent generalized effective action  $\Gamma_k(T)$  agrees with the zero-temperature effective action as long as temperature fluctuations are suppressed,

$$\Gamma_k(T) = \Gamma_k(T = 0) \quad \text{if} \quad 2\pi T \ll k. \quad (\text{B.1})$$

This property enables us to reduce the computational effort by one to two orders of magnitude. First we compute the  $T = 0$  generalized effective action, starting at a large perturbative scale of typically  $\Lambda = 60$  GeV from the classical action. To obtain the temperature-dependent effective action, we integrate the flow equation starting from the generalized effective action  $\Gamma_{\Lambda_T}(T) = \Gamma_{\Lambda_T}(T = 0)$  at a lower, temperature-dependent cutoff scale,

$$\Lambda_T = \max(\lambda 2\pi T, \Lambda_T^{\text{min}}). \quad (\text{B.2})$$

Here,  $\Lambda_T^{\text{min}}$  has been introduced to avoid the interference of the lowered starting scale with the dynamical mass generation of the gluon. This is necessary, because truncation artifacts require us to re-adjust the gluon mass parameter at  $\Lambda_T$ , see Sec. 8.2.3. Consequently, we choose  $\Lambda_T^{\text{min}} \approx 1$  GeV as the scale where the vacuum gluon propagator dressing becomes maximal. We show the dependence of the electric gluon propagator on the dimensionless start scale  $\lambda$  in Fig. B.1b. The gluon propagator as well as all other quantities do not depend on the start scale if  $\lambda \geq 2$ . In our numerical computation we use  $\lambda = 4$  although  $\lambda = 2$  is sufficient, as argued in Sec. 8.2.3.

To demonstrate the numerical advantage of the temperature-dependent initial scale, we consider the numerical vacuum integration,

$$\int_q = \int \frac{d^4 q}{(2\pi)^4} = \int_0^L \frac{dq}{(2\pi)^4} q^3 \int d\Omega.$$

Numerically, it is advantageous to choose a  $k$ -dependent numerical cutoff  $L = lk$ , where  $l = 3$  is sufficient for the exponential regulator due to the regulator derivative appearing in all diagrams, see Fig. 3.2. This persists in the Matsubara formalism and we can limit the summation to frequencies  $\omega = 2\pi T n$  smaller than  $L = lk$ ,

$$\int_q = \int_0^L \frac{dq}{(2\pi)^3} q^2 \int d\Omega T \sum_n^{w \leq L}.$$

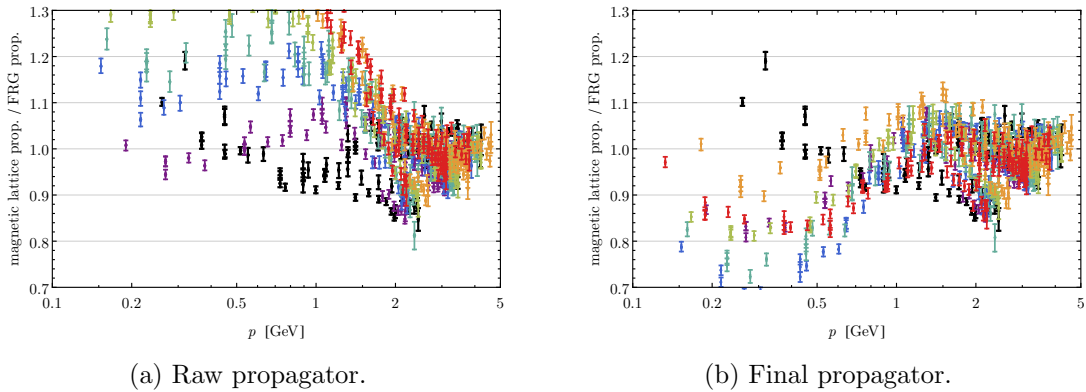


Figure B.3.: Magnetic  $SU(2)$  lattice propagator [250, 309] divided by the magnetic FRG propagator, see Fig. 8.9a for the color coding.

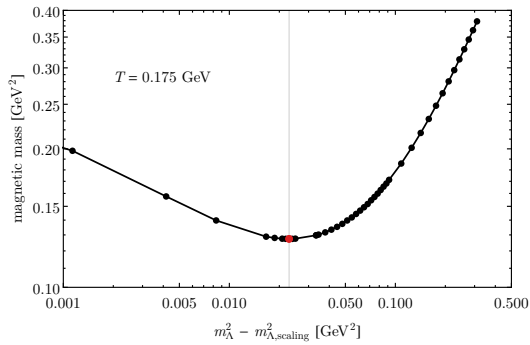
Thus, the number of required integrand evaluations grows linearly with  $k$  and with  $1/T$ . Exploiting (B.1) by (B.2) therefore reduces the number of required integrand evaluations significantly, especially for small temperatures.

### B.3. Mass Tuning and Decoupling

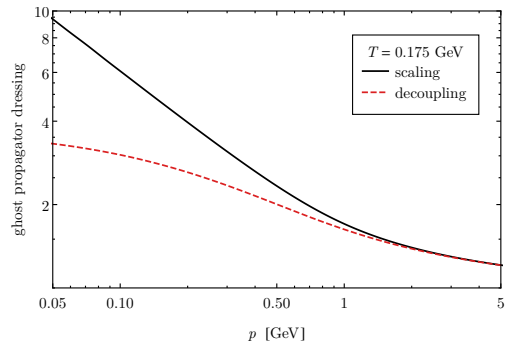
In Sec. 8.2.3 we found it necessary to adjust the gluon mass parameter temperature-dependently at the cutoff scale to account for the lack of a BRST-consistent level of the truncation, see (8.17). Without adjusting the gluon mass parameter, the theory runs into Landau-pole like singularities. After integrating the flow, we remove this truncation artifact via (8.18). To assess the effect of this procedure, we compare the raw to the final propagators in Fig. B.2. We observe a sizable influence of the correction (8.18) on the final result, also at high temperatures. This indicates a non-converged truncation which is in line with the findings in Appendix A on the importance of non-classical four-gluon vertex tensors. We plot the raw and the final magnetic gluon propagator each normalized by the magnetic lattice propagator in Fig. B.3. Since the lattice data have to be renormalized for each temperature separately, agreement is always found at the corresponding momentum scale, see Sec. C.4. At lower scales, the raw propagator quickly deviates from the lattice results. Contrarily, the final propagator shows better agreement, which we interpret as support for our subtraction procedure (8.18).

In Chapter 8 we have only shown scaling results for which the (temperature-dependent) gluon mass parameter  $m_\Lambda^2$  is unique. To understand the full theory space, it is useful to look at solutions with a different gluon mass parameters. Those are displayed in Fig. B.4 for a fixed temperature,  $T = 0.175$  GeV.

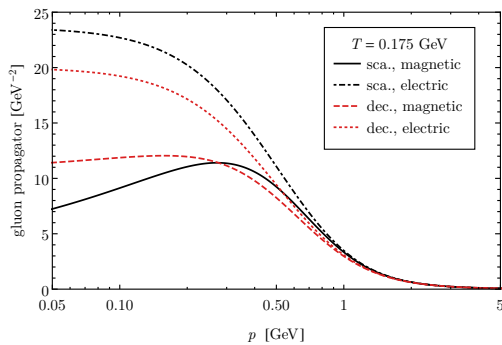
The magnetic mass at vanishing RG scale as a function of the gluon mass parameter is shown in Fig. B.4a. As in the vacuum (cf. Fig. 5.18), the magnetic mass is a non-monotonous function of the gluon mass parameter and has minimum at  $m_{\min}^2$ . As argued in Sec. 5.3.4 and 5.4.3, gluon mass parameters larger than  $m_{\min}^2$  yield unphysical, deconfined solutions. In the following we name the solution we get for  $m_\Lambda^2 = m_{\min}^2$  decoupling solution, but stress that we obtain decoupling solutions for all values of the gluon mass parameters that fulfill  $m_{\Lambda, \text{scaling}}^2 < m_\Lambda^2 \leq m_{\min}^2$ . As discussed in detail in Chapter 5, we cannot further constrain the gluon mass parameter without solving the mSTI or the longitudinal



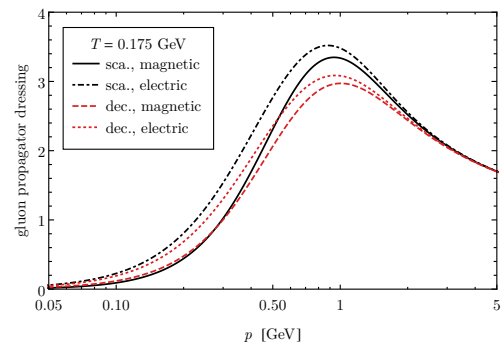
(a) Magnetic mass over gluon mass parameter.



(b) Ghost propagator dressing.



(c) Gluon propagators.



(d) Gluon propagator dressings.

Figure B.4.: Gluon mass analysis at fixed temperature  $T = 0.175$  GeV. We vary the gluon mass parameter at the cutoff scale and find a non-monotonous behavior of the magnetic gluon mass gap. We label the solution with the lowest magnetic mass decoupling solution.

sector. The ghost propagator dressings corresponding to the different solutions are shown in Fig. B.4b, the gluon propagators in Fig. B.4c and B.4d. For the scaling as well as the decoupling solution the temperature-dependent mass artifact is subtracted via (8.18). As in the vacuum, see Fig. 5.19, the different solutions show sizable differences also in the mid-momentum regime that ask for further, more detailed investigations. The differences are, however, in line with our no family argument from Sec. 5.4.3.

## C. Technicalities

The numerical calculations in this dissertation are intricate. This appendix provides technical details for the sake of completeness and reproducibility. Section C.1 describes the workflow of the fQCD collaboration, parts of which were established during this thesis. In Sec. C.2, we discuss the construction of projection operators. Finally, we specify the used regulator parameterizations and scale setting procedures in Sec. C.3 and C.4.

### C.1. fQCD Workflow

In this dissertation the tools established by the fQCD collaboration [64] are employed to solve the coupled integro-differential equations. The most important steps of the computations and the tools used are outlined below.

1. Symbolic equations: DoFun [140, 141] is a Mathematica package that allows deriving symbolic Dyson-Schwinger as well as functional renormalization group equations from a given (symbolic) action.
2. Algebraic equations: Given a representation of all correlation functions in terms of basis tensors and corresponding dressings, the symbolic equations are translated into algebraic equations with DoFun [141].
3. Projecting: To obtain numerically solvable scalar flow equations, the tensorial algebraic equations are projected as described in Sec. C.2.
4. Tracing: The projected flow equations are traced with FormTracer [2] that uses FORM [171–174] and its color package [180]. Since the traced equations are very large, they are optimized for numerical evaluation with FORM’s optimization algorithm [173].
5. Code generation: The integrands on the right-hand sides of the coupled flow equations depend on many variables and momentum- and scale-dependent dressing functions. Thus, evaluating them requires a lot of straightforward code. To cope with this task, and to avoid human errors, a Mathematica package called *CreateKernels* is used to generate the kernel files. Its development was initiated in this thesis.
6. Numerical simulation: The calculation is performed with *frgsolver*, a flexible, object-orientated, parallelized C++ library developed by the authors of [65]. It uses the adaptive ordinary differential equation solver from the BOOST libraries [327], the Eigen linear algebra library [328], and an adaptive multidimensional integration routine from [329] which implements [330, 331].

## C.2. Projecting Tensor Equations

While the flow equation for the generalized effective action is a scalar equation, the flow equations for the  $n$ -point functions are tensor-valued. Since projection operators that project the tensor equations onto scalar dressing functions are frequently used throughout this thesis, we discuss their construction in the following.

To this end, we consider an  $n$ -point function  $\Gamma_\alpha$  with a complete tensor basis  $\mathcal{T}_\alpha$  and superindex  $\alpha$  that consists of all Dirac, Lorentz, and gauge group indices. Denoting the dressings of the basis tensors by  $\lambda$ , the  $n$ -point function is given by

$$\Gamma_\alpha = \lambda^m \mathcal{T}_\alpha^m,$$

where summation over repeated dressing indices is implied and momentum arguments are suppressed. The general projection operator  $P$  has the form

$$P_\alpha^i = A^{in} \mathcal{T}_\alpha^n,$$

where  $A$  is a matrix whose  $i$ -th row contains the scalar coefficients of the  $i$ -th projection operator. We want to construct  $A$  such that  $P_\alpha^i \cdot \Gamma_\alpha$  yields the  $i$ -th dressing function, i.e.,

$$P_\alpha^i \cdot \Gamma_\alpha = \lambda^m A^{in} \underbrace{\mathcal{T}_\alpha^n \cdot \mathcal{T}_\alpha^m}_{\equiv M^{nm}} \stackrel{!}{=} \lambda^i, \quad (\text{C.1})$$

where  $M$  is the metric tensor of the tensor space. Equation (C.1) is fulfilled if

$$A^{in} M^{nm} = \mathbb{1}^{im}. \quad (\text{C.2})$$

If the tensor basis is linearly independent, the metric tensor  $M$  is invertible and the projection operators are given by

$$P_\alpha^i = (M^{-1})^{in} \mathcal{T}_\alpha^n. \quad (\text{C.3})$$

In general, using a degenerate basis is possible since it is sufficient that (C.2) is fulfilled. In this case, one has some freedom to choose the entries in  $A$ . In the case of an orthogonal basis, (C.3) reduces to  $P_\alpha^i = \frac{\mathcal{T}_\alpha^i}{\mathcal{T}_\alpha^i \cdot \mathcal{T}_\alpha^i}$  (where summation is not implied in the denominator).

### C.2.1. Incomplete Tensor Bases

We illustrate the consequences of incomplete tensor bases with a simple example. Consider a tensor space spanned by two real Euclidean vectors,  $\Gamma_\mu = \lambda^p p_\mu + \lambda^q q_\mu$ . To project onto, say,  $\lambda^p$ , we apply (C.3) to obtain the projection operator,  $P_\mu^p = \frac{q^2 p_\mu - p \cdot q q_\mu}{p^2 q^2 - p \cdot q^2}$ , which yields  $P_\mu^p \Gamma_\mu = \lambda^p$  as desired. If we work with an incomplete tensor basis instead, and, e.g., take only  $p_\mu$  into account, the projection operator we obtain from (C.3) is  $\tilde{P}_\mu^p = \frac{p_\mu}{p^2}$ . Applying this projection operator yields  $\tilde{P}_\mu^p \Gamma_\mu = \lambda^p + \frac{p \cdot q}{p^2} \lambda^q \neq \lambda^p$ . Hence, unless  $\lambda^q = 0$ , we get a non-physical contribution to  $\lambda^p$  due to the projection operator. Even worse, if  $\lambda^q$  does not vanish linearly with  $p$ , this contribution is divergent. Thus, using an incomplete basis relies on the assumption that the dressings of non-included basis tensors are small. In this light, we were lucky that the simple, incomplete transverse tensor bases we used in Chapter 5 did not cause any problems. Resolving the longitudinal sector requires more elaborate tensor bases since divergent artifacts quickly arise in the longitudinal sector.



### C.3. Regulator Parameterization

In the FRG, the choice of the regulator, together with the choice of the cutoff-independent parts of the initial effective action corresponds to defining a renormalization scheme, see [25] for a detailed discussion. In general, the regulators are subject to optimization, i.e., they can be chosen to minimize the systematic errors, see [25, 147, 332], and [333, 334] for recent extensions and applications. However, in our advanced truncation the results are independent of the regulator choice, see Sec. 3.1.2. Thus, there is no need to optimize and we use the regulators as specified below.

#### Chapter 5 and 6 – Vacuum Yang-Mills Theory

At vanishing temperature, we regulate the ghost and gluon fluctuations with

$$\begin{aligned} R_k^{c,ab}(q) &= \tilde{Z}_c r(q^2/k^2) q^2 \delta^{ab}, \\ R_{k,\mu\nu}^{A,ab}(q) &= \tilde{Z}_A r(q^2/k^2) q^2 \delta^{ab} \Pi_{\mu\nu}^\perp(q), \end{aligned} \quad (\text{C.4})$$

respectively. For historical reasons, the results in [1], and thus Sec. 5.1 – 5.3, were obtained with a smooth version of the flat regulator with  $a = 0.02$ , see (3.10) for its definition. The results in Sec. 5.4 and Chapter 6 are computed with the exponential regulator shape function (3.11) with  $m = 2$ .

In (C.4) we multiply the regulators with scaling factors  $\tilde{Z}$ , related to the corresponding wave function renormalizations of the gluon and ghost fields,

$$\begin{aligned} \tilde{Z}_c &:= Z_{c,k}(p = k), \\ \tilde{Z}_A &:= Z_{A,k}(p = (k^n + \bar{k}^n)^{1/n}), \end{aligned} \quad (\text{C.5})$$

where we choose  $n \approx 6$  and  $\bar{k} \approx 1 \text{ GeV}$ . The cutoff scale running of  $\tilde{Z}_A$  is held constant below scales of about 1 GeV since the gluon wave function renormalization  $Z_{A,k}(p \approx k)$  diverges for  $k \rightarrow 0$ . Separating the tensor structure by

$$[\Gamma_{AA}^{(2)}]_{\mu\nu}^{ab}(p) =: \Gamma_{AA,k}^{(2)}(p) \delta^{ab} \Pi_{\mu\nu}^\perp(p),$$

we parameterize  $\Gamma_{AA,k}^{(2)}(p)$  by

$$\Gamma_{AA,k}^{(2)}(p) =: Z_{A,k}(p) \cdot p^2 \equiv \bar{Z}_{A,k}(p) \cdot p^2 + m_k^2 \equiv \hat{Z}_{A,k}(p) \cdot (p^2 + m_k^2), \quad (\text{C.6})$$

where we define  $m_k^2 := \Gamma_{AA,k}^{(2)}(0)$  to guarantee the uniqueness of  $\bar{Z}_{A,k}$  and  $\hat{Z}_{A,k}$ . As shown in Fig. C.1, these choices differ considerably in the non-perturbative regime. In particular the naive choice  $Z_{A,k}$  diverges since it carries the gluon mass gap. Consequently, we freeze  $Z_{A,k}$  at a scale  $\bar{k}$  close to 1 GeV. Varying the value of  $\bar{k}$  and  $n$  in (C.5) has no influence on the results.

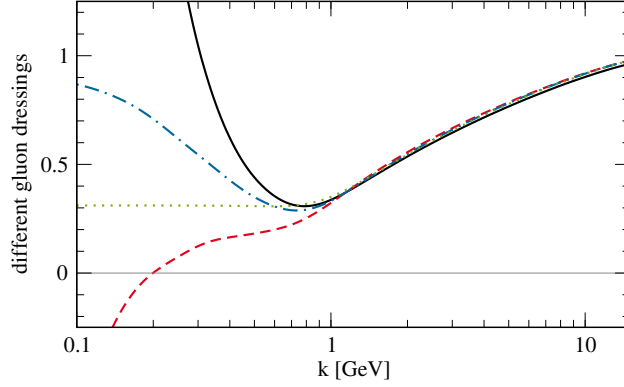


Figure C.1.: Possible choices for the scaling prefactor in the gluon regulator:  $Z_{A,k}(k)$  (black, solid),  $\bar{Z}_{A,k}(k)$  (red, dashed),  $\hat{Z}_{A,k}(k)$  (blue, dot-dashed) and  $\tilde{Z}_A$  (green, dotted) as defined in (C.5) and (C.6). Our results are independent of the choice of the scaling prefactor.

### Chapter 7 – Unquenched Two-Flavor QCD

The ghost and gluon regulators are taken over from the Yang-Mills system. It remains to specify the regulators for the quark and meson fields in (7.1). These are given by

$$R_k^q(q) = \tilde{Z}_q r(q^2/k^2) \not{q},$$

$$R_k^\phi(q) = \tilde{Z}_\phi r(q^2/k^2) q^2,$$

where  $\tilde{Z}_q = Z_{q,k}(p=0)$  and  $\tilde{Z}_\phi = Z_{\phi,k}(p=0)$  are the respective wave function renormalizations evaluated at vanishing momentum. For the unquenched system we use the exponential regulator (3.11) with  $m=2$ .

### Chapter 8 – Finite-Temperature Yang-Mills theory

At finite temperature we use (C.4) and (C.5) with minor modifications. To determine the scaling factor  $\tilde{Z}_A$ , we use the magnetic wave function renormalization,  $Z_{A,k}(p) = Z_{A,k}^M(p)$ . One can just as well use the electric wave function renormalization since they are equal in the ultraviolet where the scaling factors might be relevant. Equation (C.4) and the identity  $\Pi_{\mu\nu}^\perp(p) = \Pi_{\mu\nu}^M(p) + \Pi_{\mu\nu}^E(p)$  imply the same regularization for electric and magnetic modes. We use the exponential regulator shape function (3.11) with  $m=2$  due to its advantages for numerical calculations of thermodynamic quantities [252, 302], see also Sec. 8.2.1.

## C.4. Scale Setting and Renormalization

In first-principle QCD calculations, the scale is implicitly set by the value for the strong running coupling at the renormalization scale. The internal units are then translated into physical units by the use of an observable. In this dissertation we set scale with the bump of the gluon propagator dressing  $1/Z_A(p)$  at vanishing temperature, see, e.g., Fig. 5.5. We rescale all dimensionful quantities such that the bump lies at the corresponding lattice scale. To compare to lattice results, the global normalizations of the fields have to be adjusted. In the following two sections we provide details on this normalization that are too technical for the main text.

### Chapter 5 – Yang-Mills Correlators

We rescale the gluon dressing by  $Z_A^{-1}(p) \rightarrow a Z_A^{-1}(p)$  with  $a$  chosen such that it minimizes

$$N(a) = \sum_i \frac{\Delta x_i}{\Delta E_i^2} \left[ \left( a Z_A^{-1}(p_i) - Z_A^{L,-1}(p_i) \right)^2 + \left( a \partial_p Z_A^{-1}(p_i) - \partial_p Z_A^{L,-1}(p_i) \right)^2 \right], \quad (\text{C.7})$$

where we sum over all lattice points that fulfill  $0.8 \text{ GeV} \leq p_i \leq 4 \text{ GeV}$ . We do not include points with smaller momenta since they can be affected by the global gauge fixing procedure. Points with momentum larger than  $4 \text{ GeV}$  are also not included since they might contain finite volume effects. In (C.7), we weight the lattice points with  $\Delta x_i / \Delta E_i^2$ , where  $\Delta x_i$  denotes the distance to the next point and  $\Delta E_i$  is the statistical error. The superscript  $L$  in (C.7) marks lattice dressing functions. The ghost dressing is re-scaled analogously.

### Chapter 8 – Finite-Temperature Yang-Mills theory

The temperatures of the  $SU(2)$  lattice results from [250, 309] are given in units of the critical temperature. In order to compare, we use  $T_c^{SU(2)} = 0.7091 \sqrt{\sigma} = 312 \text{ MeV}$  [335] to convert the temperature into units of GeV, where the string tension  $\sigma$  is given by  $\sigma = 0.440 \text{ GeV}^2$ . These lattice results need to be renormalized for each temperature separately. We determine the temperature-dependent renormalization constants by fitting all lattice points above  $p \geq \max(2\pi T, 1 \text{ GeV})$  to our results.

The  $SU(3)$  lattice results from [311] do not include the vacuum case  $T = 0$ . Therefore, we allow for a scale mismatch by introducing a temperature-independent relative scale factor  $r_s$ , in addition to the temperature-independent wave function renormalization constant  $z_L$ . We determine  $r_s$  and  $z_L$  by fitting the magnetic gluon dressing function  $1/(z_L Z_A^M(r_s T, r_s p))$  simultaneously for all temperatures to all lattice points above  $p \geq 0.5 \text{ GeV}$ . Subsequently, we use  $r_s$  and  $z_L$  to re-scale the magnetic as well as the electric lattice propagators to our data. We find the relative scale mismatch  $r_s - 1$  to be small, of the order of 2%. The temperatures in [311] are given in units of GeV. In order to simplify the discussion, we convert the temperatures into units of the critical temperature, using their value for the  $SU(3)$  phase transition temperature,  $T_c = 270 \text{ MeV}$ .

## C.5. Tensor Bases of Higher Vertices

In this section we provide the tensor bases of higher vertices. They are identical to (and taken from) [3]. We suppress transverse projection operators attached to all gluon legs.

### Two-Quark-Two-Gluon Vertex

The transversely projected two-quark-two-gluon vertex,

$$\Gamma_{\bar{q}qA^2}^{(4)}(p_1, p_2, p_3) = \mathbb{1}_f \sum_{i=1}^{18} \lambda_{\bar{q}qA^2}^{(i)}(\bar{p}) \mathcal{T}_{\bar{q}qA^2}^{(i)}(p_1, p_2, p_3, p_4),$$

receives contributions from  $\bar{q} \not{D}^n q$  with  $n \geq 2$ .

We take into account the tensors corresponding to  $\bar{q} \not{D}^2 q$ ,

$$\begin{aligned} \mathcal{T}_{\bar{q}qA^2}^{(16)} &= \gamma_\mu \gamma_\nu T_c^a T_c^b + \gamma_\nu \gamma_\mu T_c^b T_c^a, & \mathcal{T}_{\bar{q}qA^2}^{(17)} &= \gamma_\mu \gamma_\nu T_c^b T_c^a + \gamma_\nu \gamma_\mu T_c^a T_c^b, \\ \mathcal{T}_{\bar{q}qA^2}^{(18)} &= (\gamma_\mu \gamma_\nu + \gamma_\nu \gamma_\mu) \delta^{ab}, \end{aligned}$$

and  $\bar{q} \not{D}^3 q$ ,

$$\begin{aligned} \mathcal{T}_{\bar{q}qA^2}^{(1)} &= i(p_{1,\mu} \gamma_\nu + p_{1,\nu} \gamma_\mu) \delta^{ab}, & \mathcal{T}_{\bar{q}qA^2}^{(2)} &= i(p_{2,\mu} \gamma_\nu + p_{2,\nu} \gamma_\mu) \delta^{ab}, \\ \mathcal{T}_{\bar{q}qA^2}^{(3)} &= i(p_{1,\mu} \gamma_\nu T_c^a T_c^b + p_{1,\nu} \gamma_\mu T_c^b T_c^a), & \mathcal{T}_{\bar{q}qA^2}^{(4)} &= i(p_{2,\mu} \gamma_\nu T_c^a T_c^b + p_{2,\nu} \gamma_\mu T_c^b T_c^a), \\ \mathcal{T}_{\bar{q}qA^2}^{(5)} &= i(p_{1,\mu} \gamma_\nu T_c^b T_c^a + p_{1,\nu} \gamma_\mu T_c^a T_c^b), & \mathcal{T}_{\bar{q}qA^2}^{(6)} &= i(p_{2,\mu} \gamma_\nu T_c^b T_c^a + p_{2,\nu} \gamma_\mu T_c^a T_c^b), \\ \mathcal{T}_{\bar{q}qA^2}^{(7)} &= i(\gamma_\mu \not{p}_1 \gamma_\nu + \gamma_\nu \not{p}_1 \gamma_\mu) \delta^{ab}, & \mathcal{T}_{\bar{q}qA^2}^{(8)} &= i(\gamma_\mu \not{p}_2 \gamma_\nu + \gamma_\nu \not{p}_2 \gamma_\mu) \delta^{ab}, \\ \mathcal{T}_{\bar{q}qA^2}^{(9)} &= i(\gamma_\mu \not{p}_1 \gamma_\nu T_c^a T_c^b + \gamma_\nu \not{p}_1 \gamma_\mu T_c^b T_c^a), & \mathcal{T}_{\bar{q}qA^2}^{(10)} &= i(\gamma_\mu \not{p}_2 \gamma_\nu T_c^a T_c^b + \gamma_\nu \not{p}_2 \gamma_\mu T_c^b T_c^a), \\ \mathcal{T}_{\bar{q}qA^2}^{(11)} &= i(\gamma_\mu \not{p}_1 \gamma_\nu T_c^b T_c^a + \gamma_\nu \not{p}_1 \gamma_\mu T_c^a T_c^b), & \mathcal{T}_{\bar{q}qA^2}^{(12)} &= i(\gamma_\mu \not{p}_2 \gamma_\nu T_c^b T_c^a + \gamma_\nu \not{p}_2 \gamma_\mu T_c^a T_c^b), \\ \mathcal{T}_{\bar{q}qA^2}^{(13)} &= i(\gamma_\mu \not{p}_3 \gamma_\nu + \gamma_\nu \not{p}_3 \gamma_\mu) \delta^{ab}, & \mathcal{T}_{\bar{q}qA^2}^{(14)} &= i(\gamma_\mu \not{p}_3 \gamma_\nu T_c^a T_c^b + \gamma_\nu \not{p}_3 \gamma_\mu T_c^b T_c^a), \\ \mathcal{T}_{\bar{q}qA^2}^{(15)} &= i(\gamma_\mu \not{p}_3 \gamma_\nu T_c^b T_c^a + \gamma_\nu \not{p}_3 \gamma_\mu T_c^a T_c^b), \end{aligned}$$

that are symmetric under  $A_\mu^a \leftrightarrow A_\nu^b$ .

### Two-Quark-Three-Gluon Vertex

The transversely projected two-quark-three-gluon vertex,

$$\Gamma_{\bar{q}qA^3}^{(5)}(p_1, p_2, p_3, p_4) = \mathbb{1}_f \sum_{i=1}^5 \lambda_{\bar{q}qA^3}^{(i)}(\bar{p}) \mathcal{T}_{\bar{q}qA^3}^{(i)}(p_1, p_2, p_3, p_4, p_5),$$

receives contributions from  $\bar{q} \not{D}^n q$  with  $n \geq 3$ . We take the tensors symmetric under  $A_\mu^a \leftrightarrow A_\nu^b \leftrightarrow A_\rho^c$  and corresponding to  $\bar{q} \not{D}^3 q$  into account:

$$\begin{aligned} \mathcal{T}_{\bar{q}qA^3}^{(1)} &= -(\gamma^\mu \gamma^\nu \gamma^\rho - \gamma^\mu \gamma^\rho \gamma^\nu + \dots) f^{abc}, & \mathcal{T}_{\bar{q}qA^3}^{(2)} &= i(\gamma^\mu \gamma^\nu \gamma^\rho T_c^a T_c^b T_c^c + \text{perm.}), \\ \mathcal{T}_{\bar{q}qA^3}^{(3)} &= i(\gamma^\mu \gamma^\nu \gamma^\rho T_c^c T_c^a T_c^b + \text{perm.}), & \mathcal{T}_{\bar{q}qA^3}^{(4)} &= i(\gamma^\mu \gamma^\nu \gamma^\rho T_c^b T_c^c T_c^a + \text{perm.}), \\ \mathcal{T}_{\bar{q}qA^3}^{(5)} &= i(\gamma^\mu \gamma^\nu \gamma^\rho T_c^b T_c^a T_c^c + \text{perm.}). \end{aligned}$$

### Quark-Pion Yukawa Vertex

Using the generators of the  $SU(2)$  flavor group  $T_f^a$ ,  $a \in \{1, 2, 3\}$ , the quark-pion Yukawa vertex is expanded by [336]:

$$\Gamma_{\bar{q}q\pi}^{(3)}(p, q) = \mathbb{1}_c T_f^a \gamma_5 i \sum_{i=1}^4 h_{\bar{q}q\pi}^{(i)}(p_{\text{soft}}) \mathcal{T}_{\bar{q}q\pi}^{(i)}(p, q).$$

The basis elements are given by

$$\begin{aligned} \mathcal{T}_{\bar{q}q\pi}^{(1)}(p, q) &= \mathbb{1}_s, & \mathcal{T}_{\bar{q}q\pi}^{(2)}(p, q) &= i (\not{p} + \not{q}), \\ \mathcal{T}_{\bar{q}q\pi}^{(3)}(p, q) &= i (\not{p} - \not{q}), & \mathcal{T}_{\bar{q}q\pi}^{(4)}(p, q) &= -\frac{1}{2} [\not{p}, \not{q}]. \end{aligned} \quad (\text{C.8})$$

We compute the momentum dependence of the dressing functions of the Yukawa interaction from the soft-pion channel, i.e., the quark and antiquark have opposite momenta. This is the channel that is most important for the momentum-dependent version of the dynamical hadronization [65]. The full momentum dependence is approximated by

$$h_{\bar{q}q\pi}^{(i)}(p, q) = h_{\bar{q}q\pi}^{(i)} \left( \sqrt{\frac{(p_1 - p_2)^2}{4} + (p_1 + p_2)^2} \right).$$

This choice is the outcome of explicit checks [65]. See [3, 57] for more details on higher order quark-meson interactions and their explicit tensor bases.

## D. FormTracer Details

This appendix is based on [2] and contains details on FormTracer. Section D.1 explains its usage. FormTracer is compared to other tools in Sec. D.2. Finally, we provide information on algorithmic details in Sec. D.3.

### D.1. Installation and Usage

We first describe the installation process and then show an explicit usage example.

#### D.1.1. Quick-Start Guide

FormTracer requires FORM<sup>1</sup> version 4.1 and Mathematica 10.0 or higher. We recommend installing FormTracer with the fully automated installation script, which can be downloaded and started by evaluating

```
In[1]:= Import["https://raw.githubusercontent.com/FormTracer/\n             FormTracer/master/src/FormTracerInstaller.m"]
```

in a Mathematica input cell. If FORM is not already installed on your computer, it can be installed automatically during the installation process. As an alternative to the automatic installation, one can also download FormTracer manually from [170] and install it by copying it into Mathematica's application folder. Three notebooks with examples are available for download:

- <https://raw.githubusercontent.com/FormTracer/FormTracer/master/src/Examples/FormTracerShowcase.nb>
- <https://raw.githubusercontent.com/FormTracer/FormTracer/master/src/Examples/FormTracerMinimalExample.nb>
- <https://raw.githubusercontent.com/FormTracer/FormTracer/master/src/Examples/FourQuarkInteraction.nb>

The first notebook provides an extensive overview over the features of FormTracer based on many example traces, whereas the second provides the minimal prerequisite for being able to perform simple traces over spacetime, spinor and gauge group indices. To demonstrate FormTracer's performance, we provide a third notebook with a more complicated example, namely the tracing of four-quark interaction diagrams performed in [65]. All examples can also be found in the examples folder in the installation directory. The first two examples provide an input cell to execute the automatic installation script as shown above. While these example files should be understood as quick-start guides to start using FormTracer as fast as possible, we also provide an extensive documentation in Mathematica's Documentation Center. A good overview is given on the main page that can be accessed by searching for *FormTracer* in the Documentation Center.

---

<sup>1</sup>The source code as well as compiled executables can be obtained from [337].

### D.1.2. Basic Usage Examples

Once installed, FormTracer is loaded via

```
In[2]:= Needs["FormTracer`"]
```

FormTracer requires to define a custom notation which makes it easily adaptable to the output of external diagram generators. Below, we define our notation for Lorentz tensors and group tensors for two  $SU(N)$  groups. For more information on the individual functions, see the respective help pages in Mathematica's Documentation Center.

```
In[3]:= DefineLorentzTensors[deltaLorentz[mu, nu], vec[p, mu], sp[p, q],
    eps[], deltaDirac[i, j], gamma[mu, i, j], gamma5[i, j]];
DefineGroupTensors[{
    {SUNfund, {color, Nc}, deltaAdj[a, b],
    f[a, b, c], deltaFund[i, j], T[a, i, j]},
    {SUNfund, {flavor, Nf}, deltaAdjFlav[a, b], fFlav[a, b, c],
    deltaFundFlav[i, j], TFlav[a, i, j]}}];
DefineExtraVars[alpha, Mpsi, Zpsi, xi, g];
```

FormTracer requires all further external variables to be declared before usage since FORM necessitates it. In the last line, we defined all variables that are used in the examples below. Now, one can start tracing, e.g.,  $p_\mu \delta_{\mu\nu} p_\nu \delta^{ij} \delta^{ji}$ :

```
In[4]:= FormTrace[vec[p, nu] deltaLorentz[mu, nu]
    vec[q, mu] deltaFund[i, j] deltaFund[j, i]]
```

```
Out[4]= Nc sp[p, q]
```

or,  $\text{Tr } \gamma^\mu \not{p} \not{q} \gamma^\mu$ ,

```
In[5]:= FormTrace[vec[p, nu] vec[q, rho] gamma[mu, i1, i2]
    gamma[nu, i2, i3] gamma[rho, i3, i4] gamma[mu, i4, i1]]
```

```
Out[5]= 16 sp[p, q]
```

FormTracer supports a shorthand notation for Dirac matrices that allows omitting auxiliary indices. For example, one can evaluate the above Dirac trace  $\text{Tr } \gamma^\mu \not{p} \not{q} \gamma^\mu$  via

```
In[6]:= FormTrace[gamma[{mu, vec[p], vec[q], mu}]]
```

```
Out[6]= 16 sp[p, q]
```

As a more complex example from QCD, consider one-loop quark contribution to the gluon propagator that is given by the following uncontracted expression

```
In[7]:= testExpr = deltaAdj[colAdja, colAdjb]*
    (deltaLorentz[Mu, Nu] + xi (vec[p, Mu] vec[p, Nu])/sp[p, p])*
    g*gamma[Mu, i1, i4]*deltaFundFlav[flavFunda, flavFundd]*
    T[colAdja, colFunda, colFundd]*(deltaDirac[i2, i1] Mpsi +
    I gamma[Rho, i2, i1] vec[-p - q, Rho] Zpsi )/
    (Mpsi^2 + sp[p + q, p + q] Zpsi^2)*
```

```

deltaFundFlav[flavFundb, flavFunda]*
deltaFund[colFundb, colFunda]*g*gamma[Nu, i3, i2]*
deltaFundFlav[flavFundc, flavFundb]*
T[colAdj, colFundc, colFundb]*
(deltaDirac[i4, i3] Mpsi + I gamma[Sigma, i4, i3]*
vec[q, Sigma] Zpsi)/(Mpsi^2 + sp[q, q] Zpsi^2)*
deltaFundFlav[flavFundd, flavFundc]*
deltaFund[colFundd, colFundc];

```

which yields

```

In[8]:= Simplify[FormTrace[testExpr]]

Out[8]= (2 g^2 (-1 + Nc^2) Nf (2 xi Zpsi^2 sp[p, q] sp[p, p + q] +
sp[p, p] (Mpsi^2 (4 + xi) - (2 + xi) Zpsi^2 sp[q, p + q]))) /
(sp[p, p] (Mpsi^2 + Zpsi^2 sp[q, q]) (Mpsi^2 +
Zpsi^2 sp[p + q, p + q]))

```

For further usage examples consult the documentation in Mathematica's Documentation Center or one of the example notebooks.

## D.2. Comparison with Other Programs

FormTracer is designed for the specific task of evaluating Lorentz, Dirac and group traces. The focus in its development was on usability, performance and the ability to handle very large expressions. In a typical workflow, these expressions are provided by further external programs that generate diagrams. One example for such a tool with particular relevance for calculations in non-perturbative functional methods is DoFun [141]. In perturbative applications, input, e.g., from FeynArts [338] or QGRAF [339] as popular Feynman diagram generators is feasible.

Many tools exist that partially overlap with FormTracer in their functionalities, see for example [167–169] for reviews on computer-algebraic methods in perturbative applications. In the following, we provide a comparison to programs that are from our point of view most straightforwardly adaptable to tracing applications in the context of non-perturbative functional method calculations. Although these tools were designed with more general applications in mind, we restrict the following comparison to their tracing capabilities.

- FORM [171–173] is a dedicated tool for high-performance symbolic calculations. It is a standalone program that comes with its own specialized input language. Furthermore, it has a built-in capability of taking Lorentz and Dirac traces as well as group traces involving arbitrary simple Lie groups using the color package [180]. The primary focus of FORM lies in speed and the ability to handle even very large symbolic expressions. However, the usage of FORM poses a rather steep learning curve for the beginner. FormTracer aims to overcome this limitation by combining a Mathematica front end in combination with a specialized expansion algorithm in Mathematica while still making use of the computational power of FORM in the background. By construction, it is always possible to write native FORM code for a specific tracing application that is as fast as the code generated automatically by FormTracer, but the latter is for many applications the more convenient choice.



FormLink [340] provides a way of accessing FORM via Mathematica to execute FORM commands and imports results back into Mathematica. However, it still requires the user to write FORM code and is therefore very close to FORM itself in its usage.

- FeynCalc [341–343] is a Mathematica package for the symbolic semi-automatic evaluation of Feynman diagrams and allows in particular to evaluate Dirac and Lorentz traces in arbitrary dimensions as well as fundamental  $SU(N)$  group traces. Unlike FormTracer, it includes a rich set of tools beyond the ability of taking traces such as tensor reduction algorithms for one-loop integrals that make it particularly suited for perturbative applications. On the other hand, FormTracer is a specialized tracing tool and the complexity of expressions it can handle as well as its performance are typically only limited by FORM itself. As a consequence, FormTracer is often more than an order of magnitude faster than FeynCalc in examples typically occurring in non-perturbative functional QCD calculations.
- HEPMath [344] is a Mathematica package extending the functionality of Tracer [345]. It provides algorithms for high energy physics computations and therefore includes support for Lorentz, Dirac and  $SU(3)$  group traces. In its functionality, HEPMath is similar to FeynCalc, which it aims to surpass in usability and flexibility without focus on performance. It is designed as a convenience tool with a more general scope than FormTracer however with a significantly smaller functionality in the tracing capability itself.

Apart from this incomplete selection, we want to acknowledge dedicated tools for the evaluation of diagrams such as Mincer [346], CompHEP [347], DIANA [348], FormCalc [349], MATAD [350], GRACE [351], SANCscope [352], MadLoop [353], GOSAM [354], Package X [355, 356] and Forcer [357] as well as computer algebra systems/packages for tensor algebra with tracing capabilities like GiNaC [358] GAMMA [359], Cadabra [360], SymPy [361], xAct [362, 363] and Redberry [364].

### D.3. Additional Algorithmic Details

The decomposition of an untraced expression into Lie groups and a Lorentz part was discussed in Sec. 4.2. FormTracer can take control over how FORM deals with the tracing of the Lorentz part, which is detailed in the next subsection. Thereafter, some general algorithmic tricks are briefly discussed.

#### D.3.1. Partial Traces over Lorentz Tensors

In some cases, where the scalars  $L_{i_0 i_1 \dots i_n}$  in (4.1) are very large, a further decomposition can improve the performance by splitting the full trace into partial intermediate traces. The decomposition can be turned on with the option `DisentangleLorentzStructures[True]`, which first groups the expressions  $L_{i_0 i_1 \dots i_n}$  into a sum of Lorentz and Dirac scalars

$$L_{i_0 i_1 \dots i_n} = \sum_j l_{i_0 i_1 \dots i_n; j}.$$

Next, each of these summands is written as,

$$l_{i_0 i_1 \dots i_n; j} = \prod_{f=1}^{N_j} \left( \prod_{g=1}^{N_{jf}} l_{i_0 i_1 \dots i_n; jfg}^{\{\mu_{jfg}\}} \right).$$

Here, the factors of the outer product are the smallest possible Lorentz scalars and the factors of the inner product the smallest possible, already traced, Dirac scalars that allow for such a representation. The superscripts  $\{\mu_{jfg}\}$  denote a set of Lorentz indices and the factors are ordered such that

$$\{\mu_{jfg}\} \cap \{\mu_{jfg+1}\} \neq \emptyset.$$

This ordering is not unique and subject to optimization. However, as of now no ordering optimization is implemented and FormTracer simply chooses an ordering. To avoid large expressions by possibly exploiting intermediate simplifications, the Lorentz traces are evaluated successively,

$$\text{Tr} \left( \prod_{g=1}^{N_{jf}} l_{i_0 i_1 \dots i_n; jfg}^{\{\mu_{jfg}\}} \right) = \text{Tr} \left( l_{i_0 i_1 \dots i_n; jf1}^{\{\mu_{jf1}\}} \text{Tr} \left( \dots \text{Tr} \left( l_{i_0 i_1 \dots i_n; jf(N_{jf}-1)}^{\{\mu_{jf(N_{jf}-1)}\}} l_{i_0 i_1 \dots i_n; jfN_{jf}}^{\{\mu_{jfN_{jf}}\}} \right) \right) \right),$$

and the results are multiplied and summed only at the very end. This feature has been crucial for quantum gravity applications, in particular for tracing the four-graviton vertex equation [178].

### D.3.2. Other Algorithmic Improvements

We implemented two further improvements that greatly reduce the number of terms in many of our standard applications. Internal loop momenta are in general sums of the loop and external momenta. Simply expanding all vector sums (e.g.  $(p+q)_\mu \rightarrow p_\mu + q_\mu$ ) leads to an unnecessarily large number of terms. Thus, we replace sums of vectors by abbreviations and reinsert the explicit momenta after the tracing process. Although this can prevent cancellations in the final result, we found these abbreviations to be very advantageous for the performance as well as the size of the final result in the general case involving off-shell momenta.

By default, FORM expands all powers of sums, even if the sums only contain scalars. In this special case, however, an expansion is not necessary to evaluate the traces. Therefore, we prevent FORM from expanding powers over sums of scalars by using a user-defined power function symbol in the FORM code.

# Acknowledgments

I am indebted to many people who helped me in one way or another with writing this thesis. Nonetheless, I restrict the list of names to those with whom I discussed physical aspects in depth. Needless to say, the support from the others was equally indispensable.

First of all, I want to express my gratitude to my supervisor Jan M. Pawłowski. Countless long discussions contributed significantly to my understanding of physics and the progress of my work. His open door and an informal atmosphere made working with him very enjoyable. Without his constant support, this thesis would not have been possible.

I am grateful to Joerg Jaeckel for being my second referee.

My special thanks go to my closest two collaborators, Mario Mitter and Nils Strodthoff. They allowed me to join their team, shared their code, and, very importantly, taught me a lot about QCD and the FRG. Furthermore, I thank Lukas Corell for working on Yang-Mills theory in three dimensions.

Additionally, I thank Jürgen Berges, Lukas Corell, and Markus Heller for many insights on non-equilibrium quantum field theory that I gained during our meetings.

I greatly appreciate many discussions with Daniel Rosenblüh, Alexander Rothkopf, and Nicolas Wink on spectral functions.

Furthermore, I am thankful to the members of the fQCD-collaboration not named yet, Jens Braun, Wei-jie Fu, Marc Leonhardt, Martin Pospiech, and Fabian Rennecke.

During many conferences, schools, and visits, I enjoyed discussions with, among others, Reinhard Alkofer, Adrian Blum, Christian Fischer, Ouraman Hajizadeh, Lukas Holicki, Markus Huber, Axel Maas, Walid Mian, Bernd-Jochen Schäfer, Julien Serreau, Vladyslav Shtabovenko, Lorenz von Smekal, Richard Williams, and Nicolás Wschebor.

Especially in the beginning of my time in Heidelberg, I benefited from discussions with Igor Boettcher, Nicolai Christiansen, Leonard Fister, Tina Herbst, and Andreas Rodigast.

Moreover, I want to thank Laura Classen, Manuel Reichert, and Felix Ziegler for jointly organizing the Cold Quantum Coffee.

I am indebted to Eduardo Grossi, Markus Heller, Fabian Rennecke, Nicolas Wink, and Felix Ziegler for critical reading of parts of the manuscript.

I acknowledge financial support by the German Academic Scholarship Foundation.

Last but not least, I want to express my utmost gratitude to my family and my girlfriend.

# Bibliography

- [1] A. K. Cyrol, L. Fister, M. Mitter, J. M. Pawłowski, and N. Strodthoff, “Landau gauge Yang-Mills correlation functions,” *Phys. Rev. D* **94**, 054005 (2016), arXiv:1605.01856 [hep-ph].
- [2] A. K. Cyrol, M. Mitter, and N. Strodthoff, “FormTracer - A Mathematica Tracing Package Using FORM,” *Comput. Phys. Commun.* **C219**, 346 (2017), arXiv:1610.09331 [hep-ph].
- [3] A. K. Cyrol, M. Mitter, J. M. Pawłowski, and N. Strodthoff, “Non-perturbative quark, gluon and meson correlators of unquenched QCD,” (2017), arXiv:1706.06326 [hep-ph].
- [4] A. K. Cyrol, M. Mitter, J. M. Pawłowski, and N. Strodthoff, “Non-perturbative finite-temperature Yang-Mills theory,” (2017), arXiv:1708.03482 [hep-ph].
- [5] A. K. Cyrol, M. Q. Huber, and L. von Smekal, “A Dyson–Schwinger study of the four-gluon vertex,” *Eur. Phys. J.* **C75**, 102 (2015), arXiv:1408.5409 [hep-ph].
- [6] C.-N. Yang and R. L. Mills, “Conservation of Isotopic Spin and Isotopic Gauge Invariance,” *Phys. Rev.* **96**, 191 (1954).
- [7] G. Aad *et al.* (ATLAS), “Observation of a new particle in the search for the Standard Model Higgs boson with the ATLAS detector at the LHC,” *Phys. Lett. B* **716**, 1 (2012), arXiv:1207.7214 [hep-ex].
- [8] S. Chatrchyan *et al.* (CMS), “Observation of a new boson at a mass of 125 GeV with the CMS experiment at the LHC,” *Phys. Lett. B* **716**, 30 (2012), arXiv:1207.7235 [hep-ex].
- [9] F. Englert and R. Brout, “Broken Symmetry and the Mass of Gauge Vector Mesons,” *Phys. Rev. Lett.* **13**, 321 (1964).
- [10] P. W. Higgs, “Broken Symmetries and the Masses of Gauge Bosons,” *Phys. Rev. Lett.* **13**, 508 (1964).
- [11] G. S. Guralnik, C. R. Hagen, and T. W. B. Kibble, “Global Conservation Laws and Massless Particles,” *Phys. Rev. Lett.* **13**, 585 (1964).
- [12] J. Jaeckel and A. Ringwald, “The Low-Energy Frontier of Particle Physics,” *Ann. Rev. Nucl. Part. Sci.* **60**, 405 (2010), arXiv:1002.0329 [hep-ph].
- [13] N. Brambilla *et al.*, “QCD and Strongly Coupled Gauge Theories: Challenges and Perspectives,” *Eur. Phys. J.* **C74**, 2981 (2014), arXiv:1404.3723 [hep-ph].
- [14] C. Patrignani *et al.* (Particle Data Group), “Review of Particle Physics,” *Chin. Phys.* **C40**, 100001 (2016).

- [15] S. Durr *et al.*, “Ab-Initio Determination of Light Hadron Masses,” *Science* 322, 1224 (2008), arXiv:0906.3599 [hep-lat].
- [16] S. Borsanyi *et al.*, “Ab initio calculation of the neutron-proton mass difference,” *Science* 347, 1452 (2015), arXiv:1406.4088 [hep-lat].
- [17] E. Salpeter and H. Bethe, “A Relativistic equation for bound state problems,” *Phys. Rev.* 84, 1232 (1951).
- [18] G. Eichmann, H. Sanchis-Alepuz, R. Williams, R. Alkofer, and C. S. Fischer, “Baryons as relativistic three-quark bound states,” *Prog. Part. Nucl. Phys.* 91, 1 (2016), arXiv:1606.09602 [hep-ph].
- [19] C. Wetterich, “Exact evolution equation for the effective potential,” *Phys. Lett.* B301, 90 (1993).
- [20] F. J. Dyson, “The S matrix in quantum electrodynamics,” *Phys. Rev.* 75, 1736 (1949).
- [21] J. S. Schwinger, “On the Green’s functions of quantized fields. 1.” *Proc. Nat. Acad. Sci.* 37, 452 (1951).
- [22] J. S. Schwinger, “On the Green’s functions of quantized fields. 2.” *Proc. Nat. Acad. Sci.* 37, 455 (1951).
- [23] J. M. Cornwall, R. Jackiw, and E. Tomboulis, “Effective Action for Composite Operators,” *Phys. Rev.* D10, 2428 (1974).
- [24] J. Berges, N. Tetradis, and C. Wetterich, “Non-perturbative renormalization flow in quantum field theory and statistical physics,” *Phys. Rept.* 363, 223 (2002), arXiv:hep-ph/0005122.
- [25] J. M. Pawłowski, “Aspects of the functional renormalisation group,” *Annals Phys.* 322, 2831 (2007), arXiv:hep-th/0512261.
- [26] H. Gies, “Introduction to the functional RG and applications to gauge theories,” *Lect. Notes Phys.* 852, 287 (2012), arXiv:hep-ph/0611146.
- [27] B.-J. Schaefer and J. Wambach, “Renormalization group approach towards the QCD phase diagram,” *Phys. Part. Nucl.* 39, 1025 (2008), arXiv:hep-ph/0611191.
- [28] O. J. Rosten, “Fundamentals of the Exact Renormalization Group,” *Phys. Rept.* 511, 177 (2012), arXiv:1003.1366 [hep-th].
- [29] J. Braun, “Fermion Interactions and Universal Behavior in Strongly Interacting Theories,” *J. Phys.* G39, 033001 (2012), arXiv:1108.4449 [hep-ph].
- [30] L. von Smekal, “Universal Aspects of QCD-like Theories,” *Nucl. Phys. Proc. Suppl.* 228, 179 (2012), arXiv:1205.4205 [hep-ph].
- [31] C. D. Roberts and A. G. Williams, “Dyson-Schwinger equations and their application to hadronic physics,” *Prog. Part. Nucl. Phys.* 33, 477 (1994), arXiv:hep-ph/9403224.

- [32] R. Alkofer and L. von Smekal, “The infrared behavior of QCD Green’s functions: Confinement, dynamical symmetry breaking, and hadrons as relativistic bound states,” *Phys. Rept.* 353, 281 (2001), arXiv:hep-ph/0007355.
- [33] C. S. Fischer, “Infrared properties of QCD from Dyson-Schwinger equations,” *J. Phys. G* G32, R253 (2006), arXiv:hep-ph/0605173.
- [34] D. Binosi and J. Papavassiliou, “Pinch Technique: Theory and Applications,” *Phys. Rept.* 479, 1 (2009), arXiv:0909.2536 [hep-ph].
- [35] A. Maas, “Describing gauge bosons at zero and finite temperature,” *Phys. Rept.* 524, 203 (2013), arXiv:1106.3942 [hep-ph].
- [36] P. Boucaud, J. Leroy, A. L. Yaouanc, J. Micheli, O. Pene, *et al.*, “The Infrared Behaviour of the Pure Yang-Mills Green Functions,” *Few Body Syst.* 53, 387 (2012), arXiv:1109.1936 [hep-ph].
- [37] H. Sanchis-Alepuz and R. Williams, “Hadronic Observables from Dyson-Schwinger and Bethe-Salpeter equations,” *J. Phys. Conf. Ser.* 631, 012064 (2015), arXiv:1503.05896 [hep-ph].
- [38] K.-c. Chou, Z.-b. Su, B.-l. Hao, and L. Yu, “Equilibrium and Nonequilibrium Formalisms Made Unified,” *Phys. Rept.* 118, 1 (1985).
- [39] J. Berges, “Introduction to nonequilibrium quantum field theory,” *AIP Conf. Proc.* 739, 3 (2005), arXiv:hep-ph/0409233.
- [40] T. Gasenzer and J. M. Pawłowski, “Towards far-from-equilibrium quantum field dynamics: A functional renormalisation-group approach,” *Phys. Lett.* B670, 135 (2008).
- [41] J. Berges and G. Hoffmeister, “Nonthermal fixed points and the functional renormalization group,” *Nucl. Phys.* B813, 383 (2009), arXiv:0809.5208 [hep-th].
- [42] P. de Forcrand, “Simulating QCD at finite density,” *PoS LAT2009*, 010 (2009), arXiv:1005.0539 [hep-lat].
- [43] D. H. Rischke, “The Quark gluon plasma in equilibrium,” *Prog. Part. Nucl. Phys.* 52, 197 (2004), arXiv:nucl-th/0305030.
- [44] Relativistic Heavy Ion Collider (RHIC), <https://www.bnl.gov/rhic/>.
- [45] Large Hadron Collider (LHC), <https://home.cern/>.
- [46] Facility for Antiproton and Ion Research (FAIR), <http://www.fair-center.eu/>.
- [47] Nuclotron-based Ion Collider fAcility (NICA), <http://nica.jinr.ru/>.
- [48] M. G. Alford, A. Schmitt, K. Rajagopal, and T. Schäfer, “Color superconductivity in dense quark matter,” *Rev. Mod. Phys.* 80, 1455 (2008), arXiv:0709.4635 [hep-ph].
- [49] K. Fukushima and T. Hatsuda, “The phase diagram of dense QCD,” *Rept. Prog. Phys.* 74, 014001 (2011), arXiv:1005.4814 [hep-ph].

- [50] G. Aarts, “Introductory lectures on lattice QCD at nonzero baryon number,” J. Phys. Conf. Ser. 706, 022004 (2016), arXiv:1512.05145 [hep-lat].
- [51] Y. Aoki, G. Endrodi, Z. Fodor, S. Katz, and K. Szabo, “The Order of the quantum chromodynamics transition predicted by the standard model of particle physics,” Nature 443, 675 (2006), arXiv:hep-lat/0611014.
- [52] S. Borsanyi *et al.* (Wuppertal-Budapest Collaboration), “Is there still any  $T_c$  mystery in lattice QCD? Results with physical masses in the continuum limit III,” JHEP 1009, 073 (2010), arXiv:1005.3508 [hep-lat].
- [53] J. Braun, L. M. Haas, F. Marhauser, and J. M. Pawłowski, “Phase Structure of Two-Flavor QCD at Finite Chemical Potential,” Phys. Rev. Lett. 106, 022002 (2011), arXiv:0908.0008 [hep-ph].
- [54] M. A. Stephanov, K. Rajagopal, and E. V. Shuryak, “Signatures of the tricritical point in QCD,” Phys. Rev. Lett. 81, 4816 (1998), arXiv:hep-ph/9806219.
- [55] B.-J. Schaefer, J. M. Pawłowski, and J. Wambach, “The Phase Structure of the Polyakov–Quark-Meson Model,” Phys. Rev. D76, 074023 (2007), arXiv:0704.3234 [hep-ph].
- [56] T. K. Herbst, J. M. Pawłowski, and B.-J. Schaefer, “Phase structure and thermodynamics of QCD,” Phys. Rev. D88, 014007 (2013), arXiv:1302.1426 [hep-ph].
- [57] J. M. Pawłowski and F. Rennecke, “Higher order quark-mesonic scattering processes and the phase structure of QCD,” Phys. Rev. D90, 076002 (2014), arXiv:1403.1179 [hep-ph].
- [58] F. Rennecke and B.-J. Schaefer, “Fluctuation-induced modifications of the phase structure in (2+1)-flavor QCD,” Phys. Rev. D96, 016009 (2017), arXiv:1610.08748 [hep-ph].
- [59] C. S. Fischer, J. Luecker, and J. A. Mueller, “Chiral and deconfinement phase transitions of two-flavour QCD at finite temperature and chemical potential,” Phys. Lett. B702, 438 (2011), arXiv:1104.1564 [hep-ph].
- [60] C. S. Fischer and J. Luecker, “Propagators and phase structure of  $N_f = 2$  and  $N_f = 2 + 1$  QCD,” Phys. Lett. B718, 1036 (2013), arXiv:1206.5191 [hep-ph].
- [61] C. S. Fischer, J. Luecker, and C. A. Welzbacher, “Phase structure of three and four flavor QCD,” Phys. Rev. D90, 034022 (2014), arXiv:1405.4762 [hep-ph].
- [62] R. Contant and M. Q. Huber, “The quark propagators of QCD and QCD-like theories,” (2017) arXiv:1709.03326 [hep-ph].
- [63] A. J. Helmboldt, J. M. Pawłowski, and N. Strodthoff, “Towards quantitative precision in the chiral crossover: masses and fluctuation scales,” Phys. Rev. D91, 054010 (2015), arXiv:1409.8414 [hep-ph].
- [64] fQCD Collaboration, J. Braun, L. Corell, A. K. Cyrol, W.-J. Fu, M. Leonhardt, M. Mitter, J. M. Pawłowski, M. Pospiech, F. Rennecke, N. Strodthoff, N. Wink.

- [65] M. Mitter, J. M. Pawłowski, and N. Strodthoff, “Chiral symmetry breaking in continuum QCD,” *Phys. Rev. D* **91**, 054035 (2015), arXiv:1411.7978 [hep-ph].
- [66] L. M. Haas, R. Stiele, J. Braun, J. M. Pawłowski, and J. Schaffner-Bielich, “Improved Polyakov-loop potential for effective models from functional calculations,” *Phys. Rev. D* **87**, 076004 (2013), arXiv:1302.1993 [hep-ph].
- [67] T. K. Herbst, M. Mitter, J. M. Pawłowski, B.-J. Schaefer, and R. Stiele, “Thermodynamics of QCD at vanishing density,” *Phys. Lett. B* **731**, 248 (2014), arXiv:1308.3621 [hep-ph].
- [68] J. Braun, L. Fister, J. M. Pawłowski, and F. Rennecke, “From Quarks and Gluons to Hadrons: Chiral Symmetry Breaking in Dynamical QCD,” *Phys. Rev. D* **94**, 034016 (2016), arXiv:1412.1045 [hep-ph].
- [69] F. Rennecke, “Vacuum structure of vector mesons in QCD,” *Phys. Rev. D* **92**, 076012 (2015), arXiv:1504.03585 [hep-ph].
- [70] W.-J. Fu and J. M. Pawłowski, “On the relevance of matter and glue dynamics for baryon number fluctuations,” *Phys. Rev. D* **92**, 116006 (2015), arXiv:1508.06504 [hep-ph].
- [71] M. Heller and M. Mitter, “Pion and  $\eta$ -meson mass splitting at the two-flavour chiral crossover,” *Phys. Rev. D* **94**, 074002 (2016), arXiv:1512.05241 [hep-ph].
- [72] W.-j. Fu, J. M. Pawłowski, F. Rennecke, and B.-J. Schaefer, “Baryon number fluctuations at finite temperature and density,” *Phys. Rev. D* **94**, 116020 (2016), arXiv:1608.04302 [hep-ph].
- [73] J. Braun, M. Leonhardt, and M. Pospiech, “A Fierz-complete NJL model study: fixed points and phase structure at finite temperature and density,” (2017), arXiv:1705.00074 [hep-ph].
- [74] A. K. Cyrol, *Gluonic Vertices of Landau Gauge Yang-Mills Theory in the Dyson-Schwinger Approach*, Master’s thesis, Darmstadt University of Technology (2014).
- [75] M. E. Peskin and D. V. Schroeder, *An Introduction to quantum field theory* (Addison-Wesley, Reading, USA, 1995).
- [76] T. Muta, *Foundations of Quantum Chromodynamics* (World Scientific, Hackensack, N.J., 2010).
- [77] L. H. Ryder, *Quantum Field Theory* (Cambridge University Press, 1996).
- [78] A. K. Das, *Finite Temperature Field Theory* (World Scientific, New York, 1997).
- [79] L. Faddeev and V. Popov, “Feynman Diagrams for the Yang-Mills Field,” *Phys. Lett. B* **25**, 29 (1967).
- [80] V. N. Gribov, “Quantization of non-Abelian gauge theories,” *Nucl. Phys. B* **139**, 1 (1978).



- [81] I. M. Singer, “Some Remarks on the Gribov Ambiguity,” *Commun. Math. Phys.* 60, 7 (1978).
- [82] C. Becchi, A. Rouet, and R. Stora, “Renormalization of Gauge Theories,” *Annals Phys.* 98, 287 (1976).
- [83] M. Z. Iofa and I. V. Tyutin, “Gauge Invariance of Spontaneously Broken Nonabelian Theories in the Bogolyubov-Parasiuk-HEPP-Zimmerman Method,” *Teor. Mat. Fiz.* 27, 38 (1976).
- [84] J. C. Taylor, “Ward Identities and Charge Renormalization of the Yang-Mills Field,” *Nucl. Phys.* B33, 436 (1971).
- [85] A. A. Slavnov, “Ward Identities in Gauge Theories,” *Theor. Math. Phys.* 10, 99 (1972), [*Teor. Mat. Fiz.*10,153(1972)].
- [86] D. J. Gross and F. Wilczek, “Ultraviolet Behavior of Nonabelian Gauge Theories,” *Phys. Rev. Lett.* 30, 1343 (1973).
- [87] H. D. Politzer, “Reliable Perturbative Results for Strong Interactions?” *Phys. Rev. Lett.* 30, 1346 (1973).
- [88] W. E. Caswell, “Asymptotic Behavior of Nonabelian Gauge Theories to Two Loop Order,” *Phys. Rev. Lett.* 33, 244 (1974).
- [89] D. R. T. Jones, “Two Loop Diagrams in Yang-Mills Theory,” *Nucl. Phys.* B75, 531 (1974).
- [90] E. Egorian and O. V. Tarasov, “Two Loop Renormalization of the QCD in an Arbitrary Gauge,” *Teor. Mat. Fiz.* 41, 26 (1979), [*Theor. Math. Phys.*41,863(1979)].
- [91] J. D. Bjorken, “Asymptotic Sum Rules at Infinite Momentum,” *Phys. Rev.* 179, 1547 (1969).
- [92] O. V. Tarasov, A. A. Vladimirov, and A. Yu. Zharkov, “The Gell-Mann-Low Function of QCD in the Three Loop Approximation,” *Phys. Lett.* 93B, 429 (1980).
- [93] S. A. Larin and J. A. M. Vermaseren, “The Three loop QCD Beta function and anomalous dimensions,” *Phys. Lett.* B303, 334 (1993), arXiv:hep-ph/9302208.
- [94] T. van Ritbergen, J. A. M. Vermaseren, and S. A. Larin, “The Four loop beta function in quantum chromodynamics,” *Phys. Lett.* B400, 379 (1997), arXiv:hep-ph/9701390.
- [95] M. Czakon, “The Four-loop QCD beta-function and anomalous dimensions,” *Nucl. Phys.* B710, 485 (2005), arXiv:hep-ph/0411261.
- [96] F. Herzog, B. Ruijl, T. Ueda, J. A. M. Vermaseren, and A. Vogt, “The five-loop beta function of Yang-Mills theory with fermions,” *JHEP* 02, 090 (2017), arXiv:1701.01404 [hep-ph].
- [97] T. Luthe, A. Maier, P. Marquard, and Y. Schroder, “Complete renormalization of QCD at five loops,” *JHEP* 03, 020 (2017), arXiv:1701.07068 [hep-ph].

- [98] R. Alkofer and J. Greensite, “Quark Confinement: The Hard Problem of Hadron Physics,” *J. Phys.* G34, S3 (2007), arXiv:hep-ph/0610365.
- [99] N. Vandersickel and D. Zwanziger, “The Gribov problem and QCD dynamics,” *Phys. Rept.* 520, 175 (2012), arXiv:1202.1491 [hep-th].
- [100] J. Greensite, “The confinement problem in lattice gauge theory,” *Prog. Part. Nucl. Phys.* 51, 1 (2003), arXiv:hep-lat/0301023.
- [101] D. Diakonov, “Topology and confinement,” *Nucl. Phys. Proc. Suppl.* 195, 5 (2009), arXiv:0906.2456 [hep-ph].
- [102] A. Jaffe and E. Witten, “Quantum Yang-Mills Theory,” (2000).
- [103] C. J. Morningstar and M. J. Peardon, “The Glueball spectrum from an anisotropic lattice study,” *Phys. Rev.* D60, 034509 (1999), arXiv:hep-lat/9901004.
- [104] K. G. Wilson, “Confinement of Quarks,” *Phys. Rev.* D10, 2445 (1974), [,45(1974)].
- [105] G. S. Bali, “QCD forces and heavy quark bound states,” *Phys. Rept.* 343, 1 (2001), arXiv:hep-ph/0001312.
- [106] G. S. Bali, H. Neff, T. Duessel, T. Lippert, and K. Schilling (SESAM), “Observation of string breaking in QCD,” *Phys. Rev.* D71, 114513 (2005), arXiv:hep-lat/0505012.
- [107] A. M. Polyakov, “Thermal Properties of Gauge Fields and Quark Liberation,” *Phys. Lett.* 72B, 477 (1978).
- [108] J. Braun, H. Gies, and J. M. Pawłowski, “Quark Confinement from Color Confinement,” *Phys. Lett.* B684, 262 (2010), arXiv:0708.2413 [hep-th].
- [109] L. Fister and J. M. Pawłowski, “Confinement from Correlation Functions,” *Phys. Rev.* D88, 045010 (2013), arXiv:1301.4163 [hep-ph].
- [110] K. Osterwalder and R. Schrader, “Axioms For Euclidean Green’s Functions,” *Commun. Math. Phys.* 31, 83 (1973).
- [111] K. Osterwalder and R. Schrader, “Axioms for Euclidean Green’s Functions. 2.” *Commun. Math. Phys.* 42, 281 (1975).
- [112] C. S. Fischer, A. Maas, and J. M. Pawłowski, “On the infrared behavior of Landau gauge Yang-Mills theory,” *Annals Phys.* 324, 2408 (2009), arXiv:0810.1987 [hep-ph].
- [113] T. Kugo and I. Ojima, “Local Covariant Operator Formalism of Nonabelian Gauge Theories and Quark Confinement Problem,” *Prog. Theor. Phys. Suppl.* 66, 1 (1979).
- [114] T. Kugo, “The universal renormalization factors  $Z(1) / Z(3)$  and color confinement condition in non-Abelian gauge theory,” (1995), arXiv:hep-th/9511033.
- [115] N. Nakanishi and I. Ojima, “Covariant operator formalism of gauge theories and quantum gravity,” *World Sci. Lect. Notes Phys.* 27, 1 (1990).

- [116] L. von Smekal, R. Alkofer, and A. Hauck, “The Infrared behavior of gluon and ghost propagators in Landau gauge QCD,” *Phys. Rev. Lett.* 79, 3591 (1997), arXiv:hep-ph/9705242.
- [117] L. von Smekal, A. Hauck, and R. Alkofer, “A Solution to Coupled Dyson–Schwinger Equations for Gluons and Ghosts in Landau Gauge,” *Annals Phys.* 267, 1 (1998), [Erratum: *Annals Phys.* 269,182(1998)], arXiv:hep-ph/9707327.
- [118] D. Zwanziger, “Non-perturbative Landau gauge and infrared critical exponents in QCD,” *Phys. Rev. D* 65, 094039 (2002), arXiv:hep-th/0109224.
- [119] C. Lerche and L. von Smekal, “On the infrared exponent for gluon and ghost propagation in Landau gauge QCD,” *Phys. Rev. D* 65, 125006 (2002), arXiv:hep-ph/0202194.
- [120] C. S. Fischer, R. Alkofer, and H. Reinhardt, “The elusiveness of infrared critical exponents in Landau gauge Yang-Mills theories,” *Phys. Rev. D* 65, 094008 (2002), arXiv:hep-ph/0202195.
- [121] J. M. Pawłowski, D. F. Litim, S. Nedelko, and L. von Smekal, “Infrared behavior and fixed points in Landau gauge QCD,” *Phys. Rev. Lett.* 93, 152002 (2004), arXiv:hep-th/0312324.
- [122] A. Cucchieri and T. Mendes, “What’s up with IR gluon and ghost propagators in Landau gauge? A puzzling answer from huge lattices,” *PoS LAT2007*, 297 (2007), arXiv:0710.0412 [hep-lat].
- [123] A. Cucchieri and T. Mendes, “Constraints on the IR behavior of the gluon propagator in Yang-Mills theories,” *Phys. Rev. Lett.* 100, 241601 (2008), arXiv:0712.3517 [hep-lat].
- [124] I. Bogolubsky, E. Ilgenfritz, M. Müller-Preussker, and A. Sternbeck, “The Landau gauge gluon and ghost propagators in 4D SU(3) gluodynamics in large lattice volumes,” *PoS LAT2007*, 290 (2007), arXiv:0710.1968 [hep-lat].
- [125] D. Zwanziger, “Fundamental modular region, Boltzmann factor and area law in lattice gauge theory,” *Nucl. Phys. B* 412, 657 (1994).
- [126] D. Zwanziger, “Nonperturbative Faddeev-Popov formula and infrared limit of QCD,” *Phys. Rev. D* 69, 016002 (2004), arXiv:hep-ph/0303028.
- [127] G. Dell’Antonio and D. Zwanziger, “Every gauge orbit passes inside the Gribov horizon,” *Commun. Math. Phys.* 138, 291 (1991).
- [128] P. van Baal, “More (thoughts on) Gribov copies,” *Nucl. Phys. B* 369, 259 (1992).
- [129] A. Maas, “Dependence of the propagators on the sampling of Gribov copies inside the first Gribov region of Landau gauge,” (2017), arXiv:1705.03812 [hep-lat].
- [130] D. Dudal, S. Sorella, N. Vandersickel, and H. Verschelde, “New features of the gluon and ghost propagator in the infrared region from the Gribov-Zwanziger approach,” *Phys. Rev. D* 77, 071501 (2008), arXiv:0711.4496 [hep-th].

- [131] D. Dudal, J. A. Gracey, S. P. Sorella, N. Vandersickel, and H. Verschelde, “A Refinement of the Gribov-Zwanziger approach in the Landau gauge: Infrared propagators in harmony with the lattice results,” *Phys. Rev. D* **78**, 065047 (2008), arXiv:0806.4348 [hep-th].
- [132] A. C. Aguilar, D. Binosi, and J. Papavassiliou, “Gluon and ghost propagators in the Landau gauge: Deriving lattice results from Schwinger-Dyson equations,” *Phys. Rev. D* **78**, 025010 (2008), arXiv:0802.1870 [hep-ph].
- [133] P. Boucaud *et al.*, “On the IR behaviour of the Landau-gauge ghost propagator,” *JHEP* **06**, 099 (2008), arXiv:0803.2161 [hep-ph].
- [134] J. S. Bell and R. Jackiw, “A PCAC puzzle:  $\pi^0 \rightarrow \gamma\gamma$  in the sigma model,” *Nuovo Cim. A* **60**, 47 (1969).
- [135] S. L. Adler, “Axial vector vertex in spinor electrodynamics,” *Phys. Rev.* **177**, 2426 (1969).
- [136] S. L. Adler and W. A. Bardeen, “Absence of higher order corrections in the anomalous axial vector divergence equation,” *Phys. Rev.* **182**, 1517 (1969).
- [137] K. Fujikawa, “Path Integral Measure for Gauge Invariant Fermion Theories,” *Phys. Rev. Lett.* **42**, 1195 (1979).
- [138] G. 't Hooft, “Symmetry Breaking Through Bell-Jackiw Anomalies,” *Phys. Rev. Lett.* **37**, 8 (1976).
- [139] J. Berges, “N-particle irreducible effective action techniques for gauge theories,” *Phys. Rev. D* **70**, 105010 (2004), arXiv:hep-ph/0401172.
- [140] R. Alkofer, M. Q. Huber, and K. Schwenzer, “Algorithmic derivation of Dyson-Schwinger Equations,” *Comput. Phys. Commun.* **180**, 965 (2009), doDSE, arXiv:0808.2939 [hep-th].
- [141] M. Q. Huber and J. Braun, “Algorithmic derivation of functional renormalization group equations and Dyson-Schwinger equations,” *Comput. Phys. Commun.* **183**, 1290 (2012), arXiv:1102.5307 [hep-th].
- [142] K. G. Wilson and J. B. Kogut, “The Renormalization group and the epsilon expansion,” *Phys. Rept.* **12**, 75 (1974).
- [143] T. Gasenzer, S. Kessler, and J. M. Pawłowski, “Far-from-equilibrium quantum many-body dynamics,” *Eur. Phys. J. C* **70**, 423 (2010), arXiv:1003.4163 [cond-mat.quant-gas].
- [144] J. Berges and D. Mesterházy, “Introduction to the nonequilibrium functional renormalization group,” *Nucl. Phys. Proc. Suppl.* **228**, 37 (2012), arXiv:1204.1489 [hep-ph].
- [145] J. M. Pawłowski and N. Strodthoff, “Real time correlation functions and the functional renormalization group,” *Phys. Rev. D* **92**, 094009 (2015), arXiv:1508.01160 [hep-ph].

- [146] J. Berges, L. Corell, A. K. Cyrol, M. Heller, J. M. Pawłowski, work in progress.
- [147] D. F. Litim, “Optimization of the exact renormalization group,” *Phys. Lett.* B486, 92 (2000), arXiv:hep-th/0005245.
- [148] A. Sternbeck, E. M. Ilgenfritz, M. Müller-Preussker, A. Schiller, and I. L. Bogolubsky, “Lattice study of the infrared behavior of QCD Green’s functions in Landau gauge,” *PoS LAT2006*, 076 (2006), arXiv:hep-lat/0610053.
- [149] V. Branchina, K. A. Meissner, and G. Veneziano, “The Price of an exact, gauge invariant RG flow equation,” *Phys. Lett.* B574, 319 (2003), arXiv:hep-th/0309234.
- [150] J. M. Pawłowski, “Geometrical effective action and Wilsonian flows,” (2003), arXiv:hep-th/0310018.
- [151] S. Arnone, T. R. Morris, and O. J. Rosten, “A Generalised manifestly gauge invariant exact renormalisation group for SU(N) Yang-Mills,” *Eur. Phys. J.* C50, 467 (2007), arXiv:hep-th/0507154.
- [152] O. J. Rosten, “A Manifestly gauge invariant and universal calculus for SU(N) Yang-Mills,” *Int. J. Mod. Phys.* A21, 4627 (2006), arXiv:hep-th/0602229.
- [153] C. Wetterich, “Gauge invariant flow equation,” (2016), arXiv:1607.02989 [hep-th].
- [154] U. Ellwanger, “Flow equations and BRS invariance for Yang-Mills theories,” *Phys. Lett.* B335, 364 (1994), arXiv:hep-th/9402077.
- [155] U. Ellwanger, M. Hirsch, and A. Weber, “Flow equations for the relevant part of the pure Yang-Mills action,” *Z. Phys.* C69, 687 (1996), arXiv:hep-th/9506019.
- [156] M. D’Attanasio and T. R. Morris, “Gauge invariance, the quantum action principle, and the renormalization group,” *Phys. Lett.* B378, 213 (1996), arXiv:hep-th/9602156.
- [157] D. F. Litim and J. M. Pawłowski, “Flow equations for Yang-Mills theories in general axial gauges,” *Phys. Lett.* B435, 181 (1998), arXiv:hep-th/9802064.
- [158] Y. Igarashi, K. Itoh, and H. So, “BRS symmetry, the quantum master equation, and the Wilsonian renormalization group,” *Prog. Theor. Phys.* 106, 149 (2001), arXiv:hep-th/0101101.
- [159] Y. Igarashi, K. Itoh, and J. M. Pawłowski, “Functional flows in QED and the modified Ward–Takahashi identity,” *J. Phys.* A49, 405401 (2016), arXiv:1604.08327 [hep-th].
- [160] Y. Takahashi, “Canonical Quantization and Generalized Ward Relations,” in *Positano Symp. 0019* (1985) p. 19.
- [161] K.-I. Kondo, “Transverse Ward-Takahashi identity, anomaly and Schwinger-Dyson equation,” *Int. J. Mod. Phys.* A12, 5651 (1997), arXiv:hep-th/9608100.
- [162] H.-X. He, F. C. Khanna, and Y. Takahashi, “Transverse Ward-Takahashi identity for the fermion boson vertex in gauge theories,” *Phys. Lett.* B480, 222 (2000).

- [163] S.-X. Qin, L. Chang, Y.-X. Liu, C. D. Roberts, and S. M. Schmidt, “Practical corollaries of transverse Ward-Green-Takahashi identities,” *Phys. Lett. B* **722**, 384 (2013), arXiv:1302.3276 [nucl-th].
- [164] A. Aguilar, D. Binosi, D. Ibáñez, and J. Papavassiliou, “New method for determining the quark-gluon vertex,” *Phys. Rev. D* **90**, 065027 (2014), arXiv:1405.3506 [hep-ph].
- [165] A. Blum, M. Q. Huber, M. Mitter, and L. von Smekal, “Gluonic three-point correlations in pure Landau gauge QCD,” *Phys. Rev. D* **89**, 061703 (2014), arXiv:1401.0713 [hep-ph].
- [166] G. Eichmann, R. Williams, R. Alkofer, and M. Vujanovic, “The three-gluon vertex in Landau gauge,” *Phys. Rev. D* **89**, 105014 (2014), arXiv:1402.1365 [hep-ph].
- [167] R. Harlander and M. Steinhauser, “Automatic computation of Feynman diagrams,” *Prog. Part. Nucl. Phys.* **43**, 167 (1999), arXiv:hep-ph/9812357.
- [168] U. Baur, “Precision calculations for future colliders,” *Int. J. Mod. Phys. E* **17**, 826 (2008), arXiv:hep-ph/0701164.
- [169] G. Luisoni, S. Poslavsky, and Y. Schroder, “Track 3: Computations in theoretical physics – techniques and methods,” *J. Phys. Conf. Ser.* **762**, 012077 (2016), arXiv:1604.03370 [hep-ph].
- [170] A. K. Cyrol, M. Mitter, J. M. Pawłowski, and N. Strodthoff, “FormTracer GitHub Repository,” (2016), <https://github.com/FormTracer/FormTracer>.
- [171] J. Vermaseren, “New features of FORM,” (2000), arXiv:math-ph/0010025 [math-ph].
- [172] J. Kuipers, T. Ueda, J. A. M. Vermaseren, and J. Vollinga, “FORM version 4.0,” *Comput. Phys. Commun.* **184**, 1453 (2013), arXiv:1203.6543 [cs.SC].
- [173] J. Kuipers, T. Ueda, and J. A. M. Vermaseren, “Code Optimization in FORM,” *Comput. Phys. Commun.* **189**, 1 (2015), arXiv:1310.7007 [cs.SC].
- [174] B. Ruijl, T. Ueda, and J. Vermaseren, “FORM version 4.2,” (2017), arXiv:1707.06453 [hep-ph].
- [175] N. Strodthoff, “Self-consistent spectral functions in the  $O(N)$  model from the functional renormalization group,” *Phys. Rev. D* **95**, 076002 (2017), arXiv:1611.05036 [hep-th].
- [176] A. Eichhorn, A. Held, and J. M. Pawłowski, “Quantum-gravity effects on a Higgs-Yukawa model,” *Phys. Rev. D* **94**, 104027 (2016), arXiv:1604.02041 [hep-th].
- [177] N. Christiansen, “Four-Derivative Quantum Gravity Beyond Perturbation Theory,” (2016), arXiv:1612.06223 [hep-th].
- [178] T. Denz, J. M. Pawłowski, and M. Reichert, “Towards apparent convergence in asymptotically safe quantum gravity,” (2016), arXiv:1612.07315 [hep-th].

- [179] A. Eichhorn and A. Held, “Viability of quantum-gravity induced ultraviolet completions for matter,” (2017), arXiv:1705.02342 [gr-qc].
- [180] T. van Ritbergen, A. N. Schellekens, and J. A. M. Vermaseren, “Group theory factors for Feynman diagrams,” *Int. J. Mod. Phys. A*14, 41 (1999), arXiv:hep-ph/9802376.
- [181] P. Cvitanovic, “Group theory for Feynman diagrams in non-Abelian gauge theories,” *Phys. Rev. D*14, 1536 (1976).
- [182] S. A. Larin, “The Renormalization of the axial anomaly in dimensional regularization,” *Phys. Lett. B*303, 113 (1993), arXiv:hep-ph/9302240.
- [183] S. Moch, J. A. M. Vermaseren, and A. Vogt, “On  $\gamma_5$  in higher-order QCD calculations and the NNLO evolution of the polarized valence distribution,” *Phys. Lett. B*748, 432 (2015), arXiv:1506.04517 [hep-ph].
- [184] B. Bergerhoff and C. Wetterich, “Effective quark interactions and QCD propagators,” *Phys. Rev. D*57, 1591 (1998), arXiv:hep-ph/9708425.
- [185] H. Gies, “Running coupling in Yang-Mills theory: A flow equation study,” *Phys. Rev. D*66, 025006 (2002), arXiv:hep-th/0202207.
- [186] C. S. Fischer and H. Gies, “Renormalization flow of Yang-Mills propagators,” *JHEP* 10, 048 (2004), arXiv:hep-ph/0408089.
- [187] C. Feuchter and H. Reinhardt, “Variational solution of the Yang-Mills Schrodinger equation in Coulomb gauge,” *Phys. Rev. D*70, 105021 (2004), arXiv:hep-th/0408236.
- [188] C. Kellermann and C. S. Fischer, “The running coupling from the four-gluon vertex in Landau gauge Yang-Mills theory,” *Phys. Rev. D*78, 025015 (2008), arXiv:0801.2697 [hep-ph].
- [189] M. Tissier and N. Wschebor, “Infrared propagators of Yang-Mills theory from perturbation theory,” *Phys. Rev. D*82, 101701 (2010), arXiv:1004.1607 [hep-ph].
- [190] M. Leder, J. M. Pawłowski, H. Reinhardt, and A. Weber, “Hamiltonian Flow in Coulomb Gauge Yang-Mills Theory,” *Phys. Rev. D*83, 025010 (2011), arXiv:1006.5710 [hep-th].
- [191] M. Q. Huber and L. von Smekal, “On the influence of three-point functions on the propagators of Landau gauge Yang-Mills theory,” *JHEP* 1304, 149 (2013), arXiv:1211.6092 [hep-th].
- [192] A. C. Aguilar, D. Ibáñez, and J. Papavassiliou, “Ghost propagator and ghost-gluon vertex from Schwinger-Dyson equations,” *Phys. Rev. D*87, 114020 (2013), arXiv:1303.3609 [hep-ph].
- [193] M. Peláez, M. Tissier, and N. Wschebor, “Three-point correlation functions in Yang-Mills theory,” *Phys. Rev. D*88, 125003 (2013), arXiv:1310.2594 [hep-th].

- [194] M. Q. Huber and L. von Smekal, “Spurious divergences in Dyson-Schwinger equations,” *JHEP* 06, 015 (2014), arXiv:1404.3642 [hep-ph].
- [195] J. Gracey, “Off-shell two loop QCD vertices,” *Phys. Rev. D* 90, 025014 (2014), arXiv:1406.0649 [hep-ph].
- [196] J. A. Gracey, “Symmetric point quartic gluon vertex and momentum subtraction,” *Phys. Rev. D* 90, 025011 (2014), arXiv:1406.1618 [hep-ph].
- [197] M. Q. Huber, D. R. Campagnari, and H. Reinhardt, “Vertex functions of Coulomb gauge Yang–Mills theory,” *Phys. Rev. D* 91, 025014 (2015), arXiv:1410.4766 [hep-ph].
- [198] R. Williams, C. S. Fischer, and W. Heupel, “Light mesons in QCD and unquenching effects from the 3PI effective action,” *Phys. Rev. D* 93, 034026 (2016), arXiv:1512.00455 [hep-ph].
- [199] D. Binosi, D. Ibáñez, and J. Papavassiliou, “Nonperturbative study of the four gluon vertex,” *JHEP* 09, 059 (2014), arXiv:1407.3677 [hep-ph].
- [200] M. Quandt, H. Reinhardt, and J. Heffner, “Covariant variational approach to Yang-Mills theory,” *Phys. Rev. D* 89, 065037 (2014), arXiv:1310.5950 [hep-th].
- [201] M. Q. Huber, “Correlation functions of three-dimensional Yang-Mills theory from Dyson-Schwinger equations,” *Phys. Rev. D* 93, 085033 (2016), arXiv:1602.02038 [hep-th].
- [202] U. Reinosa, J. Serreau, M. Tissier, and N. Wschebor, “How nonperturbative is the infrared regime of Landau gauge Yang-Mills correlators?” *Phys. Rev. D* 96, 014005 (2017), arXiv:1703.04041 [hep-th].
- [203] L. von Smekal, K. Maltman, and A. Sternbeck, “The strong coupling and its running to four loops in a minimal MOM scheme,” *Phys. Lett. B* 681, 336 (2009), arXiv:0903.1696 [hep-ph].
- [204] F. Marhauser and J. M. Pawłowski, “Confinement in Polyakov Gauge,” (2008), arXiv:0812.1144 [hep-ph].
- [205] J. Braun, A. Eichhorn, H. Gies, and J. M. Pawłowski, “On the Nature of the Phase Transition in  $SU(N)$ ,  $Sp(2)$  and  $E(7)$  Yang-Mills theory,” *Eur. Phys. J. C* 70, 689 (2010), arXiv:1007.2619 [hep-ph].
- [206] T. K. Herbst, J. Luecker, and J. M. Pawłowski, “Confinement order parameters and fluctuations,” (2015), arXiv:1510.03830 [hep-ph].
- [207] A. Dumitru, Y. Guo, Y. Hidaka, C. P. K. Altes, and R. D. Pisarski, “Effective Matrix Model for Deconfinement in Pure Gauge Theories,” *Phys. Rev. D* 86, 105017 (2012), arXiv:1205.0137 [hep-ph].
- [208] K. Fukushima and K. Kashiwa, “Polyakov loop and QCD thermodynamics from the gluon and ghost propagators,” *Phys. Lett. B* 723, 360 (2013), arXiv:1206.0685 [hep-ph].



- [209] U. Reinosa, J. Serreau, M. Tissier, and N. Wschebor, “Deconfinement transition in  $SU(2)$  Yang-Mills theory: A two-loop study,” *Phys. Rev. D* **91**, 045035 (2015), arXiv:1412.5672 [hep-th].
- [210] U. Reinosa, J. Serreau, M. Tissier, and N. Wschebor, “Two-loop study of the deconfinement transition in Yang-Mills theories:  $SU(3)$  and beyond,” *Phys. Rev. D* **93**, 105002 (2016), arXiv:1511.07690 [hep-th].
- [211] M. Quandt and H. Reinhardt, “Covariant variational approach to Yang-Mills Theory: effective potential of the Polyakov loop,” *Phys. Rev. D* **94**, 065015 (2016), arXiv:1603.08058 [hep-th].
- [212] K. Fukushima and V. Skokov, “Polyakov loop modeling for hot QCD,” *Prog. Part. Nucl. Phys.* **96**, 154 (2017), arXiv:1705.00718 [hep-ph].
- [213] D. Dudal, S. Sorella, N. Vandersickel, and H. Verschelde, “Gribov no-pole condition, Zwanziger horizon function, Kugo-Ojima confinement criterion, boundary conditions, BRST breaking and all that,” *Phys. Rev. D* **79**, 121701 (2009), arXiv:0904.0641 [hep-th].
- [214] D. Dudal, S. Sorella, and N. Vandersickel, “The dynamical origin of the refinement of the Gribov-Zwanziger theory,” *Phys. Rev. D* **84**, 065039 (2011), arXiv:1105.3371 [hep-th].
- [215] M. A. L. Capri, D. Dudal, D. Fiorentini, M. S. Guimaraes, I. F. Justo, A. D. Pereira, B. W. Mintz, L. F. Palhares, R. F. Sobreiro, and S. P. Sorella, “Exact nilpotent nonperturbative BRST symmetry for the Gribov-Zwanziger action in the linear covariant gauge,” *Phys. Rev. D* **92**, 045039 (2015), arXiv:1506.06995 [hep-th].
- [216] R. Alkofer, C. S. Fischer, and F. J. Llanes-Estrada, “Vertex functions and infrared fixed point in Landau gauge  $SU(N)$  Yang-Mills theory,” *Phys. Lett. B* **611**, 279 (2005), arXiv:hep-th/0412330.
- [217] C. S. Fischer and J. M. Pawłowski, “Uniqueness of infrared asymptotics in Landau gauge Yang-Mills theory,” *Phys. Rev. D* **75**, 025012 (2007), arXiv:hep-th/0609009.
- [218] R. Alkofer, M. Q. Huber, and K. Schwenzer, “Infrared singularities in Landau gauge Yang-Mills theory,” *Phys. Rev. D* **81**, 105010 (2010), arXiv:0801.2762 [hep-th].
- [219] C. S. Fischer and J. M. Pawłowski, “Uniqueness of infrared asymptotics in Landau gauge Yang-Mills theory II,” *Phys. Rev. D* **80**, 025023 (2009), arXiv:0903.2193 [hep-th].
- [220] J. M. Cornwall, “Dynamical Mass Generation in Continuum QCD,” *Phys. Rev. D* **26**, 1453 (1982).
- [221] P. Boucaud, J. P. Leroy, A. Le Yaouanc, A. Y. Lokhov, J. Micheli, O. Pene, J. Rodriguez-Quintero, and C. Roiesnel, “The Infrared behaviour of the pure Yang-Mills green functions,” (2005), arXiv:hep-ph/0507104.

- [222] P. Boucaud *et al.*, “Constraints on the IR behaviour of gluon and ghost propagator from Ward-Slavnov-Taylor identities,” *Eur. Phys. J. A*31, 750 (2007), arXiv:hep-ph/0701114.
- [223] P. Boucaud, J. P. Leroy, A. Le Yaouanc, A. Y. Lokhov, J. Micheli, O. Pene, J. Rodriguez-Quintero, and C. Roiesnel, “Divergent IR gluon propagator from Ward-Slavnov-Taylor identities?” *JHEP* 03, 076 (2007), arXiv:hep-ph/0702092.
- [224] A. Maas and D. Zwanziger, “Analytic and numerical study of the free energy in gauge theory,” *Phys. Rev. D*89, 034011 (2014), arXiv:1309.1957 [hep-lat].
- [225] G. K. Savvidy, “Infrared Instability of the Vacuum State of Gauge Theories and Asymptotic Freedom,” *Phys. Lett.* B71, 133 (1977).
- [226] A. Eichhorn, H. Gies, and J. M. Pawłowski, “Gluon condensation and scaling exponents for the propagators in Yang-Mills theory,” *Phys. Rev. D*83, 045014 (2011), arXiv:1010.2153 [hep-ph].
- [227] A. C. Aguilar, D. Binosi, and J. Papavassiliou, “The dynamical equation of the effective gluon mass,” *Phys. Rev. D*84, 085026 (2011), arXiv:1107.3968 [hep-ph].
- [228] A. C. Aguilar, D. Ibáñez, V. Mathieu, and J. Papavassiliou, “Massless bound-state excitations and the Schwinger mechanism in QCD,” *Phys. Rev. D*85, 014018 (2012), arXiv:1110.2633 [hep-ph].
- [229] C. T. Figueiredo and A. C. Aguilar, “Mass generation and the problem of seagull divergences,” (2016) arXiv:1601.05004 [hep-ph].
- [230] R. Alkofer, M. Q. Huber, and K. Schwenzer, “Infrared Behavior of Three-Point Functions in Landau Gauge Yang-Mills Theory,” *Eur. Phys. J. C*62, 761 (2009), arXiv:0812.4045 [hep-ph].
- [231] A. G. Duarte, O. Oliveira, and P. J. Silva, “Lattice Gluon and Ghost Propagators, and the Strong Coupling in Pure SU(3) Yang-Mills Theory: Finite Lattice Spacing and Volume Effects,” *Phys. Rev. D*94, 014502 (2016), arXiv:1605.00594 [hep-lat].
- [232] A. Cucchieri and T. Mendes, “Constraints on the IR behavior of the ghost propagator in Yang-Mills theories,” *Phys. Rev. D*78, 094503 (2008), arXiv:0804.2371 [hep-lat].
- [233] A. Maas, J. M. Pawłowski, D. Spielmann, A. Sternbeck, and L. von Smekal, “Strong-coupling study of the Gribov ambiguity in lattice Landau gauge,” *Eur. Phys. J. C*68, 183 (2010), arXiv:0912.4203 [hep-lat].
- [234] A. Maas, “Some more details of minimal-Landau-gauge SU(2) Yang-Mills propagators,” *Phys. Rev. D*91, 034502 (2015), arXiv:1402.5050 [hep-lat].
- [235] A. Maas, “Constructing non-perturbative gauges using correlation functions,” *Phys. Lett.* B689, 107 (2010), arXiv:0907.5185 [hep-lat].
- [236] A. Sternbeck and M. Müller-Preussker, “Lattice evidence for the family of decoupling solutions of Landau gauge Yang-Mills theory,” *Phys. Lett.* B726, 396 (2013), arXiv:1211.3057 [hep-lat].

- [237] A. Maas, “More on the properties of the first Gribov region in Landau gauge,” Phys. Rev. D93, 054504 (2016), arXiv:1510.08407 [hep-lat].
- [238] A. Cucchieri, A. Maas, and T. Mendes, “Exploratory study of three-point Green’s functions in Landau-gauge Yang-Mills theory,” Phys. Rev. D74, 014503 (2006), arXiv:hep-lat/0605011.
- [239] A. Cucchieri, A. Maas, and T. Mendes, “Three-point vertices in Landau-gauge Yang-Mills theory,” Phys. Rev. D77, 094510 (2008), arXiv:0803.1798 [hep-lat].
- [240] M. Tissier and N. Wschebor, “An Infrared Safe perturbative approach to Yang-Mills correlators,” Phys. Rev. D84, 045018 (2011), arXiv:1105.2475 [hep-th].
- [241] A. Aguilar, D. Binosi, D. Ibáñez, and J. Papavassiliou, “Effects of divergent ghost loops on the Green’s functions of QCD,” Phys. Rev. D89, 085008 (2014), arXiv:1312.1212 [hep-ph].
- [242] A. Athenodorou, D. Binosi, P. Boucaud, F. De Soto, J. Papavassiliou, J. Rodriguez-Quintero, and S. Zafeiropoulos, “On the zero crossing of the three-gluon vertex,” Phys. Lett. B761, 444 (2016), arXiv:1607.01278 [hep-ph].
- [243] A. G. Duarte, O. Oliveira, and P. J. Silva, “Further Evidence For Zero Crossing On The Three Gluon Vertex,” Phys. Rev. D94, 074502 (2016), arXiv:1607.03831 [hep-lat].
- [244] P. Boucaud, F. De Soto, J. Rodriguez-Quintero, and S. Zafeiropoulos, “Refining the detection of the zero crossing for the three-gluon vertex in symmetric and asymmetric momentum subtraction schemes,” Phys. Rev. D95, 114503 (2017), arXiv:1701.07390 [hep-lat].
- [245] R. Williams, “The quark-gluon vertex in Landau gauge bound-state studies,” Eur. Phys. J. A51, 57 (2015), arXiv:1404.2545 [hep-ph].
- [246] M. Q. Huber, private communication.
- [247] R. Williams, private communication.
- [248] M. Peláez, M. Tissier, and N. Wschebor, “Two-point correlation functions of QCD in the Landau gauge,” Phys. Rev. D90, 065031 (2014), arXiv:1407.2005 [hep-th].
- [249] F. Siringo, “Perturbative study of Yang-Mills theory in the infrared,” (2015), arXiv:1509.05891 [hep-ph].
- [250] A. Maas, private communication.
- [251] (2017), A. Maas, in preparation.
- [252] L. Fister, *On the Phase Diagram of QCD with Dynamical Quarks*, Ph.D. thesis, Heidelberg University (2012).
- [253] A. Cucchieri, T. Mendes, O. Oliveira, and P. J. Silva, “Just how different are SU(2) and SU(3) Landau-gauge propagators in the IR regime?” Phys. Rev. D76, 114507 (2007), arXiv:0705.3367 [hep-lat].

- [254] A. Sternbeck, L. von Smekal, D. B. Leinweber, and A. G. Williams, “Comparing SU(2) to SU(3) gluodynamics on large lattices,” PoS LAT2007, 340 (2007), arXiv:0710.1982 [hep-lat].
- [255] M. J. Teper, “SU(N) gauge theories in 2+1 dimensions,” Phys. Rev. D59, 014512 (1999), arXiv:hep-lat/9804008.
- [256] A. Cucchieri, “Infrared behavior of the gluon propagator in lattice Landau gauge: The Three-dimensional case,” Phys. Rev. D60, 034508 (1999), arXiv:hep-lat/9902023.
- [257] A. Cucchieri, T. Mendes, and A. R. Taurines, “SU(2) Landau gluon propagator on a  $140^3$  lattice,” Phys. Rev. D67, 091502 (2003), arXiv:hep-lat/0302022.
- [258] A. Cucchieri, T. Mendes, and A. R. Taurines, “Positivity violation for the lattice Landau gluon propagator,” Phys. Rev. D71, 051902 (2005), arXiv:hep-lat/0406020.
- [259] A. Maas, “More on Gribov copies and propagators in Landau-gauge Yang-Mills theory,” Phys. Rev. D79, 014505 (2009), arXiv:0808.3047 [hep-lat].
- [260] A. Cucchieri and T. Mendes, “Landau-gauge propagators in Yang-Mills theories at beta = 0: massive solution versus conformal scaling,” Phys. Rev. D81, 016005 (2010), arXiv:0904.4033 [hep-lat].
- [261] A. Maas, “On the gauge-algebra dependence of Landau-gauge Yang-Mills propagators,” JHEP 1102, 076 (2011), arXiv:1012.4284 [hep-lat].
- [262] A. Cucchieri, D. Dudal, T. Mendes, and N. Vandersickel, “Modeling the Gluon Propagator in Landau Gauge: Lattice Estimates of Pole Masses and Dimension-Two Condensates,” Phys. Rev. D85, 094513 (2012), arXiv:1111.2327 [hep-lat].
- [263] V. G. Bornyakov, V. K. Mitrjushkin, and R. N. Rogalyov, “Gluon Propagators in 3D SU(2) Theory and Effects of Gribov Copies,” Phys. Rev. D86, 114503 (2012), arXiv:1112.4975 [hep-lat].
- [264] V. G. Bornyakov, V. K. Mitrjushkin, and R. N. Rogalyov, “Infinite volume and continuum limits for the gluon propagator in 3d SU(2) lattice gauge theory,” Phys. Rev. D89, 054504 (2014), arXiv:1304.8130 [hep-lat].
- [265] A. Cucchieri and T. Mendes, “Bloch Waves in Minimal Landau Gauge and the Infinite-Volume Limit of Lattice Gauge Theory,” Phys. Rev. Lett. 118, 192002 (2017), arXiv:1612.01279 [hep-lat].
- [266] A. Maas, J. Wambach, B. Gruter, and R. Alkofer, “High-temperature limit of Landau-gauge Yang-Mills theory,” Eur. Phys. J. C37, 335 (2004), arXiv:hep-ph/0408074.
- [267] M. Q. Huber, R. Alkofer, C. S. Fischer, and K. Schwenzer, “The infrared behavior of Landau gauge Yang-Mills theory in  $d=2, 3$  and 4 dimensions,” Phys. Lett. B659, 434 (2008), arXiv:0705.3809 [hep-ph].

- [268] D. Dudal, J. Gracey, S. Sorella, N. Vandersickel, and H. Verschelde, “The Landau gauge gluon and ghost propagator in the refined Gribov-Zwanziger framework in 3 dimensions,” *Phys. Rev. D* **78**, 125012 (2008), arXiv:0808.0893 [hep-th].
- [269] A. C. Aguilar, D. Binosi, and J. Papavassiliou, “Nonperturbative gluon and ghost propagators for d=3 Yang- Mills,” *Phys. Rev. D* **81**, 125025 (2010), decoupling 3d, arXiv:1004.2011 [hep-ph].
- [270] J. M. Cornwall, “Exploring dynamical gluon mass generation in three dimensions,” *Phys. Rev. D* **93**, 025021 (2016), arXiv:1510.03453 [hep-ph].
- [271] K. Kajantie, M. Laine, K. Rummukainen, and M. E. Shaposhnikov, “Generic rules for high temperature dimensional reduction and their application to the standard model,” *Nucl. Phys. B* **458**, 90 (1996), arXiv:hep-ph/9508379.
- [272] L. Corell, *Landau Gauge Yang-Mills Theory in Three Space-Time Dimensions*, Master’s thesis, University of Heidelberg (2016).
- [273] L. Corell, A. K. Cyrol, M. Mitter, J. M. Pawłowski and N. Strodthoff, in preparation.
- [274] C. S. Fischer and R. Alkofer, “Non-perturbative Propagators, Running Coupling and Dynamical Quark Mass of Landau gauge QCD,” *Phys. Rev. D* **67**, 094020 (2003), arXiv:hep-ph/0301094.
- [275] R. Alkofer, C. S. Fischer, F. J. Llanes-Estrada, and K. Schwenzer, “The quark-gluon vertex in Landau gauge QCD: Its role in dynamical chiral symmetry breaking and quark confinement,” *Annals Phys.* **324**, 106 (2009), arXiv:0804.3042 [hep-ph].
- [276] M. Pak and H. Reinhardt, “Chiral Symmetry Breaking in Hamiltonian QCD in Coulomb Gauge,” *Phys. Lett. B* **707**, 566 (2012), arXiv:1107.5263 [hep-ph].
- [277] A. C. Aguilar, D. Binosi, and J. Papavassiliou, “Unquenching the gluon propagator with Schwinger-Dyson equations,” *Phys. Rev. D* **86**, 014032 (2012), arXiv:1204.3868 [hep-ph].
- [278] A. Ayala, A. Bashir, D. Binosi, M. Cristoforetti, and J. Rodriguez-Quintero, “Quark flavour effects on gluon and ghost propagators,” *Phys. Rev. D* **86**, 074512 (2012), arXiv:1208.0795 [hep-ph].
- [279] M. Hopfer, A. Windisch, and R. Alkofer, “The Quark-Gluon Vertex in Landau gauge QCD,” *PoS ConfinementX*, 073 (2012), arXiv:1301.3672 [hep-ph].
- [280] M. Pak and H. Reinhardt, “Quark Sector of the QCD Groundstate in Coulomb Gauge,” *Phys. Rev. D* **88**, 125021 (2013), arXiv:1310.1797 [hep-ph].
- [281] D. Binosi, L. Chang, J. Papavassiliou, and C. D. Roberts, “Bridging a gap between continuum-QCD and ab initio predictions of hadron observables,” *Phys. Lett. B* **742**, 183 (2015), arXiv:1412.4782 [nucl-th].

- [282] P. Vastag, H. Reinhardt, and D. Campagnari, “Improved variational approach to QCD in Coulomb gauge,” *Phys. Rev. D* **93**, 065003 (2016), arXiv:1512.06733 [hep-ph].
- [283] D. R. Campagnari, E. Ebadati, H. Reinhardt, and P. Vastag, “Revised variational approach to QCD in Coulomb gauge,” *Phys. Rev. D* **94**, 074027 (2016), arXiv:1608.06820 [hep-ph].
- [284] R. Bermudez, L. Albino, L. X. Gutierrez-Guerrero, M. E. Tejeda-Yeomans, and A. Bashir, “Quark-gluon Vertex: A Perturbation Theory Primer and Beyond,” *Phys. Rev. D* **95**, 034041 (2017), arXiv:1702.04437 [hep-ph].
- [285] J. A. Gracey, “Symmetric point four-point functions at one loop in QCD,” *Phys. Rev. D* **95**, 065013 (2017), arXiv:1703.01094 [hep-ph].
- [286] M. Peláez, U. Reinosa, J. Serreau, M. Tissier, and N. Wschebor, “Small parameters in infrared quantum chromodynamics,” (2017), arXiv:1703.10288 [hep-th].
- [287] R. Contant and M. Q. Huber, “Phase structure and propagators at non-vanishing temperature for QCD and QCD-like theories,” (2017), arXiv:1706.00943 [hep-ph].
- [288] D. Binosi, L. Chang, J. Papavassiliou, S.-X. Qin, and C. D. Roberts, “Natural constraints on the gluon-quark vertex,” *Phys. Rev. D* **95**, 031501 (2017), arXiv:1609.02568 [nucl-th].
- [289] A. C. Aguilar, J. C. Cardona, M. N. Ferreira, and J. Papavassiliou, “Non-Abelian Ball-Chiu vertex for arbitrary Euclidean momenta,” *Phys. Rev. D* **96**, 014029 (2017), arXiv:1610.06158 [hep-ph].
- [290] A. I. Davydychev, P. Osland, and L. Saks, “Quark gluon vertex in arbitrary gauge and dimension,” *Phys. Rev. D* **63**, 014022 (2001), arXiv:hep-ph/0008171.
- [291] A. C. Aguilar and J. Papavassiliou, “Chiral symmetry breaking with lattice propagators,” *Phys. Rev. D* **83**, 014013 (2011), arXiv:1010.5815 [hep-ph].
- [292] E. Rojas, J. P. B. C. de Melo, B. El-Bennich, O. Oliveira, and T. Frederico, “On the Quark-Gluon Vertex and Quark-Ghost Kernel: combining Lattice Simulations with Dyson-Schwinger equations,” *JHEP* **10**, 193 (2013), arXiv:1306.3022 [hep-ph].
- [293] H. Gies and C. Wetterich, “Renormalization flow of bound states,” *Phys. Rev. D* **65**, 065001 (2002), arXiv:hep-th/0107221.
- [294] F. Rennecke, *The Chiral Phase Transition of QCD*, Ph.D. thesis, Heidelberg University (2015).
- [295] S. Floerchinger and C. Wetterich, “Exact flow equation for composite operators,” *Phys. Lett. B* **680**, 371 (2009), arXiv:0905.0915 [hep-th].
- [296] A. Sternbeck, K. Maltman, M. Muller-Preussker, and L. von Smekal, “Determination of LambdaMS from the gluon and ghost propagators in Landau gauge,” *PoS LAT2012*, 243 (2012), arXiv:1212.2039.

- [297] O. Oliveira, A. Kizilersu, P. J. Silva, J.-I. Skullerud, A. Sternbeck, and A. G. Williams, “Lattice Landau gauge quark propagator and the quark-gluon vertex,” (2016) arXiv:1605.09632 [hep-lat].
- [298] A. Sternbeck, private communication.
- [299] C. S. Fischer, D. Nickel, and R. Williams, “On Gribov’s supercriticality picture of quark confinement,” *Eur. Phys. J. C* **60**, 1434 (2008), arXiv:0807.3486 [hep-ph].
- [300] C. S. Fischer and R. Williams, “Beyond the rainbow: effects from pion back-coupling,” *Phys. Rev. D* **78**, 074006 (2008), arXiv:0808.3372 [hep-ph].
- [301] J. S. Ball and T.-W. Chiu, “Analytic Properties of the Vertex Function in Gauge Theories. 1.” *Phys. Rev. D* **22**, 2542 (1980).
- [302] L. Fister and J. M. Pawłowski, “Yang-Mills correlation functions at finite temperature,” (2011), arXiv:1112.5440 [hep-ph].
- [303] M. Quandt and H. Reinhardt, “A covariant variational approach to Yang-Mills Theory at finite temperatures,” *Phys. Rev. D* **92**, 025051 (2015), arXiv:1503.06993 [hep-th].
- [304] U. Reinosa, J. Serreau, M. Tissier, and N. Wschebor, “Yang-Mills correlators at finite temperature: A perturbative perspective,” *Phys. Rev. D* **89**, 105016 (2014), arXiv:1311.6116 [hep-th].
- [305] U. Reinosa, J. Serreau, M. Tissier, and A. Tresmontant, “Yang-Mills correlators across the deconfinement phase transition,” *Phys. Rev. D* **95**, 045014 (2017), arXiv:1606.08012 [hep-th].
- [306] A. Cucchieri, A. Maas, and T. Mendes, “Infrared properties of propagators in Landau-gauge pure Yang-Mills theory at finite temperature,” *Phys. Rev. D* **75**, 076003 (2007), arXiv:hep-lat/0702022.
- [307] C. S. Fischer, A. Maas, and J. A. Müller, “Chiral and deconfinement transition from correlation functions: SU(2) vs. SU(3),” *Eur. Phys. J. C* **68**, 165 (2010), arXiv:1003.1960 [hep-ph].
- [308] R. Aouane, V. G. Bornyakov, E. M. Ilgenfritz, V. K. Mitrjushkin, M. Müller-Preussker, and A. Sternbeck, “Landau gauge gluon and ghost propagators at finite temperature from quenched lattice QCD,” *Phys. Rev. D* **85**, 034501 (2012), arXiv:1108.1735 [hep-lat].
- [309] A. Maas, J. M. Pawłowski, L. von Smekal, and D. Spielmann, “The Gluon propagator close to criticality,” *Phys. Rev. D* **85**, 034037 (2012), arXiv:1110.6340 [hep-lat].
- [310] A. Cucchieri, D. Dudal, T. Mendes, and N. Vandersickel, “Massive gluon propagator at zero and finite temperature,” (2012), arXiv:1202.0639 [hep-lat].
- [311] P. J. Silva, O. Oliveira, P. Bicudo, and N. Cardoso, “Gluon screening mass at finite temperature from the Landau gauge gluon propagator in lattice QCD,” *Phys. Rev. D* **89**, 074503 (2014), arXiv:1310.5629 [hep-lat].

- [312] L. Fister and A. Maas, “Exploratory study of the temperature dependence of magnetic vertices in SU(2) Landau gauge Yang–Mills theory,” *Phys. Rev. D* **90**, 056008 (2014), arXiv:1406.0638 [hep-lat].
- [313] M. Q. Huber, “An exploratory study of Yang–Mills three-point functions at non-zero temperature,” *EPJ Web Conf.* **137**, 07009 (2017), arXiv:1611.06136 [hep-ph].
- [314] M. Haas, L. Fister, and J. M. Pawłowski, “Gluon spectral functions and transport coefficients in Yang–Mills theory,” *Phys. Rev. D* **90**, 091501 (2014), arXiv:1308.4960 [hep-ph].
- [315] N. Christiansen, M. Haas, J. M. Pawłowski, and N. Strodthoff, “Transport Coefficients in Yang–Mills Theory and QCD,” *Phys. Rev. Lett.* **115**, 112002 (2015), arXiv:1411.7986 [hep-ph].
- [316] U. M. Heller, F. Karsch, and J. Rank, “Gluon propagator at high temperature: Screening, improvement and nonzero momenta,” *Phys. Rev. D* **57**, 1438 (1998), arXiv:hep-lat/9710033.
- [317] S. Datta and S. Gupta, “Screening masses in SU(2) pure gauge theory,” *Phys. Lett. B* **471**, 382 (2000), arXiv:hep-lat/9906023.
- [318] A. Cucchieri, F. Karsch, and P. Petreczky, “Propagators and Dimensional Reduction of Hot SU(2) Gauge Theory,” *Phys. Rev. D* **64**, 036001 (2001), arXiv:hep-lat/0103009.
- [319] A. Nakamura, T. Saito, and S. Sakai, “Lattice calculation of gluon screening masses,” *Phys. Rev. D* **69**, 014506 (2004), arXiv:hep-lat/0311024.
- [320] P. B. Arnold and L. G. Yaffe, “The NonAbelian Debye screening length beyond leading order,” *Phys. Rev. D* **52**, 7208 (1995), arXiv:hep-ph/9508280.
- [321] E. Braaten and A. Nieto, “On the convergence of perturbative QCD at high temperature,” *Phys. Rev. Lett.* **76**, 1417 (1996), arXiv:hep-ph/9508406.
- [322] E. Braaten and A. Nieto, “Free energy of QCD at high temperature,” *Phys. Rev. D* **53**, 3421 (1996), arXiv:hep-ph/9510408.
- [323] J. O. Andersen, M. Strickland, and N. Su, “Gluon Thermodynamics at Intermediate Coupling,” *Phys. Rev. Lett.* **104**, 122003 (2010), arXiv:0911.0676 [hep-ph].
- [324] J. O. Andersen, M. Strickland, and N. Su, “Three-loop HTL gluon thermodynamics at intermediate coupling,” *JHEP* **1008**, 113 (2010), arXiv:1005.1603 [hep-ph].
- [325] L. Fister and J. M. Pawłowski, “Functional renormalization group in a finite volume,” *Phys. Rev. D* **92**, 076009 (2015), arXiv:1504.05166 [hep-ph].
- [326] M. Tentyukov and J. A. M. Vermaseren, “The Multithreaded version of FORM,” *Comput. Phys. Commun.* **181**, 1419 (2010), arXiv:hep-ph/0702279.



- [327] K. Ahnert and M. Mulansky, [http://www.boost.org/doc/libs/1\\_60\\_0/libs/numeric/odeint/doc/html/index.html](http://www.boost.org/doc/libs/1_60_0/libs/numeric/odeint/doc/html/index.html).
- [328] Guennebaud, G. and Jacob, B., Eigen v3 (linear algebra library) <http://eigen.tuxfamily.org>.
- [329] S. G. Johnson, Cubature (multi-dimensional integration), <http://ab-initio.mit.edu/wiki/index.php/Cubature>.
- [330] J. Berntsen, T. O. Espelid, and A. Genz, “An adaptive algorithm for the approximate calculation of multiple integrals,” *ACM Transactions on Mathematical Software (TOMS)* 17, 437 (1991).
- [331] A. C. Genz and A. Malik, “Remarks on algorithm 006: An adaptive algorithm for numerical integration over an n-dimensional rectangular region,” *Journal of Computational and Applied mathematics* 6, 295 (1980).
- [332] D. F. Litim, “Optimized renormalization group flows,” *Phys. Rev. D* 64, 105007 (2001), arXiv:hep-th/0103195.
- [333] J. M. Pawłowski, M. M. Scherer, R. Schmidt, and S. J. Wetzel, “Physics and the choice of regulators in functional renormalisation group flows,” *Annals Phys.* 384, 165 (2017), arXiv:1512.03598 [hep-th].
- [334] D. Schnoerr, I. Boettcher, J. M. Pawłowski, and C. Wetterich, “Error estimates and specification parameters for functional renormalization,” *Annals Phys.* 334, 83 (2013), arXiv:1301.4169 [cond-mat.quant-gas].
- [335] B. Lucini, M. Teper, and U. Wenger, “The high temperature phase transition in SU(N) gauge theories,” *JHEP* 01, 061 (2004), arXiv:hep-lat/0307017.
- [336] C. H. Llewellyn-Smith, “A relativistic formulation for the quark model for mesons,” *Annals Phys.* 53, 521 (1969).
- [337] J. Vermaseren, “FORM GitHub Repository,” (2016), <https://github.com/vermaseren/form>.
- [338] T. Hahn, “Generating Feynman diagrams and amplitudes with FeynArts 3,” *Comput. Phys. Commun.* 140, 418 (2001), arXiv:hep-ph/0012260.
- [339] P. Nogueira, “Automatic Feynman graph generation,” *J. Comput. Phys.* 105, 279 (1993).
- [340] F. Feng and R. Mertig, “FormLink/FeynCalcFormLink : Embedding FORM in Mathematica and FeynCalc,” (2012), arXiv:1212.3522.
- [341] R. Mertig, M. Bohm, and A. Denner, “FEYN CALC: Computer algebraic calculation of Feynman amplitudes,” *Comput. Phys. Commun.* 64, 345 (1991).
- [342] V. Shtabovenko, R. Mertig, and F. Orellana, “New Developments in FeynCalc 9.0,” *Comput. Phys. Commun.* 207, 432 (2016), arXiv:1601.01167 [hep-ph].
- [343] V. Shtabovenko, “FeynHelpers: Connecting FeynCalc to FIRE and Package-X,” *Comput. Phys. Commun.* 218, 48 (2017), arXiv:1611.06793 [physics.comp-ph].

- [344] M. Wiebusch, “HEPMath 1.4: A mathematica package for semi-automatic computations in high energy physics,” *Comput. Phys. Commun.* 195, 172 (2015), arXiv:1412.6102 [hep-ph].
- [345] M. Jamin and M. E. Lautenbacher, “TRACER: Version 1.1: A Mathematica package for gamma algebra in arbitrary dimensions,” *Comput. Phys. Commun.* 74, 265 (1993).
- [346] S. A. Larin, F. V. Tkachov, and J. A. M. Vermaseren, “The FORM version of MINCER,” (1991).
- [347] A. Pukhov, E. Boos, M. Dubinin, V. Edneral, V. Ilyin, D. Kovalenko, A. Kryukov, V. Savrin, S. Shichanin, and A. Semenov, “CompHEP: A Package for evaluation of Feynman diagrams and integration over multiparticle phase space,” (1999), arXiv:hep-ph/9908288.
- [348] M. Tentyukov and J. Fleischer, “A Feynman diagram analyzer DIANA,” *Comput. Phys. Commun.* 132, 124 (2000), arXiv:hep-ph/9904258.
- [349] T. Hahn and M. Perez-Victoria, “Automatized one loop calculations in four-dimensions and D-dimensions,” *Comput. Phys. Commun.* 118, 153 (1999), arXiv:hep-ph/9807565.
- [350] M. Steinhauser, “MATAD: A Program package for the computation of MAssive TADpoles,” *Comput. Phys. Commun.* 134, 335 (2001), arXiv:hep-ph/0009029.
- [351] G. Belanger, F. Boudjema, J. Fujimoto, T. Ishikawa, T. Kaneko, K. Kato, and Y. Shimizu, “Automatic calculations in high energy physics and Grace at one-loop,” *Phys. Rept.* 430, 117 (2006), arXiv:hep-ph/0308080.
- [352] A. Andonov, A. Arbuzov, D. Bardin, S. Bondarenko, P. Christova, L. Kalinovskaya, G. Nanava, and W. von Schlippe, “SANCscope - v.1.00,” *Comput. Phys. Commun.* 174, 481 (2006), [Erratum: *Comput. Phys. Commun.* 177,623(2007)], arXiv:hep-ph/0411186.
- [353] V. Hirschi, R. Frederix, S. Frixione, M. V. Garzelli, F. Maltoni, and R. Pittau, “Automation of one-loop QCD corrections,” *JHEP* 05, 044 (2011), arXiv:1103.0621 [hep-ph].
- [354] G. Cullen *et al.*, “GoSam-2.0: a tool for automated one-loop calculations within the Standard Model and beyond,” *Eur. Phys. J. C* 74, 3001 (2014), arXiv:1404.7096 [hep-ph].
- [355] H. H. Patel, “Package-X: A Mathematica package for the analytic calculation of one-loop integrals,” *Comput. Phys. Commun.* 197, 276 (2015), arXiv:1503.01469 [hep-ph].
- [356] H. H. Patel, “Package-X 2.0: A Mathematica package for the analytic calculation of one-loop integrals,” *Comput. Phys. Commun.* 218, 66 (2017), arXiv:1612.00009 [hep-ph].
- [357] T. Ueda, B. Ruijl, and J. A. M. Vermaseren, “Forcer: a FORM program for 4-loop massless propagators,” *PoS LL2016*, 070 (2016), arXiv:1607.07318 [hep-ph].

- 
- [358] C. W. Bauer, A. Frink, and R. Kreckel, “Introduction to the GiNaC framework for symbolic computation within the C++ programming language,” *J. Symb. Comput.* **33**, 1 (2000), arXiv:cs/0004015 [cs-sc].
- [359] U. Gran, “GAMMA: A Mathematica package for performing gamma matrix algebra and Fierz transformations in arbitrary dimensions,” (2001), arXiv:hep-th/0105086.
- [360] K. Peeters, “A Field-theory motivated approach to symbolic computer algebra,” *Comput. Phys. Commun.* **176**, 550 (2007), arXiv:cs/0608005 [cs.SC].
- [361] SymPy Development Team, “SymPy homepage,” (2016), <http://www.sympy.org/>.
- [362] J. M. Martín-García, R. Portugal, and L. R. U. Manssur, “The Invar Tensor Package,” *Comput. Phys. Commun.* **177**, 640 (2007), arXiv:0704.1756 [cs.SC].
- [363] J. M. Martín-García, “xAct: Efficient tensor computer algebra for Mathematica.” (2016), <http://www.xact.es/>.
- [364] D. A. Bolotin and S. V. Poslavsky, “Introduction to Redberry: a computer algebra system designed for tensor manipulation,” (2013), arXiv:1302.1219 [cs.SC].